UNIVERSITAT DE BARCELONA

Towards a better characterization of submicron aerosol in the Mediterranean basin

Marta Via González

TOWARDS A BETTER CHARACTERISATION OF SUBMICRONIC AEROSOL IN THE MEDITERRANEAN BASIN

MARTA VIA GONZÁLEZ

Ph.D. Thesis

UNIVERSITAT DE BARCELONA

TOWARDS A BETTER CHARACTERISATION OF SUBMICRON AEROSOL IN THE WESTERN MEDITERRANEAN BASIN

PROGRAMA DE DOCTORAT EN FÍSICA

Autoria
Marta Via González

Direcció
Dra. María Cruz Minguillón Bengochea
Dr. Andrés Alastuey Urós

Tutoria
Joan Bech Rustullet

UNIVERSITAT DE BARCELONA

Marta Via González
Towards a better characterization of submicron aerosol in the Mediterranean basin **2019-2023**

Institute of Environmental Assessment and Water Research (IDAEA)
Spanish National Research Council (CSIC)
Environmental Geochemistry and Atmospheric Research Group
C/ Jordi Girona, 18-26
08034 Barcelona, Spain

Universiy of Barcelona
Applied Physics and Meteorology Department
C/ Martí i Franquès, 2
08034 Barcelona, Spain

Acknowledgements are explicited in the "Acknowledgements and Financial Support" (Section 8.3).

A la meva família i amistats,
si és que existeix una línia
que els diferencii.

There are no separate systems.
The world is a continuum.
Where to draw a boundary around a system
depends on the purpose of the discussion.
Donella H. Meadows

ABSTRACT

Atmospheric aerosol is an ensemble of atmospheric pollutants with a severe impact on human health and the Earth's climate. Particulate Matter (PM) effects vary depending on the composition and size. However, current air quality guidelines (AQG) from WHO and from the EU Commission only define threshold standards for bulk PM_{10} and $PM_{2.5}$ concentrations. In terms of health, the smaller the particles, the deeper they penetrate into the respiratory system, and they can even diffuse into the bloodstream and circulate to other parts of the organism. The adverse effects on the tissues in which they are deposited depend on the PM composition. Regarding climate, PM size and composition relevantly affect many aerosol-radiation direct and indirect interactions, which regulate troposphere temperature. Consequently, the consideration of these properties is relevant for present and future climate descriptions.

Barcelona, the city where this study focuses, is located in the Mediterranean basin, a region with high complexity in terms of air pollution. The particularities of this area stem from its great diversity of atmospheric circulations, hilly relief prompting many local atmospheric processes, and a wide assortment of aerosol sources, both natural and anthropogenic. This context provides a perfect breeding ground for aerosol mixture, aerosol transformation, and highly-polluted episodes. For all of this, the nature of this enclave requires thorough monitoring of PM in order to protect the population from exposition accurately. This dissertation focuses on aerosol evolution over the last decade, with a more detailed study for May 2014 - May 2015 and September 2017 - October 2018.

Submicronic PM (PM_1) levels in Barcelona already exceeded the $PM_{2.5}$ WHO AQG values both annually and episodically in the 2014-2018 period. A reason for the surpasses of these thresholds is the lack of understanding of the nature of the bulk PM, which hinders the effectiveness of the design of abatement regulations. In this direction, the European Commission published in October 2022 a document announcing a revision of the legislated pollution thresholds. This document also enforces the measurement of, amongst others, PM composition, since its bulk reduction has to be tackled by aiming at its sources. The Barcelona PM composition and origins are the matter of research of this dissertation, focusing on the unregulated

submicronic particles with the purpose of providing a solid background for future threshold design.

The objective of this thesis is to describe the PM_1 sources in Barcelona by means of source apportionment (SA) techniques. The Positive Matrix Factorisation (PMF) algorithm is one of the most widely used approaches for SA and is the tool used in this dissertation. A secondary aim of this study is the improvement of the SA methodology itself. This is accomplished by testing the outcomes of new methodologies involving the more automatic analysis and dataset junction with several approaches.

A field-deployed aerosol mass spectrometer was used at the Barcelona site for continuous PM_1 measurements, and SA was performed on submicronic Organic Aerosol (OA) contained in it. First, SA was tackled from a conventional methodology, the *seasonal* PMF, then, the novel *rolling* PMF methodology was tested and compared to the fore one. Finally, a comprehensive PM_1 SA was performed based on an ensemble of different datasets coming from a variety of measurement techniques. These steps enabled a progressive aerosol composition understanding and acknowledgement of subsequent aerosol trends. Moreover, the results obtained were used for a preliminary assessment of Barcelona aerosol toxicity and its effects on aerosol-radiation interactions.

A PM_1 concentrations decrease was found in the 2014-2018 period, a trend confirmed by other studies at the site. Its relative composition changed significantly; a decrease was found for SO_4^{2-}, black carbon (BC), and NH_4^+, while NO_3^- increased and OA levels were found stable. The OA SA, conducted here by means of the so-called *seasonal* PMF, revealed that its sources were: secondary OA (SOA, 55%-70%), road traffic OA (HOA, 12%-19%), cooking-like OA (COA, 14%-18%), and biomass burning OA (BBOA, 4%-6%). These sources are similar to those reported in other sites across the Mediterranean region. In this study, all the primary OA sources were found in a clear decrease from 2014 to 2018. An increasing SOA proportion and SOA oxidation state were also observed. These increments could be explained by a likely increase in the oxidation capacity of the atmosphere, related to the accumulation of oxidative radicals reported in many cities. In order to bridge the possible inter-annual variability in that period, the time period was elongated (2014-2021) detecting the same underlying trends.

Subsequently, the *rolling* PMF methodology was also applied, which, by using a moving window, allows for considering daily profile variation and facilitates PMF application on continuously-growing datasets. The evaluation of the *rolling* PMF was performed from two approaches with different assessment capabilities. On the one hand, the comparison of the outcomes of both methodologies was based on multiple real-world datasets from different European sites. On the other hand, a synthetic dataset was used, allowing for the quantification of the accuracy of each of the methodologies. Both approaches revealed similar quality results for *seasonal* PMF and *rolling* PMF, but the *rolling* PMF showed lower model residuals and higher adaptability to actual measurements. The synthetic dataset approach also highlighted the influence of the *a-priori* information introduced into the PMF algorithm, valuable information for future OA SA protocol modifications.

Then, another state-of-the-art SA methodology was used for a whole PM_1 SA, the multi-time-resolution PMF. This technique allows for coupling different instrumentation datasets in their native time resolution, in this case, ACSM (OA + secondary inorganic components), aethalometer (BC speciated regarding its liquid and solid fuel origins), and offline filter samples (metals). This method permits maintaining the combined datasets' native high resolution, as the practice of averaging to make the timestamps of all instrumentation datasets coincide was found to degrade the quality of the solution. This ensemble SA resulted in 8 PM_1 sources: ammonium sulphate and heavy oil combustion, ammonium nitrate and ammonium chloride, aged SOA, road traffic, biomass burning, fresh SOA, COA, and industry. In comparison to previous SA results on the same period, this solution is more complete due to its higher time resolution and its inclusion of more species that characterise further their time series and fingerprints. For these advantages, this technique is highly encouraged to be used in further aerosol description studies when different time-resolution datasets are available.

In this dissertation, the aerosol composition scenario change resulting from the reported trends in this thesis was assessed in terms of climate and health affectation from prior studies concerning specific sources.

Regarding climate, it is known that SOA, the pollutant of growing contribution, is a significant light extinction enhancer through light absorption and light scattering. These two direct aerosol-light interactions imply atmospheric warming and cooling,

respectively. The final effect of the reported SOA increasing trend on the troposphere temperature will have to be determined through atmospheric modelling. The retrieval of temporal variation of PM_1 sources is vital to cross-validate modelled PM levels with real-world measurements. This practice will improve atmospheric modelling accuracy and, consequently, aerosol trends impact assessment on both local and global climate.

Preliminary source toxicity assessment revealed that SOA is the major driver of oxidative potential in Barcelona. Being SOA an increasing pollutant with concerning health impact, continuous monitoring is advisable in order to fully characterise its origins, influence, and time variations to contribute to bridging the current gaps in the literature. Moreover, the outcoming source time series of this thesis is also valuable material for further epidemiological studies, which require long-term detailed information.

With the aim of further climate and health impact aerosol impact assessment, this thesis provides mid-term PM_1 sources diagnosis. One of the main findings consists of the acknowledgement of an increasing trend of SOA regardless of a PM_1 decrease related to a decrease in primary OA pollution. SOA is especially concerning in terms of health effects, hence this pollutant is to be continuously monitored to deeply understand its precursors and formation mechanisms to design effective abatement policies.

RESUM

L'aerosol atmosfèric és un conjunt de contaminants atmosfèrics amb un sever impacte en la salut humana i el clima de la Terra. La repercussió del material particulat (PM) varia depenent de la seva composició i mida. Tanmateix, les actuals directrius per a la qualitat de l'aire (AQG) de l'OMS i de la Comissió Europea només defineixen llindars estandarditzats per a concentracions de PM_{10} i $PM_{2.5}$ en massa. En termes de salut, com més petites són les partícules, més profundament penetren en el sistema respiratori i poden fins i tot entrar per difusió al rec sanguini i circular a altres parts de l'organisme. Els efectes adversos en els teixits en què es dipositin depenen de la composició del PM. Pel que fa al clima, la mida i la composició del PM afecten rellevantment moltes interaccions aerosol-radiació directes i indirectes, que regulen la temperatura de la troposfera. Per consegüent, la consideració d'aquestes propietats és rellevant per a la descripció present i futura del clima.

Barcelona, la ciutat en què es focalitza aquest estudi, està situada a la conca mediterrània, una regió amb alta complexitat en termes de qualitat de l'aire. Les particularitats d'aquesta zona resulten de la seva vasta diversitat de circulacions atmosfèriques, relleu acusat provocant processos atmosfèrics locals i un variat assortiment de fonts d'aerosol, tant naturals com antropogèniques. Aquest context suposa un perfecte camp de cultiu per a la barreja d'aerosol, transformació d'aerosol i episodis d'alta contaminació. Per tot això, la natura d'aquesta localització requereix un monitoratge conscienciós del PM amb l'objectiu de protegir la població efectivament de la seva exposició. Aquesta dissertació es concentra en l'evolució de l'aerosol al llarg de l'última dècada, amb un estudi més detallat per a maig 2014 - maig 2015 i setembre 2017 - octubre 2018.

Els nivells de PM submicrònic (PM_1) a Barcelona ja van excedir els valors AQG de $PM_{2.5}$ tant anualment com episòdicament en el període 2014-2018. Una raó per a la superació d'aquests llindars és la incomprensió de la naturalesa del PM, que dificulta el disseny de les normatives de mitigació. En aquesta direcció, la Comissió Europea va publicar l'octubre de 2022 un document anunciant una revisió dels llindars de contaminació legislats. Aquest document també imposa la mesura, d'entre altres, la composició del PM, ja que la seva reducció ha de ser adreçada apuntant a les

seves fonts. La composició i l'origen del PM a Barcelona són la matèria de recerca en aquesta dissertació, focalitzant-se en les desregulades partícules submicròniques amb el propòsit de proveir d'un sòlid coneixement per a un futur disseny de la seva normativa.

L'objectiu d'aquesta tesi és descriure les fonts de PM_1 a Barcelona per mitjà de tècniques de contribució de fonts (SA). L'algoritme de Factorització de Matriu Positiva (PMF) és un dels enfocaments més utilitzats per al SA i és l'eina emprada per a aquesta dissertació. Un objectiu secundari d'aquesta tesi és la millora de la pròpia metodologia del SA. Això és executat per mitjà del testatge a través de diferents mètodes de les noves metodologies que impliquen una anàlisi més automàtica i l'acoblament de conjunts de dades.

Un espectròmetre de masses instal·lat a l'estació de Barcelona va ser emprat per a la mesura contínua del PM_1, i el SA va ser executat per a l'Aerosol Orgànic (OA) submicrònic contingut en ell. Primer, el SA va ser aproximat des de la metodologia convencional el *seasonal* PMF, i després la novedosa metodologia *rolling* PMF va ser aplicada i comparada amb l'anterior. Finalment, un estudi detallat del SA de PM_1 va ser executat basat en un conjunt de dades provinents de diferents tècniques de mesura. Aquests passos van permetre la comprensió progressiva de la composició i el reconeixement de les tendències subjacents de l'aerosol. A més, els resultats obtinguts van ser utilitzats per a una avaluació preliminar de la toxicitat de l'aerosol de Barcelona i els seus efectes en les interaccions aerosol-radiació.

Durant el període 2014-2018 es va observar un decreixement del PM_1, una tendència confirmada per altres estudis a la mateixa estació. La seva composició relativa va canviar significativament; es va trobar una disminució del SO_4^{2-}, carbó negre (BC) i NH_4^+, mentre el NO_3^- va augmentar i els nivells d'OA van mantenir-se estables. El SA de l'OA, dut a terme aquí pèr mitjà de l'anomenat *seasonal* PMF, va revelar que les seves fonts són: OA secundari (SOA, 55%-70%), OA de trànsit rodat (HOA, 12%-19%), OA derivat de la cuina (COA, 14%-18%) i OA de crema de biomassa (BBOA, 4%-6%). Aquestes fonts són similars a les trobades en altres estacions de la regió del Mediterrani. En aquest estudi, totes les fonts d'aerosol primari es van trobar en clara tendència descendent des del 2014 al 2018. Contràriament es va observar un creixement de la proporció de SOA i també de l'estat d'oxidació del SOA. Aquests increments podrien ser explicats per un possible creixement de la capacitat oxidativa

de l'atmosfera relacionat amb l'acumulació de radicals oxidants reportada en diverses ciutats. Amb l'objectiu de salvar la possible variabilitat interanual del període, el període temporal ha estat allargat (2014-2021) i les mateixes tendències van ser reconegudes.

Posteriorment, la metodologia del *rolling* PMF també es va aplicar, la qual, emprant una finestra mòbil, permet descriure la variació diària dels perfils i facilita l'aplicació del PMF a conjunts de dades en continu creixement. L'avaluació del *rolling* PMF es va executar des de dos vessants amb capacitats de verificació diferents. D'una banda, la comparació dels resultats de les dues metodologies es va basar en la comparació de múltiples conjunts de dades de mesures atmosfèriques reals de diferents estacions d'Europa. D'altra banda, un conjunt de dades sintètic va ser utilitzat, facilitant la quantificació de l'exactitud de cadascuna de les metodologies. Les dues aproximacions van revelar resultats de qualitat similar per a les metodologies *rolling* i *seasonal*, però el *rolling* PMF va mostrar menors residus de model i major adaptabilitat a les mesures reals. El conjunt de dades sintètic també va posar de manifest la influència de la informació introduïda *a priori* a l'algoritme PMF, el qual suposa un coneixement valuós per a futures modificacions del protocol per al SA de l'OA.

Després, un altra metodologia avançada per al SA va ser usada per al PM_1 en global, el multi-resolució-temporal PMF. Aquesta tècnica permet acoblar conjunts de dades provinents de diferents instruments en la seva resolució temporal original, en aquest cas, ACSM (OA + components inorgànics secundaris), aethalòmetre (BC diferenciat segons el seu origen de combustible líquid o sòlid), i mostres de filtres offline (metalls). Aquest mètode permet mantenir la resolució temporal original dels conjunts de dades combinats, ja que la pràctica de fer la mitjana de les dades per fer coincidir els períodes de mesura es va trobar desfavorable per a la qualitat de la solució. El SA d'aquesta combinació va resultar en 8 fonts de PM_1: sulfat d'amoni i combustió de fuel pesat, nitrat d'amoni i clorur d'amoni, SOA envellit, trànsit rodat, crema de biomassa, SOA fresc, COA i indústria. En comparació amb previs resultats de SA en el mateix període, aquesta solució és més completa degut a la seva major resolució temporal i la inclusió de més espècies que caracteritzen millor la seva sèrie temporal i el seu perfil. Per tots aquests avantatges, aquesta tècnica s'aconsella per al seu ús en futurs estudis de descripció d'aerosol per a conjunts de dades amb diferent resolució temporal.

En aquesta dissertació, el canvi d'escenari de composició de l'aerosol resultant de les tendències reportades ha estat avaluat en termes de clima i salut a partir d'estudis previs que consideren fonts específiques.

Pel que fa al clima, és conegut que el SOA, el contaminant de contribució creixent, és un potenciador rellevant de l'extinció de llum a través de l'absorció de llum i la dispersió de llum. Aquestes dues interaccions directes aerosol-llum impliquen escalfament i refredament de l'atmosfera, respectivament. L'efecte final de la tendència creixent del SOA reportada a la temperatura de la troposfera haurà de ser determinat a través de modelització atmosfèrica. L'extracció de sèries temporals de les fonts de PM_1 és vital per a verificar els nivells modelitzats de PM amb mesures del món real. Aquesta pràctica millorarà l'exactitud de la modelització atmosfèrica i consegüentment l'avaluació de l'impacte de les tendències de l'aerosol en el clima local i global.

L'estudi preliminar de la toxicitat de les fonts ha revelat que el SOA és el major causant del potencial d'oxidació a Barcelona. Essent el SOA un contaminant en creixement amb un nociu efecte en la salut, un monitoreig continu és recomanable per tal de caracteritzar detalladament els seus orígens, influències i variacions temporals, i contribuïr a les actuals carències de la literatura. A més, les sèries temporals de les fonts obtingudes en aquesta tesi també són material valuós per a futurs estudis epidemiològics, que requereixen detallada informació de períodes prolongats.

Amb l'objectiu de futura descripció de l'impacte de l'aerosol sobre el clima i la salut, aquesta tesi proveeix amb una diagnosi de fonts de PM_1 de mitjana durada. Un dels resultats més rellevants consisteix en la detecció d'una tendència creixent del SOA independentment de la disminució del PM_1, relacionat amb el decreixement de l'OA primari. El SOA és especialment preocupant pels seus efectes en la salut, per tant, aquest contaminant ha de ser contínuament monitorejat per tal d'entendre els seus precursors i mecanismes de formació amb l'objectiu de dissenyar mesures de mitigació efectives.

RESUMEN

El aerosol atmosférico es un conjunto de contaminantes atmosféricos con un severo impacto en la salud humana y el clima de la Tierra. La repercusión del material particulado (PM) varía dependiendo de su composición y tamaño. Sin embargo, las actuales directrices para la calidad del aire (AQG) de la OMS y la Comisión Europea sólo definen umbrales estandarizados para concentraciones de PM_{10} y $PM_{2.5}$ en su totalidad. En términos de salud, como más pequeñas son las partículas, más profundamente penetran en el sistema respiratorio y pueden incluso entrar por difusión al riego sanguíneo y circular a otras partes del organismo. Los efectos adversos en los tejidos en los cuales sean depositadas dependen de la composición del PM. En cuánto al clima, el tamaño y la composición del PM afectan relevantemente muchas interacciones aerosol-radiación directas e indirectas, que regulan temperatura de la atmósfera. Consiguientemente, la consideración de estas propiedades es relevante para la descripción presente y futura del clima.

Barcelona, la ciudad en la que se focaliza este estudio, está situada a la cuenca mediterránea, una región con alta complejidad en términos de calidad del aire. Las particularidades de esta zona son el resultado de su vasta diversidad de circulaciones atmosféricas, relieve acusado provocando procesos atmosféricos locales y un variado surtido de fuentes de aerosol, tanto naturales como antropogénicas. Este contexto supone un perfecto campo de cultivo para la mezcla de aerosol, transformación de aerosol y episodios de alta contaminación. Por todo esto, la naturaleza de esta localización requiere un monitoreo concienzudo del PM con el objetivo de proteger la población efectivamente de su exposición. Esta disertación se concentra en la evolución del aerosol a lo largo de la última década, con un estudio más detallado para mayo 2014 - mayo 2015 y septiembre 2017 - octubre 2018.

Los niveles de PM submicrónico (PM_1) en Barcelona ya excedieron los valores AQG de $PM_{2.5}$ tanto anualmente como episódicamente en el periodo 2014-2018. Una razón de la superación de estos umbrales es la incomprensión de la naturaleza del PM, que dificulta el diseño de las normativas de mitigación. En esta dirección, la Comisión Europea publicó en octubre de 2022 un documento anunciando una revisión de los umbrales de contaminación legislados. Este documento también impone la

medida de, entre otras, la composición del PM, puesto que su reducción tiene que ser dirigida apuntando a sus fuentes. La composición y el origen del PM en Barcelona son la materia de investigación en esta disertación, focalizándose en las desreguladas partículas submicrónicas con el propósito de proveer de un sólido conocimiento para un futuro diseño de su normativa.

El objetivo de esta tesis es describir las fuentes de PM_1 en Barcelona por medio de técnicas de contribución de fuentes (SA). El algoritmo de Factorización de Matriz Positiva (PMF) es uno de los enfoques más utilizados para el SA o es la herramienta empleada para esta disertación. Un objetivo secundario de esta tesis es la mejora de la propia metodología del SA. Esto es ejecutado por medio del testeo a través de diferentes métodos de las nuevas metodologías que implican un análisis más automático y el acoplamiento de conjuntos de datos.

Un espectrómetro de masas instalado a la estación de Barcelona fue empleado para la medida continua del PM_1, y el SA fue ejecutado para el Aerosol Orgánico (OA) submicrónico contenido en él. Primero, el SA fue aproximado desde la metodología convencional *seasonal* PMF, y después la novedosa metodología *rolling* PMF fue aplicada y comparada con la anterior. Finalmente, un estudio detallado del SA de PM_1 fue ejecutado basado en un conjunto de datos provenientes de diferentes técnicas de medida. Estos pasos permitieron la comprensión progresiva de la composición y el reconocimiento de las tendencias subyacentes del aerosol. Además, los resultados obtenidos fueron utilizados para una evaluación preliminar de la toxicidad del aerosol de Barcelona y sus efectos en las interacciones aerosol-radiación.

Durante el periodo 2014-2018 se observó un decrecimiento del PM_1, una tendencia confirmada por otros estudios en la misma estación. Su composición relativa cambió significativamente; se encontró una disminución del SO_4^{2-}, carbono negro (BC) y NH_4^+, mientras el NO_3^- aumentó y los niveles de OA se mantuvieron estables. El SA de la OA, llevado a cabo aquí por medio del llamado **seasonal* PMF, reveló que sus fuentes son: OA secundario (SOA, 55%-70%), OA de tráfico rodado (HOA, 12%-19%), OA derivado de la cocina (COA, 14%-18%) y OA de crema de biomasa (BBOA, 4%-6%). Estas fuentes son similares a los encuentros en otras estaciones de la región del Mediterráneo. En este estudio, todas las fuentes de aerosol primario se encontraron en clara tendencia descendente desde el 2014 al 2018. También se observó un crecimiento de la proporción de SOA y del estado de oxidación del SOA. Estos incrementos

podrían ser explicados por un posible crecimiento de la capacidad oxidativa de la atmósfera relacionado con la acumulación de radicales oxidantes reportada varías ciudades. Con el objetivo de salvar la posible variabilidad interanual del periodo, el periodo temporal ha sido alargado (2014-2021) y las mismas tendencias fueron observadas.

Posteriormente, la metodología del *rolling* PMF también se aplicó, la cual, empleando una ventana móvil, permite describir la variación diaria del perfiles y facilita la aplicación del PMF a conjuntos de datos continuamente en crecimiento. La evaluación del *rolling* PMF se ejecutó desde dos vertientes con capacidades de verificación diferentes. Por un lado, la comparación de los resultados de las dos metodologías se basó en la comparación de múltiplos conjuntos de datos de medidas atmosféricas reales de diferentes estaciones de Europa. Por otro lado, un conjunto de datos sintético fue empleado, facilitando la cuantificación de la exactitud de cada una de las metodologías. Las dos aproximaciones revelaron resultados de calidad similar para las metodologías *rolling* y *seasonal*, pero el *rolling* PMF mostró menores residuos de modelo y mayor adaptabilidad a las medidas reales. El conjunto de datos sintético también puso de manifiesto la influencia de la información introducida *a priori* al algoritmo PMF, el cual supone un conocimiento para futuras modificaciones del protocolo para el OA SA.

Después, otra metodología avanzada para el SA fue empleada para el PM_1 en global, el multi-resolución-temporal PMF. Esta técnica permite acoplar conjuntos de datos provenientes de diferentes instrumentos en su resolución temporal original, en este caso, ACSM (OA + componentes inorgánicos secundarios), aethalómetro (BC diferenciado según su origen de combustible líquido o sólido), y muestras de filtros offline (metales). Este método permite mantener la resolución temporal original de los conjuntos de datos combinados, puesto que la práctica de promediar los datos para hacer coincidir los periodos de medida se encontró desfavorable para la calidad de la solución. El SA de esta combinación resultó en 8 fuentes de PM_1: sulfato de amonio y combustión de fuel pesado, nitrato de amonio y cloruro de amonio, SOA envejecido, tráfico rodado, quema de biomasa, SOA fresco, COA e industria. En comparación con previos resultados de SA en el mismo periodo, esta solución es más completa debido a su mayor resolución temporal y la inclusión de más especies que caracterizan mejor su serie temporal y su perfil. Por todas estas ventajas, esta técnica se aconseja para su uso en futuros estudias de descripción de aerosol para conjuntos de datos con

diferente resolución temporal.

En esta disertación, el cambio de escenario de composición del aerosol resultante de las tendencias reportadas ha sido evaluado en términos de clima y salud a partir de estudios previos que consideran fuentes específicas.

En cuanto al clima, es conocido que el SOA, el contaminante de contribución creciente, es un potenciador relevante de la extinción de luz a través de la absorción de luz y la dispersión de luz. Estas dos interacciones directas aerosol-luz implican calentamiento y enfriamiento de la atmósfera, respectivamente. El efecto final de la tendencia creciente del SOA reportada a la temperatura de la troposfera tendrá que ser determinado a través de modelización atmosférica. La extracción de series temporales de las fuentes de PM_1 es vital para verificar los niveles modelizados de PM con medidas del mundo real. Esta práctica mejorará la exactitud de la modelización atmosférica y consecuentemente la evaluación del impacto de las tendencias del aerosol en el clima local y global.

El estudio preliminar de la toxicidad de las fuentes ha revelado que el SOA es el mayor causante del potencial de oxidación en Barcelona. Siendo lo SOA un contaminante en crecimiento con un nocivo efecto en la salud, un monitoreo continuo es recomendable para caracterizar en detalle sus orígenes, influencias y variaciones temporales, y contribuir así a las actuales carencias en la literatura. Además, las series temporales de las fuentes obtenidas en esta tesis también son material valioso para futuros estudios epidemiológicos, que requieren detallada información de periodos prolongados.

Con el objetivo de futura descripción del impacto del aerosol sobre el clima y la salud, esta tesis provee con una diagnosis de fuentes de PM_1 de media duración. Uno de los hallazgos más importantes consiste en la detección de una tendencia creciente del SOA independientemente de la disminución del PM_1, relacionado con el decrecimiento del OA primario. El SOA es especialmente preocupante por sus efectos en la salud, por lo tanto, este contaminante tiene que ser continuamente monitoreado para entender sus precursores y mecanismos de formación con el objetivo de diseñar medidas de mitigación efectivas.

ACKNOWLEDGEMENTS

En primer lugar quiero agradecer el enorme apoyo que me han brindado mis directores de tesis, la Dra. María Cruz Minguillón y el Dr. Andrés Alastuey. Os estoy muy agradecida por ofrecerme la oportunidad de introducirme en este mundo y por propulsar siempre mi trabajo. Gracias por tratarme siempre con una actitud de respeto, confianza y cuidado. A Mari Cruz le agradezco especialmente su comprensión con mis errores, mis tempos y mis dudas. También todo aquello que he aprendido de ella que va más allá de la ciencia. A Andrés le agradezco el enseñarme a mirar las cosas con perspectiva y calma. Muchas gracias a los dos por estos cuatro años de doctorado que me han ayudado a entender tantas cosas.

M'agradaria agraïr al Dr. Joan Bech, de la Universitat de Barcelona, el seu suport com a tutor d'aquesta tesi i la seva confiança en introduïr-me al món de la recerca. També a la Universitat de Barcelona per fer-me arribar fins aquí.

I would like to earnestly acknowledge my EGAR group in IDAEA-CSIC. Thanks for generating such a stimulating environment for learning. Gracias a la Dra. Cristina Reche, la Dra. Noemí Pérez, el Dr. Marco Pandolfi, el Dr. Jesús Yus, Jordi Massagué, Jordi Gil, Jesús Parga, Marten In't Veld y Diana Blanco por proveerme de las medidas presentadas en esta tesis y por cuidar tanto los datos. También a todes les que estáis detrás de estos datos sin ser yo consciente, gracias. Gràcies també al Dr. Xavier Querol per liderar aquest equip i creure fermament en el que fem. Vull expressar especials agraïments també a totes aquelles que m'heu acompanyat des d'una dimensió més humana, començant pels meus estimats companys de despatx que sempre han tingut bones paraules per a mi: Adolfo, Jesús, Amaia, Marten, Inés, Jordi. Eternament agaïda pel suport. També a la Dra. Cristina Carnerero, el Dr. Pedro Trechera, el Dr. Jesús Yus i la Dra. Rosa Lara per ser referents tan propers. Moltes gràcies també a les futures doctores i doctors del grup per donar tant goig dins i fora del centre, estic segura que fareu un treball magnífic. Gràcies a totes per acompanyar-me en aquesta experiència tan completa.

Also, I would like to acknowledge all those who dealt with our ACSM issues in the ARI and ADDAIR teams, with special thanks to Dr. Philip Croteau and Dr. Vincent

Crenn.

I would like to express my gratitude to the LAC group from PSI for hosting and helping me both in my visit and my doctoral development. Special thanks for their patience with me to Dr. André Prevôt, Dr. Francesco Canonaco, Dr. Anna Tobler and Dr. Kaspar Daellenbach, your support and guidance were extremely helpful in this journey.

I would like to acknowledge all the collaborators and co-authors I have had the privilege to work with. Special thanks to the COLOSSAL community for offering me valuable formation, a piece of advice when needed, and support with the work I have carried out. I want to thank immensely the support of my colleague Ian, Dr. Gang Chen, or as I call him, my *big brother in science*.

En una nota més personal, m'agradaria fer en primer lloc un reconeixement de la importància de la música, l'art i la cultura en general. Pot semblar un agraïment inesperat i fora de context, però al final aquestes coses són les que m'han empès i fet vibrar els dies menys bons.

En distàncies encara més curtes, vull expressar el meu agraïment i afecte als qui m'heu cuidat durant aquest projecte. Moltes gràcies a l'Antoni per recollir-me tantes vegades i al meu grup D per ser sempre tan acollidores i sinceres. Gràcies a la gent del meu poble que em fa adonar-me que es poden fer grans coses amb empenta i treball. Moltes gràcies a tots els meus amics de la uni, per créixer junts com a físics i com a adults. Gràcies també a la Marina, l'Elisa i el Miguel, no hagués pogut trobar millors companys *meteofreaks*. Gràcies, Adolfo, per l'abraçada setmanal que m'ha fet tant bé. Gràcies Carla i Judit per ser casa, és un plaer compartir vida amb vosaltres. Eterns agraïments a l'Adrià per compartir tants moments tan diversos i sempre recolzar-me en tot. Albert, gràcies per fer-me els dies substancialment millors en aquesta recta final, ets un sol. Gràcies també i sobretot a les meves amigues: Sergi, Naomi, Susanna, Prats, Bermu, Sara, Júlia N., Júlia A., Gaspar, Júlia, Marina, Judit. Sou les millors i jo sense vosaltres no vull res. Per últim, vull agraïr l'inquantificable esforç i paciència que han dipositat en mi els meus pares, la Carme i el Sergi. Mai us estaré prou agraïda, us estimo.

CONTENTS

LIST OF FIGURES

LIST OF TABLES

ACRONYMS

AA Ascorbic Acid

ACTRIS Aerosol, Clouds and Trace gases Research InfraStructure network

ACSM Aerosol Chemical Speciation Monitor

ACl Ammonium chloride

AN Ammonium nitrate

AOD Aerosol Optical Depth

AS Ammonium sulphate

a.s.l. Above Sea Level

AN Ammonium sulphate

BB Biomass Burning

BBOA Biomass Burning Organic Aerosol

BC Black Carbon

BC_{lf} Black Carbon Liquid Fuel

BC_{sf} Black Carbon Solid Fuel

BCN-PR Barcelona - Palau Reial

BrC Brown Carbon

CMB Chemical Mass Balance

CCN Cloud Condensation Nuclei

CCOA Coal Combustion Organic Aerosol

CE Collection Efficiency

COA Cooking-like Organic Aerosol

COLOSSAL Chemical OnLine CompoSition and Source Apportionment of fine aerosoL

DTT Dithiothreitol

E_{abs} Absorption Enhancement

EC Elemental Carbon

EUC European Union Comission

GAW Global Atmospheric Watch

HOA Hydrocarbon-like Organic Aerosol

IE Ionisation Efficiency

IN Ice Nuclei

IN Industrial Organic Aerosol

LO-OOA Less Oxidised Oxygenated Organic Aerosol

ME-2 Multi-linear Engine 2

MLR Multi-Linear Regression

MO-OOA More Oxidised Oxygenated Organic Aerosol

MSY Montseny - El Brull

MTR Multi Time Resolution

NOAA National Ocean and Atmospheric Administration

OA Organic Aerosol

OC Organic Carbon

OM Organic Matter

ON Organonitrates

OOA Oxygenated Organic Aerosol

OS Organosulphates

OP Oxidative Potential

PCA Principal Components Analysis

POA Primary Organic Aerosol

PM_x Particulate Matter of aerodynamic diameter below x μm

PMF Positive Matrix Factorisation

PR Palau Reial

Q Quadrupole

RF Response Factor

RF_{ARI} Radiatiove Forcing due to Aerosol-Radiation Interactions

RIE Relative Ionisation Efficiency

ROS Reactive Oxidative Species

SA Source Apportionment

ShOA Shipping Organic Aerosol

SOA Secondary Organic Aerosol

SIA Secondary Inorganic Aerosol

TOA Top Of Atmosphere

ToF Time of Flight

TR Time Resolution

UMR Unit Mass Resolution

WMB Western Mediterranean Basin

XVPCA Xarxa de Vigilància i Previsió de la Contaminació Atmosfèrica

Part I

INTRODUCTION

1

INTRODUCTION

The composition of the atmosphere has evolved significantly with respect to Earth's primitive mixture. The early Earth's atmosphere consisted of hydrogen and helium, gases originating from the gassy sun disk, at such high temperatures which enabled them to escape Earth's gravity. The posterior young Earth atmosphere came from Earth itself, as the active surface volcanic activity released water vapour, NH_3 and CO_2, which dissolved into the oceans. The apparition of current atmospheric gases such as O_2 and N_2 was driven by the apparition of life and weathering. O_2 was emitted by plants and certain bacteria, generating it from sunlight and CO_2, causing a remarkable drop in the latter gas. The NH_3 molecules in the atmosphere were broken apart by sunlight, leaving N_2, a very stable gas, as the main component of the atmosphere. The other product gas from this reaction, H_2, being the lightest element, rose to the top of the atmosphere eventually drifting into space (Seinfeld & Pandis, 2008).

The current atmosphere is constituted mainly of permanent gases: 78% of nitrogen, 21% of oxygen, and 1% of argon. Other present components in very variable concentrations are water vapour, CO, NO_2, aerosols and other trace gases. Human activity has prompted rapid changes in the atmospheric content for the last two hundred years of anthropic development, due to energy production based on the combustion of fossil fuels, industrial and agricultural activities, biomass burning, and deforestation, amongst others. Anthropogenic emissions to the atmosphere take place in the three states of matter and impact severely the atmosphere composition as they: i) catalyze processes (e.g. catalytic stratospheric ozone, O_3, destruction); ii) can be more efficient than the originally involved constituents in certain ongoing processes (certain emitted anthropogenic greenhouse gases are even more efficient on retaining heat than CO_2, the most abundant greenhouse gas); iii) can be accumulated in significant amounts through the years even if the amounts are small compared to the mass of the atmosphere (Ravishankara, 2003).

1.1 ATMOSPHERIC AEROSOL

Aerosol is defined as solid, liquid, or mixed-phase particles suspended in the air (Seinfeld & Pandis, 2008), and are known to be diverse in size, number, shape, surface area, solubility, redox activity, chemical composition, and formation and sink mechanisms. Consequently, their lifetime in the atmosphere varies widely from hours to weeks. The term aerosol is usually misidentified with the Particulate Matter (PM) term, which refers to the particles of the aerosol deprived of the air in which they are suspended (Pöschl, 2005). Thus, the term aerosol (and PM) will be used hereinafter when the presence of the surrounding air is (not) significant.

Regarding their formation mechanisms, aerosol can be classified as primary, if it is directly emitted in the atmosphere, or as secondary if it is formed in the atmosphere from gaseous or gaseous and solid/liquid precursors (Meszaros et al., 1999; Seinfeld & Pandis, 2008). Regarding their origin, they can also be divided into natural or anthropogenic. Natural aerosol sources include dust, sea spray, wildfire emissions, volcanic emissions, plant debris, and other biogenic sources, either primary or secondary (Carslaw et al., 2010). Anthropogenic emissions stem from human activities and include combustion, agriculture, industry, traffic, construction, cooking, etc. Also all those secondary sources from anthropogenic precursors are considered of anthropic origin.

The aerosol climatology varies strongly depending on location due to variability in concentration and characteristics. To characterise this variation, many satellite studies measure the aerosol optical depth (AOD), the transmittance of radiation along an atmospheric column from the top of the atmosphere (TOA) to the surface accounting for aerosol extinction.

$$\tau_a = \log \frac{I_{surface}}{I_{TOA}}$$

where I is the intensity of the incident beam (Seinfeld & Pandis, 2008). This quantity allows quantifying the light extinction due to aerosol given by the Beer-Lamber-Bougher law

$$I(x) = I_{TOA} \int_{TOA}^{x} e^{-b_a \cdot \tau_a} dx$$

where b_a is the absorption coefficient of the atmosphere (m^{-1}, assumed homogeneous through the atmospheric column), and x represents the vertical coordinate. According

to Remer et al. (2008), AOD varied from 0.14 to 0.19 from ocean to land and from 0.12 in South circumpolar to 0.29 in North India regions in land. These variations give a notion of how heterogeneously aerosol are distributed in terms of latitude and longitude, related to its wide range of size, composition, and origin amongst other variables.

1.1.1 *Aerosol size ranges*

Aerosol size can range from 0.001 μm (molecular clusters) to 100 μm (small raindrops). By definition, ultrafine, fine, and coarse particles are those whose aerodynamic diameter is under 0.1 μm, 2.5 μm, and over 2.5 μm, respectively (Seinfeld & Pandis, 2008). Aerosol concentrations can be described by either the number of particles, mass, volume, or surface area per unit of air volume. Number concentration is usually dominated by smaller particles, whereas volume or mass concentrations are dominated by coarser particles (Seinfeld & Pandis, 2008) (Fig. 1). Aerosol concentrations in mass are usually expressed in $\mu g \cdot m^{-3}$ of PM_{10}, $PM_{2.5}$ or PM_1, if referring to particles with aerodynamic diameter below 10, 2.5, and 1 μm, respectively. Modes are ranges of diameters of particles categorised with similar behaviour in number or mass concentration, despite not being universally defined. In the current thesis, modes are defined as in Finlayson-Pitts and Pitts Jr (1999):

1. Nucleation mode (<25 nm): consists of molecular agglomerates formed through gas-to-particle conversion, amongst other mechanisms. Pathways of formation are still under research.

2. Aitken mode (25-100 nm): typically particles which have undergone coagulation, gas-to-particle conversion, and condensation of semi-volatile compounds.

3. Accumulation mode (100 nm - 1 μm): dominated by Aitken particles whose diameter has grown as a consequence of coagulation or condensation of semi-volatile compounds.

4. Coarse mode (>1 μm): usually primary particles generated from mechanical processes, such as marine aerosols, soil dust, vegetation debris, road dust etc. Secondary coarse particles can also arise from the interaction of gaseous precursors with mineral matter or sea salt.

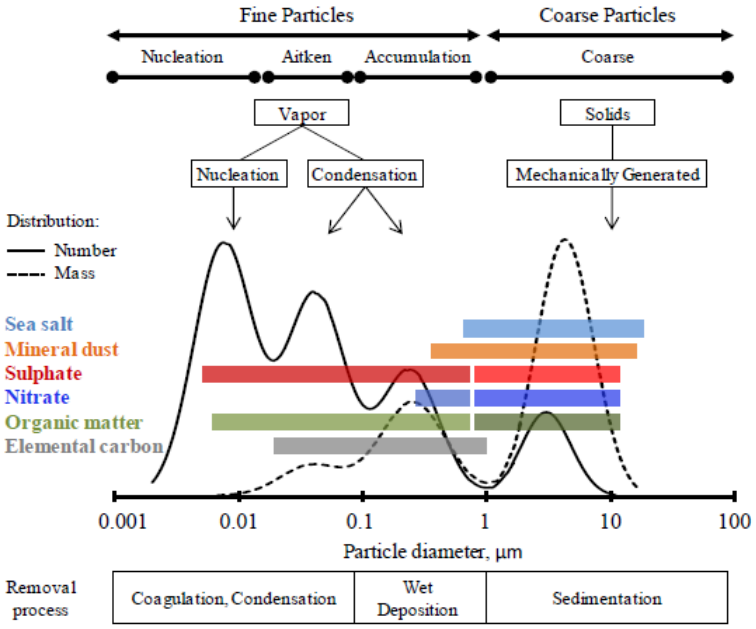

Figure 1: Schematic of the atmosphere aerosol particle mass (dotted line) and number (solid line) distribution for a typical urban aerosol. Major chemical species distribution, formation and removal processes are shown. Modes of the distribution are allocated as well as particle size classification names. Adapted from: García (2017).

Once emitted or generated, aerosol undergoes many possible processes in the atmosphere, such as condensation, aggregation, evaporation, dilution, coagulation, or sedimentation. The labelling *fine aerosol* is confusing since the same nomenclature is usually used for $PM_{2.5}$ and PM_1 indistinctly, but here will be used as an equivalent of PM_1.

It is of crucial importance in this thesis the observation of the minimum in the aerosol size distribution at 1µm. This boundary value separates the mechanical formation (fragmentation, abrasion) and chemical formation mechanisms for the coarse and the fine particles, respectively. This thesis will focus on the submicronic fraction of the aerosol, hence targeting those particles generated from pre-existing particles and vapour through nucleation and condensation. These handle all modes except for the coarse, which has been more widely described in the area of study.

1.1.2 *Aerosol components*

Aerosol components can be classified according to their chemical composition in the following categories: mineral matter, sea salt, secondary inorganic compounds (SIA, SO_4^{2-}, NO_3^-, NH_4^+, Cl^-), organic matter or organic aerosol (OM or OA, respectively), elemental carbon (EC), and trace elements. All these components exist in wide size ranges, except for mineral matter and sea salt, which are predominant in the coarse mode (Fig. 1).

According to resistance to temperature, in materials science, a material is classified as refractory if it resists heat, pressure, or chemical attack. In aerosol science, non-refractory (NR) aerosol comprises all the compounds capable of flash-vaporise at 600°C, since this is the typical temperature at which some of the most mass spectrometers vaporise aerosol. From the aforementioned components, only the SIA and the OA fall under the non-refractory definition.

i) organic aerosol

OA is not a single component in the atmosphere, but a ubiquitous ensemble of compounds with a certain amount of carbon. It is the main component of PM_1, representing 35%-65% of NR-PM_1 and 21-75% of PM_1 across Europe, with larger proportions at non-urban sites (Bressi et al., 2021; Chen et al., 2022b; Crippa et al., 2014). The largest portion of OA is present in the mode below 1µm, being generated from nucleation or condensation. The presence of OA in the coarse model corresponds to biological emissions such as plant debris, pollen, etc. Fine OA can be mainly differentiated by its origin into primary or secondary.

Primary OA (POA) consist typically of anthropogenic emissions from road traffic (also called Hydrocarbon-like OA, HOA), biomass burning OA (BBOA), cooking-like OA (COA), industry OA (INDOA), coal combustion OA (CCOA), or shipping OA (ShOA), amongst others.

Secondary OA (SOA) is a byproduct of precursor volatile organic compounds (VOC), reactive gases with both anthropic and biogenic origins. SOA formation processes are still a subject of research, although there is plenty of evidence to distinguish its main pathways.

In the dominant gas-phase mechanisms, the interaction of VOC with other atmosphere components leads to intermediate organic products of lower volatility and higher solubility. These sub-products have a high propensity to nucleate as particles or condense over pre-existing ones (Ng et al., 2008; Shrivastava et al., 2017). Particularly, the gas-phase photo-oxidation of OA involves the increase of the oxidation state and the decrease in the volatility of the compounds (Jimenez et al., 2009). Another pathway for SOA formation is aqueous-phase reactions, consisting of the oxidation of water-soluble VOCs or organic products of the gas-phase photochemistry (Sullivan et al., 2016). The SOA formation from the latter process occurs especially during nighttime (absence of solar radiation) and generates more oxidised aerosol (Cao et al., 2022; Xu et al., 2017). Usually, the oxidants with which VOCs convert to SOA are OH and O_3 radicals during daytime (in the presence of solar irradiance) and O_3 and $NO_3^{-\bullet}$ (nitrate radical) during nighttime (Dai et al., 2019a). SOA is usually differentiated regarding its oxidation state (i.e. ageing) into Less and More Oxidised Oxygenated OA (LO-OOA and MO-OOA, respectively), although previous nomenclature classified them according to their volatility into a Semi-Volatile and Low-Volatile oxygenated OA (SV-OOA, LV-OOA, respectively) and these labelling can be found in many scientific articles.

A clarification between the terms OA and Organic Carbon (OC) is needed. The OA term makes reference to organic aerosol, which includes the mass of all the atoms present in the organic compounds: C, O, H, N, etc. OM, i.e., Organic Matter, is also used equivalently to OA. The OC term makes reference to organic carbon and includes only the mass of carbon atoms present in the organic compounds. It is the term used when using thermal-optical methods for the determination of organic particle concentration, given their inability to measure species other than carbon, such as O or H. The OA-to-OC ratio is highly dependent on the site-specific aerosol composition. Typical OA/OC ratios for remote and urban areas are 2.1, and 1.8, respectively, although at hotspots it can be lower (1.4) (Aiken et al., 2008).

II) SECONDARY INORGANIC AEROSOL

Secondary Inorganic Aerosol (SIA) compounds are great contributors to PM_1 in Europe regardless of the type of site, even though its contribution is larger in urban locations (Bressi et al., 2021). These compounds include ammonium nitrate (AN,

NH_4NO_3), ammonium sulphate (AS, $(NH_4)_2SO_4$), and ammonium chloride (ACl, NH_4Cl). The NO_3^-, SO_4^{2-}, and Cl^- balance with the available NH_4^+ is well understood (Liu et al., 2020), presenting different formation pathways depending on the presence or absence of solar radiation. Generally, atmospheric sulphate (SO_4^{2-}), nitrate (NO_3^-), and ammonium (NH_4^+) are formed through the oxidation, via oxidants such as OH radicals and O_3, of SO_2, NO_2, and NH_3, respectively (Hidy, 2017), which makes them secondary aerosols. Cl^- stems mostly from sea salt emissions and exists mostly in the coarse mode in the form of ACl.

The main precursor of SO_4^{2-} is sulfuric acid (H_2SO_4), produced in the atmosphere by oxidation of sulfur dioxide (SO_2), emitted from fossil fuel combustion, volcanoes, or marine emissions. H_2SO_4 condenses under any atmospheric conditions to form aqueous SO_4^{2-} particles which can, in turn, condense on other gases such as NH_3, forming AS or organic compounds called organosulphates (Jacob, 1999). Only exceptionally SO_4^{2-} can be primary when emitted by domestic coal combustion (Dai et al., 2019b; Ng et al., 2017).

The AN and AS reactions happen usually at gas phase when RH is low and heterogeneous-phase and aqueous-phase when RH>60% (Li et al., 2017a). Nitrogen oxides (NO_x), which are NO_3^- precursors, are emitted mainly by road traffic, energy production and industrial processes, and residential heating. These compounds oxidise into nitric acid (HNO_3), which in combination with NH_3 and mineral matter neutralise into NO_3^-, $NaNO_3$, or $Ca(NO_3)_2$ (Meszaros et al., 1999). From all the mentioned compounds containing NO_3^-, only AN is below the 1μm threshold. The ammonia availability is the limiting reagent of AN and AS formation, especially at high temperatures (Schaap et al., 2004). This effect together with the fact that the nitrate gas-aerosol partitioning leads to the vaporisation of AN at high-temperature conditions makes nitrate concentrations drop significantly in summer as reported in Bressi et al. (2021).

III) BLACK CARBON

Black carbon (BC) is a term referring to atmospheric material sharing the following characteristics: i) strong absorption of visible light for freshly produced particles; ii) volatility at temperatures above 4000 K; iii) insolubility in water, organic solvents or other components of the atmospheric aerosol; iv) constitution of aggregates of small

carbon spherules of < 10 nm to approximately 50 nm in diameter; v) high fraction of sp^2-bonded carbon atoms (Petzold et al., 2013).

This terminology is applied within optical properties although, for quantitative application, it is advised to adequate the terminology to specify the particular measurement methods (Pöschl, 2005). The BC-like carbonaceous measurements are named according to their measurement principle: *equivalent BC* designs mass concentrations derived from optical absorption measurements, *elemental carbon* (EC) designs measurements derived from the carbon content of carbonaceous matter quantification methods, and *refractory BC* designs measurements derived from incandescence methods. The common qualitative term *soot* refers to the origin of BC designing carbonaceous material formed from incomplete combustion. Finally, brown carbon (BrC) refers to those particles which are externally mixed with less-absorbing particles, as absorbing OA (Andreae & Gelencsér, 2006).

Sources of atmospheric BC are mainly biomass burning (either from residential heating or wildfires), motor vehicle exhaust, furnace burning, and other fuel combustion. Particle diameters are usually within the 0.01-1 μm range. Source apportionment techniques are applied to BC in order to distinguish mostly traffic and biomass burning sources. Road traffic contributions proportion to total $PM_{2.5}$ and PM_{10} are double in kerbside sites (17% and 13%, respectively) respect to rural sites (8% and 5%, respectively) (Putaud et al., 2004). In the submicronic fraction, it accounts for a 10% in mean, ranging from 7% to 12% at European non-urban and urban sites, respectively (Chen et al., 2022b).

IV) MAJOR AND TRACE ELEMENTS

The existence of major and trace elements in the atmosphere is the result of a broad range of aerosol sources and formation processes. Their main sources are described hereunder.

Seas and oceans are one of the main coarse PM sources, emitting sea salt constituted mainly of NaCl and, in a minor contribution, of $MgCl_2$, $MgSO_4$, and Na_2SO_4 (Meszaros et al., 1999). Dimethyl sulfide (DMS) is emitted from marine phytoplankton and is one of the major submicronic sulphate precursors, oxidating into various sulphur-containing components such as SO_2 as an intermediate product (Lucas &

Prinn, 2005). Usually, marine advection can also carry shipping activity emissions (also called heavy-oil combustion emissions), which are mainly traced by V, Ni, and Co (Caumette et al., 2009; Corbin et al., 2018).

Deserts are another main source of coarse PM emissions in the form of mineral dust. Its most abundant elements are Al, Ca, Si, Fe, Ti, K and Mg although they also contain carbonates and certain trace elements such as Co, Rb, Ba, Sr, Li, Sc, Cs, and rare earth elements (Rudnick, 2018). However, its exact composition depends strongly on local geology and processes impacting the soils (Tang et al., 2019).

Road traffic is an emitter of a wide range of elements, due to the diversity of processes generating non-exhaust particles. Most of these processes emit from coarse to ultrafine PM due to mechanical and thermal/chemical processes, respectively. Brake wear is the result of the frictional process between a brake pad and a rotating disc or drum and it contributes between a 16% to a 55% to the total non-exhaust traffic-related PM in urban roads (Piscitello et al., 2021). Tyre abrasion due to contact with the road surface leads to the release of large quantities of small rubber particles (the size range includes PM_{10}), whose chemical composition and characteristics can differ from the original tyre tread due to heat, friction and incorporation of material from the road surface (Adachi & Tainosho, 2004). Road wear originates from the fragmentation of the road pavement surface due to the interaction with vehicle tyres and abrasion of the road surface consequently releasing airborne particles in the environment. Lastly, the term road dust includes any form of solid particles on the road surface that can be suspended in the atmosphere through traffic or windblown action. The main markers of each of the mentioned processes are listed in Table 1 (a). Road traffic emissions also comprise exhaust emissions, consisting of BC, OA, etc. in a wide variety of sizes (Canagaratna et al., 2007) and gaseous precursors of PM. Also, secondary aerosol arises from exhaust emissions through coagulation or accumulation of ultrafine particles (Karjalainen et al., 2014; Ropkins et al., 2009).

Industrial activities are also extensive element emitters. The composition of the emitted PM depends highly on the type of industry and processes therein, and their particle size distribution can also vary, but a large proportion is in the submicronic fraction. Some of the compounds emitted due to industry activities are listed in Table 1 (b).

Table 1: Elemental composition of PM emitted from (a) Non-exhaust emissions. (b) Industrial activities. Adapted from (a) Thorpe and Harrison (2008), (b) Querol et al. (2007).

(a) Non-exhaust emissions	Elements
Brake wear	Fe, Cu, Ba, Ti, Al.
Tyre wear	Zn, S, Se, Ti, Fe, Cu, Si.
Road surface wear	Si, Ca, K, Fe, Al, S, Cl
Resuspended road dust	All of the above, especially Cu, Mo, Co, Zr, Sn

(b) Industrial emissions	Elements
Steel metallurgy	Cr, Mn, Ni, Zn, Se, Mo, Cd, Sn, Pb.
Stainless steel metallurgy	V, Cr, Ni, Mo.
Copper metallurgy	Cu, Ga, As, Bi.
Zinc metallurgy	Zn, Cd
Petrochemical estates	V, Co, Ni, Cs, La
Tile industry	Zn, As, Se, Zn, Cs, Tl, Pb, Sb
Brick industry	Li, Be, Ti, V, Ni, Ga, Rb, Se, Cs, La, Ce, Tl.

1.1.3 *PM impact*

i) on health

The link between air pollution and mortality has been reported since the 20th century and nowadays environmental epidemiology has become a major discipline coping with human health preservation (GBD, 2017; WHO, 2021). Many studies in this direction have acknowledged the relationship between air pollution and diseases, some of which are: Alzheimer (Alemany et al., 2021), cognition deterioration (Zhang et al., 2018b), Parkinson (Kasdagli et al., 2019), changes of brain structures or functions (de Prado et al., 2018), mental health (Buoli et al., 2018), cognitive development in children (Sunyer et al., 2015) etc. Therewith, air pollution is the first environmental cause of early death in the EU (EEA, 2022) and it is the cause of 11.65% of deaths globally (Ritchie & Roser, 2017).

The World Health Organization (WHO) estimates that in 2016 $PM_{2.5}$ was responsible

for 4.2 million premature deaths worldwide and Cohen et al. (2017) showed how mortality had risen around a 20% respect to the previous 25 years. According to WHO (2016), the main causes of this mortality are ischaemic heart disease and stroke, chronic obstructive pulmonary disease, acute lower respiratory infections, and lung cancer. When $PM_{2.5}$ is inhaled, particles can both stay in the respiratory system and even penetrate the lung barrier and enter the blood system. Therefore, it is not surprising that this pollutant can trigger other kinds of illnesses besides those affecting the respiratory system. Some studies found relationship between $PM_{2.5}$ levels and diabetes (Zhang et al., 2020), obesity (Parasin et al., 2021), adverse birth outcomes (Li et al., 2019) amongst others.

II) ON CLIMATE

Climate change is often measured from the accumulated energy of the Earth system, measured as changes in the temperature of oceans, land, atmosphere, and ice. The global computation of this accrued energy, which presents less variability and hence is a better indicator of climate trends, has increased 282 zettajoules (ZJ, $\cdot 10^{21}$ J) for the period 1971-2006 and 152 ZJ from 2006-2018 (Arias et al., 2021). This excess of energy consequently implies a warming of the Earth-atmospheric system. This accumulation is thought to be caused by anthropogenic radiative forcing (RF), a human-caused imbalance of the radiative equilibrium of the atmosphere in comparison to pre-industrial times. The drivers of this imbalance are diverse and aerosol plays a significant role, both increasing and decreasing RF depending on its nature.

The aerosol effects on the radiative balance of the Earth can be differentiated into three types:

- Direct radiative effects: this agglutinates two optical interactions of aerosol. On the one hand, aerosol absorption of radiation accumulates heat, increasing its surrounding air temperature. On the other hand, aerosol light scattering can prevent aerosol absorption, promoting atmospheric cooling.
- Semi-direct radiative effects: aerosol absorption of radiation might accumulate heat used to evaporate water, reducing, therefore, RH and preventing cloud formation due to latent heat decline. Consequently, cloud cover is reduced and surface warming is enhanced. Depending on the aerosol layer (generating the

mentioned heat excess) being above or below the cloud, convection can be enhanced or suppressed, respectively.

- Indirect radiative effects: an increase of fine PM can increment Cloud Condensation Nuclei (CCN) and Ice Nuclei (IN) which might enhance the formation of smaller cloud droplets for the same liquid water content (LWC). These modifications could modify cloud albedo and disfavour precipitation, as the collisions and coalescence of water droplets decline due to less proportion of coarse droplets. As a consequence, the lifetime and reflectivity over time of clouds are elongated and latent heat accumulated, which might also derive into mixed-phase cloud freezing processes and enhancement of cloud top height.

The impact of aerosol on climate is dependent on aerosol composition, origin and size distribution. In Figure 2, RF due to aerosol-radiation interactions (RF_{ARI}) is shown regarding aerosol composition. Aerosol as a whole has a clear negative RF, however, depending on its component contributions it might vary depending on the area and time. The most cooling compound is SO_4^{2-}, followed by NO_3^- related to their high mass scattering efficiencies (Li et al., 2022a). Contrarily, BC from fossil fuel and biofuel combustion present a very positive forcing. SOA and POA from fossil fuels and biofuels are also cooling agents and biomass burning emissions are practically neutral. The uncertainties of these bars are high, for which further investigation is to be carried out in this direction, as they don't even contain certain ARI for which knowledge is still scarce (e.g. coating effects). Moreover, aerosol presents a substantial spatial and temporal variation in composition, size, origin, etc, implying the quantification of RF_{ARI} can be largely variable in time and location. With all of that, further characterisation of aerosol composition and sources worldwide and for long periods is key to estimating RF_{ARI} of specific episodes and of future years.

III) ON ECOSYSTEMS AND MATERIALS

Atmospheric PM is known to impact ecosystems in several ways, but they are mainly based on the introduction of an atmospheric particle into an ecosystem. Atmospheric pollution deposition (e.g. through acidified precipitation) can significantly change the land composition and consequently modify biogeochemical subsequent processes and cycles (Mahowald et al., 2017). Also, pollution from industrial activities has also been reported to dissolve in oceans enhancing the supply of bioavailable Fe to the oceans

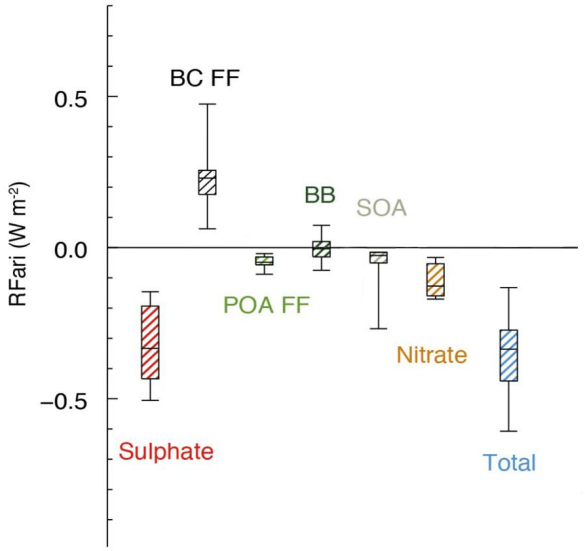

Figure 2: Annual mean top of the atmosphere radiative forcing due to aerosol-radiation interactions (RF_{ARI}) due to different anthropogenic aerosol types for the 1750-2010 period. Hatched whisker boxes show median (line), 5th to 95th percentile ranges (box) and min/max values (whiskers) from AeroCom II models (Myhre et al., 2013) corrected for the 1750-2010 period. BC FF stands for black carbon from fossil fuel and biofuel, POA FF for primary organic aerosol from fossil fuel and biofuel, BB for biomass burning aerosols, and SOA for secondary aerosols. Adapted from IPCC (2013).

(Li et al., 2017b). Tang et al. (2021) showed the effect of wildfire aerosol emission on marine algae production enhancement due to the same effect. The transport of certain atmospheric pollutants depositing into ice sheet areas can also modify cryospheric albedo (McCutcheon et al., 2021). Besides this direct impact on climate, there are many indirect effects due to aerosol-driven climate modification, affecting, for instance, plant photosynthesis and evapotranspiration due to the modifications of direct and diffuse radiation (Zhou et al., 2021).

Furthermore, atmospheric aerosol presents compelling repercussions on human everyday life. The effect of aerosol on visibility has been studied for decades (Charlson, 1969; Malm et al., 1994). The major visibility-reducing aerosol species are AS, organics, and AN, and the major visible-range reduction OA source is coal combustion, followed by engine exhaust (Cao et al., 2012). Also, several studies reported aerosol-induced degradation of buildings (Morillas et al., 2020), monuments (Ghedini et al., 2011) or archaeological sites (Sakka et al., 2020).

1.1.4 *Air quality standards*

As stated in the previous section, PM constitutes a great threat to human health. An imperative step towards atmospheric pollutants mitigation policies design and enforcement is the establishment of robust pollutant limits based on population exposure and toxicity. Target concentrations for each pollutant are designed to be used as a reference to reduce them and consequently their effect in human health, environment, and climate. Hence, when technically feasible, pollutants concentrations should be pushed downwards as much as possible since there is no threshold under which the PM effect is null. Also, the lack of standardised long-term measurement of certain pollutants prevents their proper characterisation and risk assessment, and therefore no thresholds have been proposed at present. Consequently, not all potentially or admittedly toxic pollutants are being targeted.

Another downside of the current guidelines is that they do not consider PM components but bulk PM, even though this pollutant composition (and thus, health effect) can present huge variations in space and time. For instance, In't Veld et al. (2021) has shown that even though $PM_{2.5}$ decreased in the 2009-2018 period in Barcelona, its composition changed substantially. For this reason, the threshold establishment for bulk PM is not an effective measure to reduce the aerosol impact on health. In this direction, effort should be directed to monitor aerosol compounds and their sources in order to create composition-dependent regulations leading to the reduction of PM effects.

Two organisms designing guidelines targeting air pollutants are the World Health Organisation (WHO) and the European Commission (EU). The directives from the European Commission have been extended to the Spanish legislation through the royal-decree Law 102/2011 and are mandatory to be met. The WHO value guidelines are set for health protection and are generally stricter than the EU value guideline standards. Air quality measurements are typically reported in terms of daily or annual mean concentrations of the pollutant per cubic meter of air volume (m^3). Both organisms' values are shown in Table 2. The effectivity of the EU guidelines has been estimated to reduce by 45% premature deaths attributed to exposure to fine PM in the 2005-2020 period in the EU-27 (EEA, 2022).

Table 2: PM standards given in the WHO air quality guidelines (2021) and EU air quality standards (2008, 2022). All values are given in units of $\mu g \cdot m^{-3}$.

Pollutant	Averaging period	EU Directive (2008)	WHO (2021)	New EU Directive Proposal (2022)
$PM_{2.5}$	Annual	25	5	10
	24-hours	15	-	20
PM_{10}	Annual	-	15	20
	24-hours	50 *	45	45 ⋆

* Not to be exceeded by the 99th percentile (i.e. 3-4 days/year).
⋆ Not to be exceeded more than 35 days/year.

The publication of new air quality guidelines for human protection by the WHO in 2021 with more restrictive values based on scientific evidence compared to the previous publication and the EU limits (WHO, 2021) pushed the revision of the EU air quality directives. In October 2022, the European Commission published a revision of the Ambient Air Quality Directive with the aim of aligning the pollution thresholds with those set by the WHO in 2021 (European Comission, 2022). Moreover, this revision proposes the implementation of supersites to collect long-term data on regulated pollutants, pollutants of emerging concern, and other metrics, such as ultrafine particles, BC, NH_3, oxidative potential, and $PM_{2.5}$ composition. Long-term information on these air quality markers will support the understanding of their effects on health and the environment, which will promote the implementation of abatement measures of the currently-unregulated pollutants.

1.2 SOURCE APPORTIONMENT

In order to further characterise PM composition and increase the understanding of its behaviour, the association of its components to their sources can be of great help. Moreover, it is valuable information for emission sources regulation. Source Apportionment (SA) is the identification of ambient air pollution sources and the quantification of their contribution to pollution levels (Belis et al., 2014). Let a pollution source be a group of pollutants which present similar temporal behaviour whose origin

stems from a common emission activity. The SA task can be accomplished using two main approaches:

- Source-oriented models: based on the pollution processes undergoing from the source to the sampling site such as transport, dilution, deposition etc. This category comprises Lagrangian models, eulerian models, gaussian plume models, etc.
- Receptor-oriented models: attempt to relate measured concentrations at a given site to their sources without reconstructing the dispersion pattern of the material. It requires emission inventories, which are the compilation of the emissions from all source categories in a certain geographical and year. Emissions are estimated by multiplying the intensity of each relevant activity (activity rate) by a pollutant-dependent proportionality constant (emission fingerprint).

RMs have been increasingly used in recent years worldwide (Fragkou et al., 2012), prompting also the improvement of capabilities in terms of source resolution and accuracy, dataset applicability and error estimation. These tools have the advantage of providing information derived from real-world measurements. However, there are limitations in their application to very reactive species as they assume staticity of source fingerprints.

Receptor models are based on the solution of mass conservation equations assuming the partitioning of the input model mass into several independent contributions (Friedlander, 1973). Typical datasets for source apportionment consist of two-dimensional arrays with columns representing species concentrations and rows corresponding to samples. In addition, uncertainty for every entry in the first matrix is required for some RMs e.g. positive matrix factorization (PMF) and chemical mass balance (CMB). Being x_{ij} the concentration of the j-th species at the i-th sample with dimensions nxm, g_{ik} the contribution of the k-th source to the i-th sample, f_{kj} the concentration of the jth species in the kth source and e_{ij}, and e_{ij} the adjustment error, the mass conservation equation can be written as:

$$x_{ij} = \sum_{k=1}^{p} g_{ik} \cdot f_{kj} + e_{ij} \tag{1}$$

or matricially as

$$\mathbf{X} = \mathbf{G} \cdot \mathbf{F} + \mathbf{E} \tag{2}$$

where p is the total number of factors. The concentration of each chemical element at a receptor site becomes a linear combination of the contributions of each source to the given species at that site plus the fitting error.

RMs have been traditionally classified into those which explicitly use information about the emission fingerprints and those which do not use any *a priori* information on source chemical profiles (factor analysis or multivariate models). The CMB model, firstly introduced by Watson (1979),) belongs to the first group and solves this equation by least-squares minimisation approach with a pre-fixed number of sources p and source fingerprints f_{kj} so that the only unknown term is the mass contribution of each source to each sample, g_{ik}. The most widely used factor analysis model is PMF (Paatero & Tapper, 1994), which will be described in section 1.2.1. Other factor analysis models include Principle Component Analysis, UNMIX, etc.

1.2.1 *Positive Matrix Factorization*

More than 1000 scientific papers are associated to PMF SA up to 2018 (Sun et al., 2020), applied to a wide range of environmental pollutants such as persistent organic pollutants, heavy metals, volatile organic compounds (VOCs), organic and inorganic cations and anions etc. The PMF algorithm is currently applied through the multi-linear engine 2 (ME-2, Paatero (1999)), a multi-linear equation solver program.

The diffusion of PMF as the main receptor model has also been promoted due to its use towards aerosol mass spectrometer (AMS) or Aerosol Chemical Speciation Monitor (ACSM) data (both further described in section 3.2.1), oriented to the SA of submicronic OA from mass spectral measurements in a high time resolution (TR) (less than 1 hour, depending on the instrument model). PMF applied to the spectrometric data of this instrumentation enables to associate organic functional groups generated from a common source into OA sources (Noziere et al., 2015). For the described case, as samples are generated continuously, i in equation 1 is assumed a time scale.

The cost function Q is the model parameter upon which PMF is optimised:

$$Q = \sum_{i}^{n} \sum_{j}^{m} \left(\frac{e_{ij}}{\sigma_{ij}}\right) \tag{3}$$

where σ_{ij} represents the uncertainty associated to the measurement x_{ij}. The model calculates this quantity in each iteration until it becomes smaller than a convergence

threshold. This quantity is often used for model error assessment normalised by dividing it by the model degrees of freedom (Q_{exp}).

$$Q_{exp} = m \cdot n - p \cdot (m + n) \tag{4}$$

Since the PMF does not use *a priori* information, the model is randomly initialised. However, for a given **X**, there are a huge number of **F**, **G** solution matrices which can fulfil the PMF equation and provide the same Q value. This degeneration is called rotational ambiguity. These degenerated solutions can be mathematically conceived as matrix rotations:

$$\overline{G} = G \cdot T \qquad\qquad \overline{F} = T^{-1} F \tag{5}$$

where T and T^{-1} correspond to the *pxp* non-singular rotation matrices and their inverse, respectively, and $\overline{G}$ and $\overline{F}$ are the rotated **G** and **F**, respectively. The rotational space is partially limited by the non-negativity constraint of PMF applied to the solution matrices, although the number of remaining rotations is still high (Paatero et al., 2002). In order to reduce further the rotational ambiguity of PMF whilst leading it to an environmentally-reasonable solution, the application of *a priori* information is possible. The current SA protocols advise using the *a-value* approach for such purpose, which consists of the initialisation of **F** or **G** with reference profiles (f_j^{ref}) or time series (g_i^{ref}) multiplied by a value *a*. The *a*-value, with $a \in [0, 1]$, represents the amount of variation allowed with respect to the constraint, where 0 and 1 would represent total constraint and freedom, respectively.

$$f_{ij} = f_j^{ref} \pm a \cdot f_j^{ref} \qquad\qquad g_{ij} = g_i^{ref} \pm a \cdot g_i^{ref} \tag{6}$$

The output of the PMF model consists of p profiles and time series and an error matrix of dimensions *i* x *j*. The errors are usually scaled within the measurement uncertainties

$$s_{ij} = \frac{e_{ij}}{\sigma_{ij}} \tag{7}$$

being thus called scaled residuals s_{ij}. Their distribution is reported in Paatero and Hopke (2003) to describe a unimodal Gaussian centered at zero and within a ±3 range under good model performance conditions.

1.3 STATE OF THE ART

1.3.1 *Climate studies*

The climate impact of aerosols is estimated by climate modelling coupling aerosol and meteorological variables. The aerosol concentrations are based on aerosol modelling, which still has some uncertainties (Morino et al., 2015). Therefore, even if aerosol mechanisms of influence on climate are well-known, an accurate climate impact assessment is not achieved as a consequence of the uncertainty in spatial and temporal aerosol variation (Bian et al., 2017; Tsigaridis et al., 2014).

Some of the main difficulties to assess aerosol forcing consist of: i) uncertainty associated with aerosol and aerosol precursor emissions linked to new particle formation; ii) lack of historical aerosol loadings data, especially in the pre-industrial period; iii) uncertainties in the representation of the climate-relevant properties of aerosol; iv) uncertainty in the parametrization of sub-grid processes in climate models, in particular for cloud processes; v) uncertainty in providing an adequate characterization of aerosol climate-relevant properties (spatial and temporal variability). A beneficial practice for model evaluation and improvement is model validation with real-world aerosol observations. In this direction, Mircea et al. (2019) shows that seven of the currently used chemical transport models underestimate EC and OA concentrations in Europe, pointing at the SOA as the most difficult compound to predict due to its phenomenology complexity.

Laj et al. (2020) suggests that aerosol wavelength-dependent light scattering, absorption coefficients, particle number concentration, and particle number size distribution are the main topics that should be further investigated to achieve more accuracy for aerosol-driven climate forcing estimations. However, a comprehensive understanding of these points requires broad aerosol phenomena expertise due to the interrelation of their processes.

Both absorption and scattering have been reported to be composition-dependent, which prompts the necessity of further research on coupling PM composition with optical properties.

Regarding absorption, Yus-Díez et al. (2022) points out the absorption dependency

of BC particles depending on their coating, a process for which BC is mixed with other PM compounds which modify its warming capacity. The process of particles coating over soot particles occurs rapidly in a few hours after emission and the coated particle diameter increases with particle ageing (Xing et al., 2020). The amount of light absorption enhancement due to the coating was found source-dependent according to Yus-Díez et al. (2022). A higher enhancement of BC light absorption both at long and short wavelengths is found for primary OA (POA). Other studies show the absorption efficiency drop with SOA degradation is likely due to the photobleaching of BrC chromophores (Kasthuriarachchi et al., 2020; Qin et al., 2018), which is coherent with the increase of absorption for POA coating. These findings imply that not only the climate impacts are composition-dependent, but also depend on the particle configuration, this is, the distribution of the aerosol compounds in the individual particles.

In terms of scattering efficiencies, SIA and OA are known to have a severe impact on extinction, especially in haze pollution episodes (Wang et al., 2015). The pollutants with the highest light scattering efficiency are AN, AS, SOA and CCOA.

Plenty of scientific articles account for each particle size range effect on these aerosol-climate interactions, especially for the smallest particles. Regarding the indirect effects, Romakkaniemi et al. (2012) showed the accuracy advantages of taking into account PM_1 particles in cloud-development processes modelling. Also, Zhang et al. (2002) showed that direct radiative forcing is highly sensitive to particles of similar size to the wavelength incident light (several hundred of nm, i.e. belonging to PM_1) being in this range the mass scattering efficiency peak.

For all of that, in order to monitor the implications on climate over the years, long-term PM composition and size distribution studies represent crucial knowledge. Hence, sufficient information on aerosol sources' and size distribution characterisation, acknowledgement of their spatial, temporal, and size variations, and relation with the aforementioned optical properties can help reduce the gap in knowledge for climate studies through more accurate modelling.

1.3.2 *Health studies*

Aerosol impact on health is tackled through two approaches: epidemiological and toxicity studies.

Aerosol epidemiology studies the effect on the population of pollution exposure, its effects commonly quantified mostly in terms of hospital admissions or daily mortality (Atkinson et al., 2015; Thurston et al., 1994). In this discipline, current research is focusing on the epidemiologic assessment of PM sources or components with respect to the previously established knowledge of bulk PM. The turning point of the old paradigm has been the acknowledgement that epidemiological impact is less evidently reflected by PM levels than by certain PM compounds arising from a common origin (Rich et al., 2019; Zhang et al., 2018a). The latter aforementioned study shows that hospital admissions increased after a $PM_{2.5}$ levels decrease due to a change of fine aerosol composition, acknowledging that traffic emissions are those inducing peaks of hospital cardiovascular admissions. Similarly, a study in Barcelona shows a positive correlation of PM sources as vehicle exhaust, fuel oil combustion, secondary NO_3^-/organics, minerals, secondary SO_4^{2-}/organics, and road dust, with all-cause and cardiovascular mortality (Ostro et al., 2011). Also, there is a major concern about smaller particles due to their known potential harmfulness (Sonwani et al., 2021; Yang et al., 2018).

Epidemiological studies demand long-term pollutant measurements due to the necessity of considering fluctuations of population health markers along seasons and years, this is why PM_1 and ultrafine particles epidemiological studies are scarce.

Aerosol toxicity assesses the hazards of PM in health relating to exposure to physiological deprecation processes. Regarding toxicity, studies are also shifting to the study of PM sources and different aerosol sizes' health effects instead of targeting bulk PM. In this direction, the oxidative potential (OP) of PM is recently raising concern as a relevant metric for health impact instead of PM mass concentration. So much so that the EU's future legislation will implement the compulsory measurement of this variable at all monitoring supersites at urban background locations. OP measures the intrinsic ability to generate reactive oxygen species (ROS) which drive oxidative stress in lung cells, linked to many medical conditions (asthma, COPD, IHD) (Cho et al., 2005). Many studies reflect the dependency of OP in PM regarding its composition,

compounds, particle size, and sources (Ayres et al., 2008; Daellenbach et al., 2020). However, at present, the OP source attribution is not perfectly consistent among studies. Some causes for conflicted results are the different sensitivity of OP essays to certain aerosol substances, composition, sources, and photochemical oxidation (Bates et al., 2019). Nonetheless, plenty of studies have underlined the toxicity of traffic and SOA as the most OP driver sources in fine aerosol (Daellenbach et al., 2020). Hence, monitoring PM sources and gathering information about their evolution is mandatory to target potential severe OP episodes, although the amount of studies in this direction is still scarce, especially for submicronic particles.

The main cause for these literature gaps is the lack of long-term studies on PM_1 composition and sources needed for the association to epidemiological variables. This thesis, focused on submicronic PM, aims to generate and treat long source-speciated PM_1 time series which can be furtherly used for the so-needed source-specific health impact assessment studies.

1.3.3 *Recent SA developments*

Because of the need for PM composition impact assessment on health and climate, SA has risen substantial scientific interest in recent years. It consists on a powerful tool for PM components grouping into sources, which allows for targeting the origin of PM generation. Therefore, it is highly useful for abatement policy design, as it permits to target of source-responsible emitters or precursors.

A clear application of SA potentialities for aerosol understanding is the urge for SOA description and quantification. It has been shown to deserve further investigation due to its implications for climate and health. SA techniques allow for source disentanglement, which in the case of SOA differentiation from bulk OA, enables the research on this group of secondary organic compounds, whose origin and formation mechanisms are still partially unknown. Even though SOA processes have been more well-understood due to many of environmental chamber studies, the conditions of these synthetic atmospheres can differ significantly from real atmosphere (Porter et al., 2021). Hence SOA behaviour in real life could not be fully captured. Moreover, more and more studies show new possible pathways of SOA formation such as

traffic emissions (Minguillón et al., 2016), asphalt-related emissions (Khare et al., 2020), cooking emissions (Yu et al., 2022), personal care products (Shah et al., 2019), every-day products (McDonald et al., 2018), etc. Moreover, organic sulfates (OS) and organic nitrates (ON) are also important precursors for SOA formation and actual SOA components (Iinuma et al., 2007; Ng et al., 2017), whose exploration is still scarce (Fan et al., 2022). Also, SOA formation from biogenic VOCs is known to be affected by interaction with urban pollutants (Hoyle et al., 2011), but no laboratory or modelling studies have been achieved to reproduce these interferences (Jimenez et al., 2009; Zheng et al., 2015a). Thus, further research routed towards the different SOA formation processes and their alternance has to be tackled. From an atmospheric observation point of view, this is where field measurements of SOA, retrieved by means of SA approaches, come into play.

In terms of submicronic OA SA, the flourishment of an ACSM fleet throughout Europe has promoted several recent developments in the technique. The gathering of user experience with these instrumentation data enabled the confection of a protocol for SA aiming for the homogenisation of the procedure and limitation of user subjectivity throughout the process (Chen et al., 2022b). This protocol has been applied successfully in diverse European sites and this procedural guide will be detailedly explained in Section 3.3.2.

However, there are complementary techniques which have been proven advantageous for a more exhaustive SA.

One of the most state-of-the-art post-processing of PMF results is clustering, a technique for forming closed homogeneous groups from elements of similar characteristics or properties. The *k*-means clustering technique whose algorithm partitions a group of objects to a predesignated number of groups or "clusters" based on their relative distances (Ball & Hall, 1965). This technique is applied to the output profiles of PMF in order to group them according to their main properties. This technique has been proven extremely useful particularly for measurements in pristine environments, as it promotes the identification of minor sources (Äijälä et al., 2019; Heikkinen et al., 2021).

Another widely used approach is the combination of datasets (Figure 3), joining data from different instruments, sites, or PM fractions (multi-instrument and

multi-time-resolution, multi-size, and multi-size PMF, respectively). Many studies have benefitted from joining different measurement techniques for SA purposes, retrieving more and more comprehensive sources, which can be done both with coinciding (multi-instrument) and non-coinciding TR (multi-time resolution). Some data coupling studies with different instrument combination examples are: Belis et al. (2019), Crippa et al. (2013), Slowik et al. (2010), and Tong et al. (2022). Also, a recent study combines the SIA compounds with the OA matrix for a global NR-PM_1 SA, both data groups coming from the ACSM (Zografou et al., 2022).

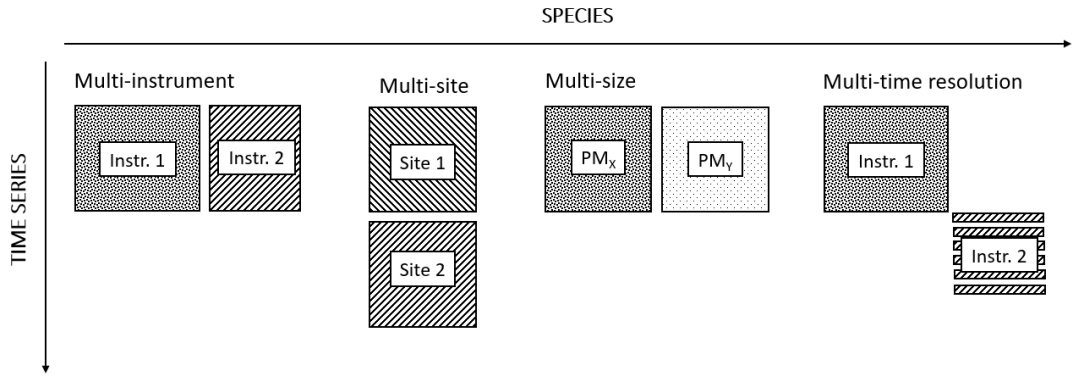

Figure 3: Scheme of the main dataset coupling SA techniques.

The multi-site SA is another frequent PMF data coupling consisting of joining datasets from the same pollutants of different sites in order to understand local emissions and long-range pollution advection (In't Veld et al., 2021; Pandolfi et al., 2020). This approach, however, presents the limitation of assuming the same source fingerprints apply to ambient measurements of each site. This is revealed in the latter article, which points out the differences with respect to the site-individual PMF profiles.

The multi-size approach has resulted extremely helpful for SA especially for handling relatively small datasets providing robust results (In't Veld et al., 2022; Scerri et al., 2019). It consists of coupling the same species in two or more PM fractions with the same timestamps into the same PMF, which provides a larger amount of data points and, hence, more information for PMF to adjust more comfortably the potential sources.

The multi-time resolution (MTR) SA technique consists of joining different

instrumental data and preserving their original time resolution so that the time series averaging or interpolation is avoided. This approach is further explained in Section 3.3.3. This technique, although conceived in the 2000s (Zhou et al., 2004), is still under study due to the particularities of each dataset application. Hence, there is a need to prove its stability and robustness along many different data couplings and design effective guidelines for its optimal implementation.

Besides dataset coupling, new techniques of SA apportionment have been recently developed for long-term datasets. The *rolling* PMF is a PMF approach in which this model is applied in rolling windows over the whole time series allowing to cover long periods without forcing staticity of the profiles throughout the whole period. This approach is comprehensively described and compared to previously used techniques in section 3.3.2.

Recently, a novel PMF technique was conceived and is being introduced in everyday source monitoring. The near-real-time PMF (NRT-PMF, Chen et al. (2022a)) is an automated process for which source profiles and time series are generated daily. This technique enables monitoring OA sources in order to detailedly grasp the affectation of each of them. However, this technique is still under development. Further work in this line should include the possibility to admit source outbreaks or disappearances as well as include other instrumental data for more robust speciation.

1.3.4 *Source apportionment studies in Barcelona*

The diversity of sources and complexity of the meteorological dynamics make the Western Mediterranean Basin (WMB) an interesting area for SA studies. Moreover, its population is large hence the exposure to aerosol is significant. These are the reasons that led to choosing Barcelona as the main urban environment for the present thesis. This section aims to summarise the gathered knowledge of sources in the WMB focusing on Barcelona.

The WMB is especially prone to suffer from episodes of PM levels above the WHO and European thresholds (Bressi et al., 2021; Chen et al., 2022b; Pey et al., 2010; Salameh et al., 2015; Van Dingenen et al., 2004). Its predominant primary sources consist of: i) road traffic, due to the densely populated cities along the coasts and comprising both exhaust and non-exhaust pollutants (Amato et al., 2016); ii) heavy-oil

combustion, related to shipping activities (Bove et al., 2016; Schembari et al., 2014); iii) Saharan dust outbreaks, happening 30-37% of days in the 2001-2011 period (Nicolás et al., 2008; Pey et al., 2013); iv) biomass burning, both from agricultural fires and residential heating (Galindo et al., 2021; Paglione et al., 2020); v) industry, including activity-specific pollutants (Chazeau et al., 2022; Querol et al., 2007); vi) cooking-like emissions (Chazeau et al., 2022; Mohr et al., 2012). Other locally identified sources are, amongst others, clinker and limestone + gypsum (Clemente et al., 2021), waste incineration (Dall'Osto et al., 2013), ceramic industry (Minguillón et al., 2007), cement industry (Yubero et al., 2011), smelter industry (Fernández-Camacho et al., 2012) etc. Also, there are secondary sources including both organic and inorganic pollutants, such as AS, AN, ACl, more or less oxygenated SOA (Amato et al., 2016; Bressi et al., 2021; Chen et al., 2022b), and biogenic SOA specifically coming from pinene or isoprene emissions (Alier et al., 2013), etc.

$PM_{2.5}$ sources have been thoroughly reported in the area of study of Barcelona. The $PM_{2.5}$ is mainly secondary as long-term studies suggest, a 63% consists of secondary aerosol (SOA, secondary NO_3^-, and secondary SO_4^{2-}) (In't Veld et al., 2021), although secondary aerosol only constitutes a 27% of the PM_{10} fraction. This study also identified heavy oil combustion, sea spray, vehicle exhaust, non-exhaust emission, metallurgical industry, and mineral sources, coincidingly with Amato et al. (2016). $PM_{2.5}$ presents a significant annual decrease in the 2004-2014 and 2009-2018 periods (Pandolfi et al., 2016), although its relative composition was modified significantly. According to In't Veld et al. (2021), in the 2009-2018 period, secondary SO_4^{2-}, heavy oil combustion and industry sources presented a decreasing trend in relative contribution to the total $PM_{2.5}$. Contrarily, non-exhaust emissions and crustal dust were reported in a positive trend. These composition changes support the need for controlling PM components rather than bulk PM concentrations, for which the SA has been proven highly advantageous to target the more increasingly concerning PM sources.

Even though PM_1 is embedded in the $PM_{2.5}$, submicronic aerosol SA usually reveals more specific sources since it removes the influence tail of the coarse mode included in $PM_{2.5}$ (Fig. 1). The origins of submicronic aerosol in Barcelona have been previously studied with a wide variety of instrumentation. Most of the studies were based on measurements with a TR of 24 hours and with OA as a bulk species (In't Veld et al., 2022; Pérez et al., 2010). Brines et al. (2019) joined daily organic and inorganic species concentrations from offline PM_1 filter samples allowing for more

specific sources such as biogenic SOA, pinene-driven, urban-mix, and two types of industry emissions.

Regarding OA SA, the use of high-resolution mass spectrometry has enabled OA SA and consequently the identification of the following sources: COA, HOA, BBOA, LO-OOA, MO-OOA (Minguillón et al., 2016; Minguillón et al., 2011; Mohr et al., 2012). Similar sources were found in nearby urban such as Marseille, Granada, París, Zurich, etc. Also, the use of this technology has enabled a more continuous characterization of NR-PM_1 compounds, enabling the intra-day cycle understanding.

The following step towards an optimal SA would be to elongate these PM_1 composition studies to longer time series and to couple a wider variety of species with the highest possible TR in order to characterise the intra-day variability of the outcoming more comprehensive sources. In the latter objective regard, the MTR-PMF technique allows for SA based on datasets with different TR, which will not only provide an improved description of the sources in terms of the contribution of a wider range of species but also in terms of time variation.

2

OBJECTIVES AND STRUCTURE

2.1 OBJECTIVES

One of the remaining gaps in the literature is the lack of long-range studies of PM composition and sources, especially for PM_1. The main objective of this thesis is the generation of knowledge of the non-refractory PM_1 compounds and sources in Barcelona, including in turn a global understanding of its atmospheric composition and transport mechanisms as a whole. The gained understanding will benefit climate impact and health studies and will help promote local and global pollution mitigation regulations.

This aim is addressed through the integration of three studies that examine PM_1 nature or the methodologies to unravel it: i. Description of the NR-PM_1 compounds' behaviour in two recent periods, focusing as well on the source apportionment of the OA, the main PM_1 component; ii. Assessment of the novel OA SA methodology, *rolling* PMF benefits with respect to the previous methodology, the *seasonal* PMF; iii. Coupling of different instruments data to provide a comprehensive PM_1 source description benefitting from previous knowledge of sources at the site.

The specific research objectives concerning the above mentioned papers are these that follow:

a) Comprehensive description of the NR-PM_1 compounds evolution, cycles, and interactions in the Barcelona site. OA sources are also to be discussed in the same terms. A study of the submicronic aerosol composition variations regarding different synoptic and mesoscale meteorological scenarios should also be appraised.

b) Assessment of the current methodologies for source SA, more specifically, comparison of the newly introduced *rolling* PMF to the established *seasonal* PMF. An inquiry to be investigated is the *rolling* PMF profile-adaptability effectivity since it represents the main upgrade of this novel technique.

c) Current OA SA protocol evaluation with insights gained from the *rolling-seasonal* intercomparison.

d) Evaluation on the PMF application on an ensemble of data from different instruments (and then different TR) to obtain SA results of the whole PM_1 mass. Comparison of the MTR-PMF results with PMF on datasets with lower TR, datasets of homogeneous TR, and datasets containing fewer species.

e) Description of the PM_1 sources retrieved by the combination of NR-PM_1, BC and metals information, benefiting from the OA sources analysis and the other compounds study.

f) Retrieval of long-term PM_1 series (and speciated in sources) for future epidemiological assessment. Also, the improvement of the SA techniques will enable more precise submicronic aerosol sources' data collection for source-specific health assessment.

g) Devising of SA methodologies for a more comprehensive submicronic aerosol SA protocol.

2.2 STRUCTURE OF THE THESIS

Following this introduction, the methodology section describes the monitoring site and instrumentation in detail, and outline the measurements and experimental techniques employed to reach the aforementioned objectives. The results section gathers the scientific articles published in peer-reviewed journals of competing scopes.

Paper I tackles the a), f), and g) objectives, **Paper II**, the b), c), and g) and **Paper III**, the d), e), and g).

Afterwards, the discussion chapter spins all results in order to generate robust answers addressing the aforementioned knowledge gaps. Additional information to that provided in the articles was used to further discuss all findings. In conjunction with the main thesis conclusions, a discussion of future research work is presented. Finally, a bibliographic section provides the references used specifically in this work, since those used in each article since are already provided in each publication. An appendix including the list of acronyms and symbols as well as the supplementary information of the scientific articles presented closes this manuscript.

Part II

METHODS

3

METHODOLOGY

3.1 MEASUREMENT SITES

The three scientific articles included in this thesis use aerosol measurements collected in Barcelona, in the Western Mediterranean Basin (WMB, Fig. 4), but the regional background measurements of the Montseny-El Brull site were also harnessed for a better pollution sources characterisation. Moreover, measurements at other urban European sites' measurements, shortly outlined in section 3.1.4, also contribute to this dissertation. This section describes all the measurement enclaves in this thesis.

3.1.1 *Western Mediterranean basin (WMB)*

The European Western Mediterranean Basin (WMB) area (shown in Figure 4) comprises the Mediterranean coastlines belonging to Spain, France, and Malta and the Tyrrhenian Sea coast and Strait of Sicily coastlines of Italy (European EU Comission, 2022). This area presents complex and heterogeneous orography and atmospheric dynamics and aerosol emission sources. Its climate is categorised as dry-summer subtropical (type Csa/b in the Köppen climate classification), characterised by hot/warm summers with scarce precipitation. However, climate projections depict a remarkable vulnerability of this region to climate change (Barrera-Escoda et al., 2014). The future climate predictions include brewing a precipitation decrease but increasing intensive rain episodes (Lehner et al., 2006), increasing stability conditions, and pronounced warming with a greater occurrence of extremely high-temperature events in future scenario (Giorgi & Lionello, 2008). In terms of advection scenarios, this area is mainly governed by the cyclone-anticyclone dipole consisting on the Açores anticyclone and the depression over Liguria, whose relative position enhances one or another airflow regime (Martin-Vide & Lopez-Bustins, 2006).

From a demographic-economical point of view, the WMB is a densely populated and industrialised area, and due to its strategic positioning, it is also one of the principal maritime corridors in the world and a consolidated tourist destination. The

ensemble of orographical confinement, the complexity of meteorological conditions, and the variety of pollution sources in this area deprecate air quality both in the background and eventual concentrations. Besides the emission of pollutants, this region is also stroke by long-range transport pollution, both with northern continental and north-African advection, making it especially affected by airborne PM (Pandolfi et al., 2014).

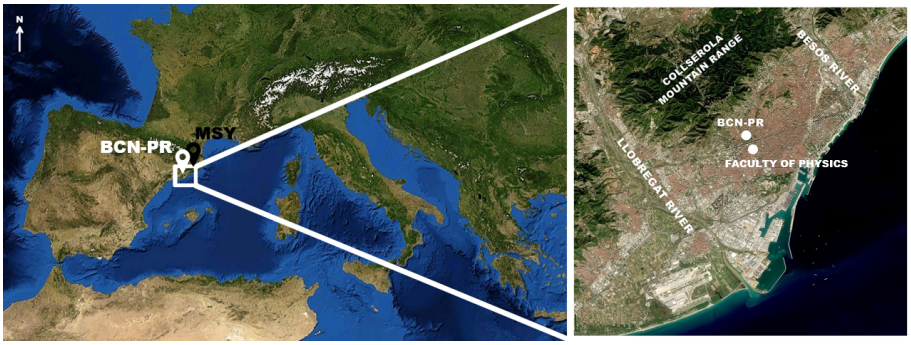

Figure 4: Weastern Mediterranean Basin map showing the location of the Barcelona-Palau Reial (BCN-PR) and Montseny - El Brull (MSY) sites. The map on the right shows the precise location of the site and the Faculty of Physics in the Barcelona area and the main surrounding relevant features. Sources: NASA World Wind and Terrametrics, National Geographic Institute.

3.1.2 *Barcelona - Palau Reial*

Barcelona is the capital and the largest city of Catalonia, and the second most populated city of Spain (over 1.6 million inhabitants within city limits and over 3.3 extending to the metropolitan area). It is also the sixth most populous urban area in the European Union and the largest metropolis on the Mediterranean Sea. The city is located on the northeastern coast of Spain, belted by the mouths of the Llobregat and the Besós rivers, at the west and northeast, respectively. The Mediterranean Sea is at the south and south-east, and the Collserola mountain range, with a maximum altitude of 512 m a.s.l, is at the north. A 20% of the metropolitan area of Barcelona territory is dedicated to residency and a 7% to industrial activity, the latter located mainly along the riverside areas (AMB, 2022). The city lies in an area of intense sea breeze developments which generate orography-modified recirculation flows of pollutants from the city to inland at low levels and reversely at high altitudes (Soler et al., 2011).

The Barcelona - Palau Reial (BCN-PR) site is located in the Institute of Environmental Assessment and Water Research (IDAEA; 41°23'14.28" N, 2°6'56.16" E, 77 m a.s.l.) in the north-west of Barcelona, northeastern Iberian Peninsula (Figure 4). The site is 200

Figure 5: Palau Reial station and Q-ACSM deployment.

m far from one of the most concurred avenues of Barcelona, 300 m away from the Faculty of Physics of the University of Barcelona, where meteorological parameters are gathered, and 5.5 km away from the Mediterranean Sea. According to Meteocat (2023), the 2017-2022 meteorological mean temperature, relative humidity, accumulated precipitation, wind speed, wind direction and solar radiation parameters were, respectively, 17.2 °C, 68%, 604.82 mm, 21.4 $m \cdot s^{-1}$, NW, 15.9 $MJ \cdot m^{-2}$. The BCN-PR station belongs to the Aerosol, Clouds and Trace Gases Research Infrastructure (ACTRIS), Global Atmospheric Watch (GAW) and Atmospheric Pollution Monitoring and Forecasting Network of the Government of Catalonia (XVPCA) atmospheric vigilance infrastructures. This site has been operating continuously since March 2003.

Measurements at the urban background station of Barcelona-Palau Reial (BCN-PR) were reported in **Paper I**, **Paper II**, **Paper III**.

3.1.3 *Montseny el Brull*

Observations made at the regional background station of Montseny (MSY, 41°46'45.41" N, 2°21'28.8" E, 720 m a.s.l., Fig. 6) were used as ancillary explanatory insights for **Paper I**. The measuring station is located at the traffic-restricted Montseny Natural Park, situated at the pre-Coastal Catalan range (maximum peak height 1712 m)

Figure 6: Montseny site.

at the NE of Barcelona. The site is also integrated into the ACTRIS, GAW, and XVPCA networks. This area was characterized by a mean annual temperature of 11.5°C, a mean relative humidity of 76% and annual precipitation of 690 mm in the 2014-2021 period. These meteorological parameters are the result of the mean of the two meteorological stations next to Montseny, PN-Tagamanent and Santa Maria de Palautordera. The MSY site has been operating uninterruptedly since February 2002.

In this region of the Iberian peninsula, daily atmospheric dynamics are characterized by the sea-land breezes activated by the sun heating the slopes orientated to the east and southeast during the morning hours (Jorba et al., 2013; Millán et al., 1997). The sea breeze enters from the south carrying pollutants from the metropolis, which is halfway from the sea to MSY. When colliding with the Montseny mountain range, the transported air masses ascend due to the orography, and when the land breeze is developed, these polluted air masses are transported back to the Mediterranean Sea at a certain altitude. This circulation justifies the diel cycle of all pollutants at this site, which increases from noon until around 6-7 PM.

O_3 was the main measurement used from this site in this thesis, which has been measured since 2013. This gas in Montseny presents diel cycles related to the Barcelona polluted plumes, which when interacting with O_3, cause a drop in O_3 concentrations. **Paper I** also used additional Montseny-El Brull data in order to provide ancillary insights for the aerosol characterisation in Barcelona.

3.1.4 *Other European sites*

Paper II uses measurements from nine European urban and non-urban sites: Barcelona - Palau Reial, Cyprus Atmoshperic Observatory - Agia Marina Xyliatou, Dublin, Atmospheric Observations in LiLle (ATOLL), Magadino, Magurele - INOE, Marseille-Longchamp, SIRTA and Tartu (Table 3, Figure 7). The aerosol measurements and OA source apportionment were carried out by the site data providers and sent to participate to this article. They are also embedded in Chen et al. (2022b) work, and each site source apportionment process description can be found in the references cited therein (Table S1 of Chen et al. (2022b)).

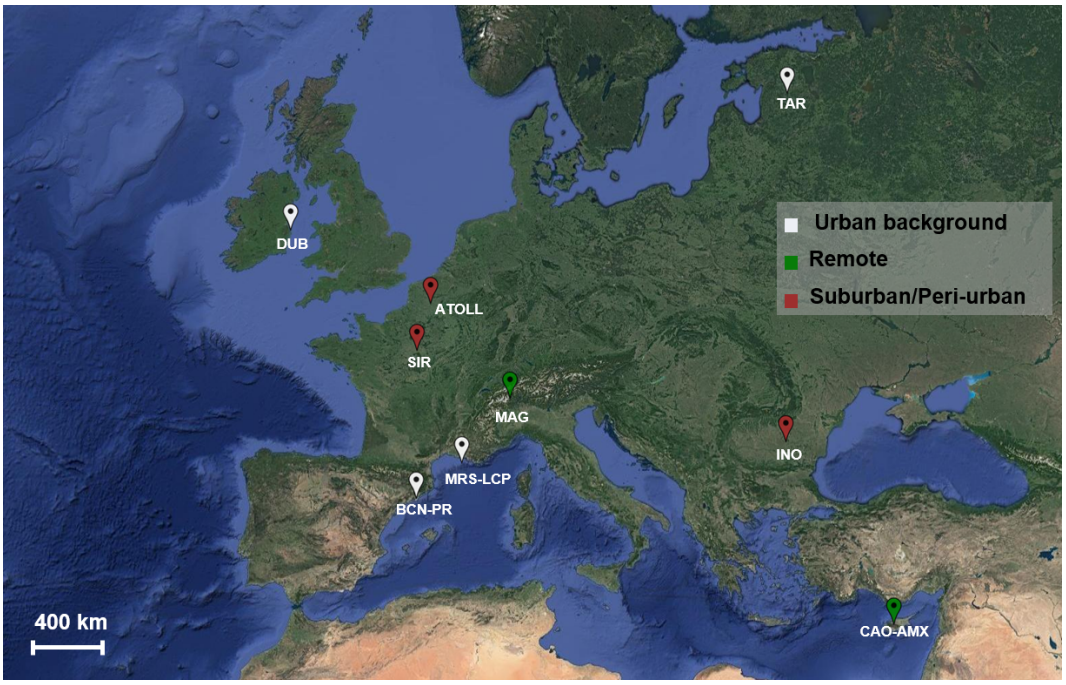

Figure 7: Location of the complementary European sites used in **Paper II**. Map source: Google INEGI, 2023.

3.2 INSTRUMENTATION

The instrumentation used at all the sites is described in Table 4. The BCN-PR site was equipped as well with a MAAP, a high volume sampler, an SMPS, and a CPC, all described in the current section.

Table 3: Description of complementary European sites used in **Paper II.**

Site	Acronym	Type	Country	Location
Cyprus Atmospheric Observatory - Agya Marina	CAO-AMX	Remote	Cyprus	35°2′19.35″N, 33°3′27.95″, 352 m
Dublin	DUB	Urban background	Ireland	53° 18′10.08″N, 06°3′4.52″, 35m
ATmospheric Observations in LiLle	ATOLL	Suburban	France	50°36′40.0″N, 03°08′25.4″E, 70m
Magadino	MGD	Rural	Switzerland	46°9′37″N, 8°56′2″E, 204m
Magurele - INOE	INO	Peri-Urban	Romania	44°20′52.08N, 26°1′43.9″E, 93m
Marseille - Longchamp	MRS-LCP	Urban background	France	43°18′18.8″N, 5°23′40.9″E, 71m
SIRTA	SIR	Suburban	France	48°42′36″N, 2°9′0″E, 163m
Tartu	TAR	Urban Background	Estonia	58°22′14.2″N, 26° 44′5.6″E, 30m

Table 4: Measurements available analysed in the articles presented in this thesis. [1] This site also used SO_2 (Teledyne 100E), UPF (TSI 3031) and SMPS (GRIMM) measurements. [2] This site also used $PM_{2.5}$ and PM_{10} (MetOne BAM1020) measurements.

Site	**Period**	**ACSM**	**Aethalometer**	**NO_x**	**O_3**
BCN-PR	May 2014 - May 2015, Sep 2017 - Oct 2018	Q	AE33	Thermo Scientific 43i	SIR S5014
MSY	May 2014 - May 2015, Sep 2017 - Oct 2018	ToF	AE33	Thermo Scientific 43i	SIR S5014
CAO-AMX	Mar 2015 - Jan 2017	Q	AE31	Ecotech 9841T	-
DUB	Sep 2015 - Aug 2017	Q	AE33	AQICN, Rathmines	-
ATOLL	Oct 2016 - Sep 2017	Q	AE33	N.A.	-
MGD	Aug 2013 - Oct 2014	Q	AE31	AQICN, Magadino	-
INO	Sep 2016 - Sep 2017	Q	AE33	Thermo Scientific 42i	-
MRS-LCP[1]	Jan 2017 - Apr 2018	ToF	AE33	Teledyne 200E	-
SIR	Jan 2016 - May 2017	Q	AE33	Teledyne T200UP	-
TAR[2]	Sep 2016 - Jul 2017	Q	AE33	Horiba APNA-360	-

3.2.1 *Submicronic Non-Refractory measurements: Aerosol Chemical Speciation Monitor*

These measurements were used in **Paper I** providing a comprehensive OA SA, in **Paper II** to test the performance of two PMF methods and on **Paper III** as the main components of an outright PM_1 SA. The two main ACSM sampling periods treated in this thesis are May 2014 - May 2015 and September 2017 - October 2018. However, a longer time series was also inspected including more sampling periods from 2014 to 2021.

i) operational principles

The Aerosol Chemical Speciation Monitor (ACSM, Aerodyne Inc., Figure 8) was built upon the same technology as the Aerosol Mass Spectrometer (AMS, Jayne et al. (2000)) but with a smaller and easier-to-use design which allows for longer sampling periods. Nevertheless, the ACSM does not provide size-resolved concentrations and its time and spectrometry resolution is lower than its predecessor. It provides real-time chemically speciated mass loadings and aerosol mass spectra of non-refractory species at unit mass resolution (UMR) at time resolutions up to 10-30 minutes for typical urban aerosol loadings (several $\mu g \cdot m^{-3}$). The first ACSM sampling on ambient air was in the DAURE campaign (2009, Minguillón et al. (2011)), at the BCN-PR and MSY sites. The guidelines for standard operation principles followed can be found as an outcome of the COST Chemical On-Line cOmpoSition and Source Apportionment of fine aerosoL (COST-COLOSSAL) Action (COST-COLOSSAL, 2021).

The Q-ACSM principles are mapped in Figure 9. The air enters through a 2.5 µm cut-off inlet with a flow rate of 3 $L \cdot min^{-1}$ and is dried so that its RH is below 40%. Then it is conducted through a critical orifice of 0.1 μm of diameter which sets a flow of 0.1 $L \cdot min^{-1}$. The incoming air is conducted through an aerodynamic lens which transmits particles between 5 and 650nm with a transmission efficiency over a 50% (Liu et al., 2007). The instrument provides particle concentration by means of a filter-ambient switching valve system. The valve alternates particle-free (filter) and particle-laden (ambient) air beams so that the software can calculate the concentration from the subtraction of these two signals. The aerosol enters the core of the instrument, consisting of four vacuum chambers pumped by three turbomolecular pumps and a

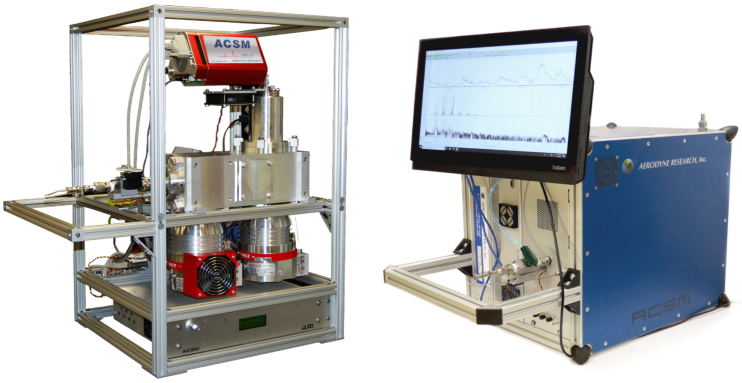

Figure 8: Q-ACSM (left) and ToF-ACSM (right).

backup diaphragm pump. At the end of the last chamber, the particle beam impacts a tungsten surface at 600°C which flash vaporises the non-refractory compounds. Then the impact of electrons released by a tungsten filament at 70 eV ionises particles and is conducted through the mass spectrometer. The ion signals are digitalised and sent to the *Tof*DAQ data recorder and to the *Igor*DAQ package (both from Tofwerk AG) running under the Igor environment (WaveMetrics Inc., OR, USA) for data analysis. A fragmentation table (Allan et al., 2004) and the response factor (RF), are used to convert the signal spectra into organic or inorganic species concentrations.

As well as its predecessor AMS, ACSM concentrations for a species s, C_s (in

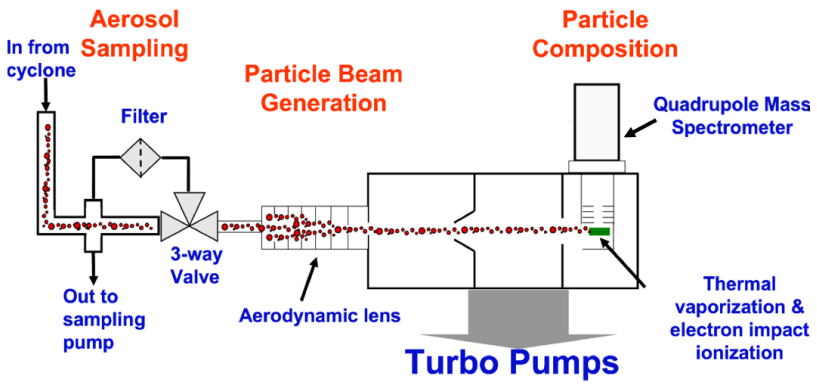

Figure 9: Schematic functioning of Q-ACSM operational principles.

$\mu g \cdot m^{-3}$) can be determined from its mass spectral fragments i (of intensity I_s, in ions/s) as follows:

$$C_s = \frac{10^{12} \cdot MW_S}{IE_s \cdot Q \cdot N_A} \sum_i I_{s,i} \tag{8}$$

where IE is the Ionisation Efficiency (in ions/molecule), N_A is the Avogadro number, MW_s is the molecular weight of the species s, Q is the volumetric sample flow rate into the instrument (in $cm^3 \cdot s^{-1}$) and the 10^{12} factor is needed for unit conversion. The IE_s refers to the Ionisation Efficiency and it is a parameter expressed relatively to NO_3^- (IE_{NO_3}, Jimenez et al. (2003)), and obtained during calibration as explained in 3.2.1.

$$\frac{IE_s}{MW_s} = RIE_s \cdot \frac{IE_{NO_3}}{MW_{NO_3}} \tag{9}$$

The standard RIE values for organic molecules, NO_3^-, SO_4^{2-}, and NH_4^+ moieties are 1.4, 1.1, 1.15, and 3.5–6, respectively (Canagaratna et al., 2007). However, Reyes-Villegas et al. (2018) pointed out the differences in the organic RIE value depending on OA composition, i.e. sources. The RIE calibration will be explained in section 3.2.1.

There are two types of ACSM depending on their spectrometer: Quadrupole ACSM (Ng et al., 2011) and Time-of-Flight ACSM (Fröhlich et al., 2013). The ToF-ACSM is reported to present a better mass resolution (M/ΔM = 600) and detection limits (below 30 $ng \cdot m^{-3}$) with respect to the Q-ACSM for a time resolution (TR) of 30 minutes, which can besides reduced to 10 minutes. These features allow for higher TRs and/or lower concentration environments sampling. Also, it is more compact and lighter than the Q-ACSM. Moreover, ToF-ACSM can even resolve peaks below UMR if proper peak fitting is conducted. Another difference between Q and ToF ACSMs is the existence/lack of an internal effusive naphthalene ($C_{10}H_8$) source inside the detection chamber, respectively. The Q-ACSM uses the *m/z128* naphthalene signal for mass-to-charge calibration and several of its signals to measure the transmission efficiency dependency on the mass-to-charge ratio of the quadrupole. In turn, the ToF-ACSM detector can dispense with this naphthalene source due to more robust electronics.

A Q-ACSM was deployed in Palau-Reial and the ToF-ACSM in Montseny, although the latter measurements were not included in the current thesis.

II) CALIBRATIONS AND SETTINGS

The calibration of the ACSM consists of a comparison of the NR-PM_1 species (NO_3^-, NH_4^+, and SO_4^{2-}) electronic response to a known input mass of these species (Jimenez et al., 2003). A detailed description of this methodology can be found at Ng et al. (2011). An atomiser (TSI model 3772) generates mono-disperse AN and AS particles, which are dried by conducting them through a diffusion Nafion drier. These particles enter a Differential Mobility Analyser (described in section 3.2.4, model TSI 3080) which only selects those of a diameter of 300 nm. Particles of this specific diameter are selected because they are big enough to be measured by the ACSM and they are unlikely to be double-charged when they are ionised at this size. This particle beam is split and is conducted both to the ACSM and to a Condensation Particle Counter, CPC model TSI 3772). With this configuration, a signal of detection is measured by the ACSM whilst the number of particles computed by the CPC allows for controlling the input mass concentration. Then, a scatterplot is generated comparing ACSM signal and input mass, which should be linearly correlated, and from the slope of the calibration line, one can calculate the IE of the species using eq. 8. Then, the RIE of the species s (NH_4^+ or SO_4^{2-}) are calculated relatively to that NO_3^- as in equation 9.

Firstly, the calibration is performed with AN to acquire the NH_4^+ RIE and subsequently, the procedure is repeated analogously with AS to acquire the SO_4^{2-} RIE. This order is mandatory to avoid the SO_4^{2-}, which is more prone to get stuck in the vaporiser walls, to interfere the AN calibration

The calibration for the Cl^- and organics is dismissed for different reasons. Firstly, the chloride detection is very noisy in the ACSM due to the incapacity to vaporise the sea salt chloride, hence its concentrations are usually disregarded. Secondly, the organics are a too wide range of compounds, yet it is not feasible to produce particles of this ensemble of compounds. The used value for OA RIE is 1.4, although Reyes-Villegas et al. (2018) showed a large variability depending on the OA sources.

3.2.2 *Submicronic refractory measurements*

These measurements were used in the three articles of this thesis. In **Paper I** and **Paper II**, to track the BC yearly evolution (expected to correlate with the HOA factor) and to get a bulk for PM_1 when summed to NR-PM_1 concentrations with the aim of comparing it to the PM_1 mass retrieved by other instrumentation (CPC, SMPS). The latter procedure mentioned is usually referred to as mass closure verification. In **Paper III**, BC concentrations were introduced to PMF as species differentiated into liquid fuel and solid fuel BCs (BC_{lf}, BC_{sf}, respectively).

i) aethalometer

A multi-wavelenghth AE33 Aethalometer (model AE33, Magee Scientific, Aerosol d.o.o; Drinovec et al. (2015)) with a $PM_{2.5}$ cut-off inlet was used to measure BC (Fig. 10 (a). This instrument measures the attenuation of light at seven different wavelengths (370, 470, 520, 590, 660, 880, and 950 nm) passing through two sample spots with different flows with respect to a reference spot. The concentration of BC particles deposited on the filter tape is calculated from the outcoming light intensity compared to that from the reference spot. Aethalometer measurements are affected by artefacts related to the presence of the filter tape, namely the filter loading effect (corrected online by the new AE33 model used in this thesis) and the multiple scattering. The latter artefact is corrected offline with the correction constant C of 2.44 proposed for the BCN-PR site by Yus-Díez et al. (2021). The artefacts correction allows for calculating the absorption coefficients from attenuation measurements at seven wavelengths. Then, the absorption at 880nm is used to calculate the BC concentrations using an appropriate mass absorption cross-section. The absorption at the seven light transmission wavelength measurements enabled BC speciation into BC_{lf} and BC_{sf} using the Sandradewi model (Sandradewi et al., 2008). The native TR of this instrument is 1 min.

ii) multi-angle absorption photometer

A multi-angle absorption photometer (MAAP, Model 5012, Thermo Inc., USA, Petzold and Schönlinner (2004), Fig. 10 (b)) was used for BC concentrations measurements. This instrument measures the light beam (wavelength of 637 nm) properties modification caused by the presence of particles in a filter through which

the sampled air is conducted. The reduction of light transmission, multiple reflection intensities, and air sample volume is continuously integrated over the sample run period to provide BC concentration measurements. The native resolution of these measurements is 1 minute and the inlet cut-off was PM_{10} at BCN-PR. The absorption measurement uncertainty of this instrument was set at 12% of the measurement (Petzold & Schönlinner, 2004).

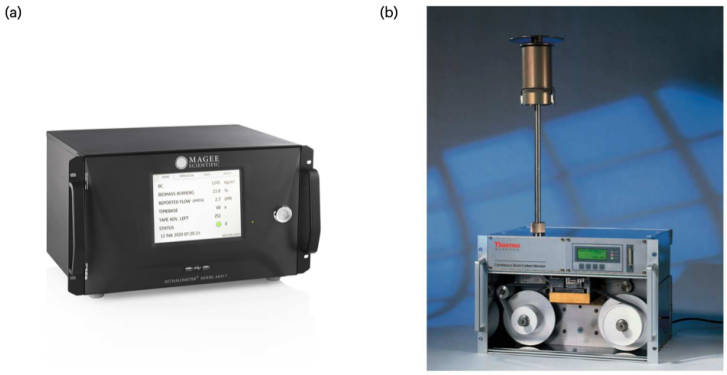

Figure 10: Optical instrumentation for refractory aerosol measurement. (a) Aethalometer AE33. (b) Multi-Angle Absorption Photometer.

3.2.3 *Offline aerosol chemical composition: filter sampling*

These measurements were used in **Paper I** to compare the ACSM SIA concentrations to the same ions in offline analysis for coherence checks between both measurements. In **Paper III** they were included as input species into the MTR-PMF, providing the metals information.

The offline sampling is carried out using DIGITEL D80 high-volume samplers (MCV, Spain) working at 30 $m^3 \cdot h^{-1}$ and equipped with a DIGITEL PM_1 head (Figure 11). A total of 83 samples were collected for the September 2017 - October 2018 period on 150 mm quartz micro-fibre filters (Pallflex 2500 QAT-UP). The sampling lasted 24 h and was carried out every four days from midnight to midnight. Each filter was divided into fourths to analyse them according to the complete chemical analysis procedure furtherly described in (Querol et al., 2001). The process undergoing each quarter is the following:

Figure 11: High-volume sampler with PM_1 head.

- Acid digestion: Quantification of the major elements (Al, Fe, K, Ca, Na, Mg, S, P, Ba, Cr, Cu, Mn, Ni, Sr, Pb, Ti, V, Zn) and the trace elements (Li, Be, B, Sc, Ti, V, Cr, Mn, Co, Ni, Cu, Zn, Ga, Ge, As, Rb, Y, Zr, Nb, Mo, Cd, Sn, Sb, Cs, La, Ce, Pr, Nd, Sm, Eu, Gd, Tb, Dy, Ho, Er, Tm, Yb, Lu, Hf, Ta, W, Tl, Pb, Th and U) by means of acidic digestion and a posterior analysis with Inductively Coupled Plasma Atomic Spectrometer (ICP-AES, IRIS Advantage TJA Solutions, THERMO), and with an Inductively Coupled Plasma Mass Spectrometry (ICP-MS, X series II, THERMO).

- Water extraction: Quantification of SO_4^{2-}, NO_3^-, NH_4^+, and Cl^- concentrations. The samples are leached and the SO_4^{2-}, NO_3^-, and Cl^- concentrations are determined through a ion chromatography system (Dionex Aquion Ion Chromatography, Thermo Fisher Scientific Inc., USA) and the NH_4^+ concentrations with an ammonia selective electrode (MODEL 710 A+, THERMO Orion).

- Thermal-optical OC-EC analysis: One punch (1.5 cm^2) of the sample is analysed through the Sunset Laboratory OCEC analyzer following the EUSAAR 2 thermal-optical transmittance (TOT) protocol (Cavalli et al., 2010).

- The remaining fourth is stored for possible future reanalysis.

One blank filter for each set of 10 filters is kept and analysed by the same aforementioned techniques in order to subtract the background concentrations from the sampled filters so that the PM concentrations are obtained. The offline measurement uncertainties were estimated as in Escrig et al. (2009).

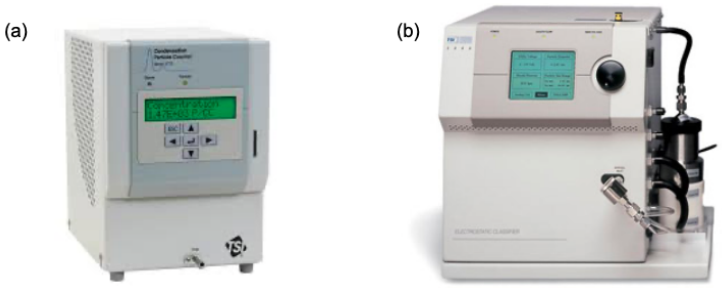

Figure 12: (a) Condensation Particle Counter (CPC) model 3772, TSI. (b) Scanning Mobility Particle Sizer (SMPS) 3080, TSI.

Also, these filters were also used for OP analysis In't Veld et al. (2022), as will be described in section 3.3.5.

3.2.4 *Particle number size distribution*

The particle number size distribution was used in this thesis for two differentiated purposes: i. In Q-ACSM IE, RIE calibration, to measure the input mass of aerosol which is to be compared with the Q-ACSM electronic signal (see section 3.2.1); ii. in the mass closure check, consisting of comparing the sum of all Q-ACSM organic and inorganic species mass plus BC concentrations with the equivalent mass of the total number of particles measured. The latter is a standard operation for quality assurance and quality control when treating ACSM data (COST-COLOSSAL, 2019) which will be explicitly reported in **Paper I** .

i) condensation particle counter

The total particle number was measured by means of a Condensation Particle Counter (CPC, Fig. 12(a)). This instrument saturates the sample of aerosol onto the working fluid particles. The condensation of the ambient particles onto the working fluid enlarges the particle size, which enables their detection by a conventional optical system detector. The particles are then channelled to the photodetector which, from the blockage of the light beam and considering the entrance flow, provides the number of particles in the sample. This instrument is operated continuously at the BCN-PR site at a 10-minute TR.

II) SCANNING MOBILITY PARTICLE SIZER

The Scanning Mobility Particle Sizer (TSI, Fig. 12 (b)) is based on a Differential Mobility Analyser (DMA), consisting of a cylindrical rod and grounded walls. The application of a high voltage in the central rod generates an electrical field which makes particles move at a velocity inversely proportional to their diameter so that they impact the rod at different points depending on their size. The particles entering the instrument are previously charge-neutralised by using a radioactive or X-ray source. The particles which impact the base of the rod are then guided to a CPC which counts the number of particles at that certain diameter. Varying the voltage applied, one can collect a particle diameter range between 12nm - 470nm. In order to obtain the total PM_1 mass, all diameter channel numbers of particles are summed and the number of particles is converted to mass concentration. This instrument works at a TR of 5 minutes.

3.2.5 *Gases and meteorological data*

Real-time gaseous pollutants measurements, NO, NO_2 (Thermo Scientific, Model 43i), CO (Ecotech EC Model 9830), O_3 (SIR Model S5014) and SO_2 (Thermo Scientific Model 43C), operated by the Department of Environment of the Autonomous Government of Catalonia, were available for the ACSM operating period at PR at a TR of 30 min. Instrument details for NO_x and O_3 measurements at other sites can be found in Table 4. Meteorological variables (temperature, relative humidity, wind speed, wind direction, and solar radiation) were provided by the Department of Meteorology of the University of Barcelona. These measurements are collected at the meteorological site of the Faculty of Physics, approximately 300 m away from the BCN-PR site (Fig. 4) with a 10-min TR.

3.3 DATA ANALYSIS

The subsequent sections describe the methodologies upon which real-time data is analysed. Unless otherwise specified, all dates and hours are presented in UTC, all the averages are arithmetic, and all linear regressions are computed from an orthogonal approach.

3.3.1 *ACSM data treatment*

The Q-ACSM data treatment guidelines followed are those described in COST-COLOSSAL (2021). Data corrections are applied to overcome the instrument limitations. These comprise ion transmission, collection efficiency and air beam correction.

- Ion transmission correction: the use of a lower quality spectrometer with respect to the AMS causes performance limitations. In the case of the quadrupole spectrometer, the decrease of ion transmission of the large *m/z*s can range up to a factor of five. In the Q-ACSM, the naphthalene source provides several signals of known intensities along the detection range in order to determine the ion transmission decay to correct it subsequently.

- Collection efficiency: some particles do not accomplish complete flash vaporization (Canagaratna et al., 2007) but stay bouncing on the chamber with the consequence that they are missed by the detector (Matthew et al., 2008; Quinn et al., 2006). This effect is addressed by introducing a collection efficiency parameter (CE) which is usually around 0.5 but depends strongly on the particle phase, being higher for liquid particles. The particle phase in the ACSM is influenced by 4 factors: humidity in the sampling line, acidity/neutrality of the SO_4^{2-} content, AN content, and organic liquid content (Middlebrook et al., 2012). With the aim to account for these parameters, a correction known as CE as a function of phase presented in this article is applied in order to mitigate the particle losses at the vaporiser to concentrations determined as in equation 8.

- Air beam correction: the decay of the air signal (*m/z28* signal) due to the detector drifts or detector loss of sensitivity with time causes miscalculation of the species concentrations. Therefore, the air beam correction, based on the signal of *m/z28*, corresponding to the N_2^+ ion as a proxy for the air signal, compensates for this drift by normalising the measured flow rate with respect to this reference air signal.

Posterior to correction, some other checks on the quality are performed on the data in order to localise defective points or periods. The data had to be filtered upon certain instrument parameter thresholds under which measurements are considered to lead to invalid data according to COST-COLOSSAL (2021). Besides, a powerful check to identify how sensible the overall concentrations is observing how accurate is the mass closure. This consists on comparing the

instrument-measured OA+SO_4^{2-}+NO_3^-+NH_4^++Cl^- plus BC concentrations vs. other instrument PM_1 measurements (obtained by SMPS or CPC). The methodology used to properly compare ACSM and other ancillary instrument data can be found in the second deliverable of the COST-COLOSSAL Action (COST-COLOSSAL, 2019). The observation of the scatter plot provides an idea of how correlated the co-located PM_1 measurements are and whether there is a systematic over/underestimation of the ACSM concentrations. This procedure is also applied species-wise, comparing ACSM speciated concentrations with the offline OM, SO_4^{2-}, NO_3^-, NH_4^+, and Cl^-. These verifications have been previously performed in Budisulistiorini et al. (2014), Minguillón et al. (2015), Poulain et al. (2020), and Ripoll et al. (2015), amongst others.

The data acquisition and treatment process is carried out by means of the *acsm local v. 1.6.0.0 and 1.6.1.6* and *Global Utils* software provided by Aeroyne Inc. (EUA) within the Igor Pro (Wavemetrics Inc.) environment. These software allow for parameter control during the acquisition monitoring and data post-processing. Moreover, it allows to generate OA concentrations and error uncertainties (the latter calculated as in Ulbrich et al. (2009)) that will be used for the OA SA.

3.3.2 *Source apportionment protocol*

The strategies upon which PMF should be applied depend on the nature of the input data. In this thesis, PMF is principally applied to ACSM organic unit-mass-resolution data with a TR of 30 minutes. This instrument provides with datasets of considerable length, i.e. from several months to years, i.e., $\sim 10^3 - 10^4$ points. Regular PMF generates a constant **F** matrix and lets only **G** account for all temporal variation, hence generating sources of a fixed composition that evolve throughout the period. Nevertheless, some studies reported seasonal differences in aerosol composition due to the variety of secondary aerosol formation processes throughout the year, for instance depending on the amount of sunlight available for secondary particle formation. In these cases, PMF applied to OA ACSM data could benefit from profile-adaptation approaches, in order to gather similar groups of pollutants even though their proportion amongst them varies throughout seasons.

A detailed description of the state-of-the-art OA SA protocol can be found in Chen et al. (2022b) as an outcome of the WG2 from COST-COLOSSAL Action, based on measurements performed within ACTRIS. The application of this protocol was

mandatory for all the datasets used in this collaborative project and therefore, for the datasets used in **Paper I** and **Paper II**. The SA analysis is performed within the *Source Finder Pro* software (SoFi, Datalystica Ltd., Villigen, Switzerland). This protocol establishes the SA procedure involving the two main methodologies upon which profile variations can be taken into consideration, *seasonal* and *rolling PMF*, which will be detailed in 3.3.2 and 3.3.2.

Even though the application of this protocol provides guidelines to be applied homogeneously and promotes less user-subjectivity, there is still certain user-driven subjectiveness for solution selection. The application of user-defined criteria, the selection of anchor profiles, or the conditions on which to accept an emerging factor or not are examples of possible user-dependent decisions which might impact the final solution.

There are further PMF procedures tackled in this thesis that are not contained in that protocol but will be presented in this section. This is the case for the multi-time resolution (MTR) PMF, which response to the necessity of feeding the model with data of multiple time resolutions.

i) seasonal pmf

Seasonal PMF allows for intra-year variations associated with seasonal source modifications usually influenced by meteorology. In order to apply *seasonal* PMF, the input PMF matrices are divided into season-long submatrices and PMF is applied to each of them. Before attempting this approach, pollution and meteorological data have to be examined in order to resolve if seasonal splitting (i.e. DJF, MAM, JJA, SON) is coherent or if other data divisions are more phenomena-representative. Each season (or modified season period, which will be hereinafter referred as a season as well) PMF application must seek the best number of factors representing the sources, residuals minimization, profile or time series anchoring assessment, environmental feasibility of sources etc. Once the optimal solution is found for each season, the sources' time series will be concatenated and seasonal profile variations evaluated to provide year-wise time series and fingerprint evolution.

The current SA protocol establishes the application of *seasonal* PMF as the first step since it allows for an exhaustive inspection of the model performance and results. Firstly, general tests on each season's data to identify the presence and stability of aerosol sources must be carried out. The following action consists of producing statistically robust results. The *seasonal* PMF specifications are listed below.

1. *Seasonal* PMF pre-tests
    a) Unconstrained runs (2-8) factors.
    b) Exploration for the presence of OA factors (in order of HOA, BBOA, COA, CCOA, special local factors (if applicable), and OOA factors).
    c) Residual analysis assessment (no structural patterns in diel profiles/time series/mass spectra).
    d) *a*-value sensitivity analysis for constrained factors (i.e. POAs).
2. *Seasonal* bootstrap analysis
    a) Constrain the POAs and site-specific factor(s) in mass spectra retrieved from base case (the satisfactory solutions from *seasonal* PMF pre-tests).
    b) Combine the bootstrap resampling strategy with random a-values with an upper a-value of 0.4–0.5 for POAs and site-specific factor(s) and a repeat of 100–1000 times.
    c) Use the criteria-based selection technique to filter out PMF runs that are not environmentally reasonable.
    d) Quality check for the bootstrapped solution.

Bootstrap (Efron, 2000) is a technique used in this context for uncertainty estimation . By randomly resampling the PMF input, the differences in PMF outcomes are quantified to assess the robustness of a solution.

II) ROLLING PMF

Rolling PMF was devised in order to account for the intra-seasonal source profile variation that the *seasonal* PMF approach misses, as some studies highlight the variability of the OA sources' chemical fingerprints, which can even be intra-seasonal (Canonaco et al., 2015). That article shows how the fresh SOA fingerprint is highly influenced by biomass burning emissions in winter and by biogenic processes in summer. Hence, the use of smaller PMF windows was proposed by Parworth et al.

(2015), and subsequently implemented in SoFi Pro as described in Canonaco et al. (2021). The *rolling* method consists of running PMF in windows of a certain length (usually 14 days, in order to capture weekly aerosol cycles) and shifting this window usually with 1-day steps, rolling throughout the whole dataset. All the overlapping runs for a certain day are averaged once a criteria-based automatic selection is applied to filter out non-environmentally feasible runs. These criteria typically consist of correlations of certain factors to co-located ancillary measurements, factor diel cycle features, or species-driven behaviours of a given factor.

The SA protocol in Chen et al. (2022b) establishes the following steps regarding the *rolling* PMF application. This step benefits from the gathered knowledge through *seasonal* PMF pre-tests so that the most appropriate anchors and a number of factors established are used in the current step. However, these two *rolling* PMF steps might have to be repeated testing different window lengths and criteria thresholds' effectiveness in excluding unreasonable PMF runs.

1. *Rolling* PMF
    a) Constraint of the primary OA profiles using published profiles or averaged site-specific profiles from *seasonal* PMF bootstrapped solutions.
    b) Constrain site-specific factor MS (if available) using the random *a*-value approach within a range of 0–0.4 and a step of 0.1. The upper limit for the BBOA a-value is 0.5.
    c) Enablement of the bootstrap statistical assessment mechanism and setting the length of the PMF window (7, 14 or 28 days).
    d) Setting the range of the number of factors based on the number of factors obtained during the *seasonal* analysis.
2. Criteria-based selection for PMF
    a) Definition of a sorting criterion for the OOA factors differentiated into different degrees of oxidation state (*f44* for the MO-OOA, *f43* for the LO-OOA) in case there are two unconstrained OOA factors.
    b) Selection criteria of PMF solutions based on correlations with external tracers.
    c) Selection criteria of PMF solutions based on time series (e.g., diel cycles, explained variation of key ions, correlation with co-located ancillary measurements etc.).

d) Definition of the "best" PMF runs using the relevant/appropriate statistical tests (e.g., t-test approach).

e) Optimization of the time windows comparing the number of non-modelled points and Q/Qexp among different time windows.

All these steps provide an averaged solution of all those runs which fulfil the criteria established as well as all factors' statistical error estimations. This solution, due to the *rolling* PMF use, contains the time evolution of the factor profiles, allowing for intra- and inter-season evolution.

3.3.3 *Multi-time resolution PMF*

The MTR-PMF methodology was first established in Zhou et al. (2004) and consists of a slight modification in the PMF equations in order to assimilate datasets of combined time resolutions:

$$x_{ij} = \frac{1}{t_{s2} - t_{s1} + 1} \Sigma_{k=1}^{p} \left(f_{jk} \Sigma_{i=t_{s1}}^{t_{s2}} g_{ik} \eta_{jm} \right) + e_{sj} \tag{10}$$

where s is the sample number, j stands for the species, t_{s2} is the end time and t_{s1} is the start time (in time units). The shortest time interval is chosen as the time unit. In this equation, all components are equally defined as in equation 1, except for the newly introduced m, accounting for the different instruments, and η, being a factor that accounts for replicated species in case a species j is measured by two different techniques. For a replicated species j, the η adjustment factor assumes that the concentration values measured by different methods are proportional, which for unreplicated species, it is not necessary and it is equal to 1. In the case where $t_1 = t_2$, the equation collapses to the regular PMF equation (eq. 1). In case a source does not contain any species from the highest TR species, the model cannot retrieve a high TR time series for it. In order to overcome this incapability, a smoothing equation is introduced in order to smooth the time series of the k source:

$$g_{i+1,k} - g_{ik} = 0 + e_i \tag{11}$$

Its application limits the variation of the k source from one timestamp i to the following to the error committed in the timestamp i. This prevents adding inconsistent spikes in the time series due to the incorporation of unstable data.

One of the main throwbacks from combining different resolution data (and originated

by different instruments) is that the coupling of uncertainties of different data subsets, which might be calculated by different methods, can lead to unbalanced datasets. This is specially frequent in AMS or ACSM due to *m/z* patterns, can imply uncertainty unbalances from one instrument to the other. This issue can impact the outcoming PMF solution in terms of solution imbalance. This will provide an unfairly weighted representation of the outcoming PMF sources, prevailing one type of data more than the other. This disadvantage can be prevented if uncertainties of the combined input matrices are balanced by weighting them as follows:

$$\sigma'_{ijm} = \frac{\sigma_{ijm}}{C_m} \tag{12}$$

The assessment of the output PMF scaled residuals is crucial to rule which weightings are those which ensure a *fair* representation of all dataset components. The *fair* MTR-PMF solution was defined by Slowik et al. (2010) as that whose different instrument scaled residuals distributions out from MTR-PMF present the same distribution as if they had been independently run. Mathematically, this can be assessed by calculating the overlapping area of the different instruments' scaled residuals distributions designated as $F_{overlap}$:

$$F_{overlap} = \int_{-a}^{a} \min\left(P_m(s_{ij})\right) \tag{13}$$

where $P_m(s_{ij})$ is the scaled residuals distribution of the *m*-instrument data and *a* represents the integration limits of such distribution. The *fairest* weightings will be those which minimise the difference of $F_{overlap}$ to $F^*_{overlap}$, where $F^*_{overlap}$is the $F_{overlap}$ of the scaled residuals overlap of the independently run PMFs for each instrument subdataset.

The MTR-PMF methodology was neither applied with *rolling* nor *seasonal* PMF in **Paper III**. PMF was run over the whole year, as otherwise, the gaps in all three types of data used would have caused different number of points in each PMF window and thus, different representativity of each instrument from window to window. Therefore, the incapability of describing variations of the source fingerprints is acknowledged during the SA discussion.

3.3.4 *Comparison between SA solutions*

Paper I, **Paper II** and **Paper III** involve comparison of SA results in one way or another. Since SA results cannot be compared to reference values, it might be difficult to assess the accuracy of a SA methodology with respect to another or even the error committed during the process. This is why the very nature of comparison is a matter of investigation throughout this thesis. **Paper I** uses the time periods A (May 2014 - May 2015) and B (September 2017 - October 2018). Period B is also the dataset used for the multi-site representation of Barcelona in **Paper II** and the high TR ACSM data employed in the MTR-PMF in **Paper III.**

In **Paper I**, the attention is set toward phenomenology results, trying to assess the pollutant levels and origin of two sampling periods. The OA SA results were restricted to the *seasonal* steps of the aforementioned protocol. Although this scientific article does aim to correlate both periods, which are both one year-long and are separated by one year in between, this cannot be done in a straightforward way. The characterization of their differences as a temporal trend, as it must take into account they might contain inter-annual differences. For such reason, other time periods of ACSM deployment in BCN-PR were also analysed, covering the whole 2014-2021 period. A matter of such special interest as the oxidation degree of SOA was carefully tackled to account not only for the ratio of LO-OOA-to-MO-OOA sources but also for the apportionment of the oxidation marker ions into each of these sources' profiles.

A different approach was taken in **Paper II**, mimicking some comparison techniques described in Belis et al. (2015). This scientific work aimed to show proof of the improvements reported from the most state-of-the-art *rolling* PMF in comparison to the preceding *seasonal* PMF. With this aim, the comparison approach had the ambitious mission to outline the main differences between both methodologies. The testing was designed in the two directions described hereunder.

First of all, a synthetic dataset, i.e., a dataset created from database profiles, model-retrieved time series, and Gaussian error was used to feed both PMF methodologies in order to be able to compare each of the outcoming SA solutions to the input sources. More details on the fabrication of this dataset can be found in Section 2.2 of **Paper II**. The comparability of the output vs. input was assessed by observing the scaled residuals of both methods and the similarity of outcoming

profiles and time series with respect to the truth ones. Also, the error assessment of both methodologies, concerning the scaled residuals and the Q/Q_{exp} ratio was also useful for their functioning evaluation.

Secondly, a more ground-based approach was designed, using nine real-world datasets from all over Europe comprising different OA sources. All of these datasets were also used in Chen et al. (2022b), therefore, all of them guaranteed having the aforementioned protocol applied when providing *rolling* and *seasonal* results. Both methodologies' time series, profiles, and residuals comparison were performed in an analogous way with respect to the synthetic dataset.

Paper III tackled the challenge of combining different instrument data with different native TR in order to obtain a comprehensive PM_1 SA. The outcomes of this SA were compared to other PMF approaches using different couplings of data. Besides, this paper also tested the convenience of averaging the original time series of certain instruments' data to match the lower time resolutions from a systematical approach. Another parameter under study in this article was the uncertainty weighting of the several instrument data subsets involved in order to obtain the fairest solution as detailed in section 3.3.3. For both parameters assessment, several TRs for the high TR data subset (R_1, 30 minutes, 1h, 2h, 3h, 6h, 12h, 24h) were run sweeping several C value combinations (C_{HR}, C_{LR}, respectively for the high and low TR data subsets). This enabled a 2-D parameter analysis of both the mathematical and environmental quality of the SA solution.

Mathematically, the best solution was established according to the scaled residuals distribution of both instruments as detailed beforehand. Also, these residuals calculation was observed throughout the different resolutions in order to filter out those runs with scaled residuals overshooting significantly the [-3, 3] range. Then, the performance of the different R_1s is evaluated regarding their Q/Q_{exp} values, which in the ideal case should be around 1. Environmentally, PMF solutions were assessed by judging how coherent could be the coupling of different species into one source comparing the results with several previous studies in the area.

3.3.5 *Other data analysis procedures*

I) ATMOSPHERIC SCENARIOS CLASSIFICATION TOOLS

Atmospheric scenarios refer to the synoptic configuration of high and low pressures generating specific airflow regimes over the area of study. Grouping days over similar synoptic flow scenarios and comparing them to pollutant levels enables examining the composition of the different air masses carrying pollutants of different sources or provenance.

The classification of atmospheric episodes has been widely performed over the WMB by means of HYSPLIT (Hybrid Single Particle Lagrangian Integrated Trajectory Model, Stein et al. (2015) from the National Oceanic and Atmospheric Administration (NOAA) Air Resources Laboratory (ARL). This model computes air parcels back-trajectories for 120h at three altitudes (750, 1500 and 2500 m a.s.l) for daily meteorological measurements. It determines the origin of air masses that reach a particular area accounting for its long-range transport. The classification of atmospheric flow regimes over PR is differentiated into the following flow regimes: i. Atlantic north (AN); ii. Winter anticyclonic stagnation (WA) (from October to March); iii. European (EU); iv. Mediterranean (MED); v. North African (NAF); vi. Summer regional (SREG, from April to September). These scenarios are further described in previous works in the area (Pey et al., 2010; Ripoll et al., 2015; Ripoll et al., 2014) and shown in Figure 13.

II) OP MEASUREMENTS

OP measurements, used in the discussion section to assess PM_1 SA sources' toxicity, are extracted from the PM_1 offline filter samples presented in 3.2.3. OP is assessed by inserting PM in simulated lung fluid and analysing its response in two acellular assays which are sensitive to redox-active PM constituents: dithiothreitol (DTT) and ascorbic acid (AA). Their main difference is their sensitivity to certain species. Whilst DTT sensitivity is balanced between transition metals and organic species, AA is more sensitive to transition metals (Calas et al., 2018). Usually, OP is presented normalised by cubic meter of air, denoted as OP^V and in units of $nmol \cdot min^{-1} \cdot m^{-3}$). Further details on the measurement of these two assays depletion can be found in In't Veld

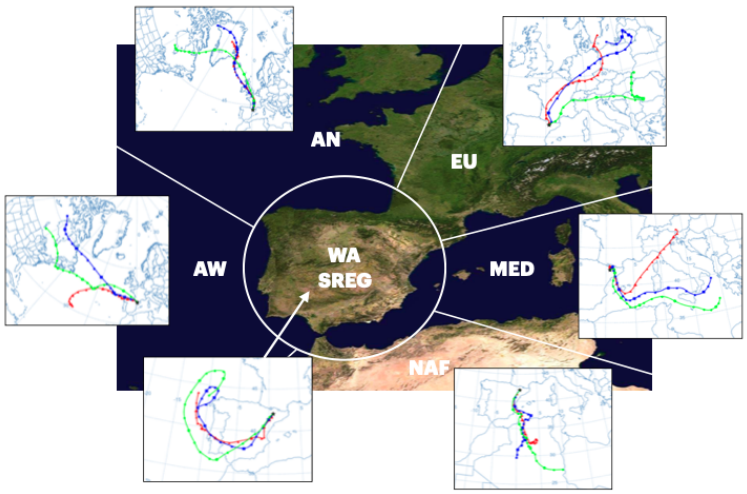

Figure 13: Classification of atmospheric episodes according to HYSPLITT backtrajectories.

et al. (2022).

III) MULTI-LINEAR REGRESSION

Several studies have approached OP SA by means of the statistical technique of multi-linear regression (MLR). The goal of this approach is to model the linear relationship between the dependent variables as a combination of multiple independent variables through the expression:

$$y_i = \beta_{i0} + \sum_{j=1}^{m} (\beta_{ij} \cdot x_{ij}) + \epsilon_i \tag{14}$$

where x accounts for the independent variables, y for the dependent variable, i for the index of samples, j for the index of independent variables, m for the number of independent variables, β for regression coefficients, and ϵ for the fitting error. The fitting is done minimising the ϵ iteratively by least mean squares, and it assumes no co-linearity amongst the independent variables.

This expression, when applied to the OP SA, in which the aim is to find the source contribution to OP, is mapped as follows:

$$OP_i^V = \beta_{i0} + \sum_{k=1}^{P} (\beta_{ik} \cdot g_{ik}) + \epsilon_i \tag{15}$$

where OP_V is the OP normalised by cubic metre of air, g is the time series matrix in the PMF equation, i refers to the time series index, k to the index of the sources, and P the number of sources. The fitting of the β coefficients, in units of $nmol \cdot min^{-1} \cdot \mu g^{-1}$, here quantifies how relevant the source k contributes to OP^V.

Part III

RESULTS

4

RESULTS

This section includes the three publications which conform the current thesis. Supplementary information is included in the Appendix.

4.1 INCREASE IN SECONDARY ORGANIC AEROSOL IN AN URBAN ENVIRONMENT

Paper I explores the SIA behaviour and OA SA of two one-year-long periods results in the Barcelona monitoring site. The SA of both periods comprised three similar primary sources and two secondary sources of significant period and seasonal variability. The PM_1 did not increase significantly from the first period to the second, but its composition changed significantly. Regarding OA, SOA increased from 46% to 70%, being, in turn, higher the proportion of aged aerosol with respect to the fresh. The oxidation of SOA was also found greater in the second period, probably linked to the increase of oxidising capacity of the atmosphere in the latter period. These behaviours were also assessed regarding atmospheric episodes, showing that SOA concentrations were boosted in long and medium-range advection episodes. For this publication, I performed assistedly the source apportionment analysis and wrote most of the manuscript.

4.2 ROLLING VS. SEASONAL PMF: A SYNTHETIC DATASET AND MULTI-SITE COMPARISON

Paper II aims to present a comprehensive and insightful comparison between the two state-of-the-art PMF current methodologies: the *rolling* and the *seasonal* PMF. Even though the recently developed *rolling* PMF technique has already been used for plenty OA SA on ACSM datasets, no study has assessed its added value compared to the more common *seasonal* PMF method using a practical approach yet. Its main contribution relies on the proof of the *rolling* PMF capturing actual factor fingerprints variation. For this purpose, two comparison approaches were employed. The first consisted of a synthetic dataset, which allowed for the comparison of both methodologies' results to the original sources. Secondly, these methodologies were applied to several real-world

datasets to test their application in different environments and dataset particularities. For this publication, I performed the intercomparison of the sites' SA results, the SA of the synthetic dataset, the evaluation of both comparisons and the writing of the manuscript.

4.3 TOWARDS A BETTER UNDERSTANDING OF SUBMICRONIC PM SOURCES: ONLINE AND OFFLINE DATASETS COMBINATION IN A SINGLE PMF

Paper III presents an exhaustive SA by combining three instrument measurements in order to account for the total PM_1 mass. The merging of the different types of data, of multiple time resolutions, forced the use of the multi-time resolution PMF approach. This methodology outcome was compared to those SA results from techniques using the same data with lower time resolution or using fewer species in order to confirm its higher power of source characterisation. For this publication, I performed multiple experiments combining the measurements from the many different approaches cited in the manuscript and wrote the totality of the manuscript.

Atmos. Chem. Phys., 21, 8323–8339, 2021
https://doi.org/10.5194/acp-21-8323-2021

Atmospheric Chemistry and Physics
Open Access
EGU

Increase in secondary organic aerosol in an urban environment

Marta Via[1,2], **María Cruz Minguillón**[1], **Cristina Reche**[1], **Xavier Querol**[1], **and Andrés Alastuey**[1]

[1]Institute of Environmental Assessment and Water Research (IDAEA-CSIC), Barcelona, 08034, Spain
[2]Department of Applied Physics, University of Barcelona, Barcelona, 08028, Spain

Correspondence: Marta Via (marta.via@idaea.csic.es) and María Cruz Minguillón (mariacruz.minguillon@idaea.csic.es)

Received: 9 December 2020 – Discussion started: 16 December 2020
Revised: 11 April 2021 – Accepted: 12 April 2021 – Published: 31 May 2021

Abstract. The evolution of fine aerosol (PM_1) species as well as the contribution of potential sources to the total organic aerosol (OA) at an urban background site in Barcelona, in the western Mediterranean basin (WMB) was investigated. For this purpose, a quadrupole aerosol chemical speciation monitor (Q-ACSM) was deployed to acquire real-time measurements for two 1-year periods: May 2014–May 2015 (period A) and September 2017–October 2018 (period B). Total PM_1 concentrations showed a slight decrease (from 10.1 to 9.6 $\mu g\,m^{-3}$ from A to B), although the relative contribution of inorganic and organic compounds varied significantly.

Regarding inorganic compounds, SO_4^{2-}, black carbon (BC) and NH_4^+ showed a significant decrease from period A to B (−21 %, −18 % and −9 %, respectively), whilst NO_3^- concentrations were higher in B (+8 %). Source apportionment revealed OA contained 46 % and 70 % secondary OA (SOA) in periods A and B, respectively. Two secondary oxygenated OA sources (OOA) were differentiated by their oxidation status (i.e. ageing): less oxidized (LO-OOA) and more oxidized (MO-OOA). Disregarding winter periods, when LO-OOA production was not favoured, LO-OOA transformation into MO-OOA was found to be more effective in period B. The lowest LO-OOA-to-MO-OOA ratio, excluding winter, was in September–October 2018 (0.65), implying an accumulation of aged OA after the high temperature and solar radiation conditions in the summer season. In addition to temperature, SOA (sum of OOA factors) was enhanced by exposure to NO_x-polluted ambient and other pollutants, especially to O_3 and during afternoon hours. The anthropogenic primary OA sources identified, cooking-related OA (COA), hydrocarbon-like OA (HOA), and biomass burning OA (BBOA), decreased from period A to B in both absolute concentrations and relative contribution (as a whole, 44 % and 30 %, respectively). However, their concentrations and proportion to OA grew rapidly during highly polluted episodes.

The influence of certain atmospheric episodes on OA sources was also assessed. Both SOA factors were boosted with long- and medium-range circulations, especially those coming from inland Europe and the Mediterranean (triggering mainly MO-OOA) and summer breeze-driven regional circulation (mainly LO-OOA). In contrast, POA was enhanced either during air-renewal episodes or stagnation anticyclonic events.

1 Introduction

Fine particles (PM_1, those with aerodynamic diameter $<1\,\mu m$) have a significant impact on human health (Trippetta et al., 2016; WHO, 2016; Yang et al., 2019), climate (Shrivastava et al., 2017) and visibility (Shi et al., 2014). Organic aerosol (OA) is the main constituent of fine aerosol in the atmosphere (Zhang et al., 2007), and it can be classified regarding its origin as primary OA (POA), consisting of directly emitted OA, or secondary OA (SOA), resulting from chemical transformation of pre-existing particles, nucleation or gas-to-particle condensation. Contributions to OA are still not fully understood due to the large variability of their fingerprints, response to atmospheric dynamics and transport, and evolution processes dependent on site-specific meteorological characteristics and precursor provision. Field-deployable aerosol mass spectrometers have been widely used to assess these variations (e.g. Jimenez et al., 2009) and POA source identification; such as hydrocarbon-like OA (HOA), biomass burning OA (BBOA) and cooking-related OA (COA). The fraction of organic mass measured at m/z 44 (f_{44}), typically dominated by the CO_2^+ ion and

related to oxygenation, and at m/z 43 (f_{43}), dominated by $C_2H_3O^+$, can contribute to retrieving information about ageing and oxidation state of SOA (Canagaratna et al., 2015). In Zurich, however, f_{44} during summer afternoons, when photochemical processes are intensified as indicated by the high oxidant OX ($O_3 + NO_2$) concentrations, were similar or lower than f_{44} on days with low OX, while f_{43} (less oxidized fragment) tended to increase (Canonaco et al., 2015). The SOA, also referred to as oxygenated OA (OOA), is often divided into two factors: less-oxidized oxygenated OA (LO-OOA) and more-oxidized oxygenated OA (MO-OOA).

The atmospheric dynamics of the western Mediterranean basin (WMB) have been described in Millán (2014) and Millán et al. (1997). The emissions of the densely populated, harbour-close, traffic-concurred and industrialized areas coupled to the breeze-driven regimes, complex topography and stagnation meteorological episodes prompt complex phenomena of transport and transformation. Previous studies in urban environments in the WMB have shown contributions of several sources to ambient PM_{10} for long time periods (>10 years), such as road traffic exhaust, mineral, secondary nitrate and sulfate, marine aerosol, fuel-combustion, and road dust resuspension or construction (Pandolfi et al., 2016). PM_1 composition and sources have also been studied, although with shorter time coverage (Brines et al., 2019; Pérez et al., 2008). Regarding the contribution to OA by its sources, previous studies in background environments in the WMB demonstrated the importance of OA in PM_1 (more than a 50 %) in Ripoll et al. (2015b), 1-year study at a mountain site. In summer, most OA (90 %) consisted of oxygenated organic aerosol (OOA), split between LO-OOA and MO-OOA with a LO-OOA-to-MO-OOA ratio of 0.4, contrastingly to winter (71 % of not-distinguished OOA). The marked diurnal cycles of OA components regardless of the air mass origin indicated that they were not only associated with anthropogenic and long-range-transported secondary OA but also with recently produced biogenic SOA. In Minguillón et al. (2015), at a regional background site (Montseny) during a 1-year study, OA was also the major component of submicron aerosol (53 % of PM_1), with a higher contribution in summer (58 %, an 85 % of which was OOA) than in winter (45 %, with a 60 % proportion of OOAs). The LO-OOA-to-MO-OOA ratio in summer was 0.9.

In urban environments in the WMB, information on OA sources was only available for relatively short periods of time. Previous high-time-resolution non-refractory PM_1 (NR-PM_1) chemical characterization and OA source apportionment consisted of two 1-month campaigns in February–March 2009 (DAURE campaign; Minguillón et al., 2011; Mohr et al., 2012, 2015) and August–September 2013 (Minguillón et al., 2016). The LO-OOA-to-MO-OOA ratio was 0.9 in February–March 2009 (Mohr et al., 2012) and 1.1 in August–September 2013 (Minguillón et al., 2016), revealing different SOA oxidation states. Moreover, in Minguillón et al. (2016) the combination of ^{14}C analysis and OA source apportionment demonstrated that the enhanced formation of non-fossil secondary OA during the high traffic periods could be attributed to the reaction of BVOC (biogenic volatile organic compound) precursors with NO_x emitted from road traffic.

On the other hand, some studies have pointed out an increase in the oxidative potential of the atmosphere attributed to NO_x reduction (Saiz-Lopez et al., 2017), which could have an impact on the oxidation state of SOA. Relatedly, Zhao et al. (2017) revealed the non-linear increasing relation of SOA production as a function of the NMOG-to-NO_x precursors ratio (NMOG being the non-methane organic gases emitted by vehicles, which include VOCs), entailing a coupled reduction of both pollutants has to be addressed in order to reduce SOA concentrations. As well as this, Dai et al. (2019) highlighted the differences in conditions of liquid water content (LWC), meteorological variables, and OX concentrations for the SOA to take the aqueous-phase chemistry or photochemistry pathways depending on the season. Despite that, there is a need for further investigation about the oxidation state of OA in consideration of different seasons, years, meteorological scenarios and precursor levels to characterize these findings in an urban background site in the WMB.

This study aims to provide an intra- and inter-annual analysis of OA sources along two 1-year periods and an evaluation of differences and potential trends throughout these four years. To this end, a quadrupole aerosol chemical speciation monitor (Q-ACSM) was deployed, together with complementary instrumentation, to comprehend the site-specific and cyclical nature of OA contributors. Accurate source characterization knowledge is necessary to design mitigating strategies of the effects of specific pollutants.

2 Methodology

2.1 Sampling site and period

The urban background site Palau Reial (PR; 41°23′15″ N, 02°07′05″ E; 80 m a.s.l.) is located in a residential area in the NW of Barcelona at 200 m distance from one of the busiest avenues of the city (>60 000 vehicles per working day in 2014–2018) (Ajuntament de Barcelona, 2019) (Fig. S1 in the Supplement). Some recent studies at this site focusing on PM_1 and including organic speciation identified sources such as hydrocarbon-like, cooking-related, biomass burning OA and diverse secondary aerosol sources, among others (Brines et al., 2019; Minguillón et al., 2016). The atmospheric dynamics of the area are dominated by breeze regimes, consisting of a nocturnal NW wind component, a diurnal breeze development turning from the SE to SW direction and highest wind speeds around noon (Pérez et al., 2004).

Two intensive monitoring campaigns were carried out during May 2014 to May 2015 and September 2017 to October 2018, which will hereinafter be called period A and period

B, respectively. Data availability for each measurement type is shown in Fig. S2. Henceforth, averages and data of any variable will correspond to the periods when Q-ACSM data are available.

2.2 ACSM settings, calibrations and data processing

A Q-ACSM (Aerodyne Research Inc.) was deployed at PR to measure NR-PM_1, distinguishing OA, SO_4^{2-}, NO_3^-, NH_4^+ and Cl^- with 30 min resolution. The Q-ACSM was connected to a general inlet with a 2.5 µm cut off and a flow rate of 3 L min^{-1}, conducted through a nafion dryer maintaining the incoming RH below 40 %. The instrument samples ambient air at 0.1 L min^{-1} through a critical orifice (100 µm in diameter) towards an aerodynamic lens which transmits particles between 75 and 650 nm (Liu et al., 2020). Particles are then flash-vaporized at 600 °C in high vacuum conditions and ionized by hard-electron impact (70 eV), and resulting fragments are analysed by a quadrupole mass spectrometer (Ng et al., 2011). The instrument is equipped with a filter-valve system, and hence concentrations reported are the result of subtraction of particle-free to particle-laden signal. A fragmentation table (Allan et al., 2004), the ion transmission correction and the response factor (RF), are used to convert the signal spectra into organic or inorganic species concentrations. Ionization efficiency (IE) and relative ion efficiency (RIE) calibrations were conducted using 300 nm monodispersed NH_4NO_3 and $(NH_4)_2SO_4$ particles (Ng et al., 2011). Final values for IE and RIEs for NH_4^+ and SO_4^{2-} respectively, were 2.38×10^{-11}, 5.27 and 0.71 in period A; and 5.10×10^{-11}, 5.16 and 0.77 in period B. The significant difference between IE values is a consequence of the change of the detector before starting campaign B.

The Q-ACSM was operated with 24 scans per measurement (alternating sample/filter scan) with a scan speed of 200 ms amu^{-1}, resulting in a 30 min time resolution. Data acquisition software (versions 1.4.4.5, 1.5.2.1 and 1.6.0.0 depending on the period) and analysis software (version 1.6.1.1) implemented in Igor Pro (WaveMetrics, Inc.) were provided by Aerodyne Research Inc. Data were corrected to account for flow rate changes and for response decay by using the N_2 signal. The composition-dependent collection efficiency correction (CE) (Middlebrook et al., 2012) was applied with minimum and maximum values of 0.45 and 0.68 for period A and 0.50 and 0.99 for period B, exceeding CE = 0.6 a 0.13 % and a 1.5 % of data, respectively.

2.3 Additional measurements and instrumentation

Black carbon (BC) concentrations were measured with 1 min time resolution by a multi-angle absorption photometer (MAAP, Thermofisher Model 5012). PM_1 concentrations were measured by summing up the particle size number distribution (ranging 12–470 nm) measured by a scanning mobility particle sizer (SMPS, TSI 3080) with 5 min time resolution and converted to mass concentrations by means of the composition-dependent aerosol density (DeCarlo et al., 2004). SO_4^{2-}, NO_3^- and NH_4^+ concentrations were determined in off-line PM_1 filters samples by ion chromatography and selective electrode methods. Organic carbon (OC) concentrations were determined from off-line PM_1 samples by thermal–optical methods following the EUSAAR 2 protocol (Cavalli et al., 2010). Procedures of filter sample analysis are detailed in Supplement Sect. S2.

Real time gaseous pollutants measurements, NO, NO_2 (Thermo Scientific, Model 43i), CO (Ecotech EC Model 9830), O_3 (SIR Model S5014) and SO_2 (Thermo Scientific Model 43C), operated by the Department of Environment of the Autonomous Government of Catalonia, were available at PR at a 30 min resolution. Meteorological variables were provided by the Department of Meteorology of the University of Barcelona (Fig. S1) with a 10 min time resolution. In all data analysis, time will always be in Coordinated Universal Time (UTC).

Standardized protocols of quality control (COLOSSAL, COST Action CA16109, 2019) were carried out in both periods. The sum of all NR-PM_1 species (OA + SO_4^{2-}+ NO_3^-+ NH_4^++ Cl^-) and BC was intercompared with co-located PM_1 measurements, assuming that the PM_1 contribution of the mineral and sea salt tail from the coarse PM or the trace elements are negligible. Also, species concentrations obtained by Q-ACSM were compared with the same components from off-line PM_1 determination except for Q-ACSM OA, which was compared with organic carbon (OC) (Sect. 3.1).

2.4 Source apportionment of OA

Source apportionment of the organic mass fraction was conducted by applying the positive matrix factorization (PMF) method (Paatero and Tapper, 1994) using the multilinear engine (ME-2) (Paatero, 1999). The SoFi (Source Finder) toolkit (Canonaco et al., 2015) version 6.8k, developed by the Paul Scherrer Institute and Datalystica Ltd., was used. The PMF consists of the decomposition of the OA mass spectral matrix **X**, with m variables (m/z ions, columns) and n time points (Q-ACSM timestamps, rows). OA mass spectra was decomposed into two matrices, **G** and **F**, for a pre-set number of factors p by iteratively minimizing Q:

$$\mathbf{X} = \mathbf{G} \cdot \mathbf{F} + \mathbf{E} = \sum_{i,j}^{n,m} g_{ik} \cdot f_{kj} + e_{ij}, \quad (1)$$

$$Q = \sum_{i,j}^{n,m} \left(\frac{e_{ij}}{\sigma_{ij}} \right)^2. \quad (2)$$

G is the contributions matrix with n time steps for p factors and **F** is the profile matrix of p factors with m m/z ions. The residual matrix **E** contains the unexplained fraction of **X**. In order to avoid local minima of the Q function, rotational

tools are used to cover the whole $m \times n$ space. ME-2 provides control over the rotational ambiguity (Paatero and Hopke, 2003). A priori information can be introduced for some of the factors using the so-called a-value approach (Paatero and Hopke, 2009; Brown et al., 2012). The a values range from 0 to 1 and determine how much deviation from the anchor profile the model allows, with a value of zero meaning it is fully constrained.

The mass spectra used ranged from 12 to 120 Th and excluded higher m/z ions which accounted for a minor fraction of total signal (<3 % on average), presented low S/N ratio or were affected by the interference with the naphthalene signal. Each dataset was separated in four subperiods for source apportionment purposes to better capture the variation in secondary OA composition (reflected on the oxidation state), and the sources only present part of the natural year. The subperiods used were April–May, June–August, September–October and November–March. The selection of these subperiods, different from standard 3-month seasons, was carried out based on (i) variation of meteorological conditions (Fig. S9); (ii) variation of source-specific markers f_{60} and f_{73}, which are tracers for BBOA contribution; and (iii) variation of the relation between f_{43} and f_{60}, using monthly scatter plots, which may indicate the presence or absence of BBOA. The three criteria were met for a solution including a potential BBOA for the November–March period. The subperiods will be hereinafter referred to as seasons.

The general steps followed to reach the presented OA source apportionment solution were those described by Crippa et al. (2014) and COLOSSAL guidelines (2021). Unconstrained PMF was performed with 3 to 8 factors. These runs were used to identify the present sources: COA, HOA, BBOA, LO-OOA and MO-OOA. Subsequently, constraints were applied to the primary sources. PMF was run with 3 to 5 or 3 to 6 factors depending on the season. Differences between solutions of different number of factors for each season are shown in Table S1 and Fig. S4. The solutions space was explored for HOA, COA and BBOA anchor profiles from Mohr et al. (2012), Crippa et al. (2013) and Ng et al. (2010) whilst OOA factors were allowed to be resolved freely. The criteria to choose the anchor profiles consisted of comparing correlations with external tracers or source markers: BC and NO_x for HOA, m/z 55 for COA, m/z 60 and m/z 73 for BBOA, SO_4^{2-} for MO-OOA, and NO_3^- for LO-OOA (Table S2). This led to the selection of the COA and HOA anchor profiles from Crippa et al. (2013) and the BBOA anchor from Ng et al. (2010). All combinations of a values within a range of 0 to 0.5, with steps of 0.1, were explored for each set of runs with the same number of factors, in order to select the most environmentally reasonable solutions. Optimization of the number of factors and a-value combinations implied considering (i) variation of the ratio between Q and Q_{exp} ($Q_{exp} = m \cdot n - p \cdot (m+n)$), which should present a steady descent from p to $p+1$, $p+2$ factors, being p the chosen number of factors; (ii) correlation of time series contributions of OA factors with tracers; (iii) scaled residuals of profiles and time series; (iv) agreement between apportioned and measured OA concentrations; and (v) gathered knowledge of site-specific atmosphere and potential sources. In Table S1 the chosen solutions for each season are shown in contrast to solutions with one less and one more factor, all of them with the optimal a-value combination according to correlation with external tracers. In almost all cases, it can be seen how the selected runs are the best compromise between the correlation with externals and the reliability of OA apportioned with respect to the OA measured. Also, the Q/Q_{exp} decrease was less steep from the selected run to the following compared to the previous to the selected one. Nevertheless, in some cases, such as April–May 2018 or November–March 2014–2015, these figures were better for $n-1$ (or $n+1$) factor solutions, being n the number of factors chosen, but this extra (or lacking) factor allowed OOA differentiation (or differentiation incapacity), which provides a more accurate solution even to the detriment of the aforementioned parameters. Moreover, in Fig. S3, in most of the cases, the solutions for n factors showed the most reasonable compromise for scaled residuals along the time series and profiles in mainly all cases.

2.5 Classification of atmospheric episodes or scenarios

Classification of atmospheric episodes was performed with the HYSPLIT model (Stein et al., 2015). Air mass backtrajectories for 120 h at three heights (750, 1500 and 2500 m a.s.l.) were computed, with vertical flux modelling, for each day of measurements and interpreted to be classified regarding their predominant transport provenance into Atlantic north (AN), winter anticyclonic (WA) (from October to March), Europe (EU), Mediterranean (MED), North African (NAF) and summer regional (SREG, from April to September), characteristics of which are discussed in previous works (Pey et al., 2010; Ripoll et al., 2014, 2015). In Fig. S4 the relative contribution of each scenario per month is shown. The main difference between period A and B is in summer months; in period B, the main episode is SREG (always >60 % of the days) whilst in A its proportion is reduced and more AN and AW episodes take place.

3 Results

3.1 Comparison of Q-ACSM data with co-located measurements

Comparison of Q-ACSM NR-PM_1 and MAAP BC with co-located PM_1 measurements can be found in Table S3 and Fig. S5a. The intercomparison correlation coefficients are $R^2 = 0.61$ and $R^2 = 0.72$ and slopes of the orthogonal distance fit 1.001 ± 0.006 and 1.177 ± 0.006 for periods A and B, respectively. The slopes are near one, especially in period A. Nevertheless, SMPS underestimation of PM_1 could

be partially attributed to differences in the particle size range measured, shifted to lower diameters for the SMPS (20–478.3 nm). Moreover, overestimation of primary OA sources by Q-ACSM by a factor of 1.2 to 1.5 has also been reported (Reyes-Villegas et al., 2018; Xu et al., 2018) as a consequence of source-unspecific OA RIE application, leading in turn to PM_1 overestimation by Q-ACSM.

The correlation coefficient for NR-PM_1 species off-line analysis of SO_4^{2-}, NO_3^- and NH_4^+ is always above $R^2 > 0.71$, and also between OA and organic carbon (OC) ($R^2 = 0.73$ in A and $R^2 = 0.86$ in B) (Table S3, Fig. S5b). Slopes of the linear regression between Q-ACSM and off-line SO_4^{2-}, NO_3^- and NH_4^+ are respectively 1.24, 1.90 and 1.73 for period A and 1.05, 1.76 and 1.68 for period B. The slopes of NO_3^- are largely above 1, likely owing to volatilization artefacts in filters. The reason for the high slope for NH_4^+ is not clear, so neither determination problems in any of the filter species nor Q-ACSM overestimation can be completely discarded. The anion Cl^- is not considered due to the very low concentrations and potential determination problems (Tobler et al., 2020).

The OA-to-OC ratio is estimated from the slope in the scatterplot between these two variables, resulting in values of 2.69 and 2.94 in periods A and B, respectively, 68 % and 84 % higher than the 1.6 value calculated with an AMS in Barcelona in the DAURE campaign (Minguillón et al., 2011; Mohr et al., 2015). The OM-to-OC ratio might have increased over the years since March 2009, which would be in accordance with an increasing SOA proportion found in these campaigns (2014–2015 and 2017–2018) with respect to DAURE. Nevertheless, the values found in the present study are too high, as the expected values of most oxidized OOA according to both chamber and ambient experiments should be around 2.3 (Canagaratna et al., 2015). These overly high OA-to-OC ratios would point to filter artefacts caused by evaporation of semi-volatile OC compounds as well as to the previous findings at Montsec (Ripoll et al., 2015) and Montseny (Minguillón et al., 2015), the aforementioned unspecific-source OA RIE overestimation for Q-ACSM. Even so, a steady increase in OOA oxidization over the years could be inferred due to the growth of this ratio from 2014–2015 to 2017–2018.

3.2 Submicron aerosol composition

Time series of co-located gases (Fig. S6) show rises of SO_2 in summer months likely related to a shipping activity increase, O_3 increases during summer linked to higher photochemical enhancement and an increase in CO during cold periods, associated with shallower boundary layers. NO and NO_2 show similar behaviours of reduction towards warm months and sudden increases in cold periods.

There are evident differences in meteorological variables from one period to the other (Fig. S7). In summer A, temperature (24.4 °C) and solar radiation (259 W) are lower, average relative humidity (71 %) is higher, and wind speed (2.0 m s^{-1}) is similar compared to period B (27.0 °C, 280 W, 70.0 %, 1.7 m s^{-1}, respectively), indicating a probably rainier or cloudier summer in period A.

A data overview for periods A and B is shown in Table S4 and NR-PM_1 species and BC time series in Figure S8. Average PM_1 concentrations (± standard deviation) resulting from the sum of NR-PM_1 components and BC were $10.1 \pm 6.7\,\mu g\,m^{-3}$ during campaign A and $9.6 \pm 6.6\,\mu g\,m^{-3}$ during campaign B (variation of a 5 % from A to B). A drop of −5 %, −21 %, −9 % and −18 % is shown for of OA, SO_4^{2-}, NH_4^+ and BC, respectively, although NO_3^- and Cl^- had a positive variation of +8 % and a +20 % from period A to B. Previous data for PM_1 (2012–2018) showed a decreasing trend according to the Mann–Kendall test (Fig. S9), and a reduction over a longer period (2005–2017) was also determined for OC and EC. These long-term reductions could imply that PM_1 and the OC- and EC-related pollutants (OA and BC) decreases found in this study reflect the tendency of the last few years.

In both periods, OA was the largest contributor to PM_1, accounting for (average ± standard deviation) 43 % ± 10 % and 44 % ± 17 % of the total average mass (Q-ACSM NR-PM_1 species + BC), followed by SO_4^{2-} (19 % ± 11 % and 18 % ± 10 %), BC (17 % ± 9 % and 13 % ± 10 %), NO_3^- (10 % ± 8 % and 13 % ± 10 %), NH_4^+ (11 % ± 8 % and 11 % ± 6 %) and Cl^- (0.4 % ± 0.8 % and 0.8 % ± 0.9 %), respectively, for periods A and B.

Seasonal variation

Seasonally averaged concentrations and time series of PM_1 and its components are displayed in Fig. 1 and Fig. S8. In period A, the highest concentrations of bulk PM_1 occurred in September–October ($12.0\,\mu g\,m^{-3}$) and the lowest were registered in summer ($7.8\,\mu g\,m^{-3}$). Contrastingly, in period B, submicron aerosol was at its maximum in summer ($10.4\,\mu g\,m^{-3}$) and minimum in winter ($8.9\,\mu g\,m^{-3}$). The differences in occurrence frequency of atmospheric episodes and data availability might be a direct cause of these mismatches of seasonal trends. The frequency of occurrence of episodes per month differs significantly from period A to period B (Fig. S4); e.g. in June, July and August the ratio of occurrence of SREG / AN is lower in period A than in period B (45 % and 77 % on average, respectively). This is coherent with lower PM_1 concentrations recorded in July of A with respect to July of B.

OA seasonal trend behaves similarly to bulk NR-PM_1 due to the same causes and photochemical enhancement in warm months due to higher sun irradiation. SO_4^{2-} concentrations are in both cases higher during warmer months, opposite to the NO_3^- concentrations trend (except for September–October 2014) as has been widely reported in previous studies (Minguillón et al., 2015; Pey et al., 2009; Ripoll et al., 2015). In period A, higher NH_4^+ concentrations happen dur-

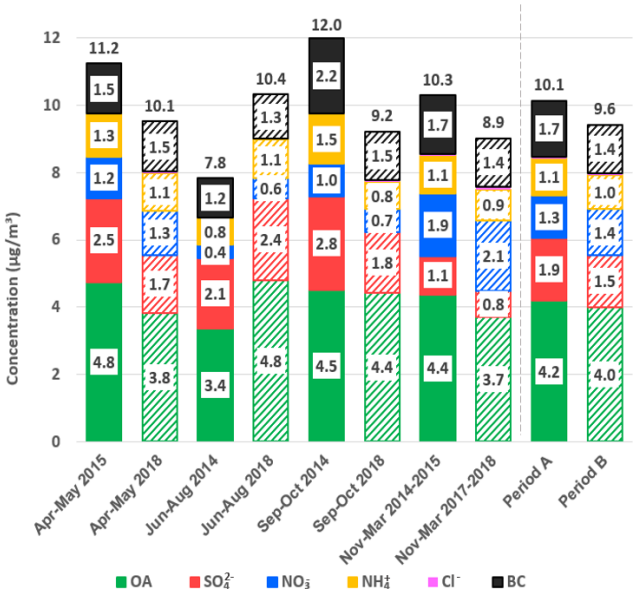

Figure 1. Seasonal bar plot of Q-ACSM species and BC mean concentrations for periods A (with solid bars) and B (with weft bars).

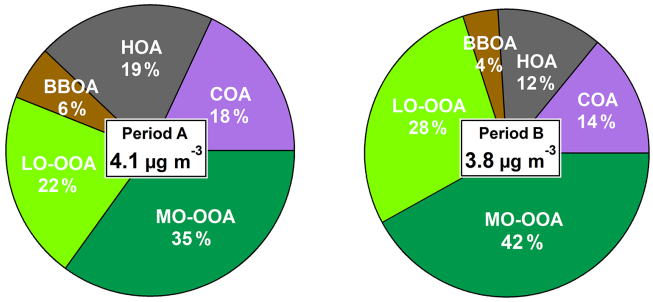

Figure 2. Average OA source apportionment for periods A and B and concentrations of apportioned OA for period A and period B.

ing winter months whilst they are seasonally stable through period B. BC shows the lowest concentrations in summer months in both periods (1.2 and 1.3 µg m^{-3}, respectively) more pronouncedly in period A.

3.3 OA source apportionment

COA accounts for 18 % and 14 % (period A and B, respectively) of OA (Fig. 2). COA profiles (Fig. 3) reflect the expected pattern of signals related to the oxygenation of fatty acids due to cooking activities (m/z 29, 55, 41, 69) (He et al., 2010). Correlation between COA and HOA is not negligible, as profiles show a Pearson coefficient of $R^2 \geq 0.71$ (Table S2). However, the time series of these factors varies independently (R^2>0.20 except for September–October 2014), which allows for some confidence in their separation. The time series of COA does not show a significant seasonal trend (Figs. S12, 4). Correlation with m/z 55, the main COA marker, is 0.58 and 0.71 in A and B, respectively. Diel cycles present peaks at around 13:00 and 20:00 UTC, coinciding with local lunch and dinner hours and another at 09:00 UTC probably entangled with the traffic peak at same hour (Fig. 5, Fig. S13). Figure 5 also reveals a much higher dinner peak than the lunch peak along almost all seasons, probably related to a much thinner planetary boundary layer (PBL) at 21:00 than at 13:00 UTC.

HOA consists mainly of ions stemming from diesel exhaust from recondensed engine lubricating oil compounds (Canagaratna et al., 2010; Chirico et al., 2010). The average contributions in periods A and B are, respectively, 19 % and 12 % (Fig. 2). HOA concentrations follow a decreasing seasonal pattern towards the summer months (Figs. 4, S12) which could be associated with lower traffic intensity in August, the thicker boundary layer, the maximum recirculation induced by the highest speeds of sea-breeze and a likely faster oxidation of the primary HOA due to higher temperatures. Diel patterns (Figs. 5, S13) reproduce two traffic-associated peaks at 07:00 and 19:00 UTC in both periods, reduced during summer months, resembling traffic cycles (Fig. S14). Correlations with BC are $R^2 = 0.63$ and 0.68 and with NO_x are $R^2 = 0.44$ and 0.65 in periods A and B, respectively, and remarkably weaker in summer periods ($R^2_{min} = 0.29$ and 0.51, respectively, for BC) in accordance with a decrease in the HOA-to-BC ratio (ratio retrieved from Figs. 1 and 4).

BBOA mass spectra are alike in both cold periods (Fig. 3) characterized by ions at m/z 29, 43, 60 and 73, the latter two corresponding to fragments of anhydrosugars, such as levoglucosan, products of cellulose pyrolysis combustion reactions (Alfarra et al., 2007). BBOA is only arising in the coldest period, from November to March (Fig. S12), and accounting for 14 % and 11 % of total OA in A and B, respectively. Diel cycles present the same trend in both periods (Figs. 5, S13), staying flat throughout the day and ascending from 18:00 to 00:00 UTC, pointing to a relation to nocturnal domestic heating or breeze-driven transported pollutants from forest or agricultural fires (Reche et al., 2012) enhanced by a narrower boundary layer. Correlations with ions m/z 60 and m/z 73 are better in period B ($R^2 = 0.91$ and 0.61, respectively) than in period A ($R^2 = 0.60$ and 0.55, respectively) (Table S2).

Secondary organic aerosol (SOA) factors are resolved freely by the model unlike the constrained POA factors. They are known to be determined mostly by m/z 43 and m/z 44, which indicate the degree of oxidation (Canagaratna et al., 2015). The fractions of m/z 44 and m/z 43 over apportioned OA (f_{44}, f_{43}) scattered per seasons are shown in Fig. S15. In cold months dots are less concentrated and they withdraw from the expected triangle proposed by Ng et al. (2010) due to a worse definition of SOA factors, and also some might be untrustworthy because they are close to the OA detection limit. Atmosphere is inferred to be more oxidized in period B, especially in summer months as clouds of points present

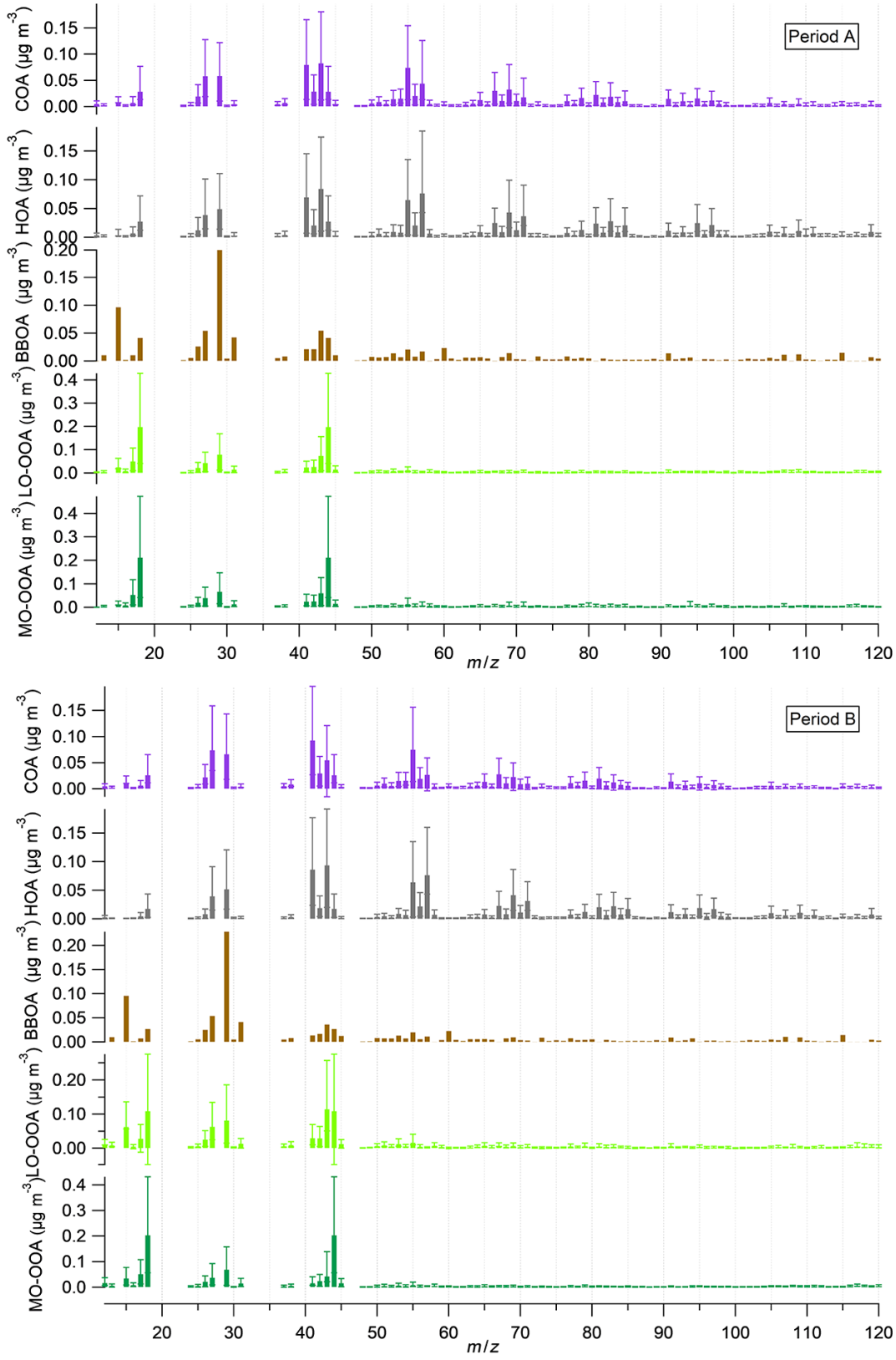

Figure 3. Mass spectra of the five OA factors for periods A and B. Stick lines are averaged values over all seasons for a given period. Error bars represent maximum and minimum values of all seasons. Thus, BBOA is lacking error bars as it is only present in one season.

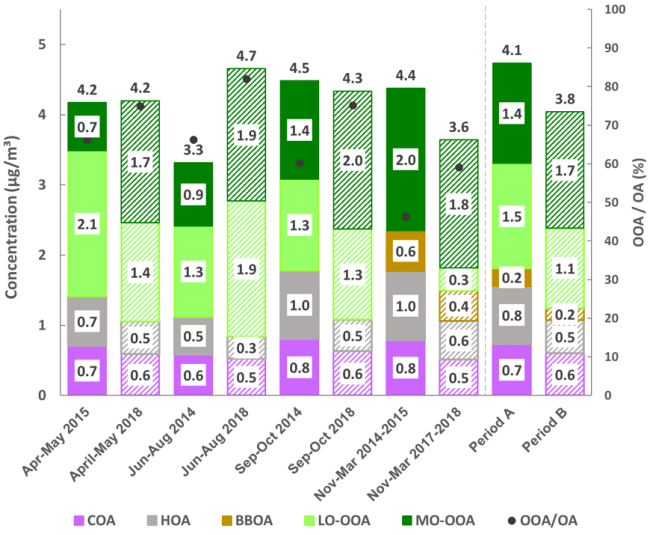

Figure 4. Seasonal OA source apportionment for period A and B (with solid and weft stacked bars, respectively) and OA concentrations at the top. Markers show the oxygenated organic aerosol proportion with respect to total OA.

lower f_{43} and higher f_{44} than in A. This is reflected in the OOA factors discussed below.

LO-OOA mass spectra differ significantly from period A to B. The m/z 43-to-m/z 44 ratio is 0.37 in period A and 1.05 in period B (Fig. 3), indicating a higher oxidation degree in period A. Contribution of LO-OOA to apportioned OA increased from period A to B although the period average is not directly comparable, as period A lacks this factor in the cold period, and hence it is considered as zero and leads to lower LO-OOA concentrations (Fig. 2). Considering only the three seasons excluding the November–March period, LO-OOA shows a slight decrease from period A to B ($1.6\,\mu g\,m^{-3}$ to $1.5\,\mu g\,m^{-3}$). Seasonally, in all cases except for the already discussed summer 2014, the amount of this source decreased from period A to B (Fig. 4). In both cases, LO-OOA concentrations rise towards warmer months, which suggests SOA formation pathways might be linked to photochemical oxidation and breeze regimes. This can also be inferred by the diel patterns of LO-OOA (Fig. 5), which are flat except for a valley of around a factor of $-30\,\%$ from 13:00 to 20:00 UTC, when temperature and irradiation reach their maximums, but also related to PBL widening and maximum sea breeze speeds at the time. The rise in LO-OOA at night could also be explained by nighttime SOA formation via NO_3 radical (as a result of anthropogenic NO_x reactions) oxidation of VOC, but especially due to the land breeze prevailing during the night and transporting previously formed OA from inland areas to the coast. The valleys around 15:00 UTC of seasonal diel cycles are more profound in April–May and June–August, and the peak-to-valley ratio is also higher in period B (Fig. S13).

MO-OOA mass spectra are similar for periods A and B, even including the OOA profile from the cold subperiod in A. Excluding the November–March subperiod, MO-OOA shows an increase of 90 % (from 1.0 to $1.9\,\mu g\,m^{-3}$ in A and B, respectively). The m/z 43-to-m/z 44 ratios are of 0.28 and 0.21, respectively, and hence, MO-OOA was less oxidized in period A (Fig. 3). MO-OOA apportions a 35 % and a 42 % of OA in periods A and B, respectively, and this difference should indeed be widened, as MO-OOA in subperiod November–March 2014–2015 is clearly overestimated (as all OOA is accounted for as MO-OOA). Figure 4 supports the increase in magnitude from A to B in all seasons and highest seasonal concentrations in November–March 2014–2015 (due to a single OOA factor) followed by September–October 2014, September–October and June–August 2018. Therefore, the origin of MO-OOA might be explainable from the photochemical transformation from LO-OOA oxidation, triggered amongst other causes by photochemical activity. Diel cycles show a slight increase in the middle hours of the day (Figs. 5, S13) and less pronounced seasonality in period B rather than in A.

Concentrations of the secondary factors as a function of temperature and NO_x and CO concentrations for winter (DJF) and summer (JJA) are shown in Fig. S16. A tendency for higher concentrations of SOA towards higher temperatures and NO_x concentrations in winter and summer can be observed. Temperature has been reported to enhance SOA photochemical pathways from VOC; these graphs indicate, as pointed out in Minguillón et al. (2016), that these reactions are also favoured over a certain NO_x concentration threshold. However, concentrations of SOA are simultaneously high with high temperature and CO levels, inferring SOA might be enhanced not only by a highly NO_x-polluted ambient, but by the ensemble of pollutants during severely contaminated episodes.

O_3 has been reported to be an atmospheric oxidant inducing SOA production, but unexpectedly, period-averaged concentrations are substantially higher in period A than in B (Tables S4). Still, Fig. S17 points out that O_3 is more reactive in period B, as the area of the difference between PR concentrations and those in the regional background site MSY (Montseny Natural Park, 720 m a.s.l., 40 km north-northeast of Barcelona and 25 km from the Mediterranean coast) is higher during period B. This corresponds to the previously reported observation that O_3 diel concentrations are flatter in MSY because mountain sites are less affected by NO titration, leading to high daily O_3 average concentrations (Massagué et al., 2019). Therefore, the higher the difference is between MSY and PR, the more O_3 has been reacting at PR. Enhanced reactivity of O_3 in period B could be attributed to the reaction with higher VOC concentrations resulting in the production of SOA. Also, by contrasting O_3 and LO-OOA diel cycles, in afternoon hours the LO-OOA increase coincides with the O_3 minimum, highlighting the O_3 capture to enhance fresh SOA.

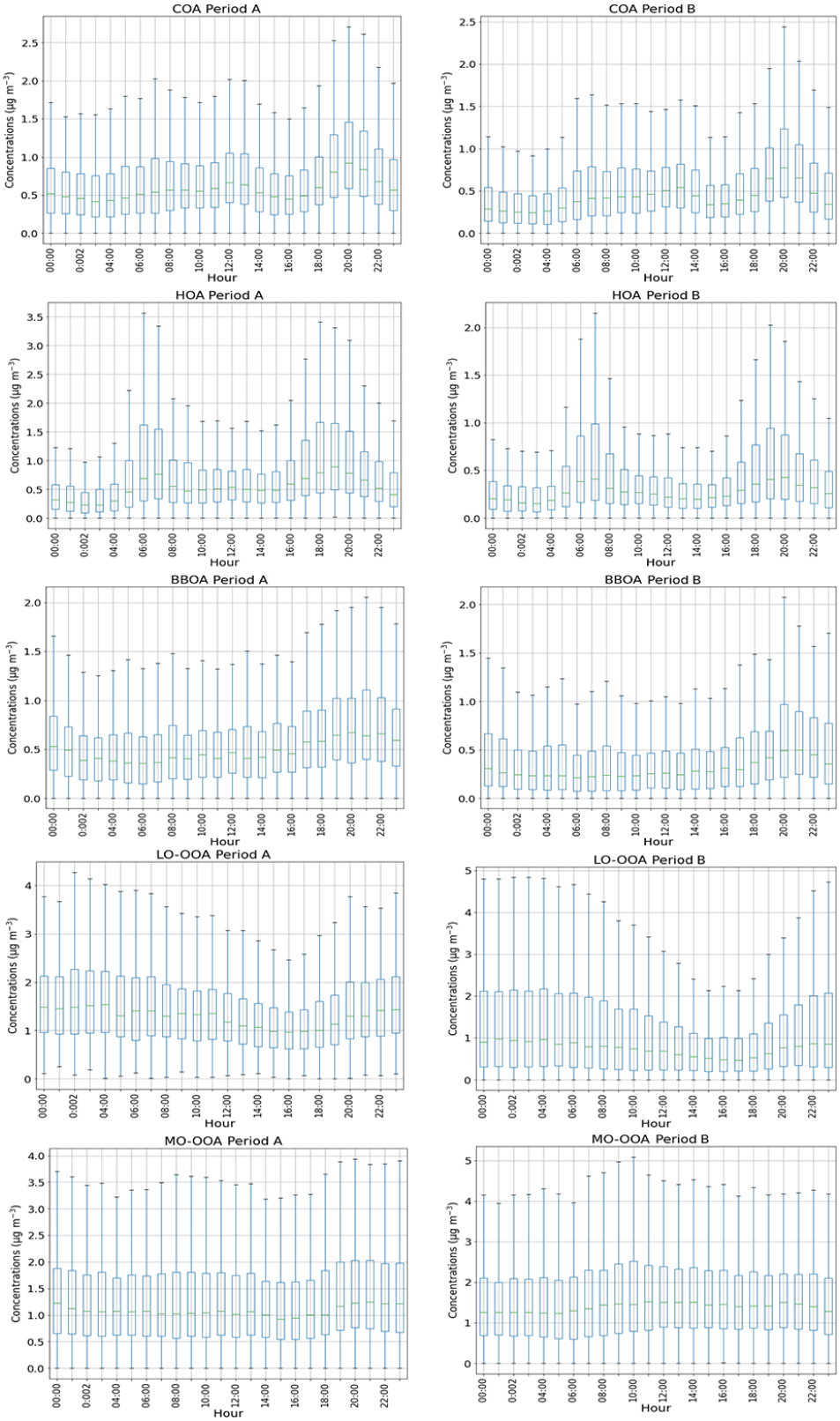

Figure 5. Diel patterns of OA factors concentrations. Boxplots represent median and interquartile range, and whiskers show maximum and minimum values. Factors are in the order COA, HOA, BBOA, LO-OOA and MO-OOA; the left column corresponds to period A and the right one to B.

The main contributors to high-pollution episodes can be targeted by monitoring the proportion of each factor to the total OA concentration as in Fig. 6 (Zhang et al., 2019). In period A, concentrations of POA decrease and then increase along with OA concentrations. However, in period B, with reduced POA concentrations with respect to A, SOA represents the main pollutant even during OA growth, and more concretely, LO-OOA increases at the expense of MO-OOA. This points out that whilst POA was more responsible for high-pollution episodes in A, this tendency was inverted over period B, as SOA is reasonably constant in B through OA growth except for the largest OA class. The highest episodes of OA in B are dominated by LO-OOA, taking the lead with respect to MO-OOA as its temperature-driven generation pathway is faster than the ageing to a more oxidized form. Thus, the sudden increase in primary pollutants might provoke a fast enhancement of LO-OOA, whilst MO-OOA response is slower to react to these stimuli.

3.4 Spatial origin of OA

Figure 7 shows wind rose plots and wind-direction-dependent concentrations of OA factors. The greatest frequencies (up to 15 %) of winds were associated with SW wind directions, and the highest wind speeds were related to NE directions (Fig. 7a). Frequencies of types of episodes by months are shown in Fig. S4, and absolute concentrations and NR-PM_1 relative concentrations by episodes are shown in Fig. S18.

The highest concentrations of COA are under northern and eastern winds under 4 and 8 $m\,s^{-1}$, respectively, indicative of advection from residential areas on the north and east of the site (Fig. 7b). HOA is the most local factor, presenting its highest values with stagnation regardless of the direction despite the proximity to one of the busiest roads of Barcelona. Hence, HOA concentrations are driven by the general variation of the urban background and not by the direct emissions from this specific road. BBOA levels are high for low wind speeds ($<6\,m\,s^{-1}$) mainly coming from W and NE directions, i.e. from residential areas nearby the site. Regional production seems to be the main cause of LO-OOA as well as northern and northwestern advection, which transport recirculating polluted air masses from the outlying industrialized areas which are canalized through the Llobregat river basin (Toll and Baldasano, 2000). MO-OOA long-range transport is deduced from the plots, since the highest concentrations are driven by stronger wind speeds from the northeast in period A and northwest, southwest and east in period B. Note that the main directions for both LO-OOA and MO-OOA in period B coincide, while the origin for LO-OOA and MO-OOA in period A seems to differ. This could be due to additional or missing source foci or changes in their advective pathways.

Regarding air masses, the proportion of OA of each source per episode is shown in Fig. 8. The maximum proportion of SOA occurs under SREG episodes, coinciding with high temperatures, and is coherent with the enhanced oxidation over time during these air mass recirculation episodes. High proportions of SOA are also recorded for the EU and MED in period B, but for the rest of episodes there is not a clear variation in terms of SOA contribution. Regarding absolute concentrations, the pattern is different for periods A and B (Fig. S18a). The highest concentrations are reached during WA episodes in period A, linked to stagnation conditions, and lowest during SREG, due to a major occurrence in an aforementioned anomalously cold, wet summer (Meteocat, 2020a, b). For period B, the highest concentrations correspond to MED and EU episodes, while the lowest were recorded during AN, associated with northern strong winds. The highest proportion of LO-OOA occurs for AW and SREG episodes, the first carrying pollutants which have crossed the whole Iberian Peninsula and the latter recirculating them along the breeze regime. MO-OOA is dominant in the highly polluted MED episodes, western advection and EU episodes, which provide long-range-driven pollutants from continental Europe. The trajectory analysis was also performed on NR-PM_1 species and BC, but no significant features were found regarding episodes (Fig. S18b).

4 Discussion

While bulk PM_1 decreased slightly from period A to B, with consistent decreases in all its main constituents except for NO_3^-, the average OA concentrations remain similar in both periods (4.2, 4.0 $\mu g\,m^{-3}$). All the same, the relative contribution of the different OA sources varies significantly. On the one hand a severe reduction of POA is found from period A to B (−27 %), mainly driven by a significant decrement of HOA (−37 %) (Fig. 2). The HOA drop is consistent with the simultaneous reduction in BC and NO_x concentrations of −18 % and −4 % pointing to an effect of the traffic-restriction policies implemented, including circulation prohibition of the most polluting vehicles during pollution episodes (enforced from December 2017) and the implementation of Euro 5 regulations. Whilst Euro 5 implies a reduction in PM emissions from diesel vehicles, the NO_x emissions remain similar to previous Euro standards. This is in accordance with the larger variation of BC compared to that of NO_x. The difference with the even larger variation in HOA could be explained by a higher oxidation potential in the atmosphere, transforming more HOA into OOA in period B. Diel patterns (Figs. 5, S13) reproduce two traffic-associated peaks at 07:00 and 20:00 UTC in both periods, reduced during summer months, resembling traffic cycles (Fig. S14). The difference in the peak time from 07:00 to 08:00 UTC for different seasons shows that the local traffic intensity is the parameter mostly driving the HOA diel variation, as both peaks correspond to 08:00 local time (due to daylight saving time), while variation in the PBL height, which both start at roughly

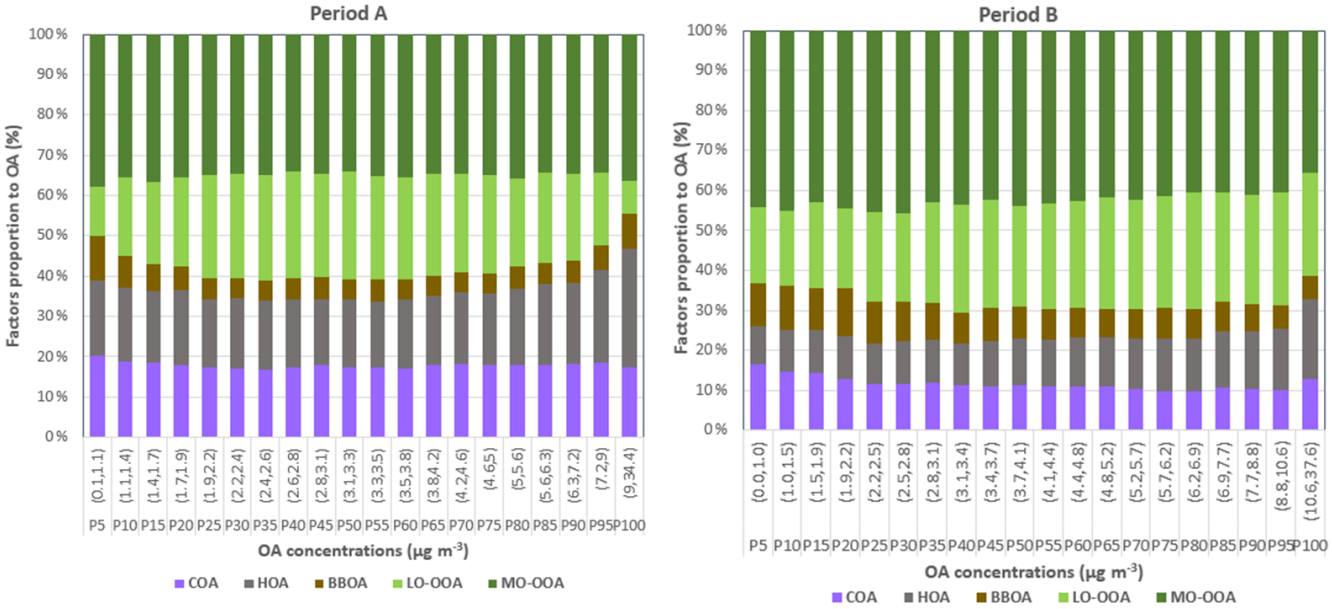

Figure 6. Relative contribution of organic sources as a function of OA concentrations. Ranges in brackets on the x axis represent the range of OA concentrations for which the relative contribution is shown in each of the bins. The OA concentration bins are determined corresponding to intervals of 5 points in the percentiles, starting with P0–P5, and increasing as shown by the percentile Px specified below the range.

that time, would result in a less evident effect on HOA concentrations. BBOA only emerged during the coldest months (November–March) as its markers inferred, and it showed no significant variation from A to B. COA, HOA and BBOA are shown to be generated locally or short-range advected from residential areas, and their relative contribution to total OA is enhanced under stagnation WA episodes (i.e., when those emissions remain in the atmosphere and no advection carries them away) but also under AN strong wind events, when despite the lower absolute concentrations (Fig. S18b), the relative contribution of primary sources increases as air is renovated and only directly emitted pollutants arise (formation of OOA is a slower pathway). Also, the removal of SOA precursors due to strong winds could be an additional cause for the SOA proportion decrease in these scenarios.

On the other hand, SOA concentrations increased from A to B in both absolute and relative terms, representing 45 % and 60 % of total OA in periods A and B, respectively. The predominance of SOA over total OA in period B also remains over 50 % for the highly polluted episodes, even with an increase in the relative POA contribution. SOA is more aged in period B, as shown by the increase in MO-OOA to the detriment of LO-OOA, becoming the first the main OA constituent in B. The local production of LO-OOA or local oxidation of existing OOA seen in Fig. 7 would be supported by the increase in MO-OOA concentrations during daylight for all the seasons (Fig. S13), and the less marked MO-OOA local focus in A (Fig. 7b) may also evidence the lower intensity of SOA oxidation happening in A compared to B. The ratio of LO-OOA to MO-OOA decreases slightly from A to B (mean averages of 1.1 and 1.0; Table S4), with lower values in autumn than summer for both A and B periods. The seasonality of the LO-OOA-to-MO-OOA ratio could be partly explained by an accumulation of MO-OOA after summer months, as higher temperatures trigger the ageing of SOA, supported by the increase in background f_{44} (and conversely reduction of f_{43}) from A to B in summer months compared to other seasons. The sensitivity to meteorological effects on the direct comparison between both summers can be avoided by comparing the LO-OOA-to-MO-OOA ratio between ordinary June and September months (avoiding anomalous and data-lacking July and August) between periods A and B. The degree of oxidation of SOA was also higher in period B (1.6 and 1.2 in June and 0.9 and 0.8 in September). The outcome of OA source apportionment in previous studies in PR compared to this one (Fig. S19) shows LO-OOA-to-MO-OOA ratios of (i) 1.15 in August–September in Minguillón et al. (2016) in contrast to 1.1 and 0.7 in the August–September in period A and B, respectively, and (ii) 0.9 in February–March in Mohr et al. (2015) in contrast to the 0.2 of the February–March mean in period B. Even though the increasing oxidation of SOA can be observed by comparison to previous works, this plot does not show a direct relation with O_3 concentrations. A note of caution is due here since both previous campaigns lasted less than a month, and therefore direct comparison of their results might be sensitive to meteorology or to unrepresentative events.

The enhanced SOA oxidation from A to B could be a result of the increment of the oxidation potential of the atmosphere, as reported in urban areas (Saiz-Lopez et al., 2017).

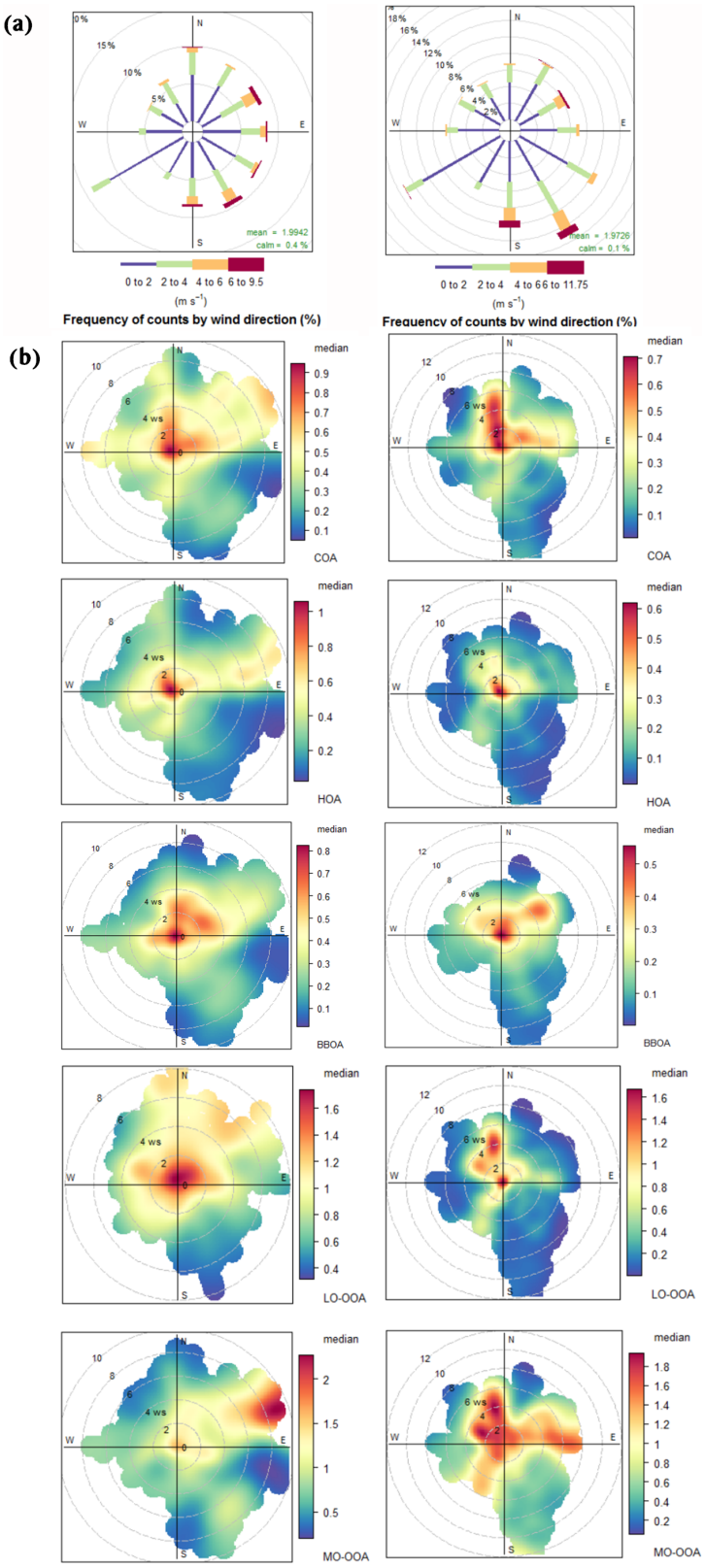

Figure 7. Wind dependence of OA factors. **(a)** Wind rose plots showing frequency of counts (in percentage) regarding wind direction and wind speed ($m\,s^{-1}$). **(b)** Polar plots colour-coded by median mass concentrations ($\mu g\,m^{-3}$) of OA factors listed below. In both cases, plots are arranged to the left for period A and to the right for period B.

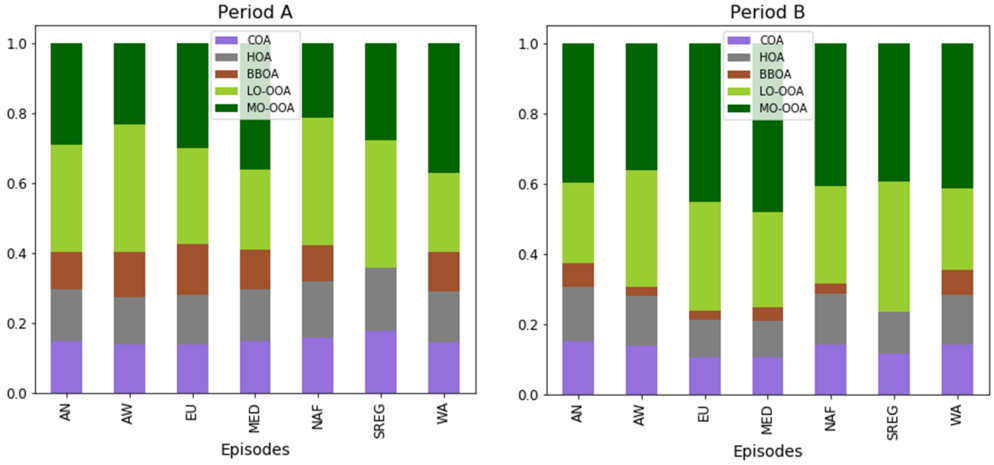

Figure 8. Bar chart of factor proportion to total concentrations per factor grouped by episodes for periods A and B.

Nevertheless, the O_3 trend, which could cause faster oxidation of SOA, is not evidently increasing, in contrast to that study's results. Even so, the non-increasing concentration of O_3 together with the increase in reactivity of O_3 in PR, as determined by the variations of urban and regional locations (Fig. S17), could indicate that the concentrations in B are indeed lower owing to the higher reactivity of this pollutant. It could be argued that these results would support the hypothesis of the increase in the atmosphere oxidative potential in urban areas, but the analysis of these two 1-year periods should not be extrapolated to other years. To develop a full picture of SOA evolution, additional year-long studies should be performed in PR with co-located precursor measurements such as VOC to properly assess the hypothesized oxidation of the atmosphere.

Regarding air mass transport, medium and long-range transport episodes (EU and MED) and SREG episodes show the highest proportions of SOA. The maximum LO-OOA-to-MO-OOA ratio corresponds to SREG episodes, pointing to local LO-OOA formation as the summer breeze recirculation might enhance fresh SOA. On the contrary, the lowest LO-OOA-to-MO-OOA ratio is recorded during EU and MED episodes, which advect air masses which have been travelling throughout the continent and therefore are more aged as a result of progressive oxidation of the LO-OOA along their trajectory.

5 Conclusions

Characterization of non-refractory fine aerosol (NR-PM_1) in the urban background of Barcelona including organic aerosol (OA) source apportionment was performed regarding two nearly 1-year periods between 2014 and 2018. Period-averaged PM_1 concentrations were 10.1 and 9.6 $\mu g\,m^{-3}$ respectively for the so-called periods A (May 2014–May 2015) and B (September 2017–October 2018). Slopes between total mass concentration of Q-ACSM species and BC and PM_1 retrieved by a scanning mobility particle sizer were near 1, but Q-ACSM overestimation caused by the use of the default relative ionization efficiency for OA, probably lower than the actual one, cannot be discarded.

Average contributions of the inorganic NR-PM_1 were 19 % and 18 % for SO_4^{2-}, 16 % and 13 % for black carbon (BC), 10 % and 13 % for NO_3^-, 11 % and 11 % for NH_4^+, and <1 % for Cl^- for periods A and B, respectively. Hence, SO_4^{2-} and BC concentrations decreased from A to B, while NO_3^- increased. Seasonal NR-PM_1 cycles consist of the maximization of OA and SO_4^{2-} in the warmer subperiods and NO_3^- (high volatility in hot conditions) and BC in the coldest. NO_x were also reduced on average from A to B, as well as O_3 and SO_2. Nevertheless, O_3 became more reactive in period B.

The OA was the major component in both periods under study, accounting for 42 % of total PM_1 in both periods. Five organic sources were identified by PMF: cooking-related OA (COA), hydrocarbon-like OA (HOA), biomass burning OA (BBOA), less-oxidized oxygenated OA (LO-OOA) and more-oxidized oxygenated OA (MO-OOA). BBOA was only present in the subperiod November–March and only one OOA (oxidized OA) factor was apportioned in this cold subperiod in 2014–2015. Secondary OA (SOA, comprised of the sum of OOAs) proportion and absolute concentrations increased from the first period to the second, while primary OA (POA) concentrations were reduced. In turn, LO-OOA and MO-OOA changed its relevance in OOA contributions, the most oxidized being the one promoted from 2014–2015 towards 2017–2018 and also from past studies in PR to the present one. The oxidation could be partially attributed to the action of solar radiation and temperature, in warm months both higher in period B, as the ratio LO-OOA-to-MO-OOA is also lower in summer. Nevertheless, the decreasing trend of NO_x and the increase in O_3 reactivity would position the

increasing potential oxidation as a feasible cause as many other urban studies have reported. Seasonal variation of OA contributions was also affected by air masses origin. Northern flows and stagnation episodes induced primary pollution events, although high-SOA events were driven by long-range episodes, comprising Mediterranean and European advection (mainly MO-OOA) and regional breeze-driven recirculation (mainly LO-OOA).

To the authors' knowledge, this is one of the first times NR-PM_1 chemical composition and OA sources have been studied with detail allowing for interannual comparison in an urban background in the western Mediterranean basin. The results obtained highlight the role of SOA as the main source of OA and its permanency even if POA is reduced. Furthermore, the remaining gaps in the oxidation of the urban-background atmosphere of Barcelona, possible pathways of production and transformation of SOA, and interfering O_3 processes could be the objective of further investigations.

Data availability. All data used in this study can be accessed here: https://doi.org/10.17632/xfv7z6jzcm.1 (Via et al., 2020).

Supplement. The supplement related to this article is available online at: https://doi.org/10.5194/acp-21-8323-2021-supplement.

Author contributions. The study was designed by MCM, AA and XQ. Measurements were carried out by MV, MCM and CR. Data analysis was done by MV and MCM. Data interpretation was done by MV, MCM and AA, with contributions from and discussions with CR and XQ. MV wrote the paper with contributions from MCM. All the authors revised the paper and agreed with its final version.

Competing interests. The authors declare that they have no conflict of interest.

Acknowledgements. Jordi Massagué is acknowledged for providing the O_3 data from the Autonomous Government of Catalonia. IDAEA-CSIC is a Centre of Excellence Severo Ochoa (Spanish Ministry of Science and Innovation, Project CEX2018-000794-S).

Financial support. This work was supported by COST Action CA16109 COLOSSAL, the Generalitat de Catalunya (grant no. AGAUR 2017 SGR41), the Spanish Ministry of Science and Innovation 70 through the CAIAC project (grant no. PID2019-108990RB-I00), and FEDER funds through EQC2018-004598-P.

Review statement. This paper was edited by Nga Lee Ng and reviewed by two anonymous referees.

References

Allan, J. D., Delia, A. E., Coe, H., Bower, K. N., Alfarra, M. R., Jimenez, J. L., Middlebrook, A. M., Drewnick, F., Onasch, T. B., Canagaratna, M. R., Jayne, J. T., and Worsnop, D. R.: A generalised method for the extraction of chemically resolved mass spectra from Aerodyne aerosol mass spectrometer data, J. Aerosol Sci., 35, 909–922, https://doi.org/10.1016/j.jaerosci.2004.02.007, 2004.

Alfarra, M. R., Prevot, A. S. H., Szidat, S., Sandradewi, J., Weimer, S., Lanz, V. A., Schreiber, D., Mohr, M., and Baltensperger, U.: Identification of the mass spectral signature of organic aerosols from wood burning emissions, Environ. Sci. Technol., 41, 5770–5777, https://doi.org/10.1021/es062289b, 2007.

Brines, M., Dall'Osto, M., Amato, F., Minguillón, M. C., Karanasiou, A., Grimalt, J. O., Alastuey, A., Querol, X., and van Drooge, B. L.: Source apportionment of urban PM_1 in Barcelona during SAPUSS using organic and inorganic components, Environ. Sci. Pollut. Res., 26, 32114–32127, https://doi.org/10.1007/s11356-019-06199-3, 2019.

Brown, S. G., Lee, T., Norris, G. A., Roberts, P. T., Collett Jr., J. L., Paatero, P., and Worsnop, D. R.: Receptor modeling of near-roadway aerosol mass spectrometer data in Las Vegas, Nevada, with EPA PMF, Atmos. Chem. Phys., 12, 309–325, https://doi.org/10.5194/acp-12-309-2012, 2012.

Canagaratna, M. R., Onasch, T. B., Wood, E. C., Herndon, S. C., Jayne, J. T., Cross, E. S., Miake-Lye, R. C., Kolb, C. E., and Worsnop, D. R.: Evolution of vehicle exhaust particles in the atmosphere, J. Air Waste Manag. Assoc., 60, 1192–1203, https://doi.org/10.3155/1047-3289.60.10.1192, 2010.

Canagaratna, M. R., Jimenez, J. L., Kroll, J. H., Chen, Q., Kessler, S. H., Massoli, P., Hildebrandt Ruiz, L., Fortner, E., Williams, L. R., Wilson, K. R., Surratt, J. D., Donahue, N. M., Jayne, J. T., and Worsnop, D. R.: Elemental ratio measurements of organic compounds using aerosol mass spectrometry: characterization, improved calibration, and implications, Atmos. Chem. Phys., 15, 253–272, https://doi.org/10.5194/acp-15-253-2015, 2015.

Canonaco, F., Slowik, J. G., Baltensperger, U., and Prévôt, A. S. H.: Seasonal differences in oxygenated organic aerosol composition: implications for emissions sources and factor analysis, Atmos. Chem. Phys., 15, 6993–7002, https://doi.org/10.5194/acp-15-6993-2015, 2015.

Cavalli, F., Viana, M., Yttri, K. E., Genberg, J., and Putaud, J.-P.: Toward a standardised thermal-optical protocol for measuring atmospheric organic and elemental carbon: the EUSAAR protocol, Atmos. Meas. Tech., 3, 79–89, https://doi.org/10.5194/amt-3-79-2010, 2010.

Chirico, R., DeCarlo, P. F., Heringa, M. F., Tritscher, T., Richter, R., Prévôt, A. S. H., Dommen, J., Weingartner, E., Wehrle, G., Gysel, M., Laborde, M., and Baltensperger, U.: Impact of aftertreatment devices on primary emissions and secondary organic aerosol formation potential from in-use diesel vehicles: results from smog chamber experiments, Atmos. Chem. Phys., 10, 11545–11563, https://doi.org/10.5194/acp-10-11545-2010, 2010.

Ajuntament de Barcelona: Traffic volume (mean daily intensity) at the principal traffic routes, 2014–2018, available at: https://www.bcn.cat/estadistica/catala/dades/anuari/cap15/C1511010.htm (last access: 13 May 2020), 2019.

COST Action CA16109 COLOSSAL: Chemical On-Line cOmposition and Source Apportionment of fine aerosoL, Working Group 1, Guidelines for real-time chemical characterization of fine atmospheric aerosols (standard operating procedure) and ACSM calibration, as output of the intercomparison exercises and experience gained during the course of the Action, Deliverable 1.1, available at: https://www.costcolossal.eu/deliverables/ (last access: 17 May 2021), in preparation, 2021.

COST Action CA16109 COLOSSAL: Chemical On-Line cOmposition and Source Apportionment of fine aerosoL, Working Group 1. Guidelines for comparison of ACSM measurement with co-located external data, Deliverable 1.2, available at: https://www.costcolossal.eu/ (last access: 17 May 2021), released in December 2019.

Crippa, M., Canonaco, F., Lanz, V. A., Äijälä, M., Allan, J. D., Carbone, S., Capes, G., Ceburnis, D., Dall'Osto, M., Day, D. A., DeCarlo, P. F., Ehn, M., Eriksson, A., Freney, E., Hildebrandt Ruiz, L., Hillamo, R., Jimenez, J. L., Junninen, H., Kiendler-Scharr, A., Kortelainen, A.-M., Kulmala, M., Laaksonen, A., Mensah, A. A., Mohr, C., Nemitz, E., O'Dowd, C., Ovadnevaite, J., Pandis, S. N., Petäjä, T., Poulain, L., Saarikoski, S., Sellegri, K., Swietlicki, E., Tiitta, P., Worsnop, D. R., Baltensperger, U., and Prévôt, A. S. H.: Organic aerosol components derived from 25 AMS data sets across Europe using a consistent ME-2 based source apportionment approach, Atmos. Chem. Phys., 14, 6159–6176, https://doi.org/10.5194/acp-14-6159-2014, 2014.

Dai, Q., Schulze, B. C., Bi, X., Bui, A. A. T., Guo, F., Wallace, H. W., Sanchez, N. P., Flynn, J. H., Lefer, B. L., Feng, Y., and Griffin, R. J.: Seasonal differences in formation processes of oxidized organic aerosol near Houston, TX, Atmos. Chem. Phys., 19, 9641–9661, https://doi.org/10.5194/acp-19-9641-2019, 2019.

DeCarlo, P. F., Slowik, J. G., Worsnop, D. R., Davidovits, P. and Jimenez, J. L.: Particle morphology and density characterization by combined mobility and aerodynamic diameter measurements. Part 1: Theory, Aerosol Sci. Technol., 38, 1185–1205, https://doi.org/10.1080/027868290903907, 2004.

He, L.-Y., Lin, Y., Huang, X.-F., Guo, S., Xue, L., Su, Q., Hu, M., Luan, S.-J., and Zhang, Y.-H.: Characterization of high-resolution aerosol mass spectra of primary organic aerosol emissions from Chinese cooking and biomass burning, Atmos. Chem. Phys., 10, 11535–11543, https://doi.org/10.5194/acp-10-11535-2010, 2010.

Jimenez, J. L., Canagaratna, M. R., Donahue, N. M., Prevot, A. S. H., Zhang, Q., Kroll, J. H., DeCarlo, P. F., Allan, J. D., Coe, H., Ng, N. L., Aiken, A. C., Docherty, K. S., Ulbrich, I. M., Grieshop, A. P., Robinson, A. L., Duplissy, J., Smith, J. D., Wilson, K. R., Lanz, V. A., Hueglin, C., Sun, Y. L., Tian, J., Laaksonen, A., Raatikainen, T., Rautiainen, J., Vaattovaara, P., Ehn, M., Kulmala, M., Tomlinson, J. M., Collins, D. R., Cubison, M. J., Dunlea, E. J., Huffman, J. A., Onasch, T. B., Alfarra, M. R., Williams, P. I., Bower, K., Kondo, Y., Schneider, J., Drewnick, F., Borrmann, S., Weimer, S., Demerjian, K., Salcedo, D., Cottrell, L., Griffin, R., Takami, A., Miyoshi, T., Hatakeyama, S., Shimono, A., Sun, J. Y., Zhang, Y. M., Dzepina, K., Kimmel, J. R., Sueper, D., Jayne, J. T., Herndon, S. C., Trimborn, A. M., Williams, L. R., Wood, E. C., Middlebrook, A. M., Kolb, C. E., Baltensperger, U., and Worsnop, D. R.: Evolution of organic aerosols in the atmosphere, Science, 326, 1525–1529, https://doi.org/10.1126/science.1180353, 2009.

Liu, P., Ye, C., Xue, C., Zhang, C., Mu, Y., and Sun, X.: Formation mechanisms of atmospheric nitrate and sulfate during the winter haze pollution periods in Beijing: gas-phase, heterogeneous and aqueous-phase chemistry, Atmos. Chem. Phys., 20, 4153–4165, https://doi.org/10.5194/acp-20-4153-2020, 2020.

Massagué, J., Carnerero, C., Escudero, M., Baldasano, J. M., Alastuey, A., and Querol, X.: 2005–2017 ozone trends and potential benefits of local measures as deduced from air quality measurements in the north of the Barcelona metropolitan area, Atmos. Chem. Phys., 19, 7445–7465, https://doi.org/10.5194/acp-19-7445-2019, 2019.

Meteocat: Hystorical of precipitation maps, Meteorological service of Catalonia, Meteocat, available at: https://www.meteo.cat/wpweb/climatologia/el-clima-ahir/historic-cartografia-climatica/historic-de-mapes-de-precipitacio-mensual/, last access: 1 July 2020a.

Meteocat: Hystorical of temperature maps, Meteorological service of Catalonia, Meteocat, available at: https://www.meteo.cat/wpweb/climatologia/el-clima-ahir/historic-cartografia-climatica/historic-de-mapes-de-temperatura-mensual/ last access: 16 June 2020b.

Middlebrook, A. M., Bahreini, R., Jimenez, J. L., and Canagaratna, M. R.: Evaluation of composition-dependent collection efficiencies for the Aerodyne aerosol mass spectrometer using field data, Aerosol Sci. Technol., 46, 258–271, https://doi.org/10.1080/02786826.2011.620041, 2012.

Millán, M. M.: Extreme hydrometeorological events and climate change predictions in Europe, J. Hydrol., 518, 206–224, https://doi.org/10.1016/j.jhydrol.2013.12.041, 2014.

Millán, M. M., Salvador, R., Mantilla, E., and Kallos, G.: Photooxidant dynamics in the Mediterranean basin in summer: Results from European research projects, J. Geophys. Res.-Atmos., 102, 8811–8823, https://doi.org/10.1029/96jd03610, 1997.

Minguillón, M. C., Perron, N., Querol, X., Szidat, S., Fahrni, S. M., Alastuey, A., Jimenez, J. L., Mohr, C., Ortega, A. M., Day, D. A., Lanz, V. A., Wacker, L., Reche, C., Cusack, M., Amato, F., Kiss, G., Hoffer, A., Decesari, S., Moretti, F., Hillamo, R., Teinilä, K., Seco, R., Peñuelas, J., Metzger, A., Schallhart, S., Müller, M., Hansel, A., Burkhart, J. F., Baltensperger, U., and Prévôt, A. S. H.: Fossil versus contemporary sources of fine elemental and organic carbonaceous particulate matter during the DAURE campaign in Northeast Spain, Atmos. Chem. Phys., 11, 12067–12084, https://doi.org/10.5194/acp-11-12067-2011, 2011.

Minguillón, M. C., Ripoll, A., Pérez, N., Prévôt, A. S. H., Canonaco, F., Querol, X., and Alastuey, A.: Chemical characterization of submicron regional background aerosols in the western Mediterranean using an Aerosol Chemical Speciation Monitor, Atmos. Chem. Phys., 15, 6379–6391, https://doi.org/10.5194/acp-15-6379-2015, 2015.

Minguillón, M. C., Pérez, N., Marchand, N., Bertrand, A., Temime-Roussel, B., Agrios, K., Szidat, S., van Drooge, B., Sylvestre, A., Alastuey, A., Reche, C., Ripoll, A., Marco, E., Grimalt, J. O., and Querol, X.: Secondary organic aerosol origin in an urban environment: influence of biogenic and fuel combustion precursors, Faraday Discuss., 189, 337–359, https://doi.org/10.1039/c5fd00182j, 2016.

Mohr, C., DeCarlo, P. F., Heringa, M. F., Chirico, R., Slowik, J. G., Richter, R., Reche, C., Alastuey, A., Querol, X., Seco, R., Peñuelas, J., Jiménez, J. L., Crippa, M., Zimmermann, R., Baltensperger, U., and Prévôt, A. S. H.: Identification and quantification of organic aerosol from cooking and other sources in Barcelona using aerosol mass spectrometer data, Atmos. Chem. Phys., 12, 1649–1665, https://doi.org/10.5194/acp-12-1649-2012, 2012.

Mohr, C., DeCarlo, P. F., Heringa, M. F., Chirico, R., Richter, R., Crippa, M., Querol, X., Baltensperger, U., and Prévôt, A. S. H.: Spatial Variation of Aerosol Chemical Composition and Organic Components Identified by Positive Matrix Factorization in the Barcelona Region, Environ. Sci. Technol., 49, 10421–10430, https://doi.org/10.1021/acs.est.5b02149, 2015.

Ng, N. L., Canagaratna, M. R., Zhang, Q., Jimenez, J. L., Tian, J., Ulbrich, I. M., Kroll, J. H., Docherty, K. S., Chhabra, P. S., Bahreini, R., Murphy, S. M., Seinfeld, J. H., Hildebrandt, L., Donahue, N. M., DeCarlo, P. F., Lanz, V. A., Prévôt, A. S. H., Dinar, E., Rudich, Y., and Worsnop, D. R.: Organic aerosol components observed in Northern Hemispheric datasets from Aerosol Mass Spectrometry, Atmos. Chem. Phys., 10, 4625–4641, https://doi.org/10.5194/acp-10-4625-2010, 2010.

Ng, N. L., Herndon, S. C., Trimborn, A., Canagaratna, M. R., Croteau, P. L., Onasch, T. B., Sueper, D., Worsnop, D. R., Zhang, Q., Sun, Y. L., and Jayne, J. T.: An Aerosol Chemical Speciation Monitor (ACSM) for routine monitoring of the composition and mass concentrations of ambient aerosol, Aerosol Sci. Technol., 45, 770–784, https://doi.org/10.1080/02786826.2011.560211, 2011.

Pandolfi, M., Alastuey, A., Pérez, N., Reche, C., Castro, I., Shatalov, V., and Querol, X.: Trends analysis of PM source contributions and chemical tracers in NE Spain during 2004–2014: a multiexponential approach, Atmos. Chem. Phys., 16, 11787–11805, https://doi.org/10.5194/acp-16-11787-2016, 2016.

Paatero, P.: The Multilinear Engine—A Table-Driven, Least Squares Program for Solving Multilinear Problems, Including the n-Way Parallel Factor Analysis Model, J. Comput. Graph. Stat., 8, 854–888, https://doi.org/10.1080/10618600.1999.10474853, 1999.

Paatero, P. and Hopke, P. K.: Discarding or downweighting high-noise variables in factor analytic models, Anal. Chim. Acta, 490, 277–289, https://doi.org/10.1016/S0003-2670(02)01643-4, 2003.

Paatero, P. and Tapper, U.: Positive matrix factorization: A non-negative factor model with optimal utilization of error estimates of data values, Environmetrics, 5, 111–126, https://doi.org/10.1002/env.3170050203, 1994.

Pérez, C., Sicard, M., Jorba, O., Comerón, A., and Baldasano, J. M.: Summertime re-circulations of air pollutants over the northeastern Iberian coast observed from systematic EARLINET lidar measurements in Barcelona, Atmos. Environ., 38, 3983–4000, https://doi.org/10.1016/j.atmosenv.2004.04.010, 2004.

Pérez, N., Pey, J., Querol, X. Ã., Alastuey, A., Lo, J. M., Viana, M. and Pe, N.: Partitioning of major and trace components in PM_{10}–$PM_{2.5}$–PM_1 at an urban site in Southern Europe, Atmos. Environ., 42, 1677–1691, https://doi.org/10.1016/j.atmosenv.2007.11.034, 2008.

Pey, J., Querol, X., Alastuey, A., Rodríguez, S., Putaud, J. P., and Van Dingenen, R.: Source apportionment of urban fine and ultra-fine particle number concentration in a Western Mediterranean city, Atmos. Environ., 43, 4407–4415, https://doi.org/10.1016/j.atmosenv.2009.05.024, 2009.

Pey, J., Pérez, N., Querol, X., Alastuey, A., Cusack, M., and Reche, C.: Intense winter atmospheric pollution episodes affecting the Western Mediterranean, Sci. Total Environ., 408, 1951–1959, https://doi.org/10.1016/j.scitotenv.2010.01.052, 2010.

Reche, C., Viana, M., Amato, F., Alastuey, A., Moreno, T., Hillamo, R., Teinilä, K., Saarnio, K., Seco, R., Peñuelas, J., Mohr, C., Prévôt, A. S. H., and Querol, X.: Biomass burning contributions to urban aerosols in a coastal Mediterranean City, Sci. Total Environ., 427–428, 175–190, https://doi.org/10.1016/j.scitotenv.2012.04.012, 2012.

Reyes-Villegas, E., Bannan, T., Le Breton, M., Mehra, A., Priestley, M., Percival, C., Coe, H., and Allan, J. D.: Online Chemical Characterization of Food-Cooking Organic Aerosols: Implications for Source Apportionment, Environ. Sci. Technol., 52, 5308–5318, https://doi.org/10.1021/acs.est.7b06278, 2018.

Ripoll, A., Pey, J., Minguillón, M. C., Pérez, N., Pandolfi, M., Querol, X., and Alastuey, A.: Three years of aerosol mass, black carbon and particle number concentrations at Montsec (southern Pyrenees, 1570 m a.s.l.), Atmos. Chem. Phys., 14, 4279–4295, https://doi.org/10.5194/acp-14-4279-2014, 2014.

Ripoll, A., Minguillón, M. C., Pey, J., Jimenez, J. L., Day, D. A., Sosedova, Y., Canonaco, F., Prévôt, A. S. H., Querol, X., and Alastuey, A.: Long-term real-time chemical characterization of submicron aerosols at Montsec (southern Pyrenees, 1570 m a.s.l.), Atmos. Chem. Phys., 15, 2935–2951, https://doi.org/10.5194/acp-15-2935-2015, 2015a.

Ripoll, A., Minguillón, M. C., Pey, J., Jimenez, J. L., Day, D. A., Sosedova, Y., Canonaco, F., Prévôt, A. S. H., Querol, X., and Alastuey, A.: Long-term real-time chemical characterization of submicron aerosols at Montsec (southern Pyrenees, 1570 m a.s.l.), Atmos. Chem. Phys., 15, 2935–2951, https://doi.org/10.5194/acp-15-2935-2015, 2015.

Saiz-Lopez, A., Borge, R., Notario, A., Adame, J. A., Paz, D. de la Paz, Querol, X., Artíñano, B., Gómez-Moreno, F. J., and Cuevas, C. A.: Unexpected increase in the oxidation capacity of the urban atmosphere of Madrid, Spain, Sci. Rep., 7, 1–11, https://doi.org/10.1038/srep45956, 2017.

Shi, Y., Chen, J., Hu, D., Wang, L., Yang, X., and Wang, X.: Airborne submicron particulate (PM1) pollution in Shanghai, China: Chemical variability, formation/dissociation of associated semi-volatile components and the impacts on visibility, Sci. Total Environ., 473–474, 199–206, https://doi.org/10.1016/J.SCITOTENV.2013.12.024, 2014.

Shrivastava, M., Cappa, C. D., Fan, J., Goldstein, A. H., Guenther, A. B., Jimenez, J. L., Kuang, C., Laskin, A., Martin, S. T., Ng, N. L., Petaja, T., Pierce, J. R., Rasch, P. J., Roldin, P., Seinfeld, J. H., Shilling, J., Smith, J. N., Thornton, J. A., Volkamer, R., Wang, J., Worsnop, D. R., Zaveri, R. A., Zelenyuk, A., and Zhang, Q.: Recent advances in understanding secondary organic aerosol: Implications for global climate forcing, Rev. Geophys., 55, 509–559, https://doi.org/10.1002/2016RG000540, 2017.

Stein, A. F., Draxler, R. R., Rolph, G. D., Stunder, B. J. B., Cohen, M. D. and Ngan, F.: Noaa's hysplit atmospheric transport and dispersion modeling system, B. Am. Meteorol. Soc., 96, 2059–2077, https://doi.org/10.1175/BAMS-D-14-00110.1, 2015.

Tobler, A. K., Skiba, A., Wang, D. S., Croteau, P., Styszko, K., Nęcki, J., Baltensperger, U., Slowik, J. G., and Prévôt, A. S. H.: Improved chloride quantification in quadrupole aerosol chemical speciation monitors (Q-ACSMs), Atmos. Meas. Tech., 13, 5293–5301, https://doi.org/10.5194/amt-13-5293-2020, 2020.

Toll, I. and Baldasano, J. M.: Modeling of photochemical air pollution in the Barcelona area with highly disaggregated anthropogenic and biogenic emissions, Atmos. Environ., 34, 3069–3084, https://doi.org/10.1016/S1352-2310(99)00498-7, 2000.

Trippetta, S., Sabia, S., and Caggiano, R.: Fine aerosol particles (PM_1): natural and anthropogenic contributions and health risk assessment, Air Qual. Atmos. Heal., 9, 621–629, https://doi.org/10.1007/s11869-015-0373-0, 2016.

Via, M., Minguillón, M. C., Reche, C., Querol, X., and Alastuey, A.: "BCN_OA_SourceApportionment_20142015_20172018", Mendeley Data, V1, https://doi.org/10.17632/xfv7z6jzcm.1, 2020.

WHO: Ambient air pollution: A global assessment of exposure and burden of disease, available at: https://www.who.int/phe/publications/air-pollution-global-assessment/en/ (last access: 25 May 2021), 2016.

Xu, W., Lambe, A., Silva, P., Hu, W., Onasch, T., Williams, L., Croteau, P., Zhang, X., Renbaum-Wolff, L., Fortner, E., Jimenez, J. L., Jayne, J., Worsnop, D., and Canagaratna, M.: Laboratory evaluation of species-dependent relative ionization efficiencies in the Aerodyne Aerosol Mass Spectrometer, Aerosol Sci. Technol., 52, 626–641, https://doi.org/10.1080/02786826.2018.1439570, 2018.

Yang, B. Y., Guo, Y., Morawska, L., Bloom, M. S., Markevych, I., Heinrich, J., Dharmage, S. C., Knibbs, L. D., Lin, S., Yim, S. H. L., Chen, G., Li, S., Zeng, X. W., Liu, K. K., Hu, L. W., and Dong, G. H.: Ambient PM_1 air pollution and cardiovascular disease prevalence: Insights from the 33 Communities Chinese Health Study, Environ. Int., 123, 310–317, https://doi.org/10.1016/j.envint.2018.12.012, 2019.

Zhang, Q., Jimenez, J. L., Canagaratna, M. R., Allan, J. D., Coe, H., Ulbrich, I., Alfarra, M. R., Takami, A., Middlebrook, A. M., Sun, Y. L., Dzepina, K., Dunlea, E., Docherty, K., DeCarlo, P. F., Salcedo, D., Onasch, T., Jayne, J. T., Miyoshi, T., Shimono, A., Hatakeyama, S., Takegawa, N., Kondo, Y., Schneider, J., Drewnick, F., Borrmann, S., Weimer, S., Demerjian, K., Williams, P., Bower, K., Bahreini, R., Cottrell, L., Griffin, R. J., Rautiainen, J., Sun, J. Y., Zhang, Y. M., and Worsnop, D. R.: Ubiquity and dominance of oxygenated species in organic aerosols in anthropogenically-influenced Northern Hemisphere midlatitudes, Geophys. Res. Lett., 34, 1–6, https://doi.org/10.1029/2007GL029979, 2007.

Zhang, Y., Favez, O., Petit, J.-E., Canonaco, F., Truong, F., Bonnaire, N., Crenn, V., Amodeo, T., Prévôt, A. S. H., Sciare, J., Gros, V., and Albinet, A.: Six-year source apportionment of submicron organic aerosols from near-continuous highly time-resolved measurements at SIRTA (Paris area, France), Atmos. Chem. Phys., 19, 14755–14776, https://doi.org/10.5194/acp-19-14755-2019, 2019.

Zhao, Y., Saleh, R., Saliba, G., Presto, A. A., Gordon, T. D., Drozd, G. T., Goldstein, A. H., Donahue, N. M., and Robinson, A. L.: Reducing secondary organic aerosol formation from gasoline vehicle exhaust, P. Natl. Acad. Sci. USA, 114, 6984-6989, https://doi.org/10.1073/pnas.1620911114, 2017.

Atmos. Meas. Tech., 15, 5479–5495, 2022
https://doi.org/10.5194/amt-15-5479-2022

Atmospheric Measurement Techniques
Open Access
EGU

Rolling vs. *seasonal* PMF: real-world multi-site and synthetic dataset comparison

Marta Via[1,2], Gang Chen[3,a], Francesco Canonaco[3,4], Kaspar R. Daellenbach[3], Benjamin Chazeau[5], Hasna Chebaicheb[6,7], Jianhui Jiang[8], Hannes Keernik[9,10], Chunshui Lin[11], Nicolas Marchand[5], Cristina Marin[12,13], Colin O'Dowd[11], Jurgita Ovadnevaite[11], Jean-Eudes Petit[14], Michael Pikridas[15], Véronique Riffault[6], Jean Sciare[15], Jay G. Slowik[3], Leïla Simon[7,13], Jeni Vasilescu[12], Yunjiang Zhang[7,13], Olivier Favez[7], André S. H. Prévôt[3], Andrés Alastuey[1], and María Cruz Minguillón[1]

[1]Institute of Environmental Assessment and Water Research, Barcelona, 08034, Spain
[2]Department of Applied Physics, University of Barcelona, Barcelona, 08028, Spain
[3]Laboratory of Atmospheric Chemistry, Paul Scherrer Institute, 5232 Villigen PSI, Switzerland
[4]Datalystica Ltd., Park innovAARE, 5234 Villigen, Switzerland
[5]Aix Marseille Univ., CNRS, LCE, Marseille, France
[6]IMT Nord Europe, Institut Mines-Télécom, Univ. Lille, Centre for Energy and Environment, 59000 Lille, France
[7]Institut National de l'Environnement Industriel et des Risques, Parc Technologique ALATA, 60550, Verneuil-en-Halatte, France
[8]Shanghai Key Lab for Urban Ecological Processes and Eco-Restoration, School of Ecological and Environmental Sciences, East China Normal University, 200241 Shanghai, China
[9]Air Quality and Climate Department, Estonian Environmental Research Centre, Marja 4d, 10617 Tallinn, Estonia
[10]Department of Software Science, Tallinn University of Technology, 19086 Tallinn, Estonia
[11]School of Physics and Centre for Climate and Air Pollution Studies, Ryan Institute, National University of Ireland Galway, University Road, H91CF50 Galway, Ireland
[12]National Institute of Research and Development for Optoelectronics INOE2000, Atomistilor 409, RO77125 Magurele, Romania
[13]Department of Physics, Politehnica University of Bucharest, 313 Spl. Independentei Str., Bucharest, Romania
[14]Laboratoire des Sciences du Climat et de l'Environnement, Orme des Merisiers, 91190 Gif-sur-Yvette, France
[15]Climate and Atmosphere Research Center, The Cyprus Institute, Nicosia, 2121, Cyprus
[a]now at: MRC Centre for Environment and Health, Environmental Research Group, Imperial College London, London, UK

Correspondence: Marta Via (marta.via@idaea.csic.es)

Received: 29 April 2022 – Discussion started: 30 May 2022
Revised: 30 August 2022 – Accepted: 31 August 2022 – Published: 27 September 2022

Abstract. Particulate matter (PM) has become a major concern in terms of human health and climate impact. In particular, the source apportionment (SA) of organic aerosols (OA) present in submicron particles (PM_1) has gained relevance as an atmospheric research field due to the diversity and complexity of its primary sources and secondary formation processes. Moreover, relatively simple but robust instruments such as the Aerosol Chemical Speciation Monitor (ACSM) are now widely available for the near-real-time online determination of the composition of the non-refractory PM_1. One of the most used tools for SA purposes is the source-receptor positive matrix factorisation (PMF) model. Even though the recently developed *rolling PMF* technique has already been used for OA SA on ACSM datasets, no study has assessed its added value compared to the more common *seasonal* PMF method using a practical approach yet. In this paper, both techniques were applied to a synthetic dataset and to nine European ACSM datasets in order to spot the main output discrepancies between methods. The main advantage of the synthetic dataset approach was that the meth-

Published by Copernicus Publications on behalf of the European Geosciences Union.

ods' outputs could be compared to the expected "true" values, i.e. the original synthetic dataset values. This approach revealed similar apportionment results amongst methods, although the *rolling* PMF profile's adaptability feature proved to be advantageous, as it generated output profiles that moved nearer to the *truth* points. Nevertheless, these results highlighted the impact of the profile anchor on the solution, as the use of a different anchor with respect to the *truth* led to significantly different results in both methods. In the multi-site study, while differences were generally not significant when considering year-long periods, their importance grew towards shorter time spans, as in intra-month or intra-day cycles. As far as correlation with external measurements is concerned, *rolling* PMF performed better than *seasonal* PMF globally for the ambient datasets investigated here, especially in periods between seasons. The results of this multi-site comparison coincide with the synthetic dataset in terms of *rolling–seasonal* similarity and *rolling* PMF reporting moderate improvements. Altogether, the results of this study provide solid evidence of the robustness of both methods and of the overall efficiency of the recently proposed *rolling* PMF approach.

1 Introduction

Air pollution is one of the biggest current and future environmental threats to human health and climate change. Results from Chen and Hoek (2020) notably relate an increased risk for all-cause mortality due to fine aerosol ($PM_{2.5}$, particulate matter with an aerodynamic particle diameter below 2.5 mm) exposure. Also, even for concentrations below the WHO guidelines threshold (annual means of $5\,\mu g\,m^{-3}$ for $PM_{2.5}$ at the time that this article was published), the life expectancy of the population of Europe has been reduced by an average of about 8.6 months. In turn, fine atmospheric aerosols also play a role in climate change (IPCC, 2021) due to both their direct (through radiation) and indirect (through cloud interaction) effects.

Exposure to submicron particulate matter (PM_1, particulate matter with an aerodynamic particle diameter of less than 1 µm) is known to have severe impacts on the respiratory system (Yang et al., 2018) and even to pass the blood–brain barrier to act directly on the central nervous system (Shih et al., 2018; Yin et al., 2020). Impact mitigation strategies must be designed to both reduce emissions (primary aerosols) and prevent the formation of indirectly emitted (or secondary) aerosols as well as to target the most harmful components, especially since recent studies have demonstrated that the mitigation strategies might be more effective in tackling specific PM sources rather than the bulk PM (Daellenbach et al., 2020). With the purpose of identifying the most appropriate reduction strategies, source apportionment (SA) methodologies, designed for identifying pollutant sources, must be constantly improved. One of the most widely used receptor models for SA is the positive matrix factorisation (PMF) model (Paatero and Tapper, 1994) along with the ME-2 engine (Paatero, 1999). This model can handle various types of data, such as online and offline PM datasets (Amato et al., 2016; Crippa et al., 2014; Rai et al., 2020, respectively), VOCs (Yuan et al., 2012), multi-wavelength absorption of refractory carbon (Forello et al., 2019) etc.; assemble different types of pollutants (Ogulei et al., 2005); and also be coupled to machine learning techniques (Heikkinen et al., 2021; Rutherford et al., 2021).

Since organic species account for 20–90 % of the total submicron aerosol mass (Chen et al., 2022; Jimenez et al., 2009), scientific interest has been set on the characterisation of these pollutants by offline and online techniques. The use of ACSM (Aerosol Chemical Speciation Monitor, Aerodyne Research Inc., Billerica, MA, USA) for continuous monitoring and quantification of submicron non-refractory compounds has become a key approach for air quality (AQ) assessment. The application of PMF to long-term ACSM submicron organic aerosol (OA) datasets (Sun et al., 2018; Zhang et al., 2019) under the Source Finder (SoFi) Pro software package (Datalystica Ltd.) allows us to quantify and identify the contribution of major groups of organic compounds. The formerly recommended methodology for OA SA was *seasonal* PMF, which requires splitting the dataset into seasons to perform PMF independently, providing *seasonal* but not an intra-seasonal variation of factor profiles, as reported in Canonaco et al. (2015). The more recently developed *rolling* PMF (Canonaco et al., 2021; Parworth et al., 2015) applies the model on moving or rolling windows of a selected length, and therefore it accounts for the temporal evolution of the OA source fingerprints. The current state of the art supports that *rolling* PMF should be more accurate and/or suitable than *seasonal* PMF due to its profile-adaptation feature and its lower computational and evaluation time, which will be the base hypothesis of this study. Nevertheless, only a few individual studies (Chazeau et al., 2021; Chen et al., 2021; Tobler et al., 2021) and an intercomparison (Chen et al., 2022) using this technique have been published so far, and no thorough *seasonal vs. rolling* comparison has been conducted thus far to the best of our knowledge.

This research aims to contribute to a deeper understanding of the advantages and weaknesses of the *rolling* and *seasonal* methods, assessing the differences regarding site or dataset characteristics and evaluating the environmental reasonability of their outcomes. This task is of great importance, as the knowledge of the strengths of each method will come in handy when choosing the best one for each study necessity, e.g. the better SA method for specific OA source outbreaks. Furthermore, conclusions from this analysis will also impact the quality of health, climate and modelling studies by means of an improved description of the main OA pollution sources.

2 Methodology

2.1 Instrumentation and datasets

This study is one of the outcomes of the Chemical On-Line cOmpoSition and Source Apportionment of fine aerosoL (COLOSSAL) project (https://cost-colossal.eu/, last access: 14 September 2022) supported by the COST programme and based on measurements performed within the ACTRIS network. It is closely related to the overview study of Chen et al. (2022), in which 22 more-than-one-year-long PMF datasets were joined for a *rolling* PMF intercomparison. Participants of the WG2 of the COST COLOSSAL Action contributed to the preparation of a protocol for SA, with the purpose of homogenising the PMF application (Chen et al., 2022). A total of 9 of the 22 datasets from that study, whose main characteristics can be found in Table 1, were also provided for this *rolling–seasonal* comparison. Some of them contain site-specific sources related to instrument artefacts or proximity to pollution hotspots. The factors identified at all sites are hydrocarbon-like OA (HOA), biomass burning OA (BBOA, except for the Dublin site), less-oxidised oxygenated OA (LO-OOA), more-oxidised oxygenated OA (MO-OOA), and oxygenated OA (OOA), which represents the sum of LO-OOA and MO-OOA. Other factors are only present at one or two sites: cooking-like OA (COA; in Barcelona–Palau Reial and Marseille–Longchamp); 58-related OA (58-OA; in Magadino); shipping and industry OA (SHINDOA; in Marseille–Longchamp); wood combustion, coal combustion, and peat combustion OA (WCOA, CCOA, PCOA, respectively; in Dublin). The 58-related OA, as explained in Chen et al. (2021), is a factor dominated by nitrogen fragments (m/z 58, m/z 84, m/z 94) that appeared as an artefact after the filament replacement in that instrument.

All data presented in the multi-site intercomparison were obtained from ACSMs, which use a mass spectrometer to measure the composition of non-refractory submicron particulate matter (NR-PM_1) in near-real time. It works at a lower mass-to-charge resolution, but it is more robust compared to the aerosol mass spectrometer (AMS, Aerodyne Research Inc, Billerica, MA, USA), allowing for long-term deployment. Both quadrupole (Q-ACSM) and time-of-flight (ToF-ACSM) ACSMs were used, further described respectively in Fröhlich et al. (2013) and Ng et al. (2011a). The resolution of ToF-ACSM datasets (10 min) was averaged to 30 min (resolution of the Q-ACSM) to have harmonised timestamps. The analysis software (version 1.6.1.1 for Q-ACSM and version 2.3.9 for ToF-ACSM), implemented in Igor Pro (WaveMetrics, Inc.), was provided by Aerodyne Research Inc. The treatment of the multi-site ACSM data to generate PMF input matrices is summarised in Table S1 in the Supplement, and more details can be found in the publications cited therein.

Ancillary measurements consisted of (i) SO_4^{2-}, NO_3^-, NH_4^+, and Cl^- measurements from ACSM; (ii) black carbon (BC) from the filter-based absorption photometer AE33 from Magee Scientific (Drinovec et al., 2015), except for those from the Cyprus Atmospheric Observatory – Agia Marina Xyliatou and Magadino, in which the AE31 was used; BC concentrations were differentiated according to their main sources into fossil fuel (BC_{ff}) and wood burning (BC_{wb}) BC by applying the Sandradewi model (Sandradewi et al., 2008); (iii) NO_X concentrations; (iv) ultra-fine particles (range 20–1000 nm) at the Marseille–Longchamp site. Details on the complementary instrumentation at each site can be found in Table S2.

2.2 Synthetic dataset

Although the principal aim of this article is to inspect the differences in the methods amongst these European sites, a synthetic dataset comparison was first tackled. The main advantage of this procedure is that it allows the real-world environmental measurements already classified in OA sources to be mimicked so that PMF results can be compared with the incoming synthetic data. We created a synthetic dataset that mimics OA mass spectral analyses of a ToF-ACSM in Zurich. For that purpose, we used source-specific OA mass spectra retrieved from the AMS spectral database (Crippa et al., 2013; Ng et al., 2011b; Ulbrich et al., 2009) and OA source concentration time series generated by the air quality model CAMx (Comprehensive Air Quality Model with Extensions) previously published by Jiang et al. (2019). Details are described in Sect. S1. The dataset used to calculate the error matrix is that from the Zurich site, which ranges from February 2011 until December 2011. Hence, the same CAMx outcoming time series period was used to generate the concentration matrix. The represented OA sources are HOA, BBOA, SOA from biogenic emissions (SOA_{bio}), SOA from biomass burning (SOA_{bb}), and SOA from traffic and other anthropogenic sources (SOA_{tr}).

The first step for the synthetic dataset creation was to select p (number of factors), POA, and SOA spectral profiles from the high-resolution AMS spectral database (Crippa et al., 2013; Ng et al., 2010; Ulbrich et al., 2009) and to multiply them by the time series of the same sources from the model output. The error matrix was generated following the same steps as for real-world data, and real-world parameters were used as detailed in the Supplement. For this purpose, the dataset used is that from the Zurich site, which ranges from February 2011 until December 2011. Hence, the same CAMx outcoming time series period was used to generate the concentration matrix. Gaussian noise was subsequently added to the outcoming matrix. The resulting matrices were used as *rolling* and *seasonal* PMF input. Before the comparison to the original factors, several tests, as in the multi-site comparison, were performed to check the quality of the output; these tests included the mass closure test and the scaled residuals profile revision.

Table 1. Participant sites.

Site	Type	Latitude	Longitude	Height (m a.s.l.)	ACSM type	Network	Period
Barcelona – Palau Reial (BCN-PR)	Urban background	41°23′11.48″ N	02°07′05.00″ E	80	*Q*	ACTRIS, GAW	Sep 2017–Oct 2018
Cyprus Atm. Obs. – Agia Marina Xyliatou (CAO-AMX)	Remote	35°2′19.35″ N	33°3′27.95″ E	352	*Q*	ACTRIS, GAW	Mar 2015–Jan 2017
Dublin (DUB)	Urban background	53°18′19.08″ N	06°3′4.52″ W	35	*Q*	ACTRIS, AQ network in Ireland: http://www.macehead.org/ (last access: Sep 2022)	Sep 2015–Aug 2017
ATmospheric Observations in liLle (ATOLL)	Suburban	50°36′40.0 N	03°08′25.4″ E	70	*Q*	ACTRIS, CARA programme (French AQ network)	Oct 2016–Sep 2017
Magadino (MGD)	Rural	46°9′37″ N	8°56′2″ E	204	*Q*	GAW	Aug 2013–Oct 2014
Magurele – INOE (INO)	Peri-urban	44°20′52.98′, N	26°1′43.93″ E	93	*Q*	ACTRIS, GAW	Sep 2016–Sep 2017
Marseille–Longchamp (MRS-LCP)	Urban background	43°18′18.84″ N	5°23′40.89″ E	71	ToF	CARA programme (French AQ network)	Jan 2017–Apr 2018
SIRTA (SIR)	Suburban	48°42″36″ N	2°9″0″ E	163	*Q*	ACTRIS	Jan 2016–May 2017
Tartu (TAR)	Urban background	58°22′14.16″ N	26°44′5.64″ E	39	*Q*	National air monitoring station	Sep 2016–Jul 2017

2.3 Positive matrix factorisation

The positive matrix factorisation model (Paatero and Tapper, 1994) describes the measured matrix **X** of n timestamps and m variables as a product of two matrices, **G** and **F**, plus a residual matrix **E** for a given number of factors p:

$$x_{ij} = \sum_{i,j}^{n,m} g_{ik} \cdot f_{kj} + e_{ij}\,. \quad (1)$$

The matrices **G** and **F** can be randomly initialised with a priori information. The model then iterates until the quantity

$$Q = \sum_{i=1}^{n} \sum_{j=1}^{m} \left(\frac{e_{ij}}{\sigma_{ij}}\right)^2, \quad (2)$$

where σ_{ij} represents the uncertainties of the input matrix **X**, is minimised with respect to all model variables.

The use of a priori information reduces the rotational ambiguity of the model, consisting of a degeneration of solutions associated with a given Q value (Canonaco et al., 2013), and it is usually done from the a-value approach. This consists of initialising **F** (or **G**) with reference profiles (or time series) and multiplying them by the percentage of variation a, $a \in [0,1]$, where 0 and 1 would represent total constraint and freedom, respectively. The Source Finder (SoFi Pro, versions 6.8 and 8.04, Datalystica Ltd., Villigen, Switzerland) applies this algorithm through the multi-linear engine 2 (ME-2) (Paatero, 1999) within the Igor Pro software environment (Wavemetrics, Inc., Portland, OR, USA). SoFi is also a powerful software package for preparing the rolling conditions for the input matrices prior to the PMF algorithm and post-processing the outcomes afterwards.

2.3.1 *Seasonal* PMF

In order to apply *seasonal* PMF, the input matrix is divided into season-long submatrices, and PMF is applied independently, adjusting the number of necessary factors to the requirements of each subperiod. In order to reach an environmentally reasonable local Q minimum, the implemen-

tation of constraints on primary organic aerosol(POA) factors has been performed according to the COLOSSAL guidelines for source apportionment (COLOSSAL, COST Action CA16109, 2019) and the protocol from Chen et al. (2022). After unconstrained results exploration, which allowed for some marker identification, constraints based on the a-value approach were applied to primary OA factors. The systematic exploration of the a-value space has been performed for each season, with the aim of determining the combination of a values that maximises the correlations between factors and external correlations and represents an environmentally reasonable OA explanation, hereafter referred to as the base-case solution. The random a-value ranges and the reference profiles employed can be found in Tables S1 and S3a.

With respect to the synthetic dataset, the 11 months from 2011 data were split into three periods (and not four seasons to avoid running PMF over too short periods): February–May, June–August, and September–December. The real-world Marseille dataset also used the co-located SO_2 time series to force an industry + shipping factor to emerge, as reported in previous studies (Bozzetti et al., 2017; El Haddad et al., 2013). The seasonal averaging of the remaining runs were complemented by bootstrapping to estimate the statistical error of the solution.

Bootstrapping (Efron, 1979) the *seasonal* PMF input together with random a-value resampling allows for a statistical and rotational uncertainty assessment. The application of a criteria-based selection, which will be deeply explained in Sect. 2.3.2, was also used to discard those runs that did not comply with the user-defined standards. The outcome of this technique consists of p (number of factors) mass spectra and time series, including their uncertainty assessment, combined season-wise together to obtain period-long OA sources. This might lead to possible factor discontinuity. Moreover, from this approach, source fingerprints are static throughout a whole season and cannot adapt to the OA processes of lifetimes below a meteorological season (i.e. 90 d) but can nevertheless evolve from one season to another.

2.3.2 *Rolling* PMF

Rolling PMF runs the model on subsets of the input matrix with a user-defined (window) length in days. Then, the window is shifted by a number of days (also chosen by the user), and PMF is applied again (Parworth et al., 2015). Consequently, many PMF runs are performed in each window length period, so in the post-analysis, one can automatically discard the runs that do not meet certain user-defined criteria (Canonaco et al., 2015). To select the most environmentally reasonable runs, the remaining solutions are averaged to generate the final solution, which will be provided with statistical and rotational uncertainties based on random input resampling (bootstrap) and random a-value resampling, respectively.

A length of 14 d and a shift of 1 d were used in the current study for the synthetic dataset and for 7 out of the 9 datasets, which is a good compromise between Q/Q_{exp} values and the percentage of modelled points, as suggested in Canonaco et al. (2021). Window lengths of 28 d were also assessed, but the correlations to ancillary measurements deteriorated in most of the cases. Exceptions to this rule were the SIRTA and Tartu sites, for which the 28 d window offered better correlations. These window lengths are consistent with the life cycle lengths of atmospheric aerosols (Textor et al., 2006), and their outcomes do not differ significantly. The application of constraints in PMF, as advised in the protocols, consists of setting random a values within a reasonable range and accepting only the runs that comply with the criteria. This procedure will lead to the selection of a values that induce more environmentally reasonable solutions and whose average will provide the final number. In some cases, the reference profiles used in *rolling* PMF are those from the *seasonal* solution, as the protocol is flexible regarding this choice. However, this constraint can have an impact on the solution, and in order to identify its implications, the profiles used in each case are detailed in Tables S1 and S3a.

A criteria-based selection was developed to automatically inspect the large number of PMF runs provided by the *rolling* method (Canonaco et al., 2021). This consists of the application of certain criteria to be fulfilled by the PMF outcoming factors. The acceptance or rejection of a run can be dictated by the thresholds retrieved from bootstrapped *seasonal* solutions or, more advisably, from a double-tailed Welch's t-test hypothesis evaluation with p values (Chen et al., 2021) chosen by the user (not exceeding 0.05). This procedure allows for factor discontinuity, as one can run PMF for two consecutive numbers of factors and choose a certain criterion upon which to select one more (or less) factor depending on the outbreak or vanishing of a factor marker. The list of criteria is specified in Table S3b for the synthetic dataset and in the respective publications for each real-world site.

2.4 SA procedure and dataset homogenisation

A method to compare source apportionment performance, analogous to Belis et al. (2015) while adjusted for our specificities, was developed in this study. The first step consisted of preliminary checks, in which the minimum requirements for solution acceptance, such as the mass closure and reasonability of profiles, must be satisfied. Secondly, the characterisation of discrepancies between methods was addressed in order to confirm the presence or absence of significant differences between *rolling* and *seasonal* PMF. The decision of which method was more suitable for certain dataset particularities was a posteriori based on the quantification of the performance goodness of both methods by means of correlation to external measurements and residual analysis. This flow process was applied to both the multi-site analysis and the synthetic dataset.

All the participants of the multi-site comparison applied the SA protocol to their own datasets, benefiting from the expertise in the previous OA SA studies at their sites. The analysis of the differences between source contribution estimates by both methods was performed for each site individually and overall. The similarity of the time series from one method to the other was assessed not only for each whole dataset but also in a "rolling" fashion, that is to say, by calculating some metrics on the windows of a given number of days with 1 d shifts between windows. This approach allowed for the identification of significant discrepancies between both approaches for the set PMF window lengths (14 d for *rolling*, 90 d for *seasonal*), a feature that was not evident in the whole long-term time series. It also enabled the watching of intra-daily differences by setting period lengths of 1 d.

A detailed study of model residuals was also beneficial to quantify the accuracy of each technique's performance. Scaled residuals represent the model error (e_{ij}) normalised by the uncertainty matrix (σ_{ij}):

$$\text{Scaled residuals}_{ij} = \frac{e_{ij}}{\sigma_{ij}}. \quad (3)$$

Their i, j sum has been reported in Paatero and Hopke (2003) to describe a unimodal histogram within a ± 3 range under good model performance conditions. The output Q quantity has been compared in both a raw and normalised way. This normalisation aims to deprive the impact of the degrees of freedom that normally depend on the input size and on the number of factors, hence computing the quantity Q/Q_{exp}, where

$$Q_{\text{exp}} = m \cdot n - p \cdot (m + n). \quad (4)$$

Then, various PMF runs can be compared in a more fundamental way. The expressions used for the normalisation arrangement have to be adapted to the particular degrees of freedom of each method:

$$\left(\frac{Q}{Q\_\text{exp}}\right)_{\text{Rolling}} = \frac{Q}{m \cdot n - p \cdot (n + m \cdot n_{14})}, \quad (5)$$

$$\left(\frac{Q}{Q_{\text{exp}}}\right)_{\text{Seasonal}} = \frac{Q}{m \cdot n - \cdot p \cdot (n + m \cdot n_{90})}. \quad (6)$$

The parameters $n_{14\,\text{d}}$ and $n_{90\,\text{d}}$ refer to the number of periods throughout the dataset of 14 and 90 d, respectively.

For the synthetic dataset, the comparison between methods had to consider the error of each. For this purpose, the metric presented in Belis et al. (2015), the uncertainty-normalised root-mean-squared error (RMSE_u) was used:

$$\text{RMSE}_u = \frac{\sqrt{\frac{1}{n}\sum_{i=1}^{n}(m_i - r_i)^2}}{2u}. \quad (7)$$

In this expression, m represents the modelled values, r the reference values, and u the mean uncertainty of the model.

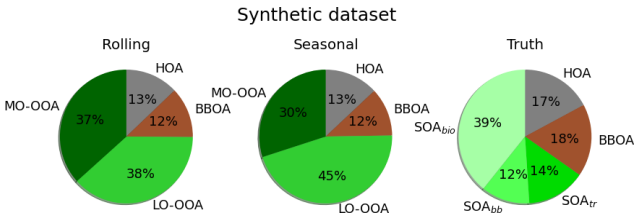

Figure 1. OA apportionment results for *rolling* and *seasonal* methods and *truth* output.

3 Results and discussion

3.1 Synthetic dataset

This section aims to assess the quality of the outcomes of the *rolling* and *seasonal* PMF methods. Relying on synthetic ToF-ACSM data offers the opportunity to compare the PMF outputs to the *truth*, which is not available for real-world measurements. We focus here on the OA sources' (factors') mean concentration and their temporal variability as well as the mean chemical composition and their temporal variability.

Regarding the OA apportionment vs. the input OA scatterplot, Table S4 presents the fitting coefficients for several resolutions, with no substantial difference between methods. Figure 1 shows the relative factor contributions to the apportioned OA for both methods. The POA factors do not differ substantially between the SA methods, but they are underestimated with respect to the *truth* (25 % of OA in *rolling* and *seasonal*, 35 % in *truth*). Also, whilst the LO-OOA-to-MO-OOA ratio is nearly 1 in the *rolling* case, it presents a much fresher secondary aerosol for the *seasonal* (1.5). Compared to the *truth*, PMF using a priori information on POA's chemical composition (HOA, BBOA) underestimates POA and overestimates SOA.

Figure 2 presents the time series, diel cycles of the *truth*, and *rolling* and *seasonal* methods as well as the scatter plots between the corresponding PMF time series. In time series and diel plots, it is noticeable that SOA is overestimated by PMF at the expense of POA (Fig. 2c). Squared Pearson correlation coefficients and slopes were similar for both *rolling* and *seasonal*, respectively, for HOA (0.89, 0.88) and OOA (0.95, 0.97) but not for BBOA, which *seasonal* resolves better (0.55, 0.72). Welch's t tests between *rolling* and *seasonal* time series rejected the similarity of all factors' concentrations. This test, applied to both methods against the *truth*, also rejected the hypothesis of significantly similar means, discarding a good method representation of *truth* results. This could be explained by the fact that *truth* profiles are static, and the methods were trying to adjust to moving fingerprints, and the anchor profiles might have influenced the results. For *rolling* and *seasonal* PMF results, the uncertainty-biased RMSE (RMSEu, Eq. 7) values are 1.10, 0.90 for HOA; 0.95, 1.98 for BBOA; and 0.05, 0.33 for

SOA, respectively. Values under 1 represent values within the range of PMF uncertainty and are therefore acceptable values, which is the case for all except the *rolling* HOA and *seasonal* BBOA. These exclusions could be explained by two, non-exclusive hypotheses: (i) the dissimilarity between methods and *truth* is large; and (ii) the uncertainties of the methods might be underestimated. In all cases except for HOA, *seasonal* presents higher RMSEu and therefore a worse fit to the *truth*. Besides, the statistical Welch's t test was performed on the synthetic dataset PMF results, testing the null hypothesis of statistically similar means with different variances.

The difference in the Pearson squared correlation coefficients between factors and their potential markers is shown as a histogram in Fig. S1 for each of the methods. The *truth* results show the worst correlation with ancillary measurements compared to modelled PMF. *Rolling* and *seasonal* results are very similar, although these correlations seem greater for *rolling* POA factors and for *seasonal* SOA factors. Slightly higher correlation coefficients were found for *rolling* in transition periods (i.e. ± 7 d before and after the change of seasons): 0.88 and 0.77 for HOA vs. BC; 0.74 and 0.65 for HOA vs. NO_X; 0.52 and 0.52 for OOA vs. NH_4; and 0.07 and 0.07 for MO-OOA vs. SO_4.

Profiles (Fig. 3a) did not show remarkable discrepancies between PMF methods, but nonetheless, these could be noticed when compared to the *truth* profiles. However, the cosine similarity method revealed high similarity of both methods to synthetic profiles (1.00 and 1.00 for HOA, 0.91 and 0.91 for BBOA, and 1.00 and 1.00 for SOA for *rolling* and *seasonal* PMF, respectively). However, it is noteworthy that both HOA's and BBOA's chemical compositions were constrained. Model HOA profiles were very similar to the *truth*, except for the lower m/z 44 and higher m/z 57 of the *truth*, and other HOA markers regarding models. Modelled BBOA presented significant differences between the *truth* and modelled profiles; the *truth* profiles contained a lower m/z 44-to-m/z 43 ratio, the lower influence of HOA markers, and much higher m/z 60 and m/z 73 BBOA tracers. Hence, modelled BBOA contained a higher proportion of other OA factor markers and lower of their own, meaning modelled profiles might have resulted in less cleanliness than the true ones. SOA PMF modelled profiles contained lower m/z 43 and m/z 44 than the *truth* profiles, although the rest remained very alike. In short, PMF results present a BBOA factor with more SOA and HOA influence as the main profile. The underestimation of POA is therefore understood to be due to a poorer modelisation of the key source identifiers, leading to a less pure profile and hence, a lower mass apportionment compared to *truth*.

The influence of reference profile constraints might have enhanced the misattribution of the profiles – for example, imposing m/z 44-to-m/z 43 ratios led to a significant difference in the degree of oxidation solution with respect to *truth*. Nevertheless, constraining profiles has provided more accurate solutions than unconstrained setups, as shown in Fig. S2. These plots show how *seasonal* constrained PMF launches always present higher similarity to *truth* in terms of key ions ratios. Moreover, OA sources of unanchored runs were less robust due to lower reproducibility along the accumulation of runs. By extension, rolling results are expected to reproduce the same results, as it has been proven that both techniques' outcomes converge sufficiently.

The adaptability of the models can be assessed from Fig. 3b, where the 60/55 vs. 44/43 (which are proxies for the BBOA–HOA differentiation and the SOA oxidation, respectively) is plotted for the *truth* and for both methods. Here we use m/z 55, since it is known to be a key marker for HOA. *Rolling* is shown to be a continuous time series, as the profiles for this method are time dependent, whilst the ratios for *seasonal* only vary from season to season. In HOA, the modelled points circle the actual *truth* and anchor profile points (which are similar or equal), but this is not the case for BBOA, in which the *rolling* and *seasonal* points are near the anchor profile but distant from the *truth*. This implies that the anchor profile, which was selected ignoring the *truth* profile characteristics, plays an important role in terms of adaptability to the actual solution. Overall, even for OA sources with nominally constant chemical composition (here HOA, BBOA), the factors resolved by PMF exhibit a varying chemical composition. Therefore, caution is required in interpreting the variability in sources of chemical variability resolved by *rolling* PMF. Oppositely, the SOA profiles, as they were unconstrained, can be compared more fairly. Both the *rolling* and *seasonal* dots are within the *truth* markers, except for some points of high 60/55, for which the highest disparity to *truth* is found for *seasonal*. This suggests a poorer PMF OOAs chemical composition profile apportionment, which in turn, might be influenced by the POA anchoring deficiencies.

The benefits of the continuity of the *rolling* profiles are reflected in time series, as can be seen in Fig. 3c, in which the behaviour of *seasonal* points is unrealistically drastic depending on the season. The profile adaptability of the *rolling* method represents a more resolute approach to positively representing the *truth*. Contrarily, the *seasonal* approach – although it can be plotted for each timestamp, as SOA is the sum of two OOAs – can only vary in lines of an equal 44/43 ratio, as the profiles are constant all through a season. In short, it can be stated that, as opposed to *seasonal* PMF or in general batch-wise PMF analysis, *rolling* PMF offers the potential to interpret changes (e.g. seasonal) in an OA sources' chemical composition, but the anchor profile selection has been shown to generate significant discrepancies when compared to the *truth* for both methods, requiring caution in interpreting such variability.

The SA method used has a severe impact on model-scaled residuals. Figure S3a shows the histogram of the scaled residuals for all the resolutions. In all cases, the *rolling* PMF histogram is significantly sharper, more centred to zero. Also,

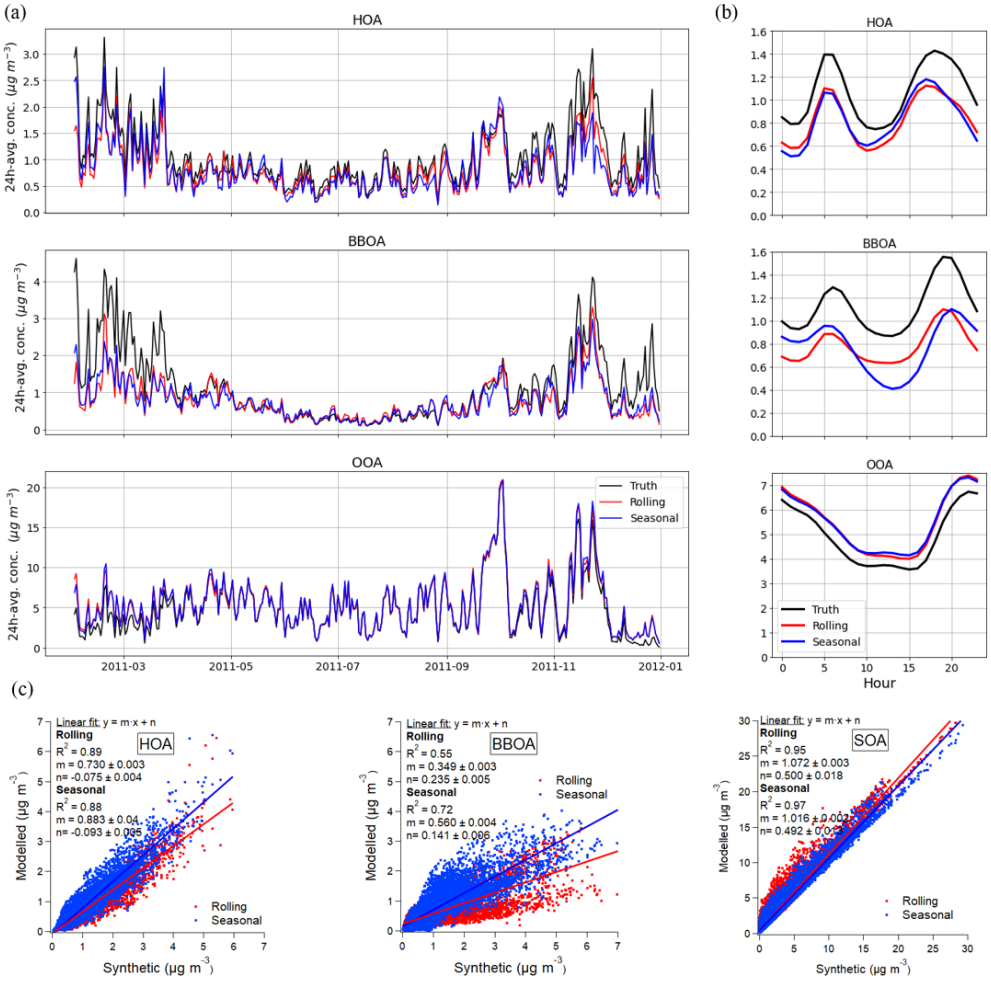

Figure 2. *Rolling*, *seasonal*, and *truth* (synthetic dataset original values) **(a)** time series (in hourly averages for the sake of clarity), **(b)** diel profiles, and **(c)** scatter plots.

the same effect is visible in the transition periods (Fig. S3b). Regarding Q values, the *rolling* value (3 838 356) is lower than the *seasonal* value (24 665 377), as expected, due to the higher extent of degrees of freedom of the former method. Q/Q_{exp} values, computed from Eqs. (5) and (6), are 7.08 and 37.58, respectively, for *rolling* and *seasonal* PMF. The fact that, when normalising by the model-specific degrees of freedom, the Q/Q_{exp} is lower for *rolling* than for *seasonal* leads to the conclusion that the minimisation of uncertainty-weighted errors is better achieved by the *rolling* method.

3.2 Multi-site comparison

3.2.1 Preliminary tests

Preliminary tests were performed to check the consistency of the reported results as well as the actual difference between the methods reported. An important performance metric is the closure of the OA mass – that is to say, the difference between the sum of all OA factor concentrations vs. the input mass. Table S4 provides the fit statistics of the input OA vs. the outcome OA for all the sites and four different time spans (the whole period, a season, a fortnight, and a day). All squared correlation coefficients are higher than 0.88, and slopes are within the 0.92–1.09 range. This ensures the quality of the PMF performance at all time resolutions and for both methods. A closer inspection of the table shows slightly higher correlation coefficients and slopes closer to 1 for *rolling*.

In order to confirm or reject the existence of systematic disparity between both methods, a two-tailed Welch's t test was performed under the null hypothesis of the time series having statistically similar expected values. In Table S5, all cells marked represent the runs that reject the null hypothesis, i.e. for which the factors retrieved from *rolling* and *seasonal* are not statistically equal (p values over 0.05). The row "all" refers to the concatenation of all the dataset time series. Apportioned OA presents the highest acceptance of the hypothesis rate, implying that the global apportionment

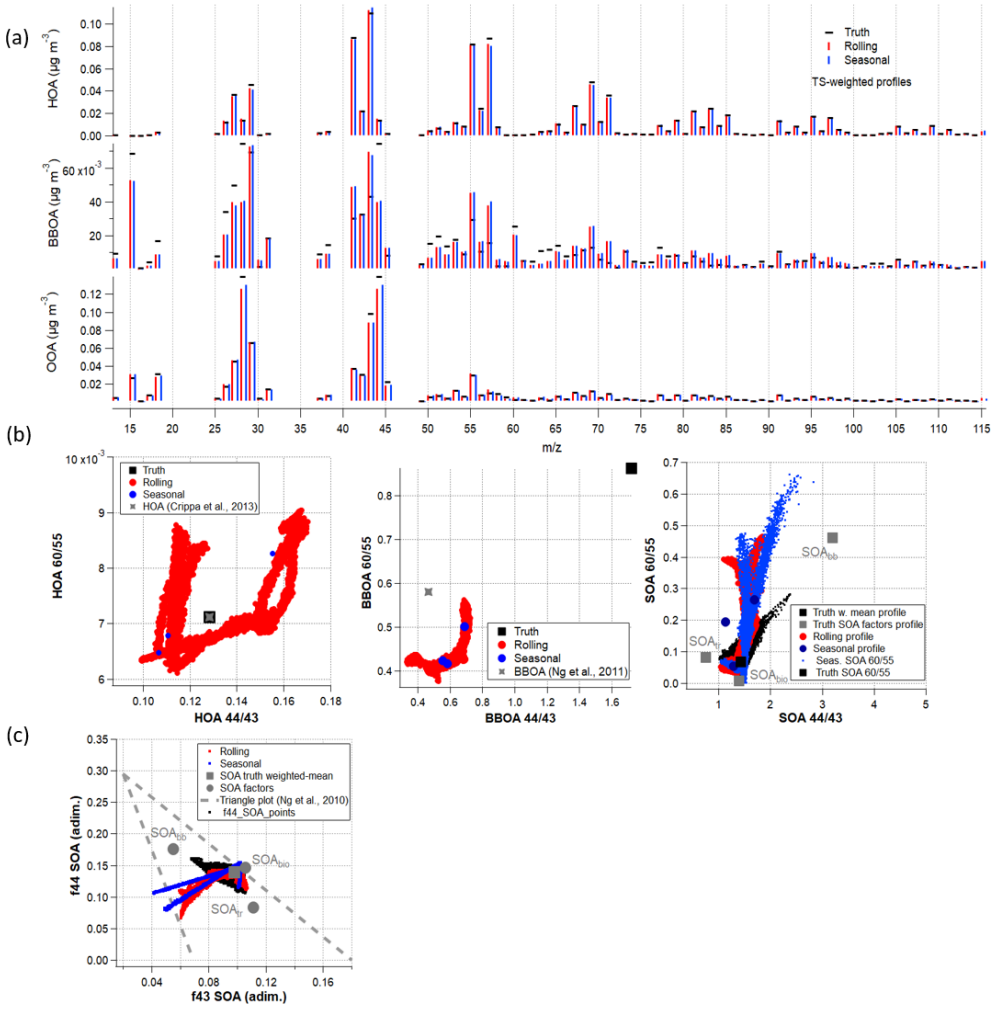

Figure 3. Synthetic dataset solution **(a)** profiles; **(b)** time-dependent profile variability of ratios 60/55 vs. 44/43; **(c)** triangle plot of f44 vs. f43 for *rolling* PMF (red), *seasonal* PMF (blue), and *truth* (black).

means are not significantly different. The factors with higher rejection rates are LO-OOA, MO-OOA, and HOA, in this order. OOA factors, as they are unconstrained, might be rather sensitive to source outbreaks or variations, which could have been caught or not by one model, although their sum (OOA) remains coherent. Period-long figures get the highest rejection rates, which decay rapidly from lower to higher resolutions, meaning the seasonal and fortnightly averages are still high despite their rapid resolution; on the other hand, for the daily resolution, this rate is very low. This fact highlights that the methods present significant differences with regard to means in intermediate resolutions.

Figure S4 compares the relative difference of the *rolling* minus *seasonal* concentrations for each factor in the all-sites ensemble. The factors with higher errors are MO-OOA and LO-OOA, tilted to positive values – that is, resulting in higher concentrations for *rolling*. This is probably related to the lack of anchors, which promotes higher freedom and hence, higher difference between methods. Also, BBOA presents significant positive whiskers, but as mean concentrations in Fig. 1 are equal, we suspect these are linked to sporadic high concentration outbreaks, which might only have been caught by the *rolling* method. Besides, the other factors are not significantly different from zero.

The pie charts in Fig. 4 show the amount of mass apportioned by the main OA sources in all datasets. These pies do not account for site-specific sources; they present the relative contribution of the all-sites ones scaled to account for the 360 degrees. OA is mainly driven by secondary organic aerosols in both cases, although the ratio of fresh-to-aged aerosol contributions – that is, LO-OOA over MO-OOA – is much higher for *rolling* (0.62) than for *seasonal* (0.54). The ratio of POA over SOA is higher for *seasonal* than for *rolling* (0.58 and 0.37, respectively), and the ratio of BBOA over HOA is considerably different (1.17 and 1.45, respectively). The fact that wood burning BC exceeds fossil fuel BC is consistent with the average ratio of 3.1 for BC_{wb} and BC_{ff}, implying that PMF reproduces this relation. Hence, *rolling*

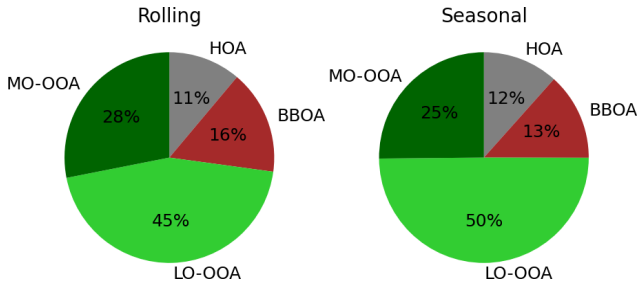

Figure 4. Pie charts of the mean concentrations of the main factors for the ensemble of all sites.

describes a more oxidised SOA, which is less prevailing than that of *seasonal*. In both, POA is governed by the biomass burning OA. Figure S5 shows the individual apportionment pies, in which the same trends can be generally recognised. In general terms, these results do not coincide with the ones from the synthetic dataset, in which the POA/SOA and LO-OOA/MO-OOA ratios were, respectively, equal and higher for *rolling*.

Figure 5 shows both the monthly and diel cycles of the *rolling* minus *seasonal* concentrations of the ensemble of sites for the main factors. In general terms, the intra-year variation is not remarkable, as all the boxes are mainly crossing the zero line. Besides, the differences between mean and median could indicate the adaptability to spiky events. The fact that HOA and BBOA are remarkably different throughout the whole period coincides with the aforementioned Welch's *t* tests. Moreover, the mean for HOA in January and December and for BBOA in July and August are positively set beyond the boxes, which could imply that the most extreme events are better captured by the *rolling*. This fact reinforces the hypothesis of a more precise capture of intra-month events. SOA factors present fewer clear trends, although an alternate sign between warm and cold months can be recognised. Figure S6 depicts the behaviour of the remaining factors, which are nearly zero except for 58-OA, which is significantly negative in summer, and SHINDOA, which alternates from positive to negative from summer to winter. In the case of 58-OA, this indicates a summertime under- or overestimation of one of the methods, and for the SHINDOA, a differing capturability of events along the year.

Regarding diel cycles (Fig. 5), the differences are evident in HOA and BBOA at night, implying that this is where the mixing between POA sources is aggravated. The SOA factors reveal that one of the methods overestimates the other throughout the daily cycle: *rolling* is greater for MO-OOA and OOA and lower for LO-OOA. Whilst these differences do not have an impact on the Welch's *t* test for LO-OOA, they do for the rest, even for HOA, for which they are not very uneven, probably due to the compensation of differences while averaging. Figure S6 shows similar behaviour for both methods in all the factors except for the WCOA, PCOA, and CCOA, which present higher differences at night. *Seasonal* concentrations, though, are remarkably higher for 58-OA throughout the period or daily cycle, somewhat superior in the COA 8h peak, and inferior in the SHINDOA afternoon. While these results do not have an impact on the *p* value for the Barcelona–Palau Reial and Magadino sites, it does for the Marseille–Longchamp site.

3.2.2 PMF goodness evaluation

Correlation with ancillary measurements

In order to assess the quality of each PMF method outcome, the correlation of factors with their potential markers was monitored from a single and global perspective. The pairs of variables compared were: HOA and BC_{ff}, HOA and NO_x, BBOA and BC_{wb}, MO-OOA and SO_4^{2-}, and OOA and NH_4^+. SHINDOA was compared to ultrafine particles with diameters of 10–20 nm coming from shipping or industry, differentiated according to Chazeau et al. (2021) and Rodríguez and Cuevas (2007). The correlation of LO-OOA vs. NO_3^- has been excluded in this study due to the plentiful sources of NO_3^-; besides, organonitrates would hamper the traceability of LO-OOA from this compound. This analysis has not been extended for the rest of the OA sources due to the lack of appropriate tracers available.

Figure 6 presents the Pearson squared correlation coefficient for all the pairs of markers and factors retrieved from *rolling* and *seasonal* PMF. Even though these marker time series are not deprived of errors, the hypothesis is that better agreement leads to better adaptation of the model to the OA source emitting these tracers. Overall, the *rolling* boxes are centred to higher correlation values than the *seasonal* ones, but their whiskers always reach the maximum value of 1 in both cases. The difference between methods is small, since medians do not differ by more than 0.05; however, the *seasonal* performance underscores these correlations slightly. This finding would support the hypothesis of the superior performance of the *rolling*, although HOA is evenly characterised in both methods, which is consistent with the great similarity in the apportionment of OA shown in Fig. 4. The histogram for the difference of Pearson squared correlation coefficients is plotted as a histogram for all sites in Fig. S7. Positivity in this graph reflects better *rolling* results matched with co-located measurements, and the histogram spreads the range of correlations. The amount of shoulders in the right half of these histograms is higher than those in the left, which implies systematic improvement of the *rolling* method with respect to *seasonal* in terms of correlation with ancillary measurements.

Periods of transition from one season to another are strategically relevant for this comparison, since the *seasonal* method, due to its profile staticity definition, could yield to discontinuities in the time series of the different components. The change of OA factors spectra for *rolling* is smooth; there-

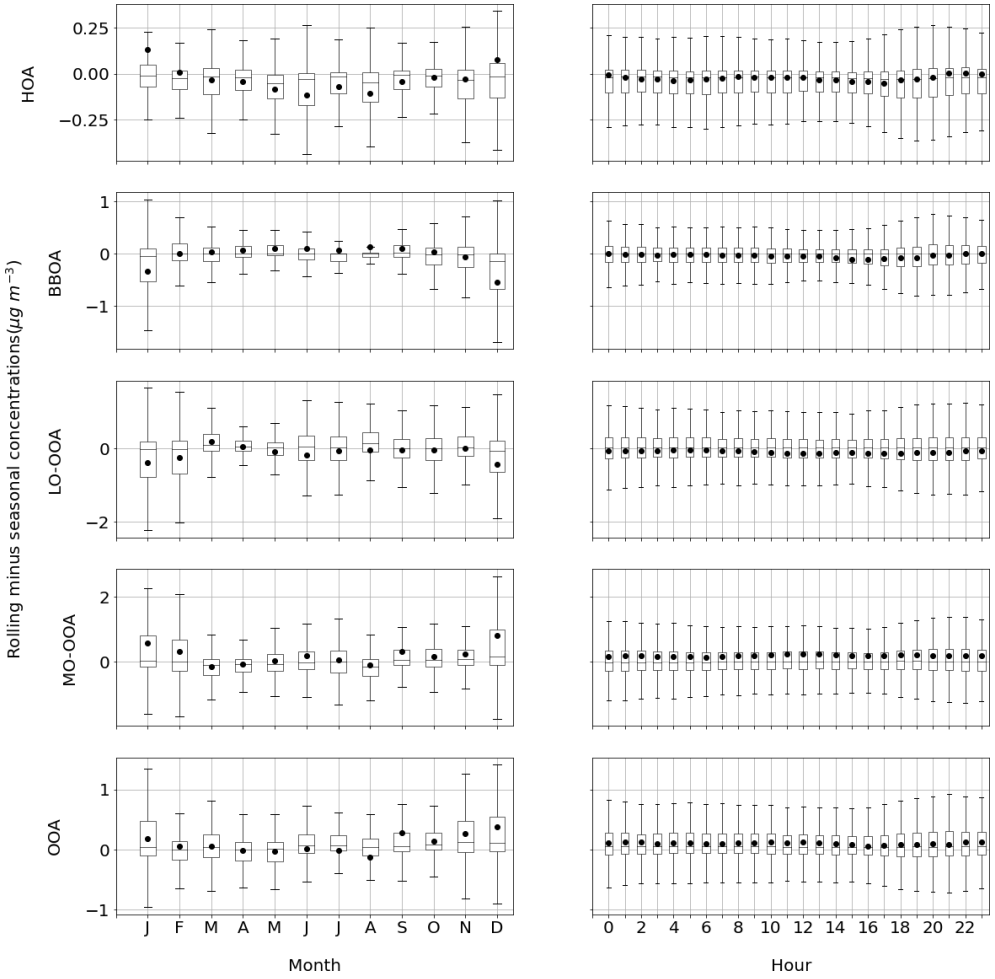

Figure 5. Boxplots of *rolling* minus *seasonal* factor absolute concentrations (in $\mu g\,m^{-3}$) per month and hour. Boxes show the Q1–Q3 range with the median (horizontal line) and the average (full circles); whiskers extend up to the range of the data.

fore, no abrupt changes should be expected in the season edges. Moreover, the *rolling* technique is capable of introducing factors depending on criteria compliance; therefore, their concentration edges are not as sharp as they would be for the *seasonal* PMF. This is the case for BBOA appearance in the cold months in Barcelona–Palau Reial and Marseille–Longchamp, and the 58-OA outbreak after the Q-ACSM filament replacement in Magadino. From these premises, one could expect to find better correlation coefficients relating to factors and their markers for the *rolling* method, which could better represent these periods. Table S6 shows the correlation of the OA factors and their markers for these periods only, both for the *rolling* and *seasonal* PMF. In all cases, the differences between methods are not extensive. However, it can be seen how the "whole" dataset figures are always greater for *rolling* than for *seasonal*. This finding supports the conjecture that the *seasonal* method presents greater difficulty in representing the edges of the seasons. The relevance of this conclusion is to be considered especially in the datasets in which the number of days near season changes is important due to data gaps.

Model residuals

Figure 7 shows the normalised scaled residuals distribution for both methods in a concatenated dataset including all the sites. Given that the uncertainty matrix was the same for both techniques, scaled residuals reflect the capacity of each technique to apportion the quantity of OA most similar to that which was entered as input. Boxplots show a tendency towards negative values for both methods, implying a systematic bias towards the overestimation of the input matrices. *Seasonal* errors present a higher spread and lower mean and medians; hence, *seasonal* results are less accurate and precise than those from *rolling*, overall. However, the span of both distributions does not exceed the $\pm 3\sigma$ threshold in any of the cases, meaning the results are acceptable for both techniques. Figure S8 shows the same plot for each of the participant sites. In general, the *rolling* histograms are more centred

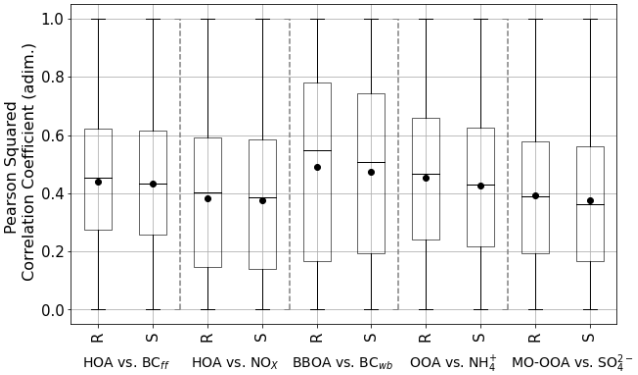

Figure 6. *Rolling* (R) and *seasonal* (S) boxplots of the Pearson squared correlation coefficient of each OA source with its respective markers for all sites.

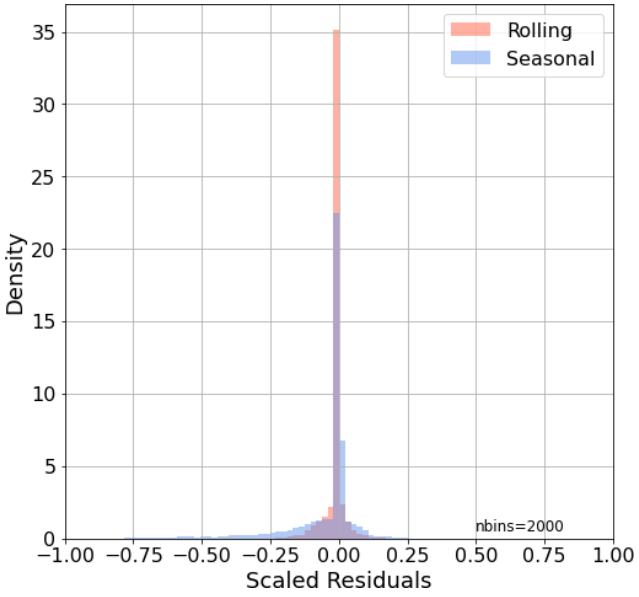

Figure 7. Normalised scaled residuals histogram for both PMF techniques.

to zero, and their sharpness is higher with respect to *seasonal* distributions. An exception to this behaviour is Marseille–Longchamp, which presents negatively shifted distributions probably related to the model's difficulty in differentiating between BBOA and LO-OOA.

Scaled residuals for the season transition periods are presented in Fig. S9. Both histograms extend largely beyond the (−3, 3) domain, implying that both methods struggle in this kind of period; however, the *seasonal* distribution of scaled residuals is much wider than that of *rolling*. Also, in the zoomed (−3, 3) range, *seasonal* results seem to present a wider distribution. Distribution shoulders are present in both – negative in *rolling* and positive in *seasonal* – indicating *rolling* overestimation and *seasonal* underestimation of input concentrations. These findings would imply that, even if the methods provide a substantial error in the transition periods, the *rolling* better captures the season change due to its profile adaptability.

Regarding Q values, the differences between techniques are presented in Table 2. Unweighted Q values show a clear pattern on lower values for *rolling* PMF, except for one site. The SIRTA datasets were treated by two different users, which might have led to different PMF steps and unreliable results. The generally greater minimisation of Q performed by the *rolling* PMF method can be explained by the major quantity of runs performed compared to *seasonal* PMF because of the proper definition of the method. By depriving the Q of the degrees of freedom effect, as shown in Eqs. (5), (6), the minimisation of both methods is signified. The trend generally points to lower figures for the *rolling* method, but whilst the minimisation of the unweighted Q was an expected fact, the implicit error reduction cannot be ensured within a theoretical frame. However, the majority of sites (excluding the aforementioned SIRTA) show lower Q/Q_{exp} values for the *rolling* method.

Table 2. Q/Q_{exp} values for *rolling* and *seasonal* solutions. Bold figures represent the lowest value in the *rolling–seasonal* comparison.

Q	Raw		Normalised	
	Rolling	Seasonal	Rolling	Seasonal
BCN – PR	**481 008**	1 766 588	**0.35**	1.14
CAO – AMX	**57 337**	5 101 949	**0.04**	2.87
DUB	**1 031 616**	1 261 451	**1.14**	1.19
ATOLL	**465 480**	477 145	0.84	**0.69**
MGD	**8 463 251**	3 117 660	**0.75**	2.46
INO	**6 138 684**	25 404 272	**4.58**	17.24
MRS – LCP	**57 337**	5 101 949	17.24	**2.87**
SIR	558 044	**44 965**	0.47	**0.10**
TAR	**82 742**	152 343	0.59	**0.34**

Adaptability tests

Adaptation tests were designed to inspect how much the methods comply with the input data. One of the main concerns to assess is the adaptability of the output profiles to short-lifetime events (order of magnitude of days), as it is the hypothesis onto which the *rolling* PMF is based. For this purpose, the check was based on the difference between main ion ratios, calculated from input values and the apportioned amounts of these ions by OOA factor profiles for both methods, e.g. $(m/z44/m/z43)_{\text{input}}$ – OOA $(m/z44/m/z43)$ Rolling or Seasonal. This can be seen in Fig. S10 in a time-series form for each site. Because $m/z44$ and $m/z43$ are also part of POA profiles, one should not expect to find a perfect match between the raw and the OOA profile ratios but rather a qualitative idea of how well the profiles adapt to the degree

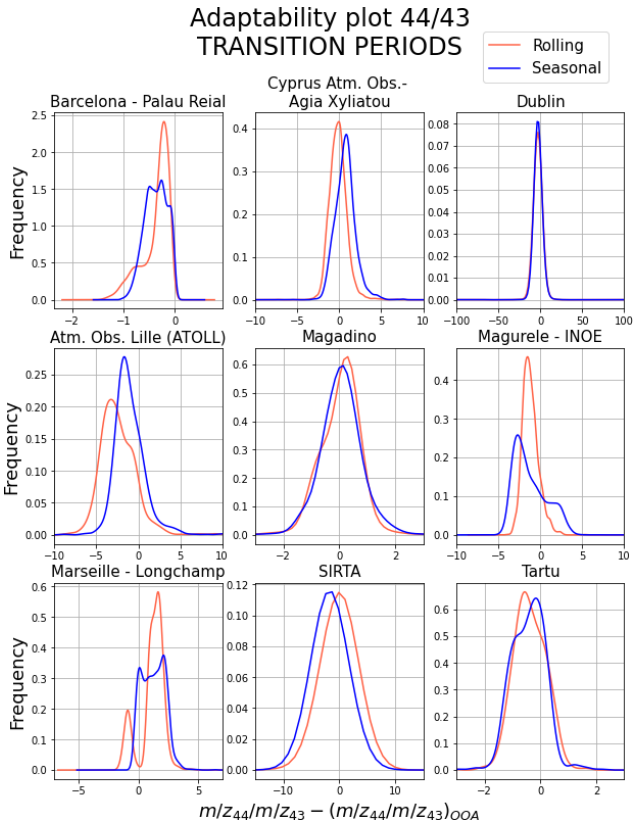

Figure 8. Kernel density estimation of the histograms of the subtraction of the m/z 44-to-43 ratio from the raw (from input matrices) time series data minus the apportioned quantity in profiles. These plots only contain those time lapses among the change of season (transition periods).

of aerosol ageing. In these plots, generally the *rolling* profile variation seems to adapt better than *seasonal*, which is a straight line along a season. Under the same logic, Fig. 8 shows the site histograms of the $(m/z44/m/z43)_{\text{input}} - \text{OOA}$ $(m/z44/m/z43)$ Rolling or Seasonal values only for periods around the change of season, which have been proven to be tricky for the PMF model.

Figure S9 shows, in general terms, how the *rolling* adapts to the main 44-to-43 trends, whilst *seasonal* can only present a single value for a whole season. Even though the *rolling* or *seasonal* SOA and the input time series are not expected to match perfectly, the main features of the variability are usually caught by the *rolling*. By taking a look only at the transition periods in Fig. 8, the tendency is that the difference between the input ratio and the *rolling* ratio is closer to zero or sharper around it than with *seasonal*. These qualitative appreciations bolster the aforementioned conclusion that *rolling* adapts the SOA profiles to specific singularities of the input time series, thus generating a more accurate solution.

4 Conclusions

The present study aimed at performing a comprehensive comparison between the two methodologies of fine organic aerosol (OA) source apportionment through the positive matrix factorisation (PMF) model: *rolling* and *seasonal* PMF.

The synthetic dataset *rolling* and *seasonal* outputs assessment has been rather fruitful for this comparison. The main highlight of this approach is that the modelled sources could be compared to the "*truth*" ones – that is, the OA sources chosen artificially during the dataset tailoring. Contrasting PMF results against the *truth* highlighted the model's overestimation of SOA and underestimation of POA (in the case of using a priori information on POA's chemical composition) for both *rolling* and *seasonal* and different degrees of SOA oxidation between methods. Nevertheless, the correlation of *rolling* and *seasonal* with the *truth* time series and profiles show very similar results in terms of concentrations. The temporal variability of OA sources' chemical composition has been shown to oscillate, even for POA components with temporally invariant chemical composition, and to be severely impacted by the selection of the profile anchors, as it differed significantly from the *truth* results when the anchor was significantly different to the *truth* profile. However, the use of profile constraints still provided solutions closer to the *truth* than unconstrained PMF. Besides, the *rolling* method has been proven to give a more sensitive representation of the continuous OA fingerprints variation. Scaled residuals minimisation also supported that the *rolling* solution was mathematically superior to *seasonal*.

The following multi-site comparison pretends to contrast both PMF methods in real-world datasets treated homogeneously under Chen et al.'s (2022) protocol to observe general performance trends. The *rolling* method generally presents a comparatively similar proportion of primary OA (POA) and a secondary OA (SOA) of a lower oxygenation degree, i.e. the ageing state. The double-tailed Welch's t test showed that the narrower the window of inspection, the higher the differences between factors retrieved from one method to the other. Moreover, towards weekly or daily periods, SOA factors differ more than POA factors. This fact is likely due to the absence of constraints for the SOA factors during PMF. Contrastingly, POA factors are more dissimilar period-wise. The ratio of BBOA to HOA differs considerably from *rolling* to *seasonal* (1.45 and 1.17, respectively) for the ensemble of sites, but in any case, it is over 1, as the ratio of BC_{wb} to BC_{ff} suggests.

In general terms, *rolling* results correlate better with ancillary measurements than those from *seasonal* for almost all of the considered external datasets at all sites. This is particularly true in the days surrounding the change of season, in which the *seasonal* profiles change drastically from one time point to the following. Model residuals also point to a better minimisation for the *rolling* PMF, although regarding scaled residuals, both methods comply with the $(-3, 3)$ range ad-

vised by the protocol. The time series of key ions also quantitatively pointed to a better adequation of the *rolling* SOA profiles to the oxygenated OA key ions. Finally, the errors also proved to be more stable for the *rolling* method, while it should be noted that the individual sites' discrepancies from the overall trends have not been discussed in this study.

Overall, these results confirm the hypothesis that the *rolling* PMF can be considered more accurate and precise, globally, than the *seasonal* one, although both meet the standards of quality required by the source apportionment protocol. Moreover, the *rolling* method was already recognised to involve less user subjectivity and computational time as well as being more suitable for long-term and evolving SA analysis, such as semi-automated online SA. This study, therefore, promotes the acceptance of this novel *rolling* method as an improved approach suitable for source apportionment studies. An additional conclusion stemming from this comparison is that the selection of anchor profiles strongly influence the OA factors, so local reference profiles are encouraged to minimise this impact.

Code availability. The codes used for this comparison can be found in https://doi.org/10.17632/nd79y8mpg3.1 (Via, 2022b).

Data availability. All data used in this study can be accessed at https://doi.org/10.17632/dsfty2rn7y.2 (Via, 2022a).

Author contributions. MV: conceptualisation, data curation, formal analysis, investigation, methodology, software, validation, visualisation, writing – original draft preparation, writing – review and editing. GC: conceptualisation, data curation, formal analysis, investigation, methodology, software, validation, writing – review and editing. FC: conceptualisation, investigation, methodology, software, supervision, validation, writing – review and editing. KRD: conceptualisation, data curation, formal analysis, funding, investigation, methodology, project administration, software, supervision, validation, writing – review and editing. BC: data curation, formal analysis, investigation, writing – review and editing. HC: data curation, formal analysis, investigation, writing – review and editing. JJ: methodology, software. HK: data curation, formal analysis, investigation, writing – review and editing. CL: data curation, formal analysis, investigation, writing – review and editing. NM: funding, project administration. CM: data curation, formal analysis, investigation, writing – review and editing. CO: conceptualisation, funding, project administration, supervision, writing – review and editing. JO: data curation, formal analysis, funding, project administration, supervision, writing – review and editing. J-EP: conceptualisation, funding, project administration, supervision, writing – review and editing. mp: data curation, formal analysis, investigation, writing – review and editing. VR: data curation, formal analysis, funding, methodology, project administration, writing – review and editing. JS: funding, project administration, writing – review and editing. JGS: conceptualisation, formal analysis, methodology, software, validation, writing – review and editing. LS: data curation, formal analysis, investigation, writing – review and editing. JV: data curation, formal analysis, funding, investigation, writing – review and editing. YZ: data curation, formal analysis, investigation, writing – review and editing. OF: conceptualisation, funding, project administration, supervision, writing – review and editing. ASHP: conceptualisation, funding, methodology, project administration, resources, supervision, writing – review and editing. AA: conceptualisation, funding, methodology, project administration, resources, supervision, validation, writing – review and editing. MCM: conceptualisation, data curation, formal analysis, funding, investigation, methodology, project administration, resources, supervision, validation, writing – review and editing.

Competing interests. The contact author has declared that none of the authors has any competing interests.

Disclaimer. Publisher's note: Copernicus Publications remains neutral with regard to jurisdictional claims in published maps and institutional affiliations.

Acknowledgements. IDAEA-CSIC is a Centre of Excellence Severo Ochoa (Spanish Ministry of Science and Innovation, Project CEX2018-000794-S). The authors gratefully acknowledge the Romanian National Air Quality Monitoring Network (NAQMN, https://www.calitateaer.ro/public/home-page/?__locale=ro, last access: September 2022) for providing NO_x data.

Financial support. This research has been supported by the Generalitat de Catalunya (grant no. AGAUR 2017 SGR41), the European Cooperation in Science and Technology (grant no. COST Action CA16109 COLOSSAL), the Ministerio de Ciencia, Innovación y Universidades (CAIAC, grant no. PID2019-108990RB-I00 and FEDER, grant no. EQC2018-004598-P.), the Horizon 2020, the Ministry of Education and Research, Romania (grant nos. PN-III-P1-1.1-TE-2019-0340 and 18PFE/30.12.2021, 18N/2019), the Agence Nationale de la Recherche (grant no. PIA, ANR-11_LABX-0005-01), the Conseil Régional Hauts-de-France (CLIMIBIO grant), the Ministère de l'Enseignement Supérieur et de la Recherche (CARA grant), the Environmental Protection Agency (AEROSOURCE, grant no. 2016-CCRP-MS-31), the Department of the Environment, Climate and Communications (AC3 network grant), and the Schweizerischer Nationalfonds zur Förderung der Wissenschaftlichen Forschung (SAMSAM, grant nos. IZCOZ9_177063 and PZPGP2_201992).

We acknowledge support of the publication fee by the CSIC Open Access Publication Support Initiative through its Unit of Information Resources for Research (URICI).

Review statement. This paper was edited by Mingjin Tang and reviewed by three anonymous referees.

References

Amato, F., Alastuey, A., Karanasiou, A., Lucarelli, F., Nava, S., Calzolai, G., Severi, M., Becagli, S., Gianelle, V. L., Colombi, C., Alves, C., Custódio, D., Nunes, T., Cerqueira, M., Pio, C., Eleftheriadis, K., Diapouli, E., Reche, C., Minguillón, M. C., Manousakas, M.-I., Maggos, T., Vratolis, S., Harrison, R. M., and Querol, X.: AIRUSE-LIFE+: a harmonized PM speciation and source apportionment in five southern European cities, Atmos. Chem. Phys., 16, 3289–3309, https://doi.org/10.5194/acp-16-3289-2016, 2016.

Belis, C. A., Pernigotti, D., Karagulian, F., Pirovano, G., Larsen, B. R., Gerboles, M., and Hopke, P. K.: A new methodology to assess the performance and uncertainty of source apportionment models in intercomparison exercises, Atmos. Environ., 119, 35–44, https://doi.org/10.1016/j.atmosenv.2015.08.002, 2015.

Bozzetti, C., El Haddad, I., Salameh, D., Daellenbach, K. R., Fermo, P., Gonzalez, R., Minguillón, M. C., Iinuma, Y., Poulain, L., Elser, M., Müller, E., Slowik, J. G., Jaffrezo, J.-L., Baltensperger, U., Marchand, N., and Prévôt, A. S. H.: Organic aerosol source apportionment by offline-AMS over a full year in Marseille, Atmos. Chem. Phys., 17, 8247–8268, https://doi.org/10.5194/acp-17-8247-2017, 2017.

Canonaco, F., Crippa, M., Slowik, J. G., Baltensperger, U., and Prévôt, A. S. H.: SoFi, an IGOR-based interface for the efficient use of the generalized multilinear engine (ME-2) for the source apportionment: ME-2 application to aerosol mass spectrometer data, Atmos. Meas. Tech., 6, 3649–3661, https://doi.org/10.5194/amt-6-3649-2013, 2013.

Canonaco, F., Slowik, J. G., Baltensperger, U., and Prévôt, A. S. H.: Seasonal differences in oxygenated organic aerosol composition: implications for emissions sources and factor analysis, Atmos. Chem. Phys., 15, 6993–7002, https://doi.org/10.5194/acp-15-6993-2015, 2015.

Canonaco, F., Tobler, A., Chen, G., Sosedova, Y., Slowik, J. G., Bozzetti, C., Daellenbach, K. R., El Haddad, I., Crippa, M., Huang, R.-J., Furger, M., Baltensperger, U., and Prévôt, A. S. H.: A new method for long-term source apportionment with time-dependent factor profiles and uncertainty assessment using SoFi Pro: application to 1 year of organic aerosol data, Atmos. Meas. Tech., 14, 923–943, https://doi.org/10.5194/amt-14-923-2021, 2021.

Chazeau, B., Temime-Roussel, B., Gille, G., Mesbah, B., D'Anna, B., Wortham, H., and Marchand, N.: Measurement report: Fourteen months of real-time characterisation of the submicronic aerosol and its atmospheric dynamics at the Marseille–Longchamp supersite, Atmos. Chem. Phys., 21, 7293–7319, https://doi.org/10.5194/acp-21-7293-2021, 2021.

Chen, G., Sosedova, Y., Canonaco, F., Fröhlich, R., Tobler, A., Vlachou, A., Daellenbach, K. R., Bozzetti, C., Hueglin, C., Graf, P., Baltensperger, U., Slowik, J. G., El Haddad, I., and Prévôt, A. S. H.: Time-dependent source apportionment of submicron organic aerosol for a rural site in an alpine valley using a rolling positive matrix factorisation (PMF) window, Atmos. Chem. Phys., 21, 15081–15101, https://doi.org/10.5194/acp-21-15081-2021, 2021.

Chen, G., Canonaco, F., Tobler, A., Aas, W., Alastuey, A., Allan, J., Atabakhsh, S., Aurela, M., Baltensperger, U., Bougiatioti, A., De Brito, J. F., Ceburnis, D., Chazeau, B., Chebaicheb, H., Daellenbach, K. R., Ehn, M., El Haddad, I., Eleftheriadis, K., Favez, O., Flentje, H., Font, A., Fossum, K., Freney, E., Gini, M., Green, D. C., Heikkinen, L., Herrmann, H., Kalogridis, A.-C., Keernik, H., Lhotka, R., Lin, C., Lunder, C., Maasikmets, M., Manousakas, M. I., Marchand, N., Marin, C., Marmureanu, L., Mihalopoulos, N., Močnik, G., Nęcki, J., O'Dowd, C., Ovadnevaite, J., Peter, T., Petit, J.-E., Pikridas, M., Platt, S. M., Pokorná, P., Poulain, L., Priestman, M., Riffault, V., Rinaldi, M., Różański, K., Schwarz, J., Sciare, J., Simon, L., Skiba, A., Slowik, J. G., Sosedova, Y., Stavroulas, I., Styszko, K., Teinemaa, E., Timonen, H., Tremper, A., Vasilescu, J., Via, M., Vodička, P., Wiedensohler, A., Zografou, O., Minguillón, M. C., and Prévôt, A. S. H.: European aerosol phenomenology – 8: Harmonised source apportionment of organic aerosol using 22 Year-long ACSM/AMS datasets, Environment International, ISSN 0160-4120, 166, https://doi.org/10.1016/j.envint.2022.107325, 2022.

Chen, J. and Hoek, G.: Long-term exposure to PM and all-cause and cause-specific mortality: A systematic review and meta-analysis, Environ. Int., 143, 105974, https://doi.org/10.1016/j.envint.2020.105974, 2020.

Crippa, M., DeCarlo, P. F., Slowik, J. G., Mohr, C., Heringa, M. F., Chirico, R., Poulain, L., Freutel, F., Sciare, J., Cozic, J., Di Marco, C. F., Elsasser, M., Nicolas, J. B., Marchand, N., Abidi, E., Wiedensohler, A., Drewnick, F., Schneider, J., Borrmann, S., Nemitz, E., Zimmermann, R., Jaffrezo, J.-L., Prévôt, A. S. H., and Baltensperger, U.: Wintertime aerosol chemical composition and source apportionment of the organic fraction in the metropolitan area of Paris, Atmos. Chem. Phys., 13, 961–981, https://doi.org/10.5194/acp-13-961-2013, 2013.

Crippa, M., Canonaco, F., Lanz, V. A., Äijälä, M., Allan, J. D., Carbone, S., Capes, G., Ceburnis, D., Dall'Osto, M., Day, D. A., DeCarlo, P. F., Ehn, M., Eriksson, A., Freney, E., Hildebrandt Ruiz, L., Hillamo, R., Jimenez, J. L., Junninen, H., Kiendler-Scharr, A., Kortelainen, A.-M., Kulmala, M., Laaksonen, A., Mensah, A. A., Mohr, C., Nemitz, E., O'Dowd, C., Ovadnevaite, J., Pandis, S. N., Petäjä, T., Poulain, L., Saarikoski, S., Sellegri, K., Swietlicki, E., Tiitta, P., Worsnop, D. R., Baltensperger, U., and Prévôt, A. S. H.: Organic aerosol components derived from 25 AMS data sets across Europe using a consistent ME-2 based source apportionment approach, Atmos. Chem. Phys., 14, 6159–6176, https://doi.org/10.5194/acp-14-6159-2014, 2014.

Daellenbach, K. R., Uzu, G., Jiang, J., Cassagnes, L. E., Leni, Z., Vlachou, A., Stefenelli, G., Canonaco, F., Weber, S., Segers, A., Kuenen, J. J. P., Schaap, M., Favez, O., Albinet, A., Aksoyoglu, S., Dommen, J., Baltensperger, U., Geiser, M., El Haddad, I., Jaffrezo, J. L., and Prévôt, A. S. H.: Sources of particulate-matter air pollution and its oxidative potential in Europe, Nature, 587, 414–419, https://doi.org/10.1038/s41586-020-2902-8, 2020.

Efron, B.: Bootstrap Methods: Another Look at the Jackknife, Ann. Stat., 7, 1–26, https://doi.org/10.1214/aos/1176344552, 1979.

El Haddad, I., D'Anna, B., Temime-Roussel, B., Nicolas, M., Boreave, A., Favez, O., Voisin, D., Sciare, J., George, C., Jaffrezo, J.-L., Wortham, H., and Marchand, N.: Towards a better understanding of the origins, chemical composition and aging of oxygenated organic aerosols: case study of a Mediterranean industrialized environment, Marseille, Atmos. Chem. Phys., 13, 7875–7894, https://doi.org/10.5194/acp-13-7875-2013, 2013.

Forello, A. C., Bernardoni, V., Calzolai, G., Lucarelli, F., Massabò, D., Nava, S., Pileci, R. E., Prati, P., Valentini, S., Valli, G., and Vecchi, R.: Exploiting multi-wavelength aerosol absorption coef-

ficients in a multi-time resolution source apportionment study to retrieve source-dependent absorption parameters, Atmos. Chem. Phys., 19, 11235–11252, https://doi.org/10.5194/acp-19-11235-2019, 2019.

Fröhlich, R., Cubison, M. J., Slowik, J. G., Bukowiecki, N., Prévôt, A. S. H., Baltensperger, U., Schneider, J., Kimmel, J. R., Gonin, M., Rohner, U., Worsnop, D. R., and Jayne, J. T.: The ToF-ACSM: a portable aerosol chemical speciation monitor with TOFMS detection, Atmos. Meas. Tech., 6, 3225–3241, https://doi.org/10.5194/amt-6-3225-2013, 2013.

Heikkinen, L., Äijälä, M., Daellenbach, K. R., Chen, G., Garmash, O., Aliaga, D., Graeffe, F., Räty, M., Luoma, K., Aalto, P., Kulmala, M., Petäjä, T., Worsnop, D., and Ehn, M.: Eight years of sub-micrometre organic aerosol composition data from the boreal forest characterized using a machine-learning approach, Atmos. Chem. Phys., 21, 10081–10109, https://doi.org/10.5194/acp-21-10081-2021, 2021.

IPCC: Climate Change 2021: The Physical Science Basis. Contribution of Working Group I to the Sixth Assessment Report of the Intergovernmental Panel on Climate Change, edited by: Masson-Delmotte, V., Zhai, P., Pirani, A., Connors, S. L., Péan, C., Berger, S., Caud, N., and Chen, Y., Cambridge Univ. Press, 3949, https://www.ipcc.ch/report/ar6/wg1/downloads/report/IPCC_AR6_WGI_Full_Report.pdf (last access: September 2022), 2021 (in press).

Jiang, J., Aksoyoglu, S., El-Haddad, I., Ciarelli, G., Denier van der Gon, H. A. C., Canonaco, F., Gilardoni, S., Paglione, M., Minguillón, M. C., Favez, O., Zhang, Y., Marchand, N., Hao, L., Virtanen, A., Florou, K., O'Dowd, C., Ovadnevaite, J., Baltensperger, U., and Prévôt, A. S. H.: Sources of organic aerosols in Europe: a modeling study using CAMx with modified volatility basis set scheme, Atmos. Chem. Phys., 19, 15247–15270, https://doi.org/10.5194/acp-19-15247-2019, 2019.

Jimenez, J. L., Canagaratna, M. R., Donahue, N. M., Prevot, A. S. H., Zhang, Q., Kroll, J. H., DeCarlo, P. F., Allan, J. D., Coe, H., Ng, N. L., Aiken, A. C., Docherty, K. S., Ulbrich, I. M., Grieshop, A. P., Robinson, A. L., Duplissy, J., Smith, J. D., Wilson, K. R., Lanz, V. A., Hueglin, C., Sun, Y. L., Tian, J., Laaksonen, A., Raatikainen, T., Rautiainen, J., Vaattovaara, P., Ehn, M., Kulmala, M., Tomlinson, J. M., Collins, D. R., Cubison, M. J., Dunlea, E. J., Huffman, J. A., Onasch, T. B., Alfarra, M. R., Williams, P. I., Bower, K., Kondo, Y., Schneider, J., Drewnick, F., Borrmann, S., Weimer, S., Demerjian, K., Salcedo, D., Cottrell, L., Griffin, R., Takami, A., Miyoshi, T., Hatakeyama, S., Shimono, A., Sun, J. Y., Zhang, Y. M., Dzepina, K., Kimmel, J. R., Sueper, D., Jayne, J. T., Herndon, S. C., Trimborn, A. M., Williams, L. R., Wood, E. C., Middlebrook, A. M., Kolb, C. E., Baltensperger, U., and Worsnop, D. R.: Evolution of organic aerosols in the atmosphere, Science, 80, 1525–1529, https://doi.org/10.1126/science.1180353, 2009.

Ng, N. L., Herndon, S. C., Trimborn, A., Canagaratna, M. R., Croteau, P. L., Onasch, T. B., Sueper, D., Worsnop, D. R., Zhang, Q., Sun, Y. L., and Jayne, J. T.: An Aerosol Chemical Speciation Monitor (ACSM) for routine monitoring of the composition and mass concentrations of ambient aerosol, Aerosol Sci. Technol., 45, 770–784, https://doi.org/10.1080/02786826.2011.560211, 2011a.

Ng, N. L., Canagaratna, M. R., Jimenez, J. L., Chhabra, P. S., Seinfeld, J. H., and Worsnop, D. R.: Changes in organic aerosol composition with aging inferred from aerosol mass spectra, Atmos. Chem. Phys., 11, 6465–6474, https://doi.org/10.5194/acp-11-6465-2011, 2011b.

Ogulei, D., Hopke, P. K., Zhou, L., Paatero, P., Park, S. S., and Ondov, J. M.: Receptor modeling for multiple time resolved species: The Baltimore supersite, Atmos. Environ., 39, 3751–3762, https://doi.org/10.1016/j.atmosenv.2005.03.012, 2005.

Paatero, P.: The Multilinear Engine – A Table-Driven, Least Squares Program for Solving Multilinear Problems, Including the n-Way Parallel Factor Analysis Model, J. Comput. Graph. Stat., 8, 854–888, https://doi.org/10.1080/10618600.1999.10474853, 1999.

Paatero, P. and Hopke, P. K.: Discarding or downweighting high-noise variables in factor analytic models, Anal. Chim. Acta, 490, 277–289, https://doi.org/10.1016/S0003-2670(02)01643-4, 2003.

Paatero, P. and Tapper, U.: Positive matrix factorization: A non-negative factor model with optimal utilization of error estimates of data values, Environmetrics, 5, 111–126, https://doi.org/10.1002/env.3170050203, 1994.

Parworth, C., Fast, J., Mei, F., Shippert, T., Sivaraman, C., Tilp, A., Watson, T., and Zhang, Q.: Long-term measurements of submicrometer aerosol chemistry at the Southern Great Plains (SGP) using an Aerosol Chemical Speciation Monitor (ACSM), Atmos. Environ., 106, 43–55, https://doi.org/10.1016/j.atmosenv.2015.01.060, 2015.

Rai, P., Furger, M., El Haddad, I., Kumar, V., Wang, L., Singh, A., Dixit, K., Bhattu, D., Petit, J. E., Ganguly, D., Rastogi, N., Baltensperger, U., Tripathi, S. N., Slowik, J. G., and Prévôt, A. S. H.: Real-time measurement and source apportionment of elements in Delhi's atmosphere, Sci. Total Environ., 742, 140332, https://doi.org/10.1016/j.scitotenv.2020.140332, 2020.

Rodríguez, S. and Cuevas, E.: The contributions of "minimum primary emissions" and "new particle formation enhancements" to the particle number concentration in urban air, J. Aerosol Sci., 38, 1207–1219, https://doi.org/10.1016/j.jaerosci.2007.09.001, 2007.

Rutherford, J. W., Larson, T. V., Gould, T., Seto, E., Novosselov, I. V., and Posner, J. D.: Source apportionment of environmental combustion sources using excitation emission matrix fluorescence spectroscopy and machine learning, Atmos. Environ., 259, 118501, https://doi.org/10.1016/j.atmosenv.2021.118501, 2021.

Shih, C.-H., Chen, J.-K., Kuo, L.-W., Cho, K.-H., Hsiao, T.-C., Lin, Z.-W., Lin, Y.-S., Kang, J.-H., Lo, Y.-C., Chuang, K.-J., Cheng, T.-J., and Chuang, H.-C.: Chronic pulmonary exposure to traffic-related fine particulate matter causes brain impairment in adult rats, Part. Fibre Toxicol., 15, 1–17, https://doi.org/10.1186/s12989-018-0281-1, 2018.

Sun, Y., Xu, W., Zhang, Q., Jiang, Q., Canonaco, F., Prévôt, A. S. H., Fu, P., Li, J., Jayne, J., Worsnop, D. R., and Wang, Z.: Source apportionment of organic aerosol from 2-year highly time-resolved measurements by an aerosol chemical speciation monitor in Beijing, China, Atmos. Chem. Phys., 18, 8469–8489, https://doi.org/10.5194/acp-18-8469-2018, 2018.

Textor, C., Schulz, M., Guibert, S., Kinne, S., Balkanski, Y., Bauer, S., Berntsen, T., Berglen, T., Boucher, O., Chin, M., Dentener, F., Diehl, T., Easter, R., Feichter, H., Fillmore, D., Ghan, S., Ginoux, P., Gong, S., Grini, A., Hendricks, J., Horowitz, L., Huang, P., Isaksen, I., Iversen, I., Kloster, S., Koch, D., Kirkevåg, A., Krist-

jansson, J. E., Krol, M., Lauer, A., Lamarque, J. F., Liu, X., Montanaro, V., Myhre, G., Penner, J., Pitari, G., Reddy, S., Seland, Ø., Stier, P., Takemura, T., and Tie, X.: Analysis and quantification of the diversities of aerosol life cycles within AeroCom, Atmos. Chem. Phys., 6, 1777–1813, https://doi.org/10.5194/acp-6-1777-2006, 2006.

Tobler, A. K., Canonaco, F., Skiba, A., Styszko, K., Nęcki, J., Slowik, J. G., and Baltensperger, U.: Characterization and source apportionment of PM 1 organic aerosol in Krakow, Poland, (April), 8299, 2021.

Ulbrich, I. M., Canagaratna, M. R., Zhang, Q., Worsnop, D. R., and Jimenez, J. L.: Interpretation of organic components from Positive Matrix Factorization of aerosol mass spectrometric data, Atmos. Chem. Phys., 9, 2891–2918, https://doi.org/10.5194/acp-9-2891-2009, 2009.

Via, M.: Rolling vs. Seasonal comparison, Mendeley Data [data set], V1, https://doi.org/10.17632/dsfty2rn7y.1, 2022.

Via, M.: "Rolling vs. Seasonal comparison", Mendeley Data [data set], V2, https://doi.org/10.17632/dsfty2rn7y.2, 2022a.

Via, M.: "Rolling vs. Seasonal PMF coding", Mendeley Data [code], v1 https://doi.org/10.17632/nd79y8mpg3.1, 2022b.

Yang, M., Chu, C., Bloom, M. S., Li, S., Chen, G., Heinrich, J., Markevych, I., Knibbs, L. D., Bowatte, G., Dharmage, S. C., Komppula, M., Leskinen, A., Hirvonen, M. R., Roponen, M., Jalava, P., Wang, S. Q., Lin, S., Zeng, X. W., Hu, L. W., Liu, K. K., Yang, B. Y., Chen, W., Guo, Y., and Dong, G. H.: Is smaller worse? New insights about associations of PM1 and respiratory health in children and adolescents, Environ. Int., 120, 516–524, https://doi.org/10.1016/j.envint.2018.08.027, 2018.

Yin, P., Guo, J., Wang, L., Fan, W., Lu, F., Guo, M., Moreno, S. B. R., Wang, Y., Wang, H., Zhou, M., and Dong, Z.: Higher Risk of Cardiovascular Disease Associated with Smaller Size-Fractioned Particulate Matter, Environ. Sci. Technol. Lett., 7, 95–101, https://doi.org/10.1021/acs.estlett.9b00735, 2020.

Yuan, B., Shao, M., De Gouw, J., Parrish, D. D., Lu, S., Wang, M., Zeng, L., Zhang, Q., Song, Y., Zhang, J., and Hu, M.: Volatile organic compounds (VOCs) in urban air: How chemistry affects the interpretation of positive matrix factorization (PMF) analysis, J. Geophys. Res.-Atmos., 117, 1–17, https://doi.org/10.1029/2012JD018236, 2012.

Zhang, Y., Favez, O., Petit, J.-E., Canonaco, F., Truong, F., Bonnaire, N., Crenn, V., Amodeo, T., Prévôt, A. S. H., Sciare, J., Gros, V., and Albinet, A.: Six-year source apportionment of submicron organic aerosols from near-continuous highly time-resolved measurements at SIRTA (Paris area, France), Atmos. Chem. Phys., 19, 14755–14776, https://doi.org/10.5194/acp-19-14755-2019, 2019.

Environment International 177 (2023) 108006

Contents lists available at ScienceDirect

Environment International

journal homepage: www.elsevier.com/locate/envint

Full length article

Towards a better understanding of fine PM sources: Online and offline datasets combination in a single PMF

Marta Via [a,b,*], Jesús Yus-Díez [a,b,1], Francesco Canonaco [c,d], Jean-Eudes Petit [e], Philip Hopke [f,g], Cristina Reche [a], Marco Pandolfi [a], Matic Ivančič [h], Martin Rigler [h], André S.H. Prevôt [c], Xavier Querol [a], Andrés Alastuey [a], María Cruz Minguillón [a]

[a] Institute of Environmental Assessment and Water Research (IDAEA-CSIC), Barcelona 08034, Spain
[b] Department of applied physics, Faculty of Physics, University of Barcelona, Barcelona 08028, Spain
[c] Laboratory of Atmospheric Chemistry, Paul Scherrer Institute, 5232 Villigen PSI, Switzerland
[d] Datalystica Ltd., Park innovAARE, 5234 Villigen, Switzerland
[e] Laboratoire des Sciences du Climat et de l'Environnement (CNRS-CEA-UVSQ), Gif-sur-Yvette, France
[f] Institute for a Sustainable Environment, Clarkson University, Potsdam NY13699, USA
[g] Department of Public Health Sciences, University of Rochester School of Medicine and Dentistry, Rochester NY14642, USA
[h] Aerosol d.o.o., Kamniška 39a, 1000 Ljubljana, Slovenia

ARTICLE INFO

Handling Editor: Marti Nadal

Keywords:
Multi-time resolution
Source apportionment
Submicronic particulate matter
Positive matrix factorisation
PMF
Multilinear engine
SoFi
ME2
Organic sources
Metals

ABSTRACT

Source apportionment (SA) techniques allocate the measured ambient pollutants with their potential source origin; thus, they are a powerful tool for designing air pollution mitigation strategies. Positive Matrix Factorization (PMF) is one of the most widely used SA approaches, and its multi-time resolution (MTR) methodology, which enables mixing different instrument data in their original time resolution, was the focus of this study. One year of co-located measurements in Barcelona, Spain, of non-refractory submicronic particulate matter (NR-PM_1), black carbon (BC) and metals were obtained by a Q-ACSM (Aerodyne Research Inc.), an aethalometer (Aerosol d.o.o.) and fine offline quartz-fibre filters, respectively. These data were combined in a MTR PMF analysis preserving the high time resolution (30 min for the NR-PM_1 and BC, and 24 h every 4th day for the offline samples). The MTR-PMF outcomes were assessed varying the time resolution of the high-resolution data subset and exploring the error weightings of both subsets. The time resolution assessment revealed that averaging the high-resolution data was disadvantageous in terms of model residuals and environmental interpretability. The MTR-PMF resolved eight PM_1 sources: ammonium sulphate + heavy oil combustion (25%), ammonium nitrate + ammonium chloride (17%), aged secondary organic aerosol (SOA) (16%), traffic (14%), biomass burning (9%), fresh SOA (8%), cooking-like organic aerosol (5%), and industry (4%). The MTR-PMF technique identified two more sources relative to the 24 h base case data subset using the same species and four more with respect to the pseudo-conventional approach mimicking offline PMF, indicating that the combination of both high and low TR data is significantly beneficial for SA. Besides the higher number of sources, the MTR-PMF technique has enabled some sources disentanglement compared to the pseudo-conventional and base case PMF as well as the characterisation of their intra-day patterns.

1. Introduction

Air pollution has become one of the most harmful threats to environmental health and climate (Kinney, 2018), being the 4th largest global cause of attributable deaths (Abbafati et al., 2020). Particulate matter (PM) is the pollutant with the highest impacts respect to adverse health effects (WHO, 2021). Identifying and quantifying pollution sources (i.e. source apportionment, SA) has become a major foci in urban air quality research, for which Positive Matrix Factorization (PMF, Paatero and Tapper, (1994)) is one of the most widely used modelling tools (Hopke et al., 2020). Although targeting one pollutant can be effective for specific mitigation strategies, the SA picture is vital

* Corresponding author.
E-mail address: marta.via@idaea.csic.es (M. Via).
[1] now at: Center for Atmospheric Research, University of Nova Gorica, Vipavska 11c, SI-5270 Ajdovščina, Slovenia.

https://doi.org/10.1016/j.envint.2023.108006
Received 13 February 2023; Received in revised form 9 May 2023; Accepted 29 May 2023
Available online 2 June 2023

to improve the understanding of the behaviour of pollution sources. In this broader framework, the multi-time resolution PMF (MTR-PMF) technique represents a handy tool for coupling several groups of species that are measured by different instrumentation and at a different time resolution (TR).

The principles of the MTR-PMF technique were first established by Zhou et al. (2004) with the aim of overcoming the averaging and interpolation practices when combining different TRs (10 min. to 24 h) data subsets. That study was able to retrieve six PM sources coupling data of several TRs, containing repeated and unrepeated species. Also, the study pointed out the higher sensitivity of the novel MTR-PMF technique to missing data in comparison with the regular PMF. Ogulei et al. (2005) used the MTR-PMF to file data gaps with concentration and uncertainty estimations. Subsequently, multiple studies benefitted from this technique, whose highlights will be mentioned hereunder.

The use of the MTR methodology has been applied in diverse inquiries. Kuo et al. (2014) demonstrated that averaging high TR data subsets to low TR data subsets' timestamps could yield the loss of factors with the same experimental data subsets and increased model error. Analogously, Liao et al. (2013) used synthetic data to demonstrate the accuracy of the model to explain the input sources and also found that averaging depreciated the correlation between input and output sources, respect to the MTR technique. Additional results from that work demonstrated that the model is more highly influenced by measurement error modifications than it is by input profile variation. The application of constraints in this work scheme reported beneficial outcomes in terms of the match with the simulated input. The use of constraints was also reported to be advantageous by Crespi et al. (2016), which, moreover, provided solution uncertainty estimation using bootstrap techniques in a constrained MTR-PMF. The use of the MTR methodology by Sofowote et al. (2018) allowed the identification of a source that was causing the major differences in $PM_{2.5}$ concentrations between a pair of nearby sites, traffic and non-traffic. This result was achieved by using several markers measured by different instrumentation leading to more comprehensive model results. In Srivastava et al. (2019), the MTR-PMF application allowed the combination of organic mass spectra and organic species leading to the identification of more factors relative to the standard PMF analysis. Forello et al. (2019) showed that, in addition to retrieving more robust sources MTR-PMF could also enhance the determination of instrumental source-dependent coefficients. This study benefitted from coupling filter samples and aethalometer data to retrieve the source dependent absorption Ångström exponent values and their variability without *a priori* assumptions.

Other studies have not used the MTR technique but instead have focused on coupling different instrument data subsets with the same TR and assessing the robustness of the outcomes depending on the subsets weightings (Crippa et al., 2013; Slowik et al., 2010a). Slowik et al. (2010b) reported that the uncertainty unbalance when coupling data from two different instruments can lead to unevenly representation of a data subset since there may be stronger internal correlations in one set versus the other. For example, in AMS data, there are characteristic m/z patterns due to the fragmentation process. This decompensation of the instruments' representation was tested by relatively changing the weighting of the uncertainty matrix of one of the instruments and assessing the scaled residuals. This work found that the solution with the lowest scaled residual means was obtained with a weighting of the PTR-MS dataset by 0.7 for winter and 0.8 for summer without changing the AMS dataset weight. Moreover, Belis et al. (2019) tuned the weighting of the instrumentally-established errors to provide the receptor model with optimum weighting for each instrumentation's data. This study proposed to adjust the weights according to the scaled residuals and Q/Q_{exp} outcomes. Thereupon, Tong et al. (2022) further explored the combination of two different instrumentation datasets by weighting their errors and assessing the outcomes by analysing the intersection between both datasets' scaled residuals histograms. That study showed that the most balanced solutions were found for weightings close to unity (scant weighting).

The origins of submicron aerosol in Barcelona have been previously studied with a wide variety of instrumentation. Most of the studies are based on measurements with a TR of 24 h and with organic aerosol (OA) as a bulk species (Pérez et al., 2008; Brines et al., 2019; In't Veld et al., 2021). Pérez et al. (2008) reported seven groups of pollutants classified by their major origin for the bulk PM_1 based on chemical analysis of offline PM_1 filter samples: Organic Matter (OM) + Elemental Carbon (EC), sea spray, crustal, ammonium, sulphate and nitrate. Similarly, In't Veld et al. (2021) identified heavy oil combustion, vehicle exhaust, non-emission vehicle emissions and a metallurgical industrial source in a 9-years, multi-site $PM_{2.5}$ time series. Brines et al. (2019) and Minguillón et al. (2012) performed SAs joining daily organic and inorganic species concentrations from offline PM_1 filter samples that yielded to better source descriptions. Regarding OA, high TR OA mass spectra PMF led to the identification of sources consisting of cooking-like OA (COA), hydrocarbon-like OA (HOA, attributed to road traffic), biomass burning OA (BBOA), and two oxygenated OA differentiated into a Less and a More Oxidised state (LO-OOA, MO-OOA) (Mohr et al., 2012; Minguillón et al., 2016; Via et al., 2021). The next step towards an optimal SA would be to couple this wide variety of species with the highest possible TR in order to characterise the intra-day variability of these sources. The MTR-PMF technique allows for SA of data subsets with different TR to provide an improved description of the sources in terms of the contribution of a wider range of species and their time variation.

The objective of the present study is twofold. It pursues in a better quantitative SA of the submicron aerosol sources, identifying different organic and inorganic soluble ions' together with black carbon (BC) and metal species, leading to a more complete source quantification and to the identification of additional potential sources. The submicron PM components used for this aim were: i. organic aerosol (OA), measured by a Quadrupole Aerosol Chemical Speciation Monitor (Q-ACSM); ii. non-refractory secondary inorganic species (SIA), including SO_4^{2-}, NO_3^-, NH_4^+, and Cl^-, also measured by a Q-ACSM; iii. BC measured by an aethalometer; iv. elemental species, from filter samples collected by high-volume samplers and analysed via ICP-AES and ICP-MS. This study also aims to examine the effect of the averaging of the high resolution (HR) data subset and of the uncertainty weighting of the datasets towards the reliance of MTR-PMF results. This parameter optimisation will provide guidance for future MTR-PMF users who seek for the optimal combined SA. To the authors' knowledge, this work provides the first study of these two parameter effects in a coupled manner from an analytical perspective to obtain the best possible SA of the submicronic aerosol.

2. Methodology

2.1. Sampling site, period and instrumentation

Measurements were performed at the Palau Reial site (PR; 41° 23′ 15″ N; 02° 07′ 05″ E; 80 m a.s.l.), an urban background site located in NW Barcelona near one of the busiest avenues of Barcelona (Diagonal Avenue, Fig. S1). More details of this site can be found in Minguillón et al. (2016) and Pey et al. (2010). The sampling period was from September 2017 to October 2018. The results from the deployed Q-ACSM and the aethalometer AE33 have been reported in Via et al. (2021), Yus-Díez et al. (2021). High volume samplers were co-located and used to collect PM_1 filter samples, as described in In't Veld et al. (2021). The combination of these three datasets has been prepared as input to PMF model both separately and for MTR-PMF.

2.1.1. Q-ACSM measurements

A Q-ACSM (Aerodyne Research Inc.) was deployed to measure NR-PM_1 particles between 75 and 650 nm. Particles are flash-vaporized at 600 °C in high vacuum conditions and ionized by hard-electron impact (70 eV), and the resulting fragments are analysed by a quadrupole mass

spectrometer (Ng et al., 2011). A fragmentation table (Allan et al., 2004) is used to convert the signal spectra into organic aerosol or inorganic species concentrations. An OA matrix with concentrations of unit mass resolution species (*m/z* from 12 to 120 Th) was generated. Ionization Efficiency (IE) and Relative Ion Efficiency (RIE) calibrations were conducted using 300-nm monodispersed NH_4NO_3 and $(NH_4)_2SO_4$ particles (Ng et al., 2011). The collection efficiency correction was applied according to Middlebrook et al. (2012), with CE values ranging 0.50–0.99. More details on calibration, settings and corrections can be found in Via et al. (2021). The OA uncertainty matrix was calculated as described by Ulbrich et al. (2009). The NR-PM_1 inorganic species' uncertainties were calculated as in Crenn et al. (2015). A thorough inspection of the signal-to-noise ratio of the input matrices was performed and all species were found in a sensitive range of 2–15. Also, the *m/z* range was upper-limited to 100 *m/z* as the mass of those ions between 100 and 120 only accounted for a 6% on average.

2.1.2. Aethalometer measurements

BC measurements were performed through an AE33 multi-wavelength Aethalometer (model AE33, Magee Scientific, Aerosol d.o.o.; Drinovec et al., 2015) with a PM_1 cut-off inlet. The AE33 is based on the measurement of light transmission at seven wavelengths (370, 470, 520, 590, 660, 880 and 950 nm) through two sample spots with different flows and particle loading relative to the reference spot. The aethalometer filter loading effect was corrected online by the dual-spot manufacturer correction (Drinovec et al., 2015), and the multiple scattering correction constant, C, was set to 2.44, as reported by Yus-Díez et al., (2021). The absorption Ångström exponents (α) for liquid fuel and solid fuel were set $\alpha_{lf} = 1$ and $\alpha_{sf} = 2$, respectively, as a rounding of the 0.9, 1.68, respectively, from Zotter et al. (2017). Posteriorly, the speciation of the BC regarding its origin into liquid fuel (BC_{lf}) and solid fuel (BC_{sf}) was obtained by applying the Sandradewi model (Sandradewi et al., 2008) to these BC measurements. The measurement uncertainty for the absorption was set to 15% of the measurement (Forello et al., 2019) for each of the seven wavelengths absorption. Error propagation was used for obtaining the uncertainty estimation of BC_{lf} and BC_{sf}. The data, generated at a 1-minute TR, was averaged into the 30-minute timestamps matching the Q-ACSM data to provide homogenised measurements. The ensemble of Q-ACSM (OA matrix and SIA) and aethalometer data (BC_{lf}, BC_{sf}) will be hereinafter referred to as the high time resolution (HR) data subset.

2.1.3. Offline measurements

A total of 83 PM_1 samples were collected at PR during the sampling period on 150 mm quartz micro-fibre filters (Pallflex 2500 QAT-UP) using high-volume samplers (DIGITEL DH80 at 30 $m^3 \cdot h^{-1}$) with a frequency of 1 out of 4 days. These 24-h (midnight-to-midnight) samples were divided into four portions to perform different analytical protocols on each. A quarter of each sample was acid digested and subsequently analysed by Inductively Coupled Plasma Optical Emission Spectrometry (ICP-OES, ICAP 6500, THERMO Scientific) and Inductively Coupled Plasma Mass Spectrometry (ICP-MS, X Series II, THERMO Electron Corporation) for the determination of major and trace element concentrations, respectively (procedure by Querol et al. (2001)). These results are summarised in In't Veld et al. (2021) and Via et al. (2021). Another quarter of each sample was water extracted and analyzed by ion chromatography for the determination of SO_4^{2-}, NO_3^-, and Cl^- concentrations and by selective electrode for the determination of NH_4^+ concentrations. A portion of the filter was analyzed by a thermal-optical method (Sunset OCEC analyser, Sunset Laboratory Inc.) following the EUSAAR2 protocol (Cavalli et al., 2010) for the EC and OC concentrations determination. The uncertainty of these measurements was calculated as described in Escrig et al., (2009). These species will be referred to as the low TR (LR) data subset.

2.2. Combination of data subsets

To prepare the input for the PMF model to be applied and achieve PM_1 mass closure, the following criteria were applied:

i. The concentrations of the species analysed by more than one technique were cross-validated, and the technique with higher TR was included for the final data set. Hence, concentrations of SO_4^{2-}, NO_3^-, NH_4^+, and Cl^- used are those from Q-ACSM after validating them against filter samples concentrations (Via et al., 2021). OA concentrations from Q-ACSM were compared and discussed with OC measurements from filter samples in Via et al. (2021) (here summarised in Table S1), and in the same way, BC concentrations from aethalometer were compared to measurements of EC from filter samples (Fig. S2); ii. The species with a signal-to-noise between 0.2 and 2 (so called weak) were kept after multiplying their uncertainties by a factor of two (Table S2).

Therefore, the HR data subset includes OA mass spectra from *m/z12* to *m/z100*, SO_4^{2-}, NO_3^-, NH_4^+, and Cl^-, and BC_{sf} and BC_{lf} (17603 datapoints); and the LR data subset comprises Ca, Al, K, Mg, Na, Ti, V, Cr, Mn, Co, Ni, Cu, Zn, As, Sn, Sb, and Pb (83 datapoints). The number of species and samples of the LR data subset provides a number of degrees of freedom per variable (72) in the 50–100 advised range (Henry et al., 1984). The elements selection was based on their signal-to-noise ratio values (0.5 threshold) and stability throughout the period.

2.3. Positive matrix factorisation analysis

2.3.1. Multi-time resolution PMF theoretical frame

When utilising subsets with different TRs, the data should be prepared in a specific manner. The diagram shown in Fig. 1 elucidates the input data disposition to be fed to the model in the present study. The PMF mass balance equation needs to be modified as in Zhou et al. (2004):

$$x_{sj} = \frac{1}{t_{s2} - t_{S1} + 1} \sum_{k=1}^{P} f_{kj} \sum_{i=t_{S1}}^{t_{s2}} g_{ik} \eta_{jm} + e_{sj} \quad (1)$$

where *s* indicates the sample, t_{s1} and t_{s2} are the starting and ending time points for the *s*th sample and η_{jm} are adjustment factors for replicated species in different TR or measured with different analytical methods (represented by the subscript *m*). In this study, η_{jm} equals to 1 in all cases coherently with the decision not to include replicated species.

The Multi-linear Engine 2 (ME-2) (Paatero, 1999) was applied to solve this problem through the Source Finder software (SoFi Pro, v8.0.4, Datalystica Ltd., Villigen, Switzerland, Canonaco et al. (2021)), within the Igor Pro software environment (Wavemetrics, Inc., Portland, OR, USA).

2.3.2. Instrument weighting

In order to generate sensible SA results, a fair representation of all

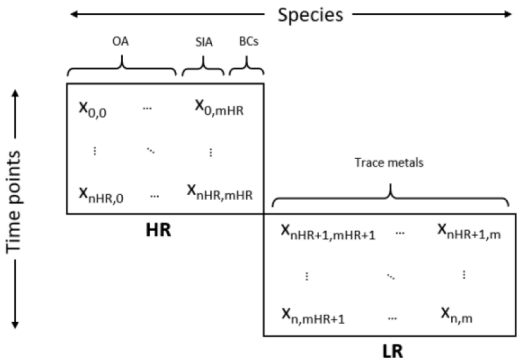

Fig. 1. Schematic of the combination of the High Resolution (HR) and Low Resolution (LR) subsets input matrix (X) for MTR-PMF.

species and groups of them must be ensured. Although the signal-to-noise ratio (Table S2) is comparable from one data subset to the other, the datasets can be uncertainty-unbalanced. An approach to evaluate the fairest uncertainty weighting is the assessment of the resulting PMF ratio of the error (e_{ij}) over the extent on which a measurement (x_{ij}) can be varied (σ_{ij}), i.e., scaled residuals. The instrument-individual uncertainty adjustment has been widely used for balancing these species' scaled residuals (Sofowote et al., 2018), which are expected to have a Gaussian distribution centred to zero (Zhou et al., 2004). However, less attention has been paid to the ensemble of all scaled residuals, which can lead to non-unimodal distributions especially if different instrumentation data is put together. A balanced PMF solution has been defined as that whose magnitude of scaled residuals is independent of the instrument (Slowik et al., 2010a). Thus, the scaled residuals distribution should be unimodal. Tong et al. (2022) showed that even for signal-to-noise-balanced input matrices and equally internally correlated ions within subsets, PMF residuals can be affected by the relative number of species included in each subset.

To address this inherent unbalanced coupling of different instrument data, weighting each subset has been proven successful (Crippa et al., 2013; Tong et al., 2022). The quantity C represents the scaling value for each of the data subsets' uncertainties (σ). In this study case, these Cs will be hereinafter called C_{HR} and C_{LR}, for the HR and LR datasets, respectively:

$$\sigma_{ij}^{HR'} = \frac{\sigma_{ij}^{HR}}{C_{HR}}, \quad \sigma_{ij}^{LR'} = \frac{\sigma_{ij}^{LR}}{C_{LR}} \tag{2}$$

The optimality assessment of a weighted PMF solution will be based on the similarity of the scaled residuals with those from PMF of the separate subsets. The quantification of this similarity among the data subsets scaled residuals was proposed by Tong et al. (2022), assessing the overlap between the histograms of the scaled residuals of the different subsets, in this case, HR and LR (example depicted in Figure S3). This quantity can be calculated by:

$$F_{overlap} = \int_{-a}^{a} \min\left[P_{HR}(s_{ij}), P_{LR}(s_{ij})\right] \tag{3}$$

where P_{HR} and P_{LR} indicate the density of probability of occurrence of the scaled residuals value s_{ij}, and a represents the integration limits. This integral is expected to cover the [0,1] range, being the extremes of this interval the null and full intersection, respectively. Defining $F^*_{overlap}$ as the overlap of the scaled residuals histograms of the independent HR and LR PMFs, the optimal solution is, as defined in Tong et al. (2022), the one which best fulfills the condition

$$F_{overlap}(C_{HR}, C_{LR}) \; F^*_{overlap} \tag{4}$$

In this study, the number of bins and the threshold range was set to 100 and 50, respectively, since these parameter values provide a wide and reasonable range of histogram intersection values. Note that the numerical integration has been tackled by means of the trapezoid integration method, which is expected to incorporate estimation errors.

2.3.3. Workflow design

With the purpose of assessing the MTR output sensitivity to the TR averaging and uncertainty weighting effects, a multi-approach procedure was designed, similarly to Belis et al. (2019).

Approach 1. HR SA. SA was performed to a data subset including the OA mass spectra, SIA species, and BC measurements separated into BC_{lf} and BC_{sf}. The TR of this data subset is 30 min.

Approach 2. LR SA. SA was performed on the data subset that contains metals concentrations at a TR of 24 h every four days.

Approach 3. Pseudo-conventional SA. SA was performed on a data subset that contains the metals, the SIA from Q-ACSM, and the BC and the OA as a bulk, all averaged to the LR data subset timestamps (24 h every four days). The BC was introduced as a species summing BC_{lf} and BC_{sf}, and the OA as the sum of all its *m/z*s to mimic the EC, OC concentrations that a conventional offline data subset would account for. Thus, the 'pseudo-conventional' naming refers to the mimicking of this data coupling to a conventional offline approach. This approach provides the reference to compare the posterior MT-PMF results with this conventional offline precursor SA methodology.

Approach 4. Base case SA. SA was performed on a data subset containing the HR data subset averaged to the LR subset timestamps (24 h every four days) and the LR data subset so that both data subsets are run under the same TR. This Approach does not apply uncertainty weightings. This data subset represents the most basic ensemble the MTR-PMF more refined results can be compared with.

Approach 5. MTR-PMF. SA performed on the dataset including OA species, SIA compounds, BC_{lf}, BC_{sf}, and metals in their native TR using the MTR-PMF technique. This data coupling requires performing first TR and C weightings assessment in order to find the most effective settings for both mathematical and environmental adequacy of the results. The determination of the highest suitability of these parameters' values was based on the scaled residuals histogram intersection between subsets. Whilst the resolution of the LR dataset remains constant (24 h every 4 days), the HR subset is averaged to different resolutions (R_1, referring to the TR of the HR dataset): R_1 = 30 min., 1 h, 2 h, 3 h, 6 h, 12 h, 24 h. Weighting scaling values combinations are: (C_{HR}, C_{LR})=(1,0.001), (1,0.01), (1,0.1), (1,1), (1,10), (0.001,1), (0.01,1), (0.1,1), (10,1), (100,1), (1000,1). The C-weightings testing experiment was afterwards repeated in a narrower range of C-values amongst the determined best combinations resulting in optimal resolution. Once the best R_1 and C_{HR}, C_{LR} parameters are found, standard SA is performed on this data subset with the optimised parameters. These results are then compared to those from Approaches 1, 2, 3, 4.

2.4. PMF settings and post-PMF data curation

Although a *rolling* PMF is a more convenient methodology with respect to the *seasonal* PMF as reported in Via et al. (2022), in this study, in which the TRs are so different and both datasets include multiple gaps, it would lead to different representation of each subsets because each has different number of points of each. To avoid this issue, PMF was run across the whole period. Constraints were not applied to allow the model to freely adapt the mass proportions of both subsets. The lack of similar studies that couple OA mass spectra, SIA, BC types and metals precludes availability of reference profiles. The application of constraints through anchor profiles would require the *a-priori* estimation of the mass proportion between LR and HR species for a given source, while this result is in fact one of the expected outputs of the present study newly applied methodology.

PMF was run in each of the aforementioned Approaches 10 times per number of factors so that the solution space is explored and the user can select the most physically reasonable solutions. To treat the unconstrained, and therefore, unsorted number of runs generated, an unsupervised non-hierarchical clustering technique was adopted. This method was applied after PMF, providing k profiles as a result of the average of all profiles within the same given cluster (more details are provided in SI Section B). The time series, explained variations and relative concentrations etc. associated to each profile were averaged within those belonging to the same profile cluster. In this way, the PMF solutions consisted of distinct, stable mean profiles and time series with their standard deviations amongst all cluster members. The k-means clustering algorithm was applied under the SciPy library environment in Python.

The SA error assessment methodology and results are extensively discussed in SI section D, including the rotational and clustering errors.

3. Results and discussion

3.1. Independent PMF

SA is performed on the different TR subsets separately, this is, the aforementioned Approach 1 and Approach 2. Their objective is to calculate the scaled residuals histogram overlap of the independent data subsets ($F^*_{overlap}$) as in Tong et al. (2022). The Approach 1 results, responding to the HR subset SA, are shortly described hereinunder and in Figure S4 and briefly here. Regarding the LR data subset SA (Approach 2), the results are not a self-explanatory SA solution since information provided by the species is limited and they only represent a 2% of the bulk PM_1 mass. However, an environmentally reasonable solution was obtained, whose scaled residuals are later used for the $F^*_{overlap}$ calculation (Eq. (3). The detailed solution is presented in the SI Section C and Figure S5.

The Approach 1 results already represent an improvement with respect to the OA SA, which led to the identification of five OA sources: HOA, COA, BBOA, LO-OOA and MO-OOA as reported by Via et al. (2021). The addition of the inorganic NR-PM_1 and BC species already proved advantageous in Zografou et al. (2022) by identifying an additional factor. Similarly, the present SA solution consists of 6 factors, 3 purely primary, 2 secondary and a potentially mixed factor (Figure S4). The mass closure of this SA shows a 12% of underestimation of the input concentrations (Fig. S4c).

The major source is the aged aerosol + ammonium sulphate (AS) factor (34%, Fig. S4d), which has a high *m/z44*-to-*m/z43* ratio, indicator of secondary organic aerosol (SOA) aging (Figs. S4a, S4d). Its diel cycle (Fig. S4e) shows an increase during the hours of maximum insolation, oppositely to the fresh OA factors since the production or reception of this source counteracted the boundary layer thickening and enhanced breeze effects. The fresher SOA is split in two factors, the fresh SOA + ammonium nitrate (AN) + ammonium chloride (ACl) and the fresh OA + Industry (Fig. S4a), considered to be actually different as they present uncorrelated time series ($R^2 = 0.06$) and different intra-annual variation (Fig. S4b). The Fresh SOA + AN + ACl source represents a 16% of the total PM mass (Fig. S4d). This factor comprises LO-OOA and almost all of the AN and ACl concentrations. It is minimal in summer and a significantly decreases during higher wind and boundary layer conditions (Fig. S4e). The Fresh SOA + Industry source represents a 14% of the output mass (Fig. S4d). The industrial contribution was not identified for this subset in previous studies, but here it was recognised by the presence of its marker *m/z58* and *m/z86* (Passig et al., 2021). These two ions are markers of amines, likely from industrial activities (Ge et al., 2011). However, this profile is LO-OOA-like since this OA factor accounts for most of the mass (Fig. S4a). This source, which presents a mix of primary and secondary species, was higher during the summer months due to the enhancement of the photo-oxidation of SOA precursors and presents a minimum during breeze-entrance hours (Fig S4e). However, it remains constant during morning as if the widening of the boundary layer was being counteracted by the enhancement of this source as a likely consequence of either the arrival of industrial plumes or the rate of SOA formation. The traffic source (16%, Fig S4d) showed the typical hydrocarbon-like OA features and is tightly linked to the BC_{lf} emissions (Fig. S4a). This source contribution is lower in summer months and its diel cycle is coherent with rush hours of the congested avenue near the site (Fig. S4e). Biomass burning is clearly identified by both the *m/z* markers and the BC_{sf} in the source profile (Fig. S4a), and it represented 13% of the modelled mass (Fig. S4d), with, as expected, significantly higher concentrations in cold periods and in evening hours (Fig. S4e). The cooking-like OA source (7%, Fig. S4e) is mixed with sulphate and BC_{lf}, indicating that this is not a pure cooking factor, but a mixture of multiple sources containing cooking marker ions, such as *m/z55* and *m/z41*, as already described in Via et al., (2021) (Fig. S4a). The diel cycle peaked right before cooking times in Barcelona and was essential to identify this factor (Fig. S4e). The large peaks for most sources in August (Fig. S4e) were attributed to the limited data availability in this month (four days) which lead to unrepresentative results relative to the other measurement periods. The data availability data can be seen in the second plot of Figure S1 in the SI of Via et al. (2021).

3.2. PMF applied to an equivalent pseudo-conventional data subset

The Approach 3 was based on the analysis of the hereinafter called pseudo-conventional data subset, consisting on those species which are used in offline SA (Amato et al., 2016; In't Veld et al., 2021): metals, SIA and the EC and OC (some studies use organic tracers as well, but these are not available for the current data subset). The aim of this SA is to provide a reference solution mimicking one without the high TR data to prove or discard the added value of the MTR-PMF. The data subset has been built with a 24-hours TR, averaging those species of originally higher TR. However, this approach does not result in very good results since its mass closure (Fig. S6c) shows an output underestimation of a 47%. This weak agreement closure could be related to the many gaps encountered in the OA and BC time series averaged to the LR timestamps.

The pseudo-conventional data subset SA provided 4 PM_1 sources: AN + biomass burning (36%), AS + heavy-oil combustion (28%), industry (28%) and road dust (8%) (Fig. S6d). The AN + biomass burning profile contains high proportion of NO_3^-, Cl^-, NH_4^+, and K as its main contributors, and represented approximately a 20% of the OA and BC mass (Fig. S6a). Its contribution was higher during cold months (Fig. S6b), being the August peak disregarded due to its low representativeness. The AS + heavy oil combustion is characterised by the V, Ni, Co, Mg elements and high SO_4^{2-} and NH_4^+ contributions, and it contains a small fraction of OA and EC (~15%) (Fig. S6a). It is higher during summer months as expected from SO_4^{2-} concentrations as seen in Figure S6b. The industry factor contains a ~ 30% of the organic mass, and several markers arising from industrial activities: Pb, As, Cd, Cr, Ni, etc (Fig. S6a). This factor does not present a substantial seasonal trend (Fig. S6b). The road traffic factor contains high concentrations of Mn, Cu, Zn, Sn, and Sb, all of them related to non-exhaust emissions; and substantial OA and EC, related to traffic-exhaust emissions (Fig. S6a). This factor presents a subtle seasonality, decreasing in the warm period due to the holiday-related traffic intensity drop and greater vertical mixing during daytime in those months (Fig S6b).

3.3. Base case for MTR-PMF

Approach 4 provided a SA of a regular PMF applied to the data subset built with all available species averaged to the lowest TR, i.e., 24-hours. No C weights ($C_{HR} = 1$, $C_{LR} = 1$) were applied during the model running. This solution will be used to evaluate the improvement resulting from the MTR-PMF application with optimised parameters. The mass closure plot (Fig. S7c) reports only a 9% underestimation of the input mass.

The SA resolved 6 PM_1 sources: Aged SOA + AS (31%), Fresh SOA + AN (26%), Heavy oil combustion (15%), Traffic (13%), Biomass Burning + Mineral (12%) and Road Dust + Industry (4%) (Fig. S7d). The number of factors is the same as that of HR data subset SA, even if the metal species were added. Nevertheless, some mixing in sources was acknowledged. For instance, the Fresh SOA + AN, which also included *m/z60, m/z73* and BC_{sf}, markers of biomass burning (Fig. S7a), even though both sources' time series are distinct enough (Fig. S7b). Another explanation for this mixing could be that the reported SOA is formed from biomass burning emissions.

3.4. MTR-PMF sensitivity to R_1 and C values

Approach 5 explores the optimal HR data subset TR and the uncertainty weights combination for the MTR-PMF analysis before proceeding with the final SA solution exploration. The number of factors of the solutions is not assessed in the parameter evaluation but in the solution

assessment (following section 3.5), which was not evaluated mathematically but with the aim to provide an environmentally interpretable sense. Hence, MTR-PMF was run for 6–8 factors for each combination of TR and (C_{HR}, C_{LR}). Although 13 C_{HR}, C_{LR} combinations were set when launching the model, not all of them produced reasonable results (or not for all resolutions) due to the model's inability to process those weighted matrices. This result was found for (C_{HR}, C_{LR}) = (1,100), (1000,1). Once this first broad scan of C values was done, another C-value analysis covering a narrower range was performed to find the most feasible combination.

3.4.1. Scaled residuals overlap

The first step in this analysis was to examine the scaled residuals of both data subsets when coupled into the MTR-PMF. Figure S8 shows the means and standard deviations of all C value combinations for HR and LR including all the TR runs. This plot assesses both the magnitude of the scaled residuals and their stability, which is severely compromised in the C combinations of (0.01,1), (0.001,1). These combinations enlarging the HR uncertainties result in a LR data subset scaled residuals increase. In terms of centrality, some C combinations present means systematically above zero, especially for the LR subset. Those C value combinations whose medians are less zero-displaced were the (1,1), (0.1,1), (0.01), (1,10), (1,1). However, some of their means were out of the range of the plots for the LR data subset, indicating the inclusion of significative outliers.

The calculation of the HR, LR histogram overlap is a powerful metric to assess the coupling of both subsets. The intersection between histograms from the standalone solutions for HR and LR (F*, eqs. (3), 4), is shown in Fig. 2. It shows an overlap of 43.4% for the 100 bins and in a range of scaled residuals of [-50,50]. Fig. 3 shows the histogram intersection of the HR and LR subsets in the resulting MTR-PMF for 100 bins and range of scaled residuals in the [-50,50] range, for all the R_1 and C combinations under study. This plot shows a maximum in the histogram intersection at 6 h C= (1, 10), but is inconsistent with similar Cs or resolutions. Therefore, it was considered as an outlier. There is a slight trend in which the higher TRs present higher histogram overlaps. Hence, R_1 = 30 min resolution will be that selected for further study. Amongst C values, the histogram overlap grows towards those combinations that reduced (increased) HR (LR) uncertainties, this is, those that make LR species weaker with respect to HR species in terms of signal-to-noise. Contrarily, the 24 h TR subset presents higher and decent histogram intersections for those C combinations which decrease the relevance of HR species. This behaviour can be described as follows: when the MTR-PMF is launched with very different number of timestamps and species, the metal species might be difficult to assimilate by the model and therefore they need to be downweighted respect to the HR ones. Nevertheless, when both subsets' TRs are more similar, the model allows

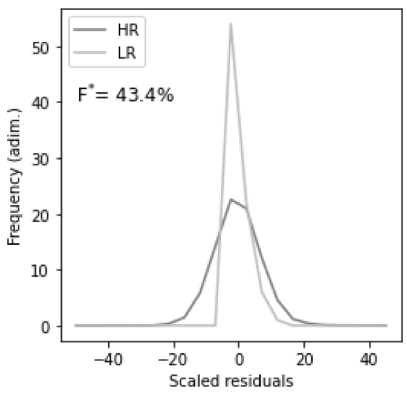

Fig. 2. Scaled residual normalized histogram intersection for the standalone HR and LR PMF results. The histogram overlap (F*) is shown in percentage in the upper left.

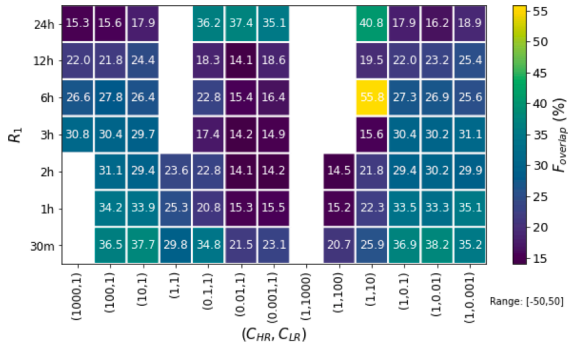

Fig. 3. Heatmap of scaled residual histogram overlap for HR, LR subsets for the range of data between (-50, 50) for each R_1, Cs combinations.

the LR class of species governate the PMF solution.

Fig. 4 shows the histogram intersection of all runs of R_1 = 30 min and for all the C-values and the mean and the standard deviation of all the repeats for each C combination. In Fig. 4a, the C-value combinations range is large and the (1,1), (1,0.1), (1,0.01), (1,0.001), (10,1) and (100,1) seem the best compromise between maximisation and stability. Taking the three highest values (all above the 30%, Fig. 4a), PMF has been re-run amongst these values and the analogous plot is shown in Fig. 4b. In this one, the highest overlap which also presents stability is the combination of (C_{HR}, C_{LR}) = (1,2). This set divides the LR uncertainties by 2. Nonetheless, even though these weightings are those which maximise the $F_{overlap}$, those runs of similar $F_{overlap}$ ($F_{overlap}$ > 30%) were also explored. The run that better explained the site pollution sources was that of (C_{HR}, C_{LR}) = (1,5) as justified in SI section E. Hence, weightings of (C_{HR}, C_{LR}) = (1,5) will be used in Approach 5.

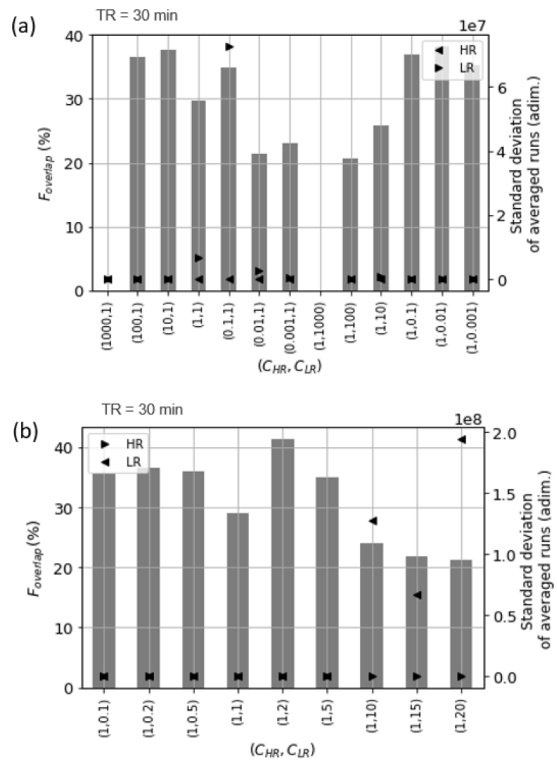

Fig. 4. Scaled residual histogram overlap, F*, for both subsets for the range of data of [-50,50] for each 30-minute C_{HR}, C_{LR}, combination (bars). Standard deviation (triangles) of residuals is shown for the standard C values exploration (top) and the narrower range exploration (bottom).

3.4.2. Q residuals

The normalised Q residuals, this is Q/Q_{exp}, were analysed R_1-wise. Each include all C value combinations. Fig. 5 shows that the 30 min Q/Q_{exp} median value is the only one above one (1.01), indicating hence that the overall fit is better than expected based on the uncertainty of the measurements. However, its values above median are small, indicating hence that there is not a systematic underestimation of the uncertainties. Contrarily, the fact that other R_1 results had medians below 1 indicate that the uncertainties were overestimated. Hence, this Q/Q_{exp} assessment supports the choice of 30 min as the best R_1 to which perform SA.

3.5. Multi-time resolution PMF source apportionment

The SA for the MTR subset, containing both HR and LR data in their original timestamps (30 min and 24 h every four days) and with uncertainty weights of $C_{HR} = 1$, $C_{LR} = 2$ (Approach 5) is shown in Figs. 6, 7. Solutions with ± 1 factor were also evaluated and disregarded due to less resolved or interpretable profiles (Fig. S9). Figs. 6 and 7 show the 8 PM_1 sources retrieved: AS + heavy oil combustion (25%), AN + ACl (17%), aged SOA (16%), traffic (14%), biomass burning (9%), fresh SOA (8%), COA (5%), and industry (4%) (Fig. 7d). The mass closure of the bulk PM_1 shows good agreement with a 12% of underestimation of the input measurements (Fig. 7c).

AS + heavy oil combustion. The AS + heavy oil combustion presents high concentrations of SO_4^{2-} and NH_4^+ (AS), and V, Ni, Co, corresponding to heavy oil combustion emissions from shipping activities (Fig. 7a) (Caumette et al., 2009; Corbin et al., 2018). More than a 50% and a 35% of the SO_4^{2-} and the NH_4^+, respectively, are attributed to this source (Fig. 6). A 24% of the mass of this factor is attributed to a MO-OOA factor (Fig. 7a). A combination of these sources was reported for the offline SA in Brines et al. (2019). This profile is consistent with the result obtained in Approach 1, where the MO-OOA + AS was also the highest contributor to the total mass. Heavy oil emissions intercepted are both locally emitted and long range transported from the shipping of the Mediterranean, carrying AS (a combination of direct SO_3 emissions (Agrawal et al., 2009) and oxidised SO_2 emissions) and aged SOA. This factor time series was enhanced in summer and its diel presents a growth around midday (especially in summer, Fig. 7e), both phenomena related to: i. the higher photochemical conversion rate of SO_2 into SO_4^{2-} in the summer season (Hidy, 1994); ii. stronger sea breeze development in warm months after noon carrying marine aerosol and aged recirculating pollutants; iii. greater photochemistry promotion at the months/hours of maximum insolation, promoting SO_2 and DMS oxidation into sulphates; iv. increase of the shipping activity in summer (Pérez et al., 2016); v. lower air mass renewal in summer (Gangoiti et al., 2001).

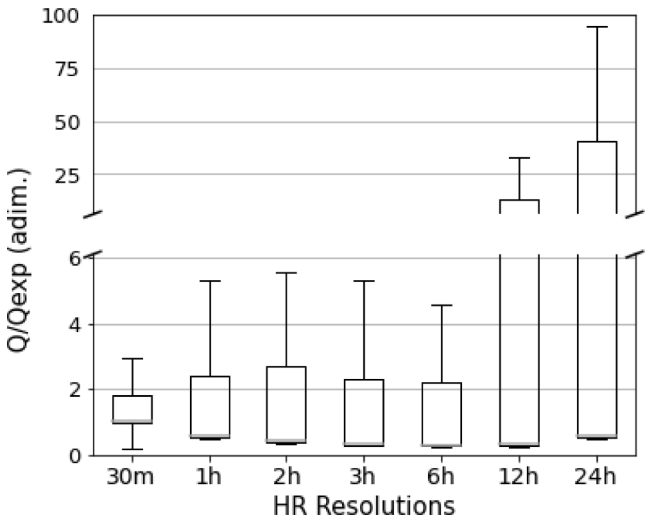

Fig. 5. Q/Q_{exp} values for all the MT-PMF experiments of different HR time resolutions. Boxes show the Q1–Q3 range, horizontal lines show the median (horizontal line), and whiskers extend up to the 1.5*IQR range (IQR = Q3-Q1).

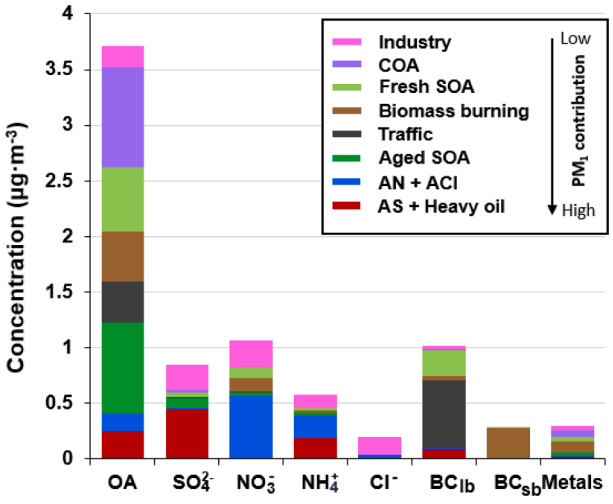

Fig. 6. Concentrations of OA (organic aerosol), SO_4^{2-}, NO_3^-, NH_4^+, Cl^-, BC_{lb}, BC_{sb} and metals in PM_1 source apportionment.

AN + ACl. The AN + ACl source contains more than a 50%, 40%, and 10% of the total apportioned mass of NO_3^-, NH_4^+, and Cl, respectively, as can be seen from the right-axis dots in Fig. 7a. The coupling of AN and ACl in the same source is likely due to their similar time variation, limited to NH_4^+ availability and with evaporation in high-temperature conditions, even if their origin is different (NO_3^- stemming mostly from traffic, Cl^- from industry or waste incineration). It apportions the majority of NO_3^- and around a third of the NH_4^+ (Fig. 6). The seasonality of this source is marked as seen in Fig. 7b, 7e, increasing in winter months because of the higher stability of the AN compound at low temperature (Harrison and Pio, 2017). This phenomenon is also observable in its diel pattern, with a decline from 11 AM to 8 PM in summer, the hours of maximum temperature, and hence, minimum stability of the AN (Fig. S7e). The maxima of the diel cycle around 8AM both in summer and winter is a result of the transformation of the NO_x emitted from traffic into HNO_3, and the availability of NH_4^+ from the traffic (Hopke and Querol, 2022).

Aged SOA. The Aged SOA factor is comprised by 82% MO-OOA, characterised by its high contribution of the *m/z44*, a product of OA oxidation (Fig. 7a). It is the second main contributor to OA after COA, representing a 23% of the total OA mass (Fig. 6). Aged aerosol has been reported to be the major constituent of OA in Via et al. (2021). However, this PMF results apportions some *m/z44* by other factors such as the AS + Heavy oil combustion or the biomass burning, hence a higher *m/z43-to-m/z44* ratio (0.39) with respect to the 0.21 in Via et al. (2021) is expected. Its monthly cycle peaks in the late summer months, due to the ageing of SOA after summer as in the aforementioned study (Fig. 7b, 7e). Its summer diel pattern (Fig. 7e) peaks at 4 AM due to nitrogen aqueous reactions conducing SOA oxidation enhancement and at 8AM due to the entrance of inland breeze carrying aged air masses, but in winter, this source grows at sea and land breeze onset hours, due to the recirculation of this aged aerosol.

Traffic. The traffic source consists of the HOA hydrocarbon pattern from vehicle exhaust and BC_{lf} concentrations (Fig. 7a). Its time series (Fig. 7b) exhibits a significant decline in summer as in Brines et al. (2019), both due to a decrease in traffic and higher atmospheric dispersion in these months. There is also a huge peak in November (Fig. 7e) due to sustained stagnation episodes and a higher traffic intensity in this month (see Figs. S6, S9 in Via et al. (2021)). Also, huge peaks appear in the time series of this factor and others (biomass burning, fresh SOA, COA), backing the explanation of stagnant conditions, which might consequently increase significantly the monthly

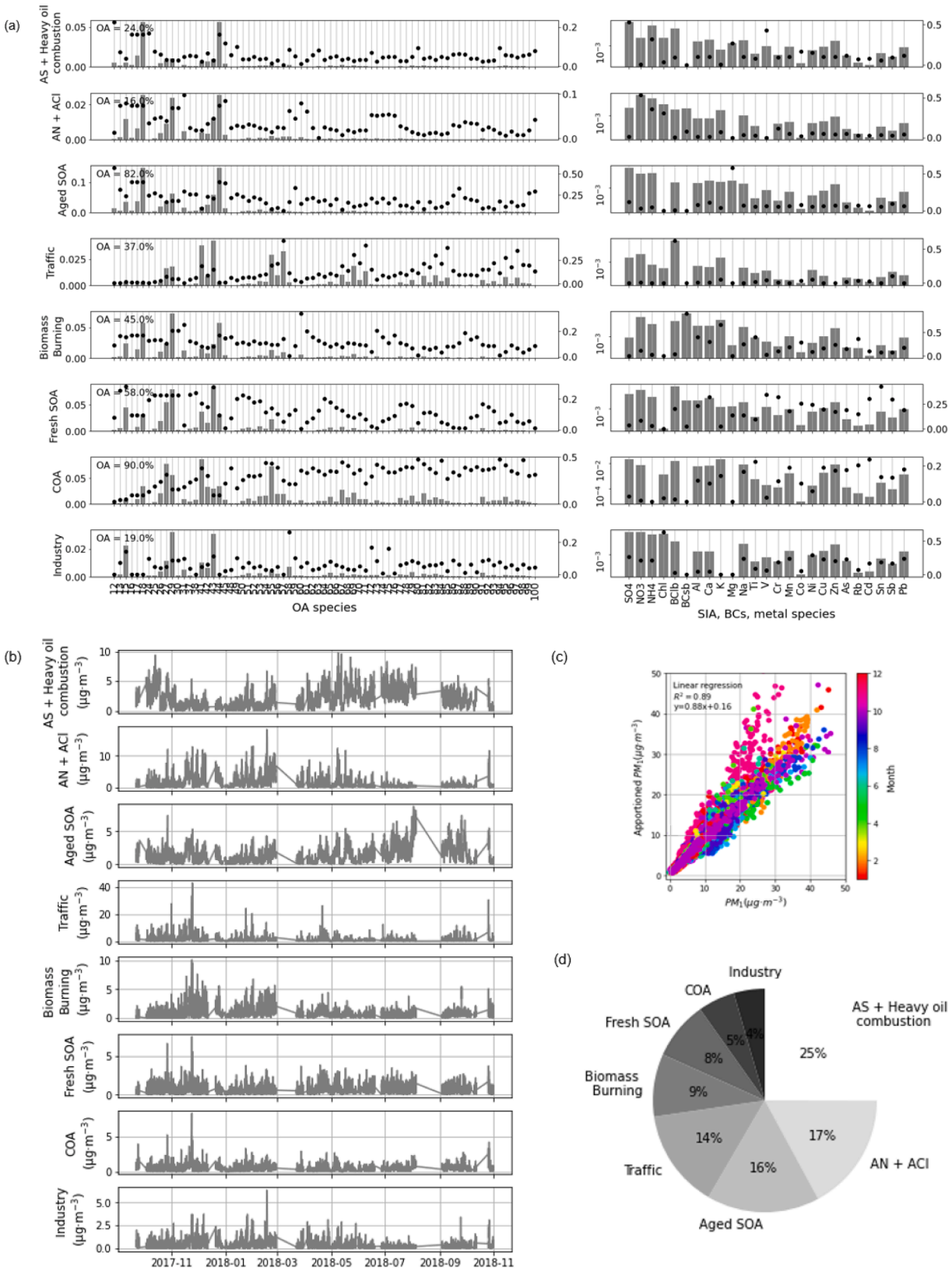

Fig. 7. Source apportionment of the multi-time resolution optimised PMF. (a) Profiles. (b) Time series (c) Mass closure (d) Pie of apportionment (e) Monthly and diel cycles. For the profiles plot (a), bars (left axis) show the normalised concentrations of each species in each factor, circles (right axis) show the percentage of each species attributed to each factor, and percentages show the proportion of OA to the total mass of that factor. Also, the left panel is dedicated to the unit-mass-resolution OA species and the right one (in log scale) to the rest of the species. The mass closure scatter plot (c) depicts the relationship between the apportioned PM_1 mass as a sum of all factors' concentrations vs. the input PM_1 mass coloured by months. Note that in (e) y-axis for the monthly means does not start at zero for more clarity in the values variation.

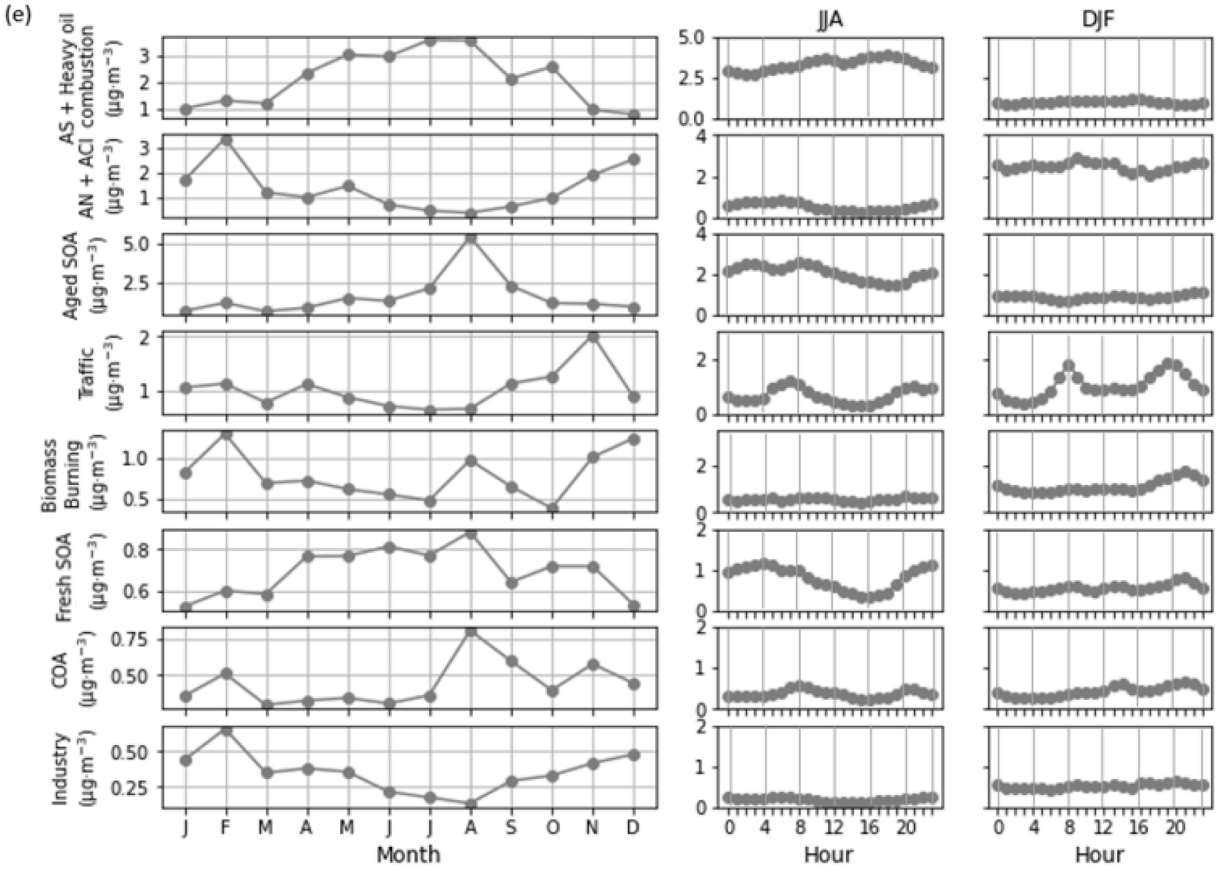

Fig. 7. (*continued*).

average. This source represents the main contribution to the total BC_{lf} (Fig. 6). However, a larger fraction of this source would be expected in the first months of the year, similarly to November and December (Fig. 7e). The proportion of traffic emissions in this study (14%, Fig. 7d) is similar to that reported by Brines et al. (2019) (14%) and slightly lower than in Amato et al. (2016); In't Veld et al. (2021) (20% and 32%, respectively, in $PM_{2.5}$). The traffic diel cycle presents two peaks, more marked in winter, around 7–8 AM and 6–8 PM (Fig. 7e), coinciding with the hours of higher traffic intensity near the site as seen in Figure S9 of Via et al. (2021).

Biomass burning. The biomass burning profile (Fig. 7a) has a high concentrations of *m/z60* and *m/z73*, organic markers of cellulose combustion (Alfarra et al., 2007; Hu et al., 2013), a high proportion of BC_{sf}, and K, a biomass burning metal tracer (Gilardoni et al., 2009; Zhao et al., 2020). This source apportions most of the BC_{sf} and a significant proportion of the NO_3^- and NH_4^+ species (Fig. 6), since AN concentrations are especially high during winter stagnation conditions coincidingly with biomass burning high levels (Reche et al., 2012), hence PMF resolves them slightly mixed. Anyhow, presence of nitrate in this source is expected as organonitrates have been reported to be related to biomass burning (Schurman et al., 2015; Yazdani et al., 2021). Its apportionment of a ~ 15% of *m/z44*, substantially higher than that from *m/z43* entails that this source is rather oxidised. Its relative contribution is similar to those from previous studies (a 14% in Brines et al. (2019), Fig. 7d). The time series of this factor is significantly higher in winter months (Fig. 7e). In the same figure, the winter diel cycle can be observed to present its maximum at evenings, suggesting this source is increased when: i. land breeze returning inland pollutants that originate from agricultural areas and rural areas burning wood for heating; ii. pollutant advection from residential heating reaching the site. The summer diel cycle is very flat due to the low concentrations.

Fresh SOA. The fresh SOA factor is composed of LO-OOA in a 58% (Fig. 7d) and apportioning a 16% of the total OA mass (Fig. 6), containing its typical pattern of C_xH_yO hydrocarbons (Fig. 7a). Its *m/z43*-to-*m/z44* ratio is 2.75, substantially higher than that found for the same period in Via et al., (2021), 1.05, since the majority of *m/z44* has been attributed to other sources as aforementioned. For the purpose of SOA description, a more differentiated OOA aerosol in terms of oxidation state (as found here with respect to the aforementioned study) can further reveal the origins of each of them due to the increased disentanglement. This difference is a consequence of the apportionment of more *m/z44* by other sources (BBOA, AS + heavy oil combustion, AN + AC), which makes sense since these sources can also be aged and share certain cyclicity related to recirculation of pollutants. This factor also apportions certain mass to BC_{lb} (around a 17%, Fig. 6) a 10% of the apportioned NO_3^- and some road dust markers (Sn, Sb, Cu, Fig. 7a). The contributions imply that this SOA formation could have been promoted by traffic emissions. It also contains other metals likely linked to industry (Cd, Ni, Cr), due to a certain entanglement with this factor. The monthly cycle showed a growth towards warm months (even disregarding August) as a consequence of a higher SOA formation due to a higher photochemical activity. In winter, the diel pattern is relatively constant and it presents slight peaks during the traffic hours. Conversely, the summer diel is minimal during the midday hours due to the higher photo-oxidation of this pollutant (and conversion into a more oxidised aerosol), the widening of the mixing layer, and the evaporation of AN due to the higher temperatures during the day.

COA. The COA factor is composed a 90% of a COA profile, containing the main cooking marker ions such as *m/z55, m/z41, m/z69, m/z29,* amongst others (Fig. 7a), and accounting for around a 24% of the total OA (Fig. 6). Although this factor is almost purely OA, it also contains certain markers in a low proportion of mineral dust and industry markers (Ti, Mn, Rb, Cd, Pb, Fig. 7a), containing around a 25% of the total metals concentrations (Fig. 6). A possible reason for this factor

including industrial, road dust, and mineral markers is that this source does not only consist of cooking emissions but on an urban ensemble of pollutants being locally recirculated. This factor does not contain a clear seasonality, but its diel cycle presents consistent peaks around 8AM, 13 and 20 PM, typical cooking times in Barcelona (Fig. 7b, 7e). This lunch peak is more evident in summer since in winter this factor is likely entangled with the traffic factor given that it peaks during the traffic rush hours (7–8 AM), which makes the noon peak less obvious. This factor accounts for a 5% of the total mass of PM_1 (Fig. 7d).

Industry. The industrial factor contributes to 4% of the total mass (Fig. 7d) and accounts for 80% of the total Cl^- mass (Fig. 7a). The apportionment of Cl^- in industrial source has been found in other industrial profiles (Brines et al., 2019; Vossler et al., 2016). Only 19% of its mass is attributed to OA (Fig. 7a), whose pattern contains mainly *m/z58*, and *m/z86*, reported industrial markers (Ge et al., 2011). These ions, related to amines, can originate from waste incineration (Leach et al., 1999), which is probably partially responsible for Cl^- emissions and was reported T the site in Brines et al. (2019). Moreover, amine production from marine emissions is not discarded. This source also incorporates high concentrations of Na, Mn, Cu, Zn, Ni, As, Pb, related to metallurgic industrial activities (Querol et al., 2007). This is coherent with previous studies reported industrial sources at this site, being characterised by the same fine inorganic species (Amato et al., 2016; Brines et al., 2019; In't Veld et al., 2021). Also, the high Cl^- and Na concentrations are not expected to be mainly from marine emissions since sea salt in the fine fraction is rather low in Barcelona, the wind rose does not point to the location of the sea (Fig. S10), and the variation of the concentrations shows no relation with the coarse fraction (Fig S11). This factor presents a descent in the warm months, probably due to an enhanced boundary layer height in the warmer periods (Fig. 7e). The diel cycle is generally flat and in summer months, a decrease can be observed as a consequence of the boundary layer widening (Fig. 7e).

3.6. PMF approaches comparison

To assess the added value of the MTR-PMF technique, its results were compared to other SA methodologies solutions. SA was also performed on the HR data subset (Approach 1), the LR data subset with only the offline species (Approach 2), a pseudo-conventional data subset (Approach 3), and an unweighted low TR base case (Approach 4) (Fig. 8). The SA of Approach 2 and Approach 3 retrieved only 4 sources, although with different fingerprints. This difference was driven by the included species. The source resolution performed by PMF can be substantially different and of more or less environmental feasibility. While the offline LR data subset SA led to the identification of road dust, it was unable to identify a road traffic source corresponding to exhaust emissions, as the data subset lacks the tracer species for that. For the pseudo-conventional data subset SA, the identified sources were mixed in some cases, which is a known limitation of this type of datasets. The clearest example is the source that included biomass burning and AN together, which are two separated factors in Approach 5 (although crossed influence is still noticeable). Additionally, it distributed quite equally the OA and EC in all factors. None of these SA results was able to identify a COA factor due to the lack of COA tracers or diel cycle, as Approach 2 only considers metal species, and Approach 3 includes OA a bulk single species and both present low TR. The base case (Approach 4) comprised all OA *m/z*s, SIA species, differentiated BC species, all averaged to the LR TR, and metals, naturally at this TR. Even though it merges different instrumentation data, no uncertainty weightings were applied, as we want to use these results to assess the final MTR result, which includes the uncertainty weightings as one of its improvements. The base case SA resulted in 6 sources, as it includes information from a wider range of species. Aged SOA + AS was differentiated from Aged SOA + heavy oil, as opposed to the results from the HR SA, which was unable to separate them. However, the AN source and fresh SOA were not separated in this approach and neither were the COA and HOA factors, the latters being clearly separated in the HR SA.

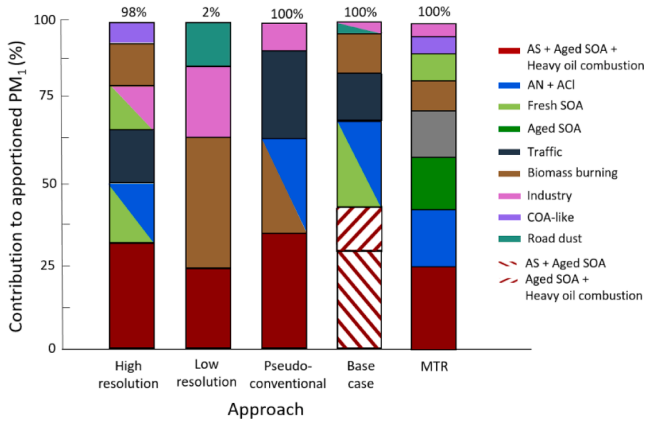

Fig. 8. Summary of source apportionment results of all input PMF datasets. Percentages at the top of each bar represent the fraction of the PM1 mass that each data subset contains depending on the species it contains. In the base case the split of factors is represented as wefted bars.

The capacity of the MTR-PMF SA for identifying and quantifying sources has been found superior to that of any of the other assessed approaches. Hence, it managed to retrieve 8 different sources, which is four more than the LR dataset or the pseudo-conventional data subset, and two more if compared to the HR data subset or the base case. The MTR-PMF merges two major advantages that cannot be applied together otherwise: a) the use of a high number of species analysed by different techniques and/or collected from the atmosphere by different methods and b) the use of the best available TR for a given species. Note that the TR can be determined by the analytical technique or by the sample collection technique; i.e. filter samples could be collected every 12 h and the dataset time resolution would be improved while applying the same analytical techniques, provided the concentrations were high enough to remain above detection limits. Thus, advantage a) would lead us from solution of Approach 1, of Approach 2 or of Approach 3 to the solution of the base case (Approach 4). Advantage b) applied independently would just give us the solution in Approach 1, where we can use the original time resolution without any restriction. The application of MTR-PMF allows the merging of both advantages and leads us from solution of base case (Approach 4) to the MTR-PMF solution.

The intra-day patterns, stemming from the use of HR TR measurements, provided significant insights into the behaviour of the sources and even enabled the identification of some sources such as COA. The comparison with the HR solution highlights the beneficial capacity of the MTR-PMF to identify more sources due to the inclusion of the metals, which are markers for some sources (heavy oil combustion, industry, biomass burning). Another advantage is the capability to match both HR and LR markers of a source resulting in a more comprehensive source description (e.g. BBOA coupled with BC_{sb}, K; OA with amine markers, likely from industrial emissions, coupled with industry markers; road traffic OA coupled with Sb). This coupling also made infer that the origin of fresh SOA could be related to traffic emissions. In addition, the MTR-PMF technique also provided separated sources for factors that had been mixed to others in the previous Approaches, isolating for example the AN from the fresh SOA. Besides, The MTR-PMF is capable to provide profiles containing mostly one kind of data and giving little mass to the rest (e.g. COA mainly containing OA; or AN + ACl and industry containing mainly non-OA measurements (<20% of OA).

4. Conclusions

A comprehensive source apportionment (SA) of the submicron particulate matter (PM_1) has been performed coupling Quadrupole Aerosol Chemical Speciation Monitor (Q-ACSM), aethalometer (AE33) and

quartz-fibre filter measurements. The species used in this SA consisted on the organic mass spectra, SO_4^{2-}, NO_3^-, NH_4^+, and Cl^- from Q-ACSM at a 30 min time resolution (TR); black carbon (BC) speciated into BC liquid fuel (BC_{lf}) and BC solid fuel (BC_{sf}) from aethalometer at 30 min TR; and metal species (Ca, Al, K, Mg, Na, Ti, V, Cr, Mn, Co, Ni, Cu, Zn, As, Sn, Sb, Pb) from offline samples at a TR of 24 h every 4th day. The use of the Positive Matrix Factorisation (PMF) model for the ensemble of the so-called high-resolution data subset (HR, 30-minutes TR) and the low-resolution data subset (LR, 24 h every 4th day TR) taken together implied the use of the multi-time resolution (MTR) PMF.

The main outcomes from this work are:

- The extended practice of averaging the high TR data subsets to reduce the TR difference with the lower TR data subsets or even to match it has been proven disadvantageous for model performance and error minimisation as also reported by Kuo et al. (2014) and Liao et al. (2013). High TRs do not represent noise to PMF since stable, robust sources are retrieved profiting the 30 min TR for disentangling sources. For instance, the COA, which was only resolved by using high TR data since its diel cycle is vital for its differentiation.
- The use of a greater number of species has enabled the characterisation of specific sources traced by key species not present in all datasets. This is the case, for instance, of the inclusion of industrial markers, which have enabled the characterisation of the industry source, whose description with only OA, SIA and BC species would have been less conclusive.
- The MTR-PMF provided an environmentally reasonable PM_1 SA with more speciated and detailed sources with respect to the other approaches and previous studies in the area using simpler SA methodologies, even if they contain longer time series or if they contain a greater number of species.
- Coherent matches of OA fingerprints and SIA, BC, and metal species were found in the MTR-PMF solution. e.g. BBOA with BC_{sb}, K; HOA with BC_{lf}, Sb; LO-OOA with AN; industry metal markers with Cl, *m/z58*, *m/z86*, etc.
- The $F_{overlap}$ method for weighting uncertainties proposed by Tong et al. (2022) does not necessarily lead to the most environmentally reasonable solution. The investigation of other runs whose $F_{overlap}$ is similar to $F^*_{overlap}$ is advisable to obtain the best SA.

To the authors' knowledge, this is the first study that applies MTR-PMF aiming to provide an exhaustive PM_1 SA assessing both the uncertainty weighting and TR SA impacts. Further research should aim to standardise these assessments to be able to include all kinds of instrument measurements to retrieve more powerful SA results aimed for both modelling and health research and mitigation policy enforcements.

Code availability

The codes used for the data analysis can be obtained upon request to the corresponding author.

Data availability

The subsets can be found in https://doi.org/10.17632/xfv7z6jzcm.1 and https://doi.org/10.17632/skp8szjhc3.1.

5. Financial support

The present work was supported by European Union's Horizon 2020 research and innovation programme under grant agreement 101,036,245 (RI-URBANS); the "Agencia Estatal de Investigación" from the Spanish Ministry of Science, Innovation and Universities, and FEDER funds under the projects CAIAC (PID2019-108990RB-I00) and HOUSE (CGL2016-78594-R); and the Generalitat de Catalunya (AGAUR 2017 SGR41) and the Direcció General de Territori.

CRediT authorship contribution statement

Marta Via: Conceptualization, Methodology, Validation, Formal analysis, Investigation, Resources, Data curation, Writing – original draft, Writing – review & editing, Visualization. **Jesús Yus-Díez:** Software, Resources, Investigation, Data curation, Writing – review & editing. **Francesco Canonaco:** Conceptualization, Methodology, Validation, Investigation, Writing – review & editing. **Jean-Eudes Petit:** Conceptualization, Writing – review & editing. **Philip Hopke:** Methodology, Validation, Writing – review & editing. **Cristina Reche:** Resources, Data curation, Writing – review & editing. **Marco Pandolfi:** Software, Resources, Investigation, Data curation, Writing – review & editing. **Matic Ivančič:** Resources, Writing – review & editing. **Martin Rigler:** Resources, Writing – review & editing. **André S.H. Prevôt:** Writing – review & editing. **Xavier Querol:** Conceptualization, Writing – review & editing, Supervision, Project administration, Funding acquisition. **Andrés Alastuey:** Conceptualization, Methodology, Validation, Resources, Writing – review & editing, Supervision, Project administration, Funding acquisition. **María Cruz Minguillón:** Conceptualization, Methodology, Validation, Formal analysis, Data curation, Resources, Writing – review & editing, Supervision, Project administration, Funding acquisition.

Declaration of Competing Interest

The authors declare that they have no known competing financial interests or personal relationships that could have appeared to influence the work reported in this paper.

Data availability

Data will be made available on request.

Acknowledgements

We acknowledge support of the COST Action CA16109 COLOSSAL. IDAEA-CSIC is a Centre of Excellence Severo Ochoa (Spanish Ministry of Science and Innovation, grant no. CEX2018-000794-S). We would like to thank Aerosol d.o.o. for lending the AE33 aethalometer.

Appendix A. Supplementary material

Supplementary data to this article can be found online at https://doi.org/10.1016/j.envint.2023.108006.

References

Agrawal, H., Eden, R., Zhang, X., Fine, P.M., Katzenstein, A., Miller, J.W., Ospital, J., Teffera, S., Cocker, D.R., 2009. Primary particulate matter from ocean-going engines in the Southern California Air Basin. Environ. Sci. Technol. 43 (14), 5398–5402. https://doi.org/10.1021/es8035016.

Alfarra, M.R., Prevot, A.S.H., Szidat, S., Sandradewi, J., Weimer, S., Lanz, V.A., Schreiber, D., Mohr, M., Baltensperger, U., 2007. Identification of the mass spectral signature of organic aerosols from wood burning emissions. Environ. Sci. Technol. 41 (16), 5770–5777. https://doi.org/10.1021/es062289b.

Allan, J.D., Delia, A.E., Coe, H., Bower, K.N., Alfarra, M.R., Jimenez, J.L., Middlebrook, A.M., Drewnick, F., Onasch, T.B., Canagaratna, M.R., Jayne, J.T., Worsnop, D.R., 2004. A generalised method for the extraction of chemically resolved mass spectra from Aerodyne aerosol mass spectrometer data. J. Aerosol Sci. 35 (7), 909–922. https://doi.org/10.1016/j.jaerosci.2004.02.007.

Amato, F., Alastuey, A., Karanasiou, A., Lucarelli, F., Nava, S., Calzolai, G., Severi, M., Becagli, S., Gianelle, V.L., Colombi, C., Alves, C., Custódio, D., Nunes, T., Cerqueira, M., Pio, C., Eleftheriadis, K., Diapouli, E., Reche, C., Minguillón, M.C., Manousakas, M.I., Maggos, T., Vratolis, S., Harrison, R.M., Querol, X., 2016. AIRUSE-LIFE+: a harmonized PM speciation and source apportionment in five southern European cities. Atmos. Chem. Phys. 16 (5), 3289–3309. https://doi.org/10.5194/acp-16-3289-2016.

Belis, C.A., Pikridas, M., Lucarelli, F., Petralia, E., Cavalli, F., Calzolai, G., Berico, M., Sciare, J., 2019. Source apportionment of fine PM by combining high time resolution organic and inorganic chemical composition datasets. Atmos. Environ. X 3, 100046. https://doi.org/10.1016/j.aeaoa.2019.100046.

Brines, M., Dall'Osto, M., Amato, F., Minguillón, M.C., Karanasiou, A., Grimalt, J.O., Alastuey, A., Querol, X., van Drooge, B.L., 2019. L.: Source apportionment of urban PM1 in Barcelona during SAPUSS using organic and inorganic components. Environ.

Sci. Pollut. Res. 26 (31), 32114–32127. https://doi.org/10.1007/s11356-019-06199-3.
Canonaco, F., Tobler, A., Chen, G., Sosedova, Y., Slowik, J.G., Bozzetti, C., Daellenbach, K.R., El Haddad, I., Crippa, M., Huang, R.-J., Furger, M., Baltensperger, U., Prévôt, A.S.H., 2021. A new method for long-term source apportionment with time-dependent factor profiles and uncertainty assessment using SoFi Pro: application to 1 year of organic aerosol data. Atmos. Meas. Tech. 14 (2), 923–943. https://doi.org/10.5194/amt-14-923-2021.
Caumette, G., Lienemann, C.P., Merdrignac, I., Bouyssiere, B., Lobinski, R., 2009. Element speciation analysis of petroleum and related materials. J. Anal. At. Spectrom. 24 (3), 263–276. https://doi.org/10.1039/b817888g.
Cavalli, F., Viana, M., Yttri, K.E., Putaud, J.P., Genberg, J., Putaud, J.-P., 2010. Toward a standardized thermal-optical protocol for measuring atmospheric organic and elemental carbon: the eusaar protocol, ACS, Div. Environ. Chem. - Prepr. Ext. Abstr. 48 (1), 443–446. https://doi.org/10.5194/amtd-2-2321-2009.
Corbin, J.C., Mensah, A.A., Pieber, S.M., Orasche, J., Michalke, B., Zanatta, M., Czech, H., Massabò, D., Buatier De Mongeot, F., Mennucci, C., El Haddad, I., Kumar, N.K., Stengel, B., Huang, Y., Zimmermann, R., Prévôt, A.S.H., Gysel, M., 2018. Trace metals in soot and PM2.5 from heavy-fuel-oil combustion in a marine engine. Environ. Sci. Technol. 52 (11), 6714–6722. https://doi.org/10.1021/acs.est.8b01764.
Crenn, V., Sciare, J., Croteau, P.L., Verlhac, S., Fröhlich, R., Belis, C.A., Aas, W., Äijälä, M., Alastuey, A., Artiñano, B., Baisnée, D., Bonnaire, N., Bressi, M., Canagaratna, M., Canonaco, F., Carbone, C., Cavalli, F., Coz, E., Cubison, M.J., Esser-Gietl, J.K., Green, D.C., Gros, V., Heikkinen, L., Herrmann, H., Lunder, C., Minguillón, M.C., Močnik, G., O'Dowd, C.D., Ovadnevaite, J., Petit, J.E., Petralia, E., Poulain, L., Priestman, M., Riffault, V., Ripoll, A., Sarda-Estève, R., Slowik, J.G., Setyan, A., Wiedensohler, A., Baltensperger, U., Prévôt, A.S.H., Jayne, J.T., Favez, O., 2015. ACTRIS ACSM intercomparison - Part 1: reproducibility of concentration and fragment results from 13 individual Quadrupole Aerosol Chemical Speciation Monitors (Q-ACSM) and consistency with co-located instruments. Atmos. Meas. Tech. 8 (12), 5063–5087. https://doi.org/10.5194/amt-8-5063-2015.
Crespi, A., Bernardoni, V., Calzolai, G., Lucarelli, F., Nava, S., Valli, G., Vecchi, R., 2016. Implementing constrained multi-time approach with bootstrap analysis in ME-2: an application to PM2.5 data from Florence (Italy). Sci. Total Environ. 541, 502–511. https://doi.org/10.1016/j.scitotenv.2015.08.159.
Crippa, M., Canonaco, F., Slowik, J.G., El Haddad, I., Decarlo, P.F., Mohr, C., Heringa, M. F., Chirico, R., Marchand, N., Temime-Roussel, B., Abidi, E., Poulain, L., Wiedensohler, A., Baltensperger, U., Prévôt, A.S.H., 2013. Primary and secondary organic aerosol origin by combined gas-particle phase source apportionment. Atmos. Chem. Phys. 13 (16), 8411–8426. https://doi.org/10.5194/acp-13-8411-2013.
Drinovec, L., Močnik, G., Zotter, P., Prévôt, A.S.H., Ruckstuhl, C., Coz, E., Rupakheti, M., Sciare, J., Müller, T., Wiedensohler, A., Hansen, A.D.A., 2015. The "dual-spot" Aethalometer: an improved measurement of aerosol black carbon with real-time loading compensation. Atmos. Meas. Tech. 8 (5), 1965–1979. https://doi.org/10.5194/amt-8-1965-2015.
Escrig Vidal, A., Monfort, E., Celades, I., Querol, X., Amato, F., Minguillón, M.C., Hopke, P.K., 2009. Application of optimally scaled target factor analysis for assessing source contribution of ambient PM10. J. Air Waste Manag. Assoc. 59 (11), 1296–1307. https://doi.org/10.3155/1047-3289.59.11.1296.
Forello, A.C., Bernardoni, V., Calzolai, G., Lucarelli, F., Massabò, D., Nava, S., Pileci, R.E., Prati, P., Valentini, S., Valli, G., Vecchi, R., 2019. Exploiting multi-wavelength aerosol absorption coefficients in a multi-time source apportionment study to retrieve source-dependent absorption parameters. Atmos. Chem. Phys. Discuss. 1–26 https://doi.org/10.5194/acp-2019-123.
Gangoiti, G., Millán, M.M., Salvador, R., Mantilla, E., 2001. Long-range transport and re-circulation of pollutants in the western Mediterranean during the project Regional Cycles of Air Pollution in the West-Central Mediterranean Area. Atmos. Environ. 35 (36), 6267–6276. https://doi.org/10.1016/S1352-2310(01)00440-X.
Ge, X., Wexler, A.S., Clegg, S.L., 2011. Atmospheric amines – Part I. a review. Atmospheric Environ. 45 (3), 524–546. https://doi.org/10.1016/j.atmosenv.2010.10.012.
Gilardoni, S., Liu, S., Takahama, S., Russell, L.M., Allan, J.D., Steinbrecher, R., Jimenez, J.L., De Carlo, P.F., Dunlea, E.J., Baumgardner, D., 2009. Characterization of organic ambient aerosol during MIRAGE 2006 on three platforms. Atmos. Chem. Phys. 9 (15), 5417–5432. https://doi.org/10.5194/acp-9-5417-2009.
Harrison, R. M. and Pio, C. A.: Tellus B : Chemical and Physical Meteorology An investigation of the atmospheric HNO 3 -NH 3 - NH 4 NO 3 equilibrium relationship in a cool , humid climate An investigation of the atmospheric equilibrium relationship in a cool , humid climate, , 0889(3), doi:10.3402/tellusb.v35i2.14795, 2017.
Henry, R.C., Lewis, C.W., Hopke, P.K., Williamson, H.J., 1984. Review of receptor model fundamentals. Atmos. Environ. 18 (8), 1507–1515. https://doi.org/10.1016/0004-6981(84)90375-5.
Hidy: Atmospheric sulfur and nitrogen oxides: Eastern north American source-receptor relationships., 1994.
Hopke, P.K., Querol, X., 2022. Is improved vehicular NOx control leading to increased urban NH3Emissions? Environ. Sci. Technol. 56 (17), 11926–11927. https://doi.org/10.1021/acs.est.2c04996.
Hopke, P.K., Dai, Q., Li, L., Feng, Y., 2020. Global review of recent source apportionments for airborne particulate matter. Sci. Total Environ. 740, 140091 https://doi.org/10.1016/j.scitotenv.2020.140091.
Hu, W.W., Hu, M., Yuan, B., Jimenez, J.L., Tang, Q., Peng, J.F., Hu, W., Shao, M., Wang, M., Zeng, L.M., Wu, Y.S., Gong, Z.H., Huang, X.F., He, L.Y., 2013. Insights on organic aerosol aging and the influence of coal combustion at a regional receptor site of central eastern China. Atmos. Chem. Phys. 13 (19), 10095–10112. https://doi.org/10.5194/acp-13-10095-2013.
P.L., K.: Interactions of Climate Change, Air Pollution, and Human Health, Curr. Environ. Heal. reports, 5(1), 179–186 [online] Available from: http://www.embase.com/search/results?subaction=viewrecord&from=export&id=L625310095%0Ahttps://doi.org/10.1007/s40572-018-0188-x, 2018.
Kuo, C.P., Liao, H.T., Chou, C.C.K., Wu, C.F., 2014. Source apportionment of particulate matter and selected volatile organic compounds with multiple time resolution data. Sci. Total Environ. 472, 880–887. https://doi.org/10.1016/j.scitotenv.2013.11.114.
Leach, J., Blanch, A., Bianchi, A.C., 1999. Volatile organic compounds in an urban airborne environment adjacent to a municipal incinerator, waste collection centre and sewage treatment plant. Atmos. Environ. 33 (26), 4309–4325. https://doi.org/10.1016/S1352-2310(99)00115-6.
Liao, H.T., Kuo, C.P., Hopke, P.K., Wu, C.F., 2013. Evaluation of a modified receptor model for solving multiple time resolution equations: a simulation study. Aerosol Air Qual. Res. 13 (4), 1253–1262. https://doi.org/10.4209/aaqr.2012.11.0322.
Middlebrook, A.M., Bahreini, R., Jimenez, J.L., Canagaratna, M.R., 2012. Evaluation of composition-dependent collection efficiencies for the Aerodyne aerosol mass spectrometer using field data. Aerosol Sci. Technol. 46 (3), 258–271. https://doi.org/10.1080/02786826.2011.620041.
Minguillón, M.C., Schembari, A., Triguero-Mas, M., de Nazelle, A., Dadvand, P., Figueras, F., Salvado, J.A., Grimalt, J.O., Nieuwenhuijsen, M., Querol, X., 2012. Source apportionment of indoor, outdoor and personal PM2.5 exposure of pregnant women in Barcelona, Spain. Atmospheric Environ. 59, 426–436. https://doi.org/10.1016/j.atmosenv.2012.04.052.
Minguillón, M.C., Pérez, N., Marchand, N., Bertrand, A., Temime-Roussel, B., Agrios, K., Szidat, S., van Drooge, B., Sylvestre, A., Alastuey, A., Reche, C., Ripoll, A., Marco, E., Grimalt, J.O., Querol, X., 2016. Secondary organic aerosol origin in an urban environment: influence of biogenic and fuel combustion precursors. Faraday Discuss 189, 337–359. https://doi.org/10.1039/c5fd00182j.
Mohr, C., DeCarlo, P.F., Heringa, M.F., Chirico, R., Slowik, J.G., Richter, R., Reche, C., Alastuey, A., Querol, X., Seco, R., Peñuelas, J., Jiménez, J.L., Crippa, M., Zimmermann, R., Baltensperger, U., Prévôt, A.S.H., 2012. Identification and quantification of organic aerosol from cooking and other sources in Barcelona using aerosol mass spectrometer data. Atmos. Chem. Phys. 12 (4), 1649–1665. https://doi.org/10.5194/acp-12-1649-2012.
Ng, N.L., Herndon, S.C., Trimborn, A., Canagaratna, M.R., Croteau, P.L., Onasch, T.B., Sueper, D., Worsnop, D.R., Zhang, Q., Sun, Y.L., Jayne, J.T., 2011. An Aerosol chemical speciation monitor (ACSM) for routine monitoring of the composition and mass concentrations of ambient aerosol. Aerosol Sci. Technol. 45 (7), 770–784. https://doi.org/10.1080/02786826.2011.560211.
Ogulei, D., Hopke, P.K., Zhou, L., Paatero, P., Park, S.S., Ondov, J.M., 2005. Receptor modeling for multiple time resolved species: the Baltimore supersite. Atmos. Environ. 39 (20), 3751–3762. https://doi.org/10.1016/j.atmosenv.2005.03.012.
Paatero, P., 1999. The multilinear engine—a table-driven, least squares program for solving multilinear problems, including the n-way parallel factor analysis model. J. Comput. Graph. Stat. 8 (4), 854–888.
Paatero, P., Tapper, U., 1994. Positive matrix factorization: a non-negative factor model with optimal utilization of error estimates of data values. Environmetrics 5 (2), 111–126. https://doi.org/10.1002/env.3170050203.
Passig, J., Schade, J., Irsig, R., Li, L., Li, X., Zhou, Z., Adam, T., Zimmermann, R., 2021. Detection of ship plumes from residual fuel operation in emission control areas using single-particle mass spectrometry. Atmos. Meas. Tech. 14 (6), 4171–4185. https://doi.org/10.5194/amt-14-4171-2021.
Pérez, N., Pey, J., Querol, X., Alastuey, A., López, J.M., Viana, M., 2008. Partitioning of major and trace components in PM10–PM2.5–PM1 at an urban site in Southern Europe. Atmospheric Environ. 42 (8), 1677–1691. https://doi.org/10.1016/j.atmosenv.2007.11.034.
Pérez, N., Pey, J., Reche, C., Cortés, J., Alastuey, A., Querol, X., 2016. Impact of harbour emissions on ambient PM10 and PM2.5 in Barcelona (Spain): Evidences of secondary aerosol formation within the urban area. Sci. Total Environ. 571, 237–250. https://doi.org/10.1016/j.scitotenv.2016.07.025.
Pey, J., Pérez, N., Querol, X., Alastuey, A., Cusack, M., Reche, C., 2010. Intense winter atmospheric pollution episodes affecting the Western Mediterranean. Sci. Total Environ. 408 (8), 1951–1959. https://doi.org/10.1016/j.scitotenv.2010.01.052.
Querol, X., Alastuey, A., Rodriguez, S., Plana, F., Ruiz, C.R., Cots, N., Massagué, G., Puig, O., 2001. PM10 and PM2.5 source apportionment in the Barcelona Metropolitan area, Catalonia, Spain. Atmos. Environ. 35 (36), 6407–6419. https://doi.org/10.1016/S1352-2310(01)00361-2.
Querol, X., Viana, M., Alastuey, A., Amato, F., Moreno, T., Castillo, S., Pey, J., de la Rosa, J., Sánchez de la Campa, A., Artíñano, B., Salvador, P., García Dos Santos, S., Fernández-Patier, R., Moreno-Grau, S., Negral, L., Minguillón, M.C., Monfort, E., Gil, J.I., Inza, A., Ortega, L.A., Santamaría, J.M., Zabalza, J., 2007. Source origin of trace elements in PM from regional background, urban and industrial sites of Spain. Atmos. Environ. 41 (34), 7219–7231. https://doi.org/10.1016/j.atmosenv.2007.05.022.
Reche, C., Viana, M., Amato, F., Alastuey, A., Moreno, T., Hillamo, R., Teinilä, K., Saarnio, K., Seco, R., Peñuelas, J., Mohr, C., Prévôt, A.S.H., Querol, X., 2012. Biomass burning contributions to urban aerosols in a coastal Mediterranean City. Sci. Total Environ. 427–428, 175–190. https://doi.org/10.1016/j.scitotenv.2012.04.012.
Sandradewi, J., Prévôt, A.S.H., Weingartner, E., Schmidhauser, R., Gysel, M., Baltensperger, U., 2008. A study of wood burning and traffic aerosols in an Alpine valley using a multi-wavelength Aethalometer. Atmos. Environ. 42 (1), 101–112. https://doi.org/10.1016/j.atmosenv.2007.09.034.

Schurman, M.I., Lee, T., Desyaterik, Y., Schichtel, B.A., Kreidenweis, S.M., Collett, J.L., 2015. Transport, biomass burning, and in-situ formation contribute to fine particle concentrations at a remote site near Grand Teton National Park. Atmos. Environ. 112, 257–268. https://doi.org/10.1016/j.atmosenv.2015.04.043.

Slowik, J.G., Stroud, C., Bottenheim, J.W., Brickell, P.C., Chang, R.Y.W., Liggio, J., Makar, P.A., Martin, R.V., Moran, M.D., Shantz, N.C., Sjostedt, S.J., Van Donkelaar, A., Vlasenko, A., Wiebe, H.A., Xia, A.G., Zhang, J., Leaitch, W.R., Abbatt, J.P.D., 2010a. Characterization of a large biogenic secondary organic aerosol event from eastern Canadian forests. Atmos. Chem. Phys. 10 (6), 2825–2845. https://doi.org/10.5194/acp-10-2825-2010.

Slowik, J.G., Vlasenko, A., McGuire, M., Evans, G.J., Abbatt, J.P.D., 2010b. Simultaneous factor analysis of organic particle and gas mass spectra: AMS and PTR-MS measurements at an urban site. Atmos. Chem. Phys. 10 (4), 1969–1988. https://doi.org/10.5194/acp-10-1969-2010.

Sofowote, U.M., Healy, R.M., Su, Y., Debosz, J., Noble, M., Munoz, A., Jeong, C.-H., Wang, J.M., Hilker, N., Evans, G.J., Hopke, P.K., 2018. Understanding the PM2.5 imbalance between a far and near-road location: results of high temporal frequency source apportionment and parameterization of black carbon. Atmospheric Environ. 173, 277–288. https://doi.org/10.1016/j.atmosenv.2017.10.063.

Srivastava, D., Favez, O., Petit, J.E., Zhang, Y., Sofowote, U.M., Hopke, P.K., Bonnaire, N., Perraudin, E., Gros, V., Villenave, E., Albinet, A., 2019. Speciation of organic fractions does matter for aerosol source apportionment. Part 3: combining off-line and on-line measurements. Sci. Total Environ. 690, 944–955. https://doi.org/10.1016/j.scitotenv.2019.06.378.

Tong, Y., Qi, L., Stefenelli, G., Canonaco, D. S. W. F., Baltensperger, U., Prevot, A. S. H. and Slowik1, J. G.: Quantification of primary and secondary organic aerosol sources by combined factor analysis of extractive electrospray ionisation and aerosol mass spectrometer measurements (EESI-TOF and AMS), Atmos. Meas. Tech., (March), 1–50, 2022.

Ulbrich, I.M., Canagaratna, M.R., Zhang, Q., Worsnop, D.R., Jimenez, J.L., 2009. Interpretation of organic components from Positive Matrix Factorization of aerosol mass spectrometric data. Atmos. Chem. Phys. 9 (9), 2891–2918. https://doi.org/10.5194/acp-9-2891-2009.

Veld, M.i.'t., Alastuey, A., Pandolfi, M., Amato, F., Pérez, N., Reche, C., Via, M., Minguillón, M.C., Escudero, M., Querol, X., 2021. Compositional changes of PM2.5 in NE Spain during 2009–2018: a trend analysis of the chemical composition and source apportionment. Sci. Total Environ. 795, 148728. https://doi.org/10.1016/j.scitotenv.2021.148728.

Via, M., Chen, G., Canonaco, F., Daellenbach, K. R., Chazeau, B., Chebaicheb, H., Jiang, J., Keernik, H., Lin, C., Marchand, N., Marin, C., O'Dowd, C., Ovadnevaite, J., Petit, J.-E., Pikridas, M., Riffault, V., Sciare, J., Slowik, J. G., Simon, L., Vasilescu, J., Zhang, Y., Favez, O., Prévôt, A. S. H., Alastuey, A. and Minguillón, M. C.: Rolling vs. Seasonal PMF: Real-world multi-site and synthetic dataset comparison, EGUsphere, 2022, 1–29 [online] Available from: https://egusphere.copernicus.org/preprints/egusphere-2022-269/, 2022.

Via, M., Minguillón, M.C., Reche, C., Querol, X., Alastuey, A., 2021. Increase in secondary organic aerosol in an urban environment. Atmos. Chem. Phys. 21 (10), 8323–8339. https://doi.org/10.5194/acp-21-8323-2021.

Vossler, T., Černikovský, L., Novák, J., Williams, R., 2016. Source apportionment with uncertainty estimates of fine particulate matter in Ostrava, Czech Republic using Positive Matrix Factorization. Atmos. Pollut. Res. 7 (3), 503–512. https://doi.org/10.1016/j.apr.2015.12.004.

WHO: WHO global air quality guidelines, Coast. Estuar. Process., 1–360, 2021.

Yazdani, A., Dudani, N., Takahama, S., Bertrand, A., Prévôt, A.S.H., El Haddad, I., Dillner, A.M., 2021. Characterization of primary and aged wood burning and coal combustion organic aerosols in an environmental chamber and its implications for atmospheric aerosols. Atmos. Chem. Phys. 21 (13), 10273–10293. https://doi.org/10.5194/acp-21-10273-2021.

Yus-Díez, J., Bernardoni, V., Močnik, G., Alastuey, A., Ciniglia, D., Ivančič, M., Querol, X., Perez, N., Reche, C., Rigler, M., Vecchi, R., Valentini, S., Pandolfi, M., 2021. Determination of the multiple-scattering correction factor and its cross-sensitivity to scattering and wavelength dependence for different AE33 Aethalometer filter tapes: a multi-instrumental approach. Atmos. Meas. Tech. Discuss. 29, 1–30. https://doi.org/10.5194/amt-2021-46.

Zhao, H., Wakil, M.A., Viljanen, J., Song, Q., Yao, Q., Kwong, C.W., Alwahabi, Z.T., 2020. In situ measurement of potassium release during biomass combustion using laser-induced breakdown spectroscopy: effect of silicate on potassium release. Energy and Fuels 34 (3), 3262–3271. https://doi.org/10.1021/acs.energyfuels.9b03966.

Zhou, L., Hopke, P.K., Paatero, P., Ondov, J.M., Pancras, J.P., Pekney, N.J., Davidson, C. I., 2004. Advanced factor analysis for multiple time resolution aerosol composition data. Atmos. Environ. 38 (29), 4909–4920. https://doi.org/10.1016/j.atmosenv.2004.05.040.

Zografou, O., Gini, M., Manousakas, M.I., Chen, G., Kalogridis, A.C., Diapouli, E., Pappa, A., Eleftheriadis, K., 2022. Combined organic and inorganic source apportionment on yearlong ToF-ACSM dataset at a suburban station in Athens. Atmos. Meas. Tech. 15 (16), 4675–4692. https://doi.org/10.5194/amt-15-4675-2022.

Zotter, P., Herich, H., Gysel, M., El-Haddad, I., Zhang, Y., Mocnik, G., Hüglin, C., Baltensperger, U., Szidat, S., Prévôt, A.S.H., 2017. Evaluation of the absorption Ångström exponents for traffic and wood burning in the Aethalometer-based source apportionment using radiocarbon measurements of ambient aerosol. Atmos. Chem. Phys. 17 (6), 4229–4249. https://doi.org/10.5194/acp-17-4229-2017.

Part IV

DISCUSSION

5

DISCUSSION

5.1 ROLLING VS. SEASONAL PMF COMPARISON OUTCOMES

This section will assess the *rolling* and *seasonal* SA methodologies from two different approaches: i. a synthetic dataset, consisting of the creation of a dataset from profiles and time series of certain sources in order to compare both PMF outcomes with the initial matrices; ii. using 9 real-world datasets from sites across Europe.

5.1.1 *Model performance*

Overall, the *rolling* vs. *seasonal* comparison has highlighted some advantages of the *rolling* results. From a mathematical point of view, this new methodology is superior since it minimises model residuals, especially in the meteorological transition periods. Environmentally-wise, the *rolling* mechanism allows for better capture of profile evolution and a consequent better OA source time series description, both for the synthetic dataset and the multi-site experiments. This methodology also provided a better correlation with co-located measurements. However, both *rolling* and *seasonal* methodologies have succeeded in producing environmentally-sensible SA results. Indeed, in Barcelona, the time series *rolling-seasonal* squared Pearson's correlation coefficients are always over 0.94 for POA and 0.83 for SOA and slopes are always in the range 0.93-0.96 for POA and 0.77-0.93 for SOA. This similarity of both methodologies' results justifies the application of the *seasonal* PMF on **Paper I**.

Regarding the synthetic dataset results, none of the PMF methodologies was capable to describe the three SOA sources used to build the synthetic dataset (biogenic, biomass burning, traffic), but only achieved to differentiate two distinct OOA factors, LO-OOA and MO-OOA. However, the correlation of the SOA ensemble for both methodologies against the truth is very good for both (R^2>0.95) and their slopes are close to one. Contrarily, the POAs are significantly underrepresented (slopes <0.88, R^2 < 0.88), being the *seasonal* PMF closer to the original time series.

In terms of profile variability, the adaptability of *rolling* profiles to actual atmospheric sources evolution was proven advantageous both for the synthetic dataset and the multi-site analysis. The *rolling* profile evolution did not produce noise but captured actual fluctuations of ion ratios. However, the variability of HOA and COA profiles is expected to be very limited, coherently with the little fluctuation found in these results. The reason that HOA and COA profiles are expected to be constant is that the exhaust composition of vehicle emissions and the types of food being cooked are neither expected to vary season-wise nor episodically. This is not the case for the BBOA, which is expected to evolve depending on the types of biomass cremation and the ageing of their plumes. Hence, tighter constraints are advised for HOA and COA profiles with respect to BBOA.

The window length, i.e. the number of days of the time span in which PMF is run, is by definition the main difference between both methodologies. For the *seasonal* PMF, the window length is usually 90 days (one season) and there is no overlap between runs. For the *rolling* PMF, the usual window length is 14 days and there is one day of shift for each run, hence, each day is overlapped by 14 PMF runs (at least, if no repeats per each run are set). Because the *rolling* PMF, which has a shorter window length, overtakes the *seasonal* PMF results, one could conclude that the shorter the window period, the better profile adaptability and thus better PMF performance. This hypothesis is refutable since the choice of window numbers of days multiples of 7 are necessary to introduce to PMF coherent weekly cycles, as some *m/z* markers, e.g. those stemming from traffic, present strong weekdays/weekend differences. For this reason, the minimum window length is 7 days.

Many sites included in Chen et al. (2022b) essayed the *rolling* PMF with other time windows, such as 7 or 28 days. The comparison of scaled residuals and correlations with ancillary measurements revealed the 14-day period outperformed the other two window lengths, and 7 out of the 9 sites preferred the 14-days window length for this study. In the two others, the 28-days window length gave better results. These findings suggest that capturing more than one weekly cycle significantly improves PMF results and the effectiveness of sensible window lengths is lower-limited.

In all, the results of this comparison have shown that the newly developed *rolling* PMF presents higher quality results with respect to the previous *seasonal* PMF methodology. Some of the major benefits of the *rolling* PMF consist of: i. profile adaptability of PMF

factors, provided by the rolling window mechanism; ii. further error minimisation; iii. higher description accuracy to environmental sources; iv. higher results robustness and computational efficiency; v. automated mechanism being capable of assimilating near-real-time data. For all of these reasons, the *rolling* PMF is acknowledged as a more suitable technique for OA SA, especially for long datasets in which OA fingerprints are expected to evolve with the meteorological variations. Hence, the presented OA SA protocol is corroborated by this study.

5.1.2 *Anchor profile choice impact*

Paper I shows the main OA sources throughout two one-year-long periods (further explained at section 5.2.1). Their profile characterisation is based on anchors from Crippa et al. (2013) and Ng et al. (2011) and still profile ion ratios vary along the seasons. Figure 14 shows the variability of the *m/z43-to-m/z44* ratio, amongst the *seasonal* LO-OOA and MO-OOA profiles. It can be seen how the differences in the same factor are great, ranging 0.3-1.4 for LO-OOA and 0.1-0.7 for MO-OOA. It could be argued that describing sources with such high seasonal variability of the ion proportions with the same OA labels might be inexact but as long as the main seasonal differences are depicted, factors can be ascertained as a group of ions of dynamic proportion. This is the framework in which the *rolling* PMF is settled, aiming to capture this profile variability. Indeed, for instance, the terms "less oxidised" and "more oxidised", only divide OOA factors in two oxidisation states, not describing a quantitative fraction between its main ions.

An unexpected outcome from **Paper II** was the acknowledgement of how influential was the choice of the profile anchors on the final solution. This finding aroused from the use of a different profile anchor (that from Ng et al. (2011)) instead of that from the synthetic dataset confection, thus, *truth* (that from Crippa et al. (2013)). This caused very different BBOA concentrations with a likely influence on SOA concentrations disparity as well (Figures 2 and 3 in **Paper II**). This can be seen particularly in Figure 3 b) of **Paper II**, in which the BBOA *m/z60-to-m/z55* vs. *mz/44-to-m/z43* ratio cloud is far from the *truth* for both *rolling* and *seasonal* methodologies.

In order to corroborate the impact of the profile anchors, two more *rolling* experiments were run, being the presented *rolling* solution the base case, which will be called henceforth *standard* solution. The first additional experiment consisted in setting a

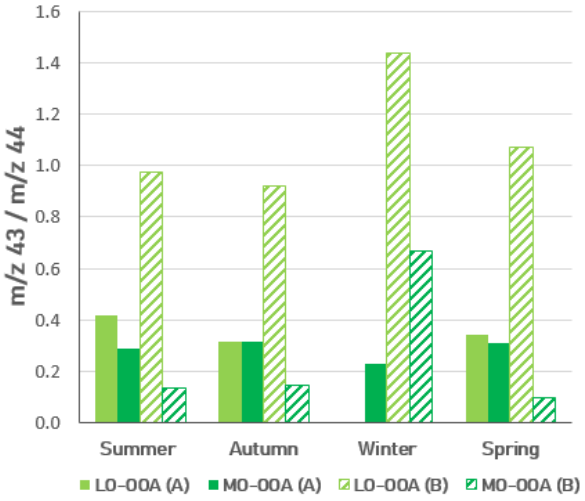

Figure 14: Seasonal variation of the ratio *m/z43-to-m/z44* for both periods A and B and both OOA factors.

higher a-value for the BBOA Ng et al. (2011) anchor profile, thus allowing for a higher variation. This experiment will be hereinafter referred as *wider aBB*. The second one used the *truth* profile as anchor, this is, the BBOA reference profile from Crippa et al. (2013) used to build the synthetic dataset. This setting is expected to present a more coincident solution compared to the *truth anchor* and will be referred to as *BB truth*.

In terms of profiles, the results of these experiments are shown in Figure 15. The three experiment ratios are plotted alongside those from the *seasonal* and *truth* outcomes. The dispersion of the scattered HOA and SOA are not very different in the cases of the wider a-value of BB and the truth anchor, although seemingly a bit more concentrated for the latter. However, the differences in the BBOA plot are critical. The experiment *wider aBB* does not improve results, it only increases the *m/z44-to-m/z43* and decreases its *m/z60-to-m/z55*. Thus, probably converting this source into a factor differing substantially from the original BBOA profile and that from other studies in Europe. On the contrary, the results from the experiment *BB truth anchor* show many comparable ratios to *truth*.

Regarding time series, the differences are scarcer as well for the *BBCrippa* experiment. The squared Pearson correlation coefficients between the *BBCrippa* experiment and the *truth* factors time series are over 0.88, being substantially lower for the other experiments (Fig. 16). However, in terms of absolute concentrations, the three

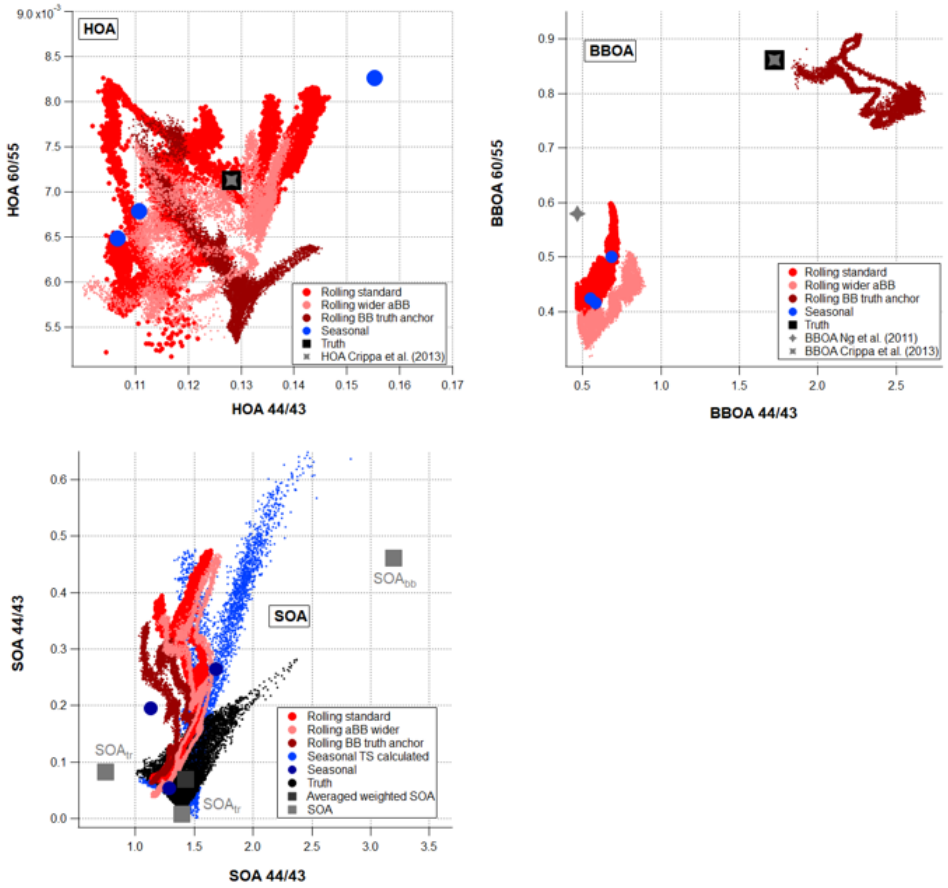

Figure 15: *Rolling* PMF time-dependent *m/z60-to-m/z55* vs. *m/z44-to-m/z43* for the standard *rolling* solution, the experiment with a wider BBOA a-value and the experiment with the same anchor profile as truth for the three main sources. The *seasonal* and *truth* solutions are also plotted.

approaches fail to describe POA concentrations with underestimations of more than 25% and 40% for HOA and BBOA, respectively, in all cases. This discrepancy is believed to be related to the impossibility to retrieve the three *truth* SOA factors from PMF (only two OOAs were retrieved). However, the slopes for the solution with the *BB truth anchor* are the closest to unity and the percentages of apportionment are the closest to the *truth*. The *wider aBB* experiment has not provided better comparability to *truth* results, but a lower quality solution.

This analysis has corroborated the importance of the anchor profile chosen to launch PMF. In real-world datasets, in which the truth is not known, this issue could

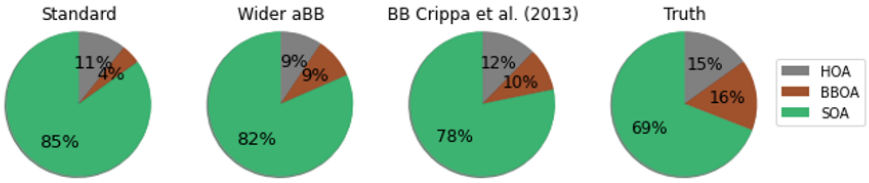

Fit to truth *(y=m·x+n)*	Standard		Wider aBB		BB Crippa	
	R^2	m	R^2	m	R^2	m
HOA	0.89	0.75	0.87	0.68	0.95	0.86
BBOA	0.32	0.12	0.50	0.29	0.88	0.58
SOA	0.94	1.06	0.94	0.58	0.98	1.06

Figure 16: (a) Pies of apportionment of all the *rolling* experiments' solutions. (b) Pearson squared correlation coefficients and slopes of the time series of the three experiment outcoming factors with respect to the *truth* factor time series.

unnoticedly lead to inaccurate results. The most sensible advice is to use the profiles retrieved from *seasonal* unconstrained runs as anchors for the *rolling* PMF. These profiles will be faithful to the aerosol reality at the site. Otherwise, forcing reference profiles into a dataset might generate inaccurate OA sources.

5.2 BARCELONA FINE AEROSOL SOURCES AND TRENDS.

5.2.1 *OA sources in Barcelona*

Paper I aims to depict the main OA sources in Barcelona from mass spectral measurements in unit mass resolution. A Q-ACSM was deployed in the Barcelona-Palau Reial for two periods: from May 2014 to May 2015 (hereinafter called period A) and from September 2017 to October 2018 (hereinafter called period B). The SA of these two periods was addressed using the *seasonal* PMF approach. However, the *rolling* PMF was also employed for SA of period B, and results are included in a harmonised European SA study (Chen et al., 2022b). The comparison between both methodologies' outputs was addressed in section 5.1. In order to present homogeneous results for both periods, for the **Paper I** discussion *seasonal* PMF results are used. The encountered OA sources in both periods A and B were [OA source (% of total OA in period A, % of total OA in period B)]: MO-OOA (35%, 43%), LO-OOA (22%, 28%), HOA (19%, 12%), COA (18%, 14%), BBOA (6%, 4%) (Fig. 2 from **Paper I**).

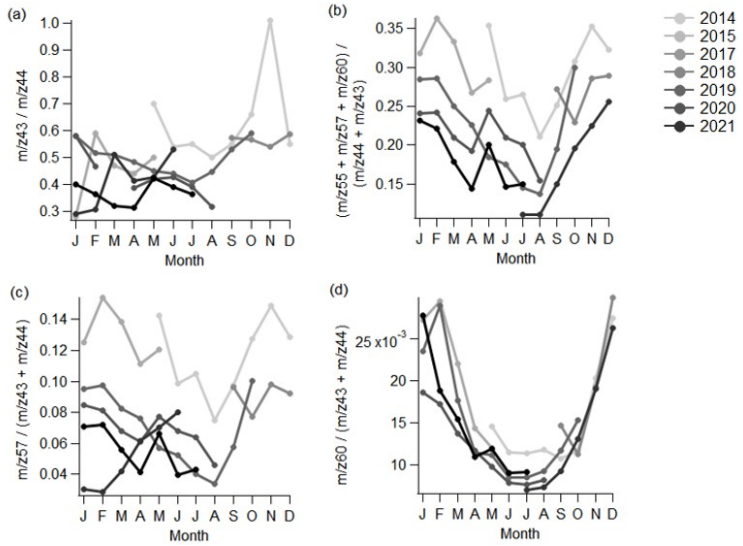

Figure 17: Monthly ratio of (a) *m/z43*/*m/z44*, (b) (*m/z55* + *m/z57* + *m/z60*)/(*m/z43* + *m/z44*), (c) *m/z57* / (*m/z43* + *m/z44*), and (d) *m/z60*/(*m/z43* + *m/z44*), for years 2014-2021. The year 2016 was not included due to the unavailable data and data from years 2019, 2020, 2021 is preliminary and unpublished.

As formerly mentioned, the study of the two presented periods cannot be ascertained as a trend assessment, as they contain different months (12 months May to May as opposed to 13 months September to October) and are three years apart, lacking information to assess the expected inter-annual variability. However, these results, when contextualised, give a glimpse of the general atmospheric trends. Despite complete OA SA is not available continuously, measurements were carried out in Barcelona in a discontinuous way from 2014 to 2021 (unpublished from 2019 on). Figure 17 (a) shows monthly averages of the *m/z43-to-m/z44* ratio from May to 2014 to July 2021, which allows the assessment of a trend in that period. A decrease can be observed, indicating a trend of increasing oxidation state of ambient OA.

Saiz-Lopez et al. (2017) showed an increase of atmospheric oxidation potential due to the concentration increase of oxidants (O_3, $NO_3^{\bullet}$, OH^-) in Madrid and a decrease of NO, NO_2 and NO/NO_2. The same trend for these pollutants was found in Barcelona (Massagué et al., 2019). The enhancement of O_3 concentrations has been partly attributed to the abatement policies of NO_x and a lack of VOC mitigation

(Massagué et al., 2019). These changes impact SOA in two different ways: i. both O_3 and NO_x prompt SOA formation through the oxidation of VOCs (Dai et al., 2019a; Na et al., 2006) and even if NO_x decrease, the increase of O_3 prompts an enhancement of SOA levels; ii. O_3 leads to other oxidation radicals such as OH^-, which promote SOA oxygenation (Kang et al., 2011; Salo et al., 2011). Hence, the increase of O_3 implies both an impulse to fresh SOA formation and oxidation of SOA, however, the mitigation of NO_x does not limit significantly SOA production (Zhao et al., 2017; Zheng et al., 2015b). Thereby, the more differentiated SOA of period B compared to period A in terms of oxidation degree is attributed due to a positive increase of these oxidants. This scenario, if not reverted, will continue promoting SOA formation and oxidation, as observed in the 2014-2021 period.

Figure 17 (b), (c), and (d) focuses on the evolution of certain POA ions (*m/z55*, *m/z57*, and *m/z60*) compared to SOA ions (*m/z43* and *m/z44*). By taking the sum of all the POA ions and dividing them by the sum of all SOA ones, one can see the evolution over the years of a proxy of the POA-to-SOA ratio (Fig. 17(b)). This graph depicts the decrease of POA proportion, which can be explained by: i. the increase of SOA due to the oxidisation of the atmosphere; ii. the reduction of the primary emissions due to the implementation of mitigation regulations.

Plots (c), (d) show the evolution of the traffic and biomass burning markers, *m/z57* and *m/z60*, respectively, divided by the SOA markers. Whilst biomass burning does not present a clear decrease over the 2014-2021 period, the decline of *m/z57* is evident. Even though 2020 might have been an exceptional year because of the COVID-19 pandemic, in which the traffic was significantly decreased (Tobías et al., 2020), the trend can be confirmed by the previous and posterior years.

With these insights, the tentative trend observed in the **Paper I** is confirmed with this 7 years trend. In essence, this trend implies an increase in SOA due to the oxidisation of the atmosphere and a decrease in POA, especially in traffic. In terms of SOA characteristics, an increase in its oxidation state was found. For all of that, concern is to be raised about the SOA precursors mitigation, as well as persisting on the abatement of the POA emissions.

5.2.2 *Barcelona in the European OA SA frame*

In this section, a contextualisation of Barcelona SA results amongst other European urban sites is pursued. However, these results in Chen et al. (2022b) may be somewhat limited as not all sites' measurement periods are perfectly overlapped. However, Barcelona's results overlay many other sites' measurements.

In terms of PM_1, the concentration in Barcelona (9.0 $\mu g \cdot m^{-3}$) is lower than the mean of European urban stations (12.2 $\mu g \cdot m^{-3}$), and even slightly lower than the mean of all stations, including those at rural or remote sites (9.8 $\mu g \cdot m^{-3}$). The OA sources found in Barcelona are consistent with those found across Europe. Chen et al. (2022b) found HOA to be a 4-9% of NR-PM_1 at European urban sites (in Barcelona it accounts for a 5%). Similarly, BBOA, with a 2% in Barcelona, is also within the European urban range (1-11%). Note that it is in the lower range, as the domestic heating contribution to this factor is lower than in northern Europe, where BBOA in urban sites ranged from 3% to 13% (except for the Helsinki site, in which it was not retrieved). Contrarily, the COA-like factor (5% of NR-PM_1 in Barcelona) was not identified at all urban stations, but only in Marseille, Zurich, Athens NOA, Athens DEM, and London, with a 6%, 3%, 8%, 8%, and 6% of the NR-PM_1 mass, respectively. Again, the difference is linked to latitude, as COA identification is not achieved in northern Europe. In all urban sites, SOA was differentiated in two OOAs of different oxidation states (LO-OOA and MO-OOA). At urban sites, the SOA ranges were 20% - 31% for LO-OOA (28% in Barcelona) and 26% - 59% for MO-OOA (44% in Barcelona). The LO-OOA-to-MO-OOA ratio, however, fluctuates between 0.4 and 0.9 (being 0.6 in Barcelona) as it might depend on the period and site conditions.

As in many other urban stations, the proportion of POA grows in Barcelona for high PM_1 concentrations, being the HOA growth especially relevant. This finding implies that traffic is the main driver of the most polluted episodes. In other European sites, this growth is also visible for the BBOA factor. Besides, the HOA and POA proportion is also larger for those episodes of lowest OA levels, indicating that after the air is cleaned (e.g. after a strong winds episode), the primary emissions are those which first pollute the atmosphere due to their continuous emission. The great influence of POA factors in high PM levels is reported in yearly and winter mean concentrations, although in summer months, in Barcelona and other urban sites (e.g. Lille, Dublin, Paris) the highest PM levels are driven by an OOA enhancement.

This fact can be explained by an increase in SOA production (overcoming the POA production) due to an enhanced photooxidation of VOCs in summer related to higher solar irradiation.

Regarding the OA oxidation state, Chen et al. (2022b) reported the *m/z43-to-m/z44* ratio in OOA (and not the ratio for bulk OA), with a median value for urban stations of 0.25 in DJF and 0.33 in JJA. These figures are slightly below the OOA *m/z43-to-m/z44* ratio in Barcelona, 0.27 and 0.38, respectively, indicating that Barcelona presents fresher SOA than most of other European urban sites. The high temperature and solar radiation in Barcelona, which enhance the photochemical pathways of SOA formation, with respect to higher latitudes could be one of the causes of the higher fresh SOA ratio. Regarding the SOA separation, in summer, Barcelona MO-OOA and LO-OOA profiles' proportion of *m/z43* and *m/z44* is in the middle of the cloud of points of the other European sites (Fig. 18). However, in winter, the Barcelona MO-OOA is less oxidised with respect to other urban sites, whilst the LO-OOA is within the average. This is coherent with the previous finding of the OOA being less oxidised than the median of other urban sites.

The tendency of SOA oxidisation observed in Section 5.2 has not yet been reported

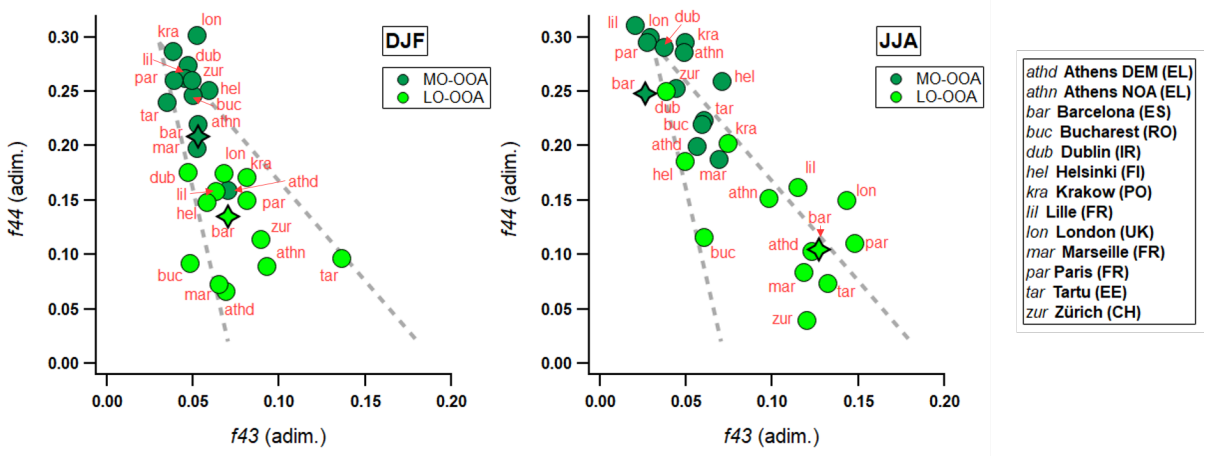

Figure 18: f44 vs. f43 intensity in winter (left) and summer (right) for resolved MO-OOA and LO-OOA in all urban sites in Chen et al. (2022b). The Barcelona points are highlighted with a star.

in other long-term European studies. However, traffic mitigation enforcements were applied across Europe, especially tackling NO_x, which could lead to increases of

atmospheric oxidants. Hence, similar changes to those concerning OA identified in **Paper I** could be taking place simultaneously in other European urban locations in further studies, but as previously discussed, an spatial (or meteorological) pattern is expected.

5.2.3 *PM_1 sources in Barcelona*

Paper III performs a more comprehensive SA analysis on period B combining OA matrices with BC (differentiated in liquid fuel and solid fuel, respectively BC_{lf} and BC_{sf}) and metals' concentration measurements. The MTR-PMF technique was used to combine the high-time resolution data (hereinafter HR data subset, referring to the 30-minute ensemble of the OA, SIA, and BC data subsets) with the low-time resolution data (hereinafter LR data subset, consisting of metal measurements, with a time resolution of 24h every four days). However, this technique implied a previous thorough assessment of the chosen time resolution (R_1) for the HR subset and uncertainty weightings (C_{HR} and C_{LR}) for the HR and LR subsets. The configuration of the time resolution of the HR subset (R_1) and uncertainty weighting that provided the best mathematical results was 30 minutes and (C_{HR}, C_{LR}) = (1,2). That time resolution (R_1 = 30 min) was also optimal environmentally wise. However, the (C_{HR}, C_{LR}) = (1, 5) weightings combination offered a better environmental explanation of the PM_1 sources than the (1, 2) pair and its outcome was presented as the final solution.

In order to assess the added value of the MTR-PMF, other PMF techniques were applied to compare the outcomes. To prove the power of the higher number of species obtained by different instrumentation, the outcomes of MTR-PMF were compared to: i. HR data subset PMF; ii. LR data subset PMF; iii. the so-called *pseudo-conventional data subset*, including the OA species summed up, the SIA species, the two origin-speciated BCs summed up, and the metals in the TR of the LR data subset (24h every 4th day). These three approaches showed more limited SA solutions, both in terms of the number of sources and environmental feasibility, with respect to the MTR-PMF SA results. With the aim of assessing the effectivity of using the highest TR for a given species, the comparison was set on the so-called *base case*, which included the same species as the MTR-PMF data ensemble but averaged to the lowest TR to homogenise all the data to the same timestamps. The results of the *base case* provided two sources less than the MTR-PMF. Moreover, it retrieved split sources which should have been together (AS + aged SOA and heavy-oil combustion), mixed others (road dust +

industry, biomass burning + mineral) and failed to identify sources of distinctive diel cycles such as COA. Thus, the performance of MTR-PMF was found superior due to its capacity to assemble data and to maintain the native high TR of measurements. For all these reasons, the MTR-PMF was found superior in these two respects.

The resolved sources from MTR-PMF in percentage over PM_1 were: AS + heavy oil combustion (25%), AN + ACl (17%), aged SOA (16%), traffic (14%), biomass burning (9%), fresh SOA (8%), cooking-like OA (5%), and industry (4%). All of these sources were environmentally feasible and coherent with previous other studies at the site.

The use of the MTR-PMF technique is the first milestone towards a comprehensive understanding of the atmosphere as a whole, as it conceives PM sources regardless of the instrumentation used or the individual pollutants characterised. This new perspective could enable more accurate mitigation enforcement, as these regulations could be tackling the sources of pollutants with more precision.

5.2.4 *Results' implications on climate*

As aforementioned, the atmospheric aerosol influences severely the climate forcing through, amongst other effects, the absorption of solar radiation which, in turn, heats the atmosphere. Among PM constituents, carbonaceous aerosol particles (BC and OA) are recognised as the most important warming agents. However, the magnitude of their climate forcing is still rather uncertain because it depends on the sources of carbonaceous particles, their chemical composition, and the physicochemical processes that these particles undergo in the atmosphere after emission or generation.

One of the factors affecting the absorption in the atmosphere is the mixing of BC particles with PM constituents which might increase their absorption efficiency with respect to pure BC, through the so-called lensing effect. Those PM constituents which internally mixed with BC are reported to contribute to a higher extent to the lensing effect are OA, and especially SOA, and to a lesser extent SIA compounds. An enhancement of BC particles absorption (absorption enhancement; E_{abs}) due to PM oxidation has been reported in Paris, London, and Barcelona (Liu et al., 2015; Yus-Díez et al., 2022; Zhang et al., 2018b). On the other side, OA particles externally mixed with BC can efficiently absorb UV-VIS radiation with POA showing higher

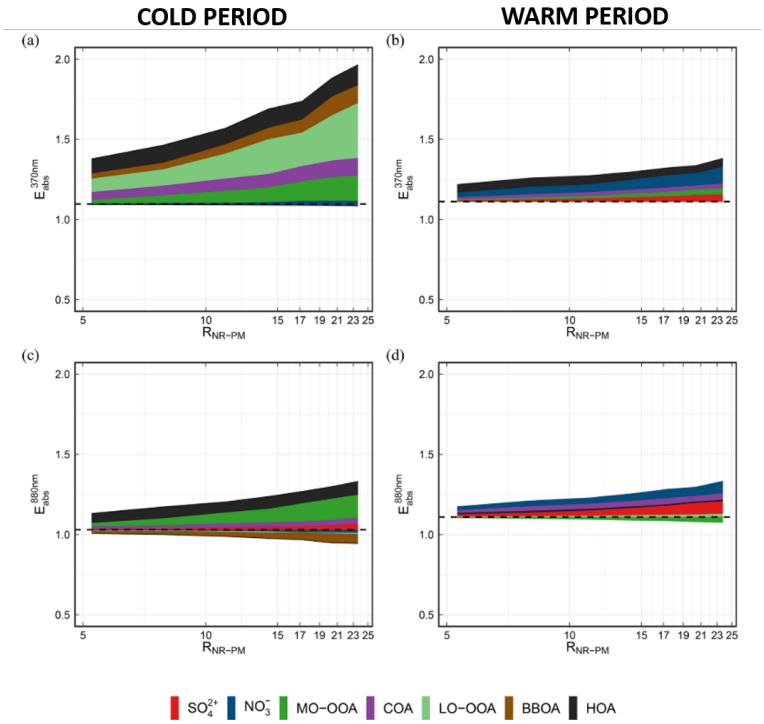

Figure 19: Absorption enhancement (E_{abs}) relative contribution of OA sources and SIA at two different wavelengths (370 and 880 nm) during the cold season (November 2017- March 2018) and the warm season (June 2018 - August 2018) as a function of $R_{NR-PM} = \frac{NR-PM_1}{EC}$. Adapted from Yus-Díez et al. (2022).

absorption efficiency compared to SOA (Kasthuriarachchi et al., 2020). Yus-Díez et al. (2022) evaluated the absorption enhancement of BC particles as a function of SIA and OA concentrations, as shown in Figure 19, where R_{NR-PM} refers to the sum of all NR-PM_1 compounds divided by EC concentrations, representing the amount of available material for BC mixing.

Figure 19 shows that in the cold period SOA is a significant enhancer of BC absorption due to both external mixing (related to BrC absorption) and internal mixing in the short and large wavelengths, respectively. Indeed, E_{abs} is substantially increased with particle aging in the colder period (Fig. 19 (a), (c)). However, in summer (Fig. 19 (b), (d)), although the SOA/POA ratio is higher, SOA does not present such a great role in E_{abs} as SIA compounds. Also, POA presents a significant impact enhancing absorption, both constituting BrC (external mixing, at 370 nm) and coating BC (internal mixing, at 880 nm). These observations not only expand the

understanding of the interactions between the refractory and the non-refractory PM, but they also relate the impact of the Barcelona aerosol compounds and sources with the climate forcing. This means that the ageing OA trend observed from 2014-2021 identified in section 5.2 could imply an increase of E_{abs} and the subsequent increase of tropospheric temperature.

Another mechanism of interaction between particles and climate is light scattering, which has also been reported to be chemically dependent (Wang et al., 2015). Amongst submicronic aerosol particles, AN, AS, and SOA are the most efficient compounds for light scattering, which also are the majority ones in PM_1 as reported in **Paper III**. All these sources summed up together account for a 62% of the PM_1 mass, which makes scattering an optical property of relevance in the troposphere of Barcelona. Hence, an upcoming tendency of SOA increase could induce greater scattering and hence atmospheric cooling. However, the neat effect of atmospheric temperature should be evaluated with the NO_3^- and SO_4^{2-} tendencies as well.

The characterisation of the aerosol absorption enhancement and scattering as a function of OA sources, and in general, of PM sources and components, is substantially relevant for climate forcing estimations through atmospheric modelling. As detailed in Section 1.1.3, RF_{ARI} estimations of each aerosol component present high uncertainties and they are not even accounting for the enhancement of the BrC particles formed from OA precursors or for BC coating with OA. Therefore, in order to calculate the final impact on tropospheric temperature, these models should turn to the addition of the absorption and scattering effects related to each PM component. For this matter, further investigation of the mechanisms of interaction of PM composition (and sources) and their extinction quantification is necessary for modellers to refine these estimations and ultimately project future climate scenarios.

5.2.5 *Results' implications on health*

PM_1 thresholds do not exist in the WHO air quality guidelines, but the levels of NR-PM_1 + BC levels are here assessed with respect to the $PM_{2.5}$ air quality guidelines established limits. Since PM_1 is embedded in $PM_{2.5}$, PM_1 levels are expected to stay lower than the $PM_{2.5}$ thresholds. The $PM_{2.5}$ reference values are 5 $\mu g \cdot m^{-3}$ as annual mean and 15 $\mu g \cdot m^{-3}$ as daily average not to be exceeded more than 3-4 days per year (WHO, 2021). The annual PM_1 means and number of days in which $PM_{2.5}$ daily

thresholds are exceeded in the 2014-2015 and 2017-2018 periods are shown in Table 5.

Table 5: Annual mean values and number of exceedances of the WHO threshold values.

Year	Period	Annual PM_1 mean ($\mu g \cdot m^{-3}$)	Number of days of exceedance
2014	19/05 - 31/12	8.9	18
2015	01/01 - 26/05	11.5	36
2017	21/09 - 31/12	8.1	7
2018	01/01 - 31/10	8.8	26

Table 5 highlights how in all years (even though none of them is complete), the mean annual concentration is above 5 $\mu g \cdot m^{-3}$ or the exceedances are well above the WHO air quality guidelines. The fact that PM_1 levels are overcoming $PM_{2.5}$ thresholds reveals that $PM_{2.5}$ will be overcoming these references even more. However, in none of the cases, the annual mean exceeds the annual $PM_{2.5}$ limit of 15 $\mu g \cdot m^{-3}$ of the EU directives.

With the aim of regulating emissions to meet the WHO values, information about PM_1 and $PM_{2.5}$ sources is necessary as well as a long-term evaluation of these pollutants' evolution. The long-term information is also required to perform epidemiological studies based not only on bulk PM concentrations or PM components but based on source contributions, to assess the health impact of specific sources, very useful information for setting regulations. So far, not many studies have tackled OA sources toxicity or epidemiology, and consistency of results is limited (Hime et al., 2018). However, many studies agree on the high toxicity of SOA in terms of OP (Wang et al., 2022; Zhou et al., 2019). Also, many epidemiology findings highlight traffic-related emissions as one of the highest causes of mortality and hospital admissions triggering especially cardiovascular and respiratory diseases (Rich et al., 2019).

The assessment of the toxicity of PM_1 to human health from the results of this study can be tackled from an OP point of view. According to In't Veld et al. (2022), the main drivers for OP^{DTT} in Barcelona in the PM_1 fraction consist of the industry, OC-rich, secondary SO_4^{2-}, combustion, and heavy oil factors. The OC-rich factor from In't Veld

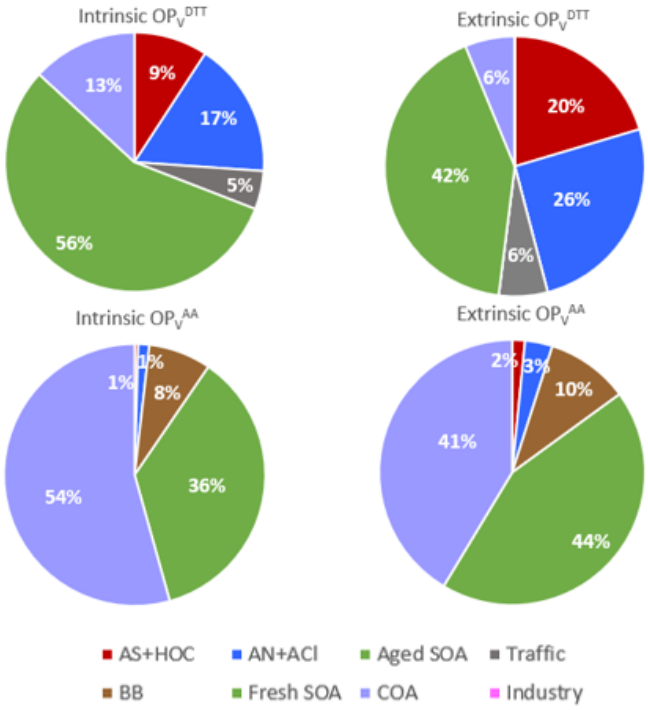

Figure 20: Results of the source apportionment of OP from DTT (left), AA (right) essays. Intrinsic OP is shown at the top and extrinsic OP at the bottom. PM_1 SA results are from **Paper III** and OP data from In't Veld et al. (2022).

et al. (2022) contains basically OC, a proxy for all the OA species (as shown in the intercomparison in **Paper I**), hence we could expect that more OP drivers information could be retrieved from an OP SA with OA-speciated sources. In this section, we discuss the OP SA using the PM_1 sources retrieved in **Paper III** analogously to the aforementioned study (Fig. 20). The results show how the fresh SOA is the factor driving the majority of OP, both intrinsically and extrinsically (i.e. accounting for the OP-toxicity of the source, and the representation of the toxicity of the source in the proportion of all sources in the atmosphere, respectively). Although the proportions of the assays vary substantially, both highlight the fresh SOA as a relevant source of OP as well as the importance of the COA, Traffic, AS + heavy oil combustion, AN + ACl, and BB. However, with a short time series of only 10 months, caution must be applied.

With all, these results are comparable to those from previous studies which highlight SOA as one of the main OP drivers, although our results only point out the OP potential for fresh SOA and not the aged SOA. This could be to the sensitivity of OP to metals, as the fresh SOA factor contains certain road dust markers due

to its likely traffic-driven origin. This inconsistency is a result of the limitations of this dataset. Nevertheless, from these results, the increase of SOA production hypothesised in section 5.2 would imply a more toxic atmosphere scenario. Another widely-reported OP driver is traffic, especially in PM_{10}, (Weber et al., 2021). However, in the presented analysis, the traffic OP contribution in Barcelona for the 2018 period is rather low, probably due to the absence of metals contribution of this source. The COA factor, which is found to be one of the most relevant OP drivers, was also found in Verma et al. (2015), although not such a high OP apportionment was expected. Other sources regarding extrinsic OP that are substantially hazardous are the AS + heavy oil combustion and the AN + ACl, coherent with other studies (In't Veld et al., 2022; Li et al., 2022b). Another unexpected result is the lack of an industrial source, which could be related to its low concentrations of this source or the limited time span of this source.

All out, research on PM sources' toxicity is still scarce and results vary depending on the SA methodology applied, the species included in PMF, and the accuracy of source identification. For these reasons, further knowledge of the SA methodologies to improve source identification and quantification is vital to eventually provide consistent outcomes. Also, further research should be carried out to make more robust the results of the toxicity of the different aerosol components. Besides, the ultimate goal in this direction could be the near-real-time health assessment of the aerosol in order to protect the population from high atmospheric toxicity events.

Part V

CONCLUSION AND FURTHER RESEARCH

6

CONCLUSIONS

The main objective of this thesis is to characterise the components and sources contributing to submicronic particulate matter (PM_1) in Barcelona and improve and assess the current source apportionment (SA) methodology. The identification of sources has been performed over two one-year periods with data provided by an Aerosol Chemical Speciation Monitor (ACSM), although additional measurements were also taken into account. In the SA study, an implicit trend was identified and the potential effects of this change were assessed in terms of climate and health studies. Further analysis on one of the two periods provided significant insights into the potentiality of combining several instrumentation for SA. Additionally, the main differences between the *rolling* and *seasonal* Positive Matrix Factorisation (PMF) methodologies were assessed, retrieving additional insights on profile anchoring effects on the final solutions. The following main conclusions were extracted from this thesis:

- ACSM is a robust instrumentation to retrieve high-time resolution online measurements of Non-Refractory (NR) PM_1 species as the intercomparison with co-located measurements of the same species has highlighted. It also allows for environmentally-sensible SA results, although there is room for organic aerosol (OA) protocol improvement. Moreover, this instrument data is remarkably suitable for near-real-time composition and SA atmospheric diagnosis.
- The current OA SA protocol from Chen et al. (2022b) advises the use of profile anchors to introduce *a priori* information to the PMF, however, this approach was found susceptible to deriving misleading results. By means of a synthetic dataset, the effect of the use of an anchor profile with significant differences to the *truth* profile caused a bad description of the aerosol, since it did affect not only the anchored profile but also those which had been unconstrained. Using a higher a-value neither promotes a better profile adjustment. However, even if the same profiles as the *truth* were used, PMF did not adjust perfectly the mass contributions with respect to the *truth*, even if consistency was improved.

Primary OA (POA) was underestimated by a 3% for hydrocarbon-like OA (HOA) and a 6% for Biomass Burning OA (BBOA), and secondary OA (SOA) was overestimated by a 9% in terms of relative contribution to OA. A possible cause for these discrepancies is the incapacity of PMF to resolve the three SOA factors (biogenic, traffic, biomass burning) and only differentiate SOA in two according to its oxidation state.

- Results from both the synthetic dataset and the multi-site comparison approaches confirm that the *rolling* PMF technique reproduces more accurately environmental sources' behaviour than *seasonal* PMF. Its profile temporal variation feature was reported to ascertain to actual atmospheric OA sources variabilities. Besides, *rolling* PMF minimises model residuals and maximises correlation of the sources with co-located markers' measurements with respect to *seasonal* PMF. These results are favourable for the near-real-time SA, whose data incorporation mechanism is based on the *rolling* PMF.

- OA accounts for around 43% of the PM_1 mass in Barcelona in the two periods under study (2014-2015, 2017-2018). Five major OA sources were found: HOA, cooking-like OA (COA), BBOA, and two secondary Oxygenated OA (OOA), differentiated into Less Oxidised OOA (LO-OOA) and More Oxidised (MO-OOA). These sources are coherent with previous studies at the site and with other similar European sites. Also, secondary inorganic aerosol (SIA) species concentrations were explored and their cycles were acknowledged. PM_1 and SIA concentrations are also similar to other urban European urban sites' levels.

- An absolute and relative increase of SOA with respect to the total OA was found from one period to the other. An increasing oxidation state of SOA was also detected. This variation could be explained by an increment of the oxidative potential of the atmosphere due to higher amounts of very reactive radicals which prone to SOA production and oxidation. Since the emission of most of these oxidants is not currently being targeted, this scenario is not expected to decline, but to consolidate.

- The increasing production and oxidisation of SOA due to the effect of these radicals will have implications on the balance of the atmosphere, since light absorption is enhanced with higher SOA concentrations in winter, leading to atmospheric warming. Nonetheless, in the warmer period, SIA were the lightest absorption enhancer.

- Coupling data of different instrumentation allows for improving the identification and quantification of PM sources with PMF due to a higher amount of species involved and better time resolution. The use of high-time resolution data allowed for the characterisation of certain PM_1 sources which required diel cycle characterisation to be identified. This is the case, for example of the COA. The use of high-time resolution mass spectrometry OA data and origin-differentiated black carbon (BC) was found advantageous for source identification and a more complete understanding of those already obtained. Also, the inclusion of more species into the same PMF allowed for a more global understanding of the sources.

- The outcoming PM_1 sources from the combination of the ACSM, aethalometer and offline filter datasets in Palau Reial for the period September 2017- October 2018 are stable and environmentally feasible. Their mass contributions to PM_1 are: ammonium sulphate + heavy oil combustion (25%), ammonium nitrate + ammonium chloride (17%), aged SOA (16%), road traffic (14%), biomass burning (9%), fresh SOA (8%), COA (5%), and industry (4%).

- The impact of the retrieved PM_1 sources on health was assessed in terms of their associated oxidative potential (OP), this is, their capacity to oxidize molecules by producing reactive oxygen species, which are harmful to human health. Results show that the most harmful source is SOA and that regarding atmosphere representativity, SOA is clearly the biggest threat. Consequently, the hypothesized scenario of SOA increase could imply a more pernicious atmosphere for the urban population. However, one must note that OP source apportionment studies methods are still budding and the number of samples is low, yet results could not be optimally accurate. Nonetheless, the use of this methodology on the instrument-combined PM_1 sources is a novel approach and sets a precedent in terms of OP source identification.

- With the ambition of substantially reducing the health effects of air pollution by 2030, the upcoming revision of the European Commission Directive on ambient air quality and cleaner air stipulates stricter limit values and will be more aligned with the World Health Organisation (WHO) air quality guidelines, for certain pollutants among which PM is one of the relevant ones. Moreover, it requires monitoring of emerging pollutants such as BC, ultrafine particles, and their number size distributions, as well as $PM_{2.5}$ composition and particles' OP by setting up monitoring supersites at urban background locations. Many

studies highlight that for health protection it may be more effective to control specific source contributions to PM rather than bulk PM mass concentrations, since OP, for instance, is source-dependent. Hence, aerosol SA is of mandatory importance. This study has shown that the combination of measurements of different parameters (BC, metals, NR-PM_1) has proved to be a more adequate strategy to identify and quantify sources, hence supporting the main goal of growing knowledge to enforce stricter pollution regulations. Moreover, the next step, the near-real-time SA, which is based on the *rolling* technique which was proven advantageous in the current thesis, will give an added value of great interest to be able to react more effectively. However, this approach is still in development and it would benefit substantially from including multiple instrumentation data at their native resolution.

7

FUTURE RESEARCH

The following list provides suggestions for future research that could allow addressing the limitations and gaps of knowledge that have been identified in this thesis.

- The implementation of near-real-time PMF will provide almost instantaneous information on the atmospheric sources' variation. This can be very helpful to promote exposure protection regulations in source-specific highly-polluted events. However, this procedure is not fully developed since it misses the capability of differentiating OOA sources, detecting source outbreaks, or including multiple instrumentations in the PMF. The next steps regarding near-real-time PMF hence consist of the tool development to get such an accurate SA as in a non-real-time SA. This comprises the recognition of emerging/disappearing sources, the OOA differentiation and the inclusion of several instrumentations in the PMF with different time resolutions.
- The reported increase in the oxidising capacity of the atmosphere due to the increase in oxidating radicals in the atmosphere has been shown to promote both the SOA production and SOA oxidation processes. This has been comprehensively studied for two one-year periods but a subsequent trend was found for the 2014-2021 period. Future research should develop long-term source apportionment with the high-time resolution data of the ACSM in order to characterise long-term variability of the SOA fingerprints and proportions with respect to POA. These long-term studies will also provide insights into the effectiveness of traffic or biomass burning mitigation regulations and their consequent changes in the OA sources.
- Improvement of SA techniques and methodologies in order to obtain better quantification and characterisation of OA and PM_1 sources. The distinction of sources near pollution hotspots can help identify more purely source fingerprints to subsequently seek for the same sources in background sites. For this purpose, future deployment of a Time of Flight (ToF) ACSM in a road site is planned,

in order to obtain distinct traffic sources, hopefully differentiated regarding the different fuel combustion materials, COA, shipping etc. The higher detection limits and spectral resolution of this instrument are expected to provide more precise OA.

- Further research is to be carried out regarding profile anchoring and more generally, the accuracy of SA results with respect to actual results. A useful methodology to tackle this task is synthetic datasets since they allow for comparison to actual results.

- OP assessment on PM sources has to be further investigated to generate cohesion amongst studies, which present significant discrepancies. With this objective, methodologies to generate more accurate results should be developed. Improvement in OP drivers identification will advocate for the enforcement of coherent regulations for human protection as well as toxicity-assessed new WHO, and EU threshold revisions. In the same direction, epidemiological studies based on the two-year periods' data benefitting from the high-time resolution data should be conducted in order to assess the long-term impact of the retrieved PM_1 sources.

- Another future step is to use the current SA results for modelled OA and PM_1 sources verification. This procedure would improve atmospheric chemistry models with the ultimate aim of forecasting highly polluted events. Besides, this could provide more insights into aerosol-climate interactions and hence a more accurate calculation of their radiative forcings, as well as helping predict future climate scenarios.

Part VI

SCIENTIFIC CONTRIBUTION

8

SCIENTIFIC CONTRIBUTION

8.1 ARTICLES IN PEER-REVIEWED SCIENTIFIC JOURNALS

8.1.1 *Publications included in this thesis*

Via, M., Minguillón, M. C., Reche, C., Querol, X., Alastuey, A. (2021). Increase in secondary organic aerosol in an urban environment. Atmospheric Chemistry and Physics, 21(10), 8323-8339.

Via, M., Chen, G., Canonaco, F., Daellenbach, K. R., Chazeau, B., Chebaicheb, H., Jiang, J., Keernik, H., Lin, C., Marchand, N., Marin, C., O'Dowd, C., Ovadnevaite, J., Petit, J. E., Pikridas, M., Riffault, V., Sciare, J., Slowik, J. G., Simon, L., Vasilescu, J., Zhang, Y., Favez, O., Prévôt, A. S., Alastuey, A., and Minguillón, M. C. (2022). Rolling vs. seasonal PMF: real-world multi-site and synthetic dataset comparison. Atmospheric Measurement Techniques, 15(18), 5479-5495.

Via, M., Yus-Díez, J., Canonaco, F., Petit, J. E., Hopke, P., Reche, C., Pandolfi, Ivančič, M., Rigler, M., Prévôt, A. S. H., Querol, X., Alastuey, A., and Minguillón, M. C. (2023). Towards a better understanding of fine PM sources: online and offline datasets combination in a single PMF. Environment International, 108006.

8.1.2 *Co-author publications*

Bressi, M., Cavalli, F., Putaud, J. P., Fröhlich, R., Petit, J. E., Aas, W., Äijälä, M., Canonaco, F., Crenn, V., Dusanter, S., Ehn, M., Elsasser, M., Flentje, H., Graf, P., Green, D. C., Heikkinen, L., Hermann, H., Holzinger, R., Hueglin, C., Keernik, H., Kiendler-Scharr, A., Kubelová, L., Lunder, C., Maasikmets, M., Make, O., Malaguti, A., Mihalopoulos, N., Nicolas, J. B., O'Dowd, C., Ovadnevaite, J., Petralia, E., Poulain, L., Priestman, M., Riffault, V., Ripoll, A., Schlag, P., Schwarz, J., Sciare, J., Slowik, J., Sosedova, Y., Stavroulas, I., Teinemaa, E., **Via, M.**, Vodicka, P, Williams, P. I., Wiedensohler, A., Young, D.E., Zhang, S., Favez, O., Minguillón, M.C., Prevot,

A. S. H. (2021). A European aerosol phenomenology-7: High-time resolution chemical characteristics of submicron particulate matter across Europe. Atmospheric environment: X, 10, 100108.

Chen, G., Canonaco, F., Tobler, A., Aas, W., Alastuey, A., Allan, J., Atakabakhsh, S., Aurela, M., Baltensperger, U., Bougiatioti, A., De Brito, J.F., Ceburnis, D., Chazeau, B., Chebaicheb, H., Daellenbach, K.R., Ehn, M., El Haddad, I., Eleftheriadis, K., Favez, O., Flentje, H., Font, A., Fossum, K., Freney, E., Gini, M., Green, D., Heikkinen, L., Herrmann, H., Kalogridis, A.C., Keernik, H., Lhotka, R., Lin, C., Lunder, C., Maasikmets, M., Mihalopoulos, N., Mocnik, G., Necki, J., O'Dowd, C., Ovadnevaite, J., Peter, T., Petit, J.E., Pikridas, M., Platt, S.M., Pokorná, P., Poulain, L., Priestmann, M., Riffault, v., Rinaldi, M., Rózanski, K., Schwarz, J., Sciare, J., Simon, L., Skiba, A., Slowik, J.G., Sosedova, Y., Stavroulas, I., Styszko, K., Teinemaa, E., Timonen, H., Tremper, A., Vasilescu, J., **Via, M.**, Vodicka, P., Wiedensohler, A., Zografou., O., Minguillón, M.C., and Prévôt, A. S. (2022). European aerosol phenomenology 8: Harmonised source apportionment of organic aerosol using 22 Year-long ACSM/AMS datasets. Environment international, 166, 107325.

In't Veld, M., Alastuey, A., Pandolfi, M., Amato, F., Perez, N., Reche, C., **Via, M.**, Minguillón, M.C., Escudero, M., Querol, X. (2021). Compositional changes of PM2. 5 in NE Spain during 2009–2018: A trend analysis of the chemical composition and source apportionment. Science of the Total Environment, 795, 148728.

Tobías, A., Carnerero, C., Reche, C., Massagué, J., **Via, M.**, Minguillón, M. C., Alastuey, A., Querol, X. (2020). Changes in air quality during the lockdown in Barcelona (Spain) one month into the SARS-CoV-2 epidemic. Science of the total environment, 726, 138540.

Yus-Díez, J., **Via, M.**, Minguillón, M. C., Karanasiou, A., Querol, X., Alastuey, A., Pandolfi, M. (2020). Lensing effect on Black Carbon particles by secondary organic aerosols and sulfates in Barcelona.

Yus-Díez, J., **Via, M.**, Alastuey, A., Karanasiou, A., Minguillón, M. C., Perez, N., Querol, X., Reche, C., Ivančič, M., Rigler, M., Pandolfi, M. (2022). Absorption enhancement of black carbon particles in a Mediterranean city and countryside: effect of particulate matter chemistry, ageing and trend analysis. Atmospheric Chemistry and Physics, 22(13), 8439-8456.

8.2 CONFERENCES PRESENTATIONS

Via, M., Yus-Díez J., Canonaco, F., Petit, J.E., Hopke, P. H, Reche, C., Pandolfi, M., Ivancic, M., Rigler, M., Prévôt, A. S. H., Querol, X., Alastuey, A., Minguillón, M. C. (2023, April 24-28). Towards a better understanding of fine PM sources: online and offline datasets combination in a single PMF. European Geosciences Union, Viena, Austria.

Via, M., Chen, G., Canonaco, F., Daellenbach, K. R., Chazeau, B., Chebaicheb, H., Jiang, J., Keernik, H., Lin, C., Marchand, N., Marin, C., O'Dowd, C., Ovadnevaite, J., Petit, J. E., Pikridas, M., Riffault, V., Sciare, J., Slowik, J. G., Simon, L., Vasilescu, J., Zhang, Y., Favez, O., Prévôt, A. S., Alastuey, A., Minguillón, M. C. (2022, September 4-9). Rolling vs. Seasonal PMF: Multi-site and synthetic dataset comparisons. International Aerosol Conference, Athens, Greece.

Via, M., Gang, C., Canonaco, F., Prévôt, A. S. H, Alastuey, A., Minguillón, M. C. (2021, August 30 - September 3) Two-site comparison of rolling and seasonal OA source apportionment results for one-year-long datasets. European Aerosol Conference, London, United Kingdom (online).

Via, M., Yus-Díez, J., Canonaco, F., Alastuey, A., Petit, J.E., Hopke, P., Reche, C., Pandolfi, M., Querol, X., Minguillón, M. C. (2021, August 30 - September 3) Insights on multi-time resolution PMF: testing different time resolutions and uncertainty weightings. European Aerosol Conference, London, United Kingdom (online).

Via, M., Yus-Díez, J., Canonaco, F., Alastuey, A., Petit, J.E., Hopke, P., Reche, C., Pandolfi, M., Querol, X., Minguillón, M. C. (2021, May 18) Insights on multi-time resolution PMF: testing different time resolutions and uncertainty weightings. ACTRIS

Innovation in Atmospheric Sciences Virtual Workshop.

Via, M., Minguillón, M. C., Reche, C., Querol, X., Alastuey, A. (2020, August 30 - September 4). Fine aerosol and organic sources variation over four years in Barcelona. European Aerosol Conference, Aachen, Germany (online).

8.3 ACKNOWLEDGEMENTS AND FINANCIAL SUPPORT

This thesis was carried out in the IDAEA-CSIC, a centre of Excellence Severo Ochoa (Spanish Ministry of Science and Innovation, Project CEX2018-000794-S).

We acknowledge support of the COST Action CA16109 COLOSSAL. IDAEA-CSIC is a Centre of Excellence Severo Ochoa (Spanish Ministry of Science and Innovation, grant no. CEX2018-000794-S). We would like to thank Aerosol d.o.o. for lending the AE33 aethalometer.

The present work was supported by European Union's Horizon 2020 research and innovation program under grant agreement 101036245 (RI-URBANS); the "Agencia Estatal de Investigación" from the Spanish Ministry of Science, Innovation and Universities, and FEDER funds under the projects CAIAC (PID2019-108990RB-I00) and EQC2018-004598-P, the Agencia Estatal Consejo Superior de Investigaciones Científicas (CSIC) under the Project 202030E261, and the Generalitat de Catalunya, by AGAUR (2021 SGR 00447) and the Direcció General de Qualitat Ambiental i Canvi Climàtic (DGQACC). We acknowledge the support of the publication fee by the CSIC Open Access Publication Support Initiative through its Unit of Information Resources for Research (URICI).

Part VII

REFERENCES

BIBLIOGRAPHY

AMB. (2022). *Location and soil use of the barcelona metropolitan area*. Retrieved September 26, 2022, from https://www.amb.cat/s/es/web/area-metropolitana/coneixer-l-area-metropolitana/localitzacio-i-usos-del-sol.html

Adachi, K., & Tainosho, Y. (2004). Characterization of heavy metal particles embedded in tire dust. *Environment International*, *30*(8), 1009–1017. https://doi.org/https://doi.org/10.1016/j.envint.2004.04.004

Äijälä, M., Daellenbach, K. R., Canonaco, F., Heikkinen, L., Junninen, H., Petäjä, T., Kulmala, M., Prévôt, A. S. H., & Ehn, M. (2019). Constructing a data-driven receptor model for organic and inorganic aerosol – a synthesis analysis of eight mass spectrometric data sets from a boreal forest site. *Atmospheric Chemistry and Physics*, *19*(6), 3645–3672. https://doi.org/10.5194/acp-19-3645-2019

Aiken, A. C., Decarlo, P. F., Kroll, J. H., Worsnop, D. R., Huffman, J. A., Docherty, K. S., Ulbrich, I. M., Mohr, C., Kimmel, J. R., Sueper, D., et al. (2008). O/c and om/oc ratios of primary, secondary, and ambient organic aerosols with high-resolution time-of-flight aerosol mass spectrometry. *Environmental science & technology*, *42*(12), 4478–4485.

Alemany, S., Crous-Bou, M., Vilor-Tejedor, N., Mila-Aloma, M., Suárez-Calvet, M., Salvadó, G., Cirach, M., Arenaza-Urquijo, E. M, Sanchez-Benavides, G., Grau-Rivera, O., et al. (2021). Associations between air pollution and biomarkers of alzheimer's disease in cognitively unimpaired individuals. *Environment international*, *157*, 106864.

Alier, M., Van Drooge, B. L., Dall'Osto, M., Querol, X., Grimalt, J. O., & T., R. (2013). Source apportionment of submicron organic aerosol at an urban background and a road site in barcelona (spain) during sapuss. *Atmospheric Chemistry and Physics*, *13*(20), 10353–10371.

Allan, J. D., Delia, A. E., Coe, H., Bower, K. N., Alfarra, M. R., Jimenez, J. L., Middlebrook, A. M., Drewnick, F., Onasch, T. B., Canagaratna, M. R., et al. (2004). A generalised method for the extraction of chemically resolved mass spectra from aerodyne aerosol mass spectrometer data. *Journal of Aerosol Science*, *35*(7), 909–922.

Amato, F., Alastuey, A., Karanasiou, A., Lucarelli, F., Nava, S., Calzolai, G., Severi, M., Becagli, S., Gianelle, V. L., Colombi, C., et al. (2016). Airuse-life+: A harmonized

pm speciation and source apportionment in five southern european cities. *Atmospheric Chemistry and Physics*, *16*(5), 3289–3309.

Andreae, M. O., & Gelencsér, A. (2006). Black carbon or brown carbon? the nature of light-absorbing carbonaceous aerosols. *Atmospheric Chemistry and Physics*, *6*(10), 3131–3148.

Arias, P., Bellouin, N., Coppola, E., Jones, R., Krinner, G., Marotzke, J., Naik, V., Palmer, M., Plattner, G.-K., Rogelj, J., Rojas, M., Sillmann, J., Storelvmo, T., Thorne, P., Trewin, B., Achuta Rao, K., Adhikary, B., Allan, R., Armour, K., ... Zickfeld, K. (2021). Technical summary. In V. Masson-Delmotte, P. Zhai, A. Pirani, S. Connors, C. Péan, S. Berger, N. Caud, Y. Chen, L. Goldfarb, M. Gomis, M. Huang, K. Leitzell, E. Lonnoy, J. Matthews, T. Maycock, T. Waterfield, O. Yelekçi, R. Yu, & B. Zhou (Eds.), *Climate change 2021: The physical science basis. contribution of working group i to the sixth assessment report of the intergovernmental panel on climate change* (33144). Cambridge University Press. https://doi.org/10.1017/9781009157896.002

Atkinson, R. W., Mills, I. C., Walton, H. A., & Anderson, H. R. (2015). Fine particle components and health—a systematic review and meta-analysis of epidemiological time series studies of daily mortality and hospital admissions. *Journal of exposure science & environmental epidemiology*, *25*(2), 208–214.

Ayres, J. G., Borm, P., Cassee, F. R., Castranova, V., Donaldson, K., Ghio, A., Harrison, R. M., Hider, R., Kelly, F., Kooter, I. M., et al. (2008). Evaluating the toxicity of airborne particulate matter and nanoparticles by measuring oxidative stress potential—a workshop report and consensus statement. *Inhalation toxicology*, *20*(1), 75–99.

Ball, G. H., & Hall, D. J. (1965). *Isodata, a novel method of data analysis and pattern classification* (tech. rep.). Stanford research inst Menlo Park CA.

Barrera-Escoda, A., Gonçalves, M., Guerreiro, D., Cunillera, J., & Baldasano, J. M. (2014). Projections of temperature and precipitation extremes in the north western mediterranean basin by dynamical downscaling of climate scenarios at high resolution (1971–2050). *Climatic Change*, *122*(4), 567–582.

Bates, J. T., Fang, T., Verma, V., Zeng, L., Weber, R. J., Tolbert, P. E., Abrams, J. Y., Sarnat, S. E., Klein, M., Mulholland, J. A., et al. (2019). Review of acellular assays of ambient particulate matter oxidative potential: Methods and relationships with composition, sources, and health effects. *Environmental science & technology*, *53*(8), 4003–4019.

Belis, C. A., Larsen, B. R., Amato, F., El Haddad, I., Favez, O., Harrison, R. M., Hopke, P. K., Nava, S., Paatero, P., Prevot, A., et al. (2014). European guide on air pollution source apportionment with receptor models. *JRC reference reports EUR26080 EN*.

Belis, C. A., Pernigotti, D., Karagulian, F., Pirovano, G., Larsen, B. R., Gerboles, M., & Hopke, P. K. (2015). A new methodology to assess the performance and uncertainty of source apportionment models in intercomparison exercises. *Atmospheric Environment*, *119*, 35–44.

Belis, C., Pikridas, M, Lucarelli, F, Petralia, E, Cavalli, F, Calzolai, G, Berico, M, & Sciare, J. (2019). Source apportionment of fine pm by combining high time resolution organic and inorganic chemical composition datasets. *Atmospheric Environment: X*, *3*, 100046.

Bian, H., Chin, M., Hauglustaine, D. A., Schulz, M., Myhre, G., Bauer, S. E., Lund, M. T., Karydis, V. A., Kucsera, T. L., Pan, X., et al. (2017). Investigation of global particulate nitrate from the aerocom phase iii experiment. *Atmospheric Chemistry and Physics*, *17*(21), 12911–12940.

Bove, M. C., Brotto, P., Calzolai, G., Cassola, F., Cavalli, F., Fermo, P., Hjorth, J., Massabò, D., Nava, S., Piazzalunga, A., et al. (2016). Pm10 source apportionment applying pmf and chemical tracer analysis to ship-borne measurements in the western mediterranean. *Atmospheric Environment*, *125*, 140–151.

Bressi, M., Cavalli, F., Putaud, J. P., Fröhlich, R., Petit, J. E., Aas, W., Äijälä, M., Alastuey, A., Allan, J. D., Aurela, M., et al. (2021). A european aerosol phenomenology-7: High-time resolution chemical characteristics of submicron particulate matter across europe. *Atmospheric environment: X*, *10*, 100108.

Brines, M., Dall'Osto, M., Amato, F., Minguillón, M. C., Karanasiou, A., Grimalt, J. O., Alastuey, A., Querol, X., & van Drooge, B. L. (2019). Source apportionment of urban pm1 in barcelona during sapuss using organic and inorganic components. *Environmental Science and Pollution Research*, *26*(31), 32114–32127.

Budisulistiorini, S. H., Canagaratna, M. R., Croteau, P. L., Baumann, K., Edgerton, E. S., Kollman, M. S., Ng, N. L., Verma, V., Shaw, S. L., Knipping, E. M., et al. (2014). Intercomparison of an aerosol chemical speciation monitor (acsm) with ambient fine aerosol measurements in downtown atlanta, georgia. *Atmospheric Measurement Techniques*, *7*(7), 1929–1941.

Buoli, M., Grassi, S., Caldiroli, A., Carnevali, G. S., Mucci, F., Iodice, S., Cantone, L., Pergoli, L., & Bollati, V. (2018). Is there a link between air pollution and mental disorders? *Environment international*, *118*, 154–168.

COST-COLOSSAL. (2019). *Guidelines for comparison of acsm measurements with co-located external data*. Retrieved December 2019, from https://cost-colossal.eu/wp-content/uploads/2019/12/COSTAction_CA16109_COLOSSAL_Deliverable1.2_20191216.pdf

COST-COLOSSAL. (2021). *Standard operation procedure*. Retrieved May 2021, from https://cost-colossal.eu/wp-content/uploads/2021/05/COLOSSAL-WG1_D1.1_Q-ACSM-Standard-Operating-Procedure_May2021.pdf

Calas, A., Uzu, G., Kelly, F. J., Houdier, S., Martins, J. M. F., Thomas, F., Molton, F., Charron, A., Dunster, C., Oliete, A., et al. (2018). Comparison between five acellular oxidative potential measurement assays performed with detailed chemistry on pm 10 samples from the city of chamonix (france). *Atmospheric Chemistry and Physics*, *18*(11), 7863–7875.

Canagaratna, M. R., Jayne, J. T., Jimenez, J. L., Allan, J. D., Alfarra, M. R., Zhang, Q., Onasch, T. B., Drewnick, F., Coe, H., Middlebrook, A., et al. (2007). Chemical and microphysical characterization of ambient aerosols with the aerodyne aerosol mass spectrometer. *Mass spectrometry reviews*, *26*(2), 185–222.

Canonaco, F., Slowik, J. G., Baltensperger, U., & Prévôt, A. S. H. (2015). Seasonal differences in oxygenated organic aerosol composition: Implications for emissions sources and factor analysis. *Atmospheric Chemistry and Physics*, *15*(12), 6993–7002.

Canonaco, F., Tobler, A., Chen, G., Sosedova, Y., Slowik, J. G., Bozzetti, C., Daellenbach, K. R., El Haddad, I., Crippa, M., Huang, R. J., et al. (2021). A new method for long-term source apportionment with time-dependent factor profiles and uncertainty assessment using sofi pro: Application to 1 year of organic aerosol data. *Atmospheric Measurement Techniques*, *14*(2), 923–943.

Cao, J., Wang, Q., Chow, J. C., Watson, J. G., Tie, X., Shen, Z., Wang, P., & An, Z. (2012). Impacts of aerosol compositions on visibility impairment in xi'an, china. *Atmospheric Environment*, *59*, 559–566.

Cao, L. M., Wei, J., He, L. Y., Zeng, H., Li, M. L., Zhu, Q., Yu, G. H., & Huang, X. F. (2022). Aqueous aging of secondary organic aerosol coating onto black carbon: Insights from simultaneous l-tof-ams and sp-ams measurements at an urban site in southern china. *Journal of Cleaner Production*, *330*, 129888.

Carslaw, K. S., Boucher, O., Spracklen, D. V., Mann, G. W., Rae, J. G. L., Woodward, S., & Kulmala, M. (2010). A review of natural aerosol interactions and feedbacks within the earth system. *Atmospheric Chemistry and Physics*, *10*(4), 1701–1737.

Caumette, G., Lienemann, C. P., Merdrignac, I., Bouyssiere, B., & Lobinski, R. (2009). Element speciation analysis of petroleum and related materials. *Journal of Analytical Atomic Spectrometry*, *24*(3), 263–276.

Cavalli, F., Viana, M., Yttri, K. E., Genberg, J., & Putaud, J. P. (2010). Toward a standardised thermal-optical protocol for measuring atmospheric organic and elemental carbon: The eusaar protocol. *Atmospheric Measurement Techniques*, *3*(1), 79–89.

Charlson, R. J. (1969). Atmospheric visibility related to aerosol mass concentration. *Environmental science & technology*, *3*(10), 913–918.

Chazeau, B., El Haddad, I., Canonaco, F., Temime-Roussel, B., d'Anna, B., Gille, G., Mesbah, B., Prévôt, A. S. H., Wortham, H., & Marchand, N. (2022). Organic aerosol source apportionment by using rolling positive matrix factorization: Application to a mediterranean coastal city. *Atmospheric environment: X*, *14*, 100176.

Chen, G., Canonaco, F., Slowik, J. G., Daellenbach, K. R., Tobler, A., Petit, J. E., Favez, O., Stavroulas, I., Mihalopoulos, N., Gerasopoulos, E., et al. (2022a). Real-time source apportionment of organic aerosols in three european cities. *Environmental science & technology*.

Chen, G., Canonaco, F., Tobler, A., Aas, W., Alastuey, A., Allan, J., Atabakhsh, S., Aurela, M., Baltensperger, U., Bougiatioti, A., et al. (2022b). European aerosol phenomenology-8: Harmonised source apportionment of organic aerosol using 22 year-long acsm/ams datasets. *Environment International*, 107325.

Cho, A. K., Sioutas, C., Miguel, A. H., Kumagai, Y., Schmitz, D. A., Singh, M., Eiguren-Fernandez, A., & Froines, J. R. (2005). Redox activity of airborne particulate matter at different sites in the los angeles basin. *Environmental research*, *99*(1), 40–47.

Clemente, Á., Yubero, E., Galindo, N., Crespo, J., Nicolás, J. F., Santacatalina, M., & Carratala, A. (2021). Quantification of the impact of port activities on pm10 levels at the port-city boundary of a mediterranean city. *Journal of Environmental Management*, *281*, 111842.

Cohen, A. J., Brauer, M., Burnett, R., Anderson, H. R., Frostad, J., Estep, K., Balakrishnan, K., Brunekreef, B., Dandona, L., Dandona, R., et al. (2017). Estimates and 25-year trends of the global burden of disease attributable to ambient air pollution: An analysis of data from the global burden of diseases study 2015. *The Lancet*, *389*(10082), 1907–1918.

Corbin, J. C., Mensah, A. A., Pieber, S. M., Orasche, J., Michalke, B., Zanatta, M., Czech, H., Massabò, D., Buatier de Mongeot, F., Mennucci, C., et al. (2018). Trace metals in soot and pm2. 5 from heavy-fuel-oil combustion in a marine engine. *Environmental science & technology*, *52*(11), 6714–6722.

Crippa, M., Canonaco, F., Slowik, J. G., El Haddad, I., DeCarlo, P. F., Mohr, C., Heringa, M. F., Chirico, R., Marchand, N., Temime-Roussel, B., et al. (2013). Primary and secondary organic aerosol origin by combined gas-particle phase source apportionment. *Atmospheric Chemistry and Physics*, *13*(16), 8411–8426.

Crippa, M., Canonaco, F, Lanz, V., Äijälä, M, Allan, J., Carbone, S, Capes, G, Ceburnis, D., Dall'Osto, M., Day, D., et al. (2014). Organic aerosol components derived from 25 ams data sets across europe using a consistent me-2 based source apportionment approach. *Atmospheric chemistry and physics*, *14*(12), 6159–6176.

Daellenbach, K. R., Uzu, G., Jiang, J., Cassagnes, L. E., Leni, Z., Vlachou, A., Stefenelli, G., Canonaco, F., Weber, S., Segers, A., et al. (2020). Sources of particulate-matter air pollution and its oxidative potential in europe. *Nature*, *587*(7834), 414–419.

Dai, Q., Bi, X., Song, W., Li, T., Liu, B., Ding, J., Xu, J., Song, C., Yang, N., Schulze, B. C., et al. (2019a). Residential coal combustion as a source of primary sulfate in xi'an, china. *Atmospheric Environment*, *196*, 66–76.

Dai, Q., Schulze, B. C., Bi, X., Bui, A. A. T., Guo, F., Wallace, H. W., Sanchez, N. P., Flynn, J. H., Lefer, B. L., Feng, Y., et al. (2019b). Seasonal differences in formation processes of oxidized organic aerosol near houston, tx. *Atmospheric Chemistry and Physics*, *19*(14), 9641–9661.

Dall'Osto, M., Querol, X., Amato, F., Karanasiou, A., Lucarelli, F., Nava, S., Calzolai, G., & Chiari, M. (2013). Hourly elemental concentrations in pm 2.5 aerosols sampled simultaneously at urban background and road site during sapuss–diurnal variations and pmf receptor modelling. *Atmospheric Chemistry and Physics*, *13*(8), 4375–4392.

de Prado, B. P., Mercader, E., H., M., Pujol, J., Sunyer, J., & Mortamais, M. (2018). The effects of air pollution on the brain: A review of studies interfacing environmental epidemiology and neuroimaging. *Current environmental health reports*, *5*(3), 351–364.

Drinovec, L., Močnik, G., Zotter, P., Prévôt, A. S. H., Ruckstuhl, C., Coz, E., Rupakheti, M., Sciare, J., Müller, T., Wiedensohler, A., et al. (2015). The" dual-spot" aethalometer: An improved measurement of aerosol black carbon

with real-time loading compensation. *Atmospheric measurement techniques*, *8*(5), 1965–1979.

EEA. (2022). *Air quality in europe 2022* (tech. rep. No. 05/2022). European Environmental Agency. doi:10.2800/488115

Efron, B. (2000). The bootstrap and modern statistics. *Journal of the American Statistical Association*, *95*(452), 1293–1296.

Escrig, A., Monfort, E., Celades, I., Querol, X., Amato, F., Minguillón, M. C., & Hopke, P. K. (2009). Application of optimally scaled target factor analysis for assessing source contribution of ambient pm10. *Journal of the Air & Waste Management Association*, *59*(11), 1296–1307.

European Comission. (2022). *Proposal for a directive of the european parliament and of the council on ambient air quality and cleaner air for europe* (tech. rep. No. 2022/524). European Comission. https://eur-lex.europa.eu/legal-content/EN/TXT/?uri=CELEX:52022PC0542

European EU Comission, E. M. S. P. P. (2022). *West mediterranean basin*. Retrieved February 22, 2022, from https://maritime-spatial-planning.ec.europa.eu/sea-basins/west-mediterranean

Fan, W., Chen, T., Zhu, Z., Zhang, H., Qiu, Y., & Yin, D. (2022). A review of secondary organic aerosols formation focusing on organosulfates and organic nitrates. *Journal of Hazardous Materials*, 128406.

Fernández-Camacho, R., Rodríguez, S., De la Rosa, J., Sánchez de la Campa, A. M., Alastuey, A., Querol, X., González-Castanedo, Y., Garcia-Orellana, I., & Nava, S. (2012). Ultrafine particle and fine trace metal (as, cd, cu, pb and zn) pollution episodes induced by industrial emissions in huelva, sw spain. *Atmospheric Environment*, *61*, 507–517.

Finlayson-Pitts, B. J., & Pitts Jr, J. N. (1999). *Chemistry of the upper and lower atmosphere: Theory, experiments, and applications*. Elsevier.

Fragkou, E., Douros, I., Moussiopoulos, N., & Belis, C. A. (2012). Current trends in the use of models for source apportionment of air pollutants in europe. *International Journal of Environment and Pollution*, *50*(1-4), 363–375.

Friedlander, S. K. (1973). Chemical element balances and identification of air pollution sources. *Environmental science & technology*, *7*(3), 235–240.

Fröhlich, R., Cubison, M. J., Slowik, J. G., Bukowiecki, N., Prévôt, A. S. H., Baltensperger, U., Schneider, J., Kimmel, J. R., Gonin, M., Rohner, U., et al. (2013). The tof-acsm: A portable aerosol chemical speciation monitor with tofms detection. *Atmospheric Measurement Techniques*, *6*(11), 3225–3241.

GBD. (2017). Global, regional, and national comparative risk assessment of 84 behavioural, environmental and occupational, and metabolic risks or clusters of risks, 1990–2016: A systematic analysis for the global burden of disease study 2016. *Lancet (London, England)*, *390*(10100), 1345.

Galindo, N., Clemente, Á., Yubero, E., Nicolás, J. F., & Crespo, J. (2021). Pm10 chemical composition at a residential site in the western mediterranean: Estimation of the contribution of biomass burning from levoglucosan and its isomers. *Environmental Research*, *196*, 110394.

García, M. I. (2017). *Origin of atmospheric aerosols transported across the north atlantic free troposphere* (Doctoral dissertation). Universidad de la Laguna.

Ghedini, N., Ozga, I., Bonazza, A., Dilillo, M., Cachier, H., & Sabbioni, C. (2011). Atmospheric aerosol monitoring as a strategy for the preventive conservation of urban monumental heritage: The florence baptistery. *Atmospheric Environment*, *45*(33), 5979–5987.

Giorgi, F., & Lionello, P. (2008). Climate change projections for the mediterranean region. *Global and planetary change*, *63*(2-3), 90–104.

Heikkinen, L., Äijälä, M., Daellenbach, K. R., Chen, G., Garmash, O., Aliaga, D., Graeffe, F., Räty, M., Luoma, K., Aalto, P., Kulmala, M., Petäjä, T., Worsnop, D., & Ehn, M. (2021). Eight years of sub-micrometre organic aerosol composition data from the boreal forest characterized using a machine-learning approach. *Atmospheric Chemistry and Physics*, *21*(13), 10081–10109. https://doi.org/10.5194/acp-21-10081-2021

Hidy, G. M. (2017). *Atmospheric sulfur and nitrogen oxides: Eastern north american source-receptor relationships*. Elsevier.

Hime, N. J., Marks, G. B., & Cowie, C. T. (2018). A comparison of the health effects of ambient particulate matter air pollution from five emission sources. *International journal of environmental research and public health*, *15*(6), 1206.

Hoyle, C. R., Boy, M., Donahue, N. M., Fry, J. L., Glasius, M., Guenther, A., Hallar, A. G., Huff Hartz, K., Petters, M. D., Petäjä, T., Rosenoern, T., & Sullivan, A. P. (2011). A review of the anthropogenic influence on biogenic secondary organic aerosol. *Atmospheric Chemistry and Physics*, *11*(1), 321–343. https://doi.org/10.5194/acp-11-321-2011

Iinuma, Y., Müller, C., Böge, O., Gnauk, T., & Herrmann, H. (2007). The formation of organic sulfate esters in the limonene ozonolysis secondary organic aerosol (soa) under acidic conditions. *Atmospheric Environment*, *41*(27), 5571–5583.

In't Veld, M., Alastuey, A., Pandolfi, M., Amato, F., Perez, N., Reche, C., Via, M., Minguillon, M. C., Escudero, M., & Querol, X. (2021). Compositional changes of pm2. 5 in ne spain during 2009–2018: A trend analysis of the chemical composition and source apportionment. *Science of the Total Environment*, *795*, 148728.

In't Veld, M., Pandolfi, M., Amato, F., Perez, N., Reche, C., Dominutti, P., Jaffrezo, J., Alastuey, A., Querol, X., & Uzu, G. (2022). Discovering oxidative potential (op) drivers of atmospheric pm10, pm2. 5, and pm1 simultaneously in north-eastern spain. *Science of the Total Environment*, *857*, 159386.

Jacob, D. J. (1999). *Introduction to atmospheric chemistry*. Princeton University Press.

Jayne, J. T., Leard, D. C., Zhang, X., Davidovits, P., Smith, K. A., Kolb, C. E., & Worsnop, D. R. (2000). Development of an aerosol mass spectrometer for size and composition analysis of submicron particles. *Aerosol Science & Technology*, *33*(1-2), 49–70.

Jimenez, J. L., Canagaratna, M. R., Donahue, N. M., Prevot, A. S. H., Zhang, Q., Kroll, J. H., DeCarlo, P. F., Allan, J. D., Coe, H., Ng, N. L., et al. (2009). Evolution of organic aerosols in the atmosphere. *science*, *326*(5959), 1525–1529.

Jimenez, J. L., Jayne, J. T., Shi, Q., Kolb, C. E., Worsnop, D. R., Yourshaw, I., Seinfeld, J. H., Flagan, R. C., Zhang, X., Smith, K. A., et al. (2003). Ambient aerosol sampling using the aerodyne aerosol mass spectrometer. *Journal of Geophysical Research: Atmospheres*, *108*(D7).

Jorba, O., Pandolfi, M., Spada, M., Baldasano, J. M., Pey, J., Alastuey, A., Arnold, D., Sicard, M., Artiñano, B., Revuelta, M. A., et al. (2013). Overview of the meteorology and transport patterns during the daure field campaign and their impact to pm observations. *Atmospheric environment*, *77*, 607–620.

Kang, E., Toohey, D. W., & Brune, W. H. (2011). Dependence of soa oxidation on organic aerosol mass concentration and oh exposure: Experimental pam chamber studies. *Atmospheric Chemistry and Physics*, *11*(4), 1837–1852. https://doi.org/10.5194/acp-11-1837-2011

Karjalainen, P., Pirjola, L., Heikkilä, J., Lähde, T., Tzamkiozis, T., Ntziachristos, L., Keskinen, J., & Rönkkö, T. (2014). Exhaust particles of modern gasoline vehicles: A laboratory and an on-road study. *Atmospheric Environment*, *97*, 262–270. https://doi.org/https://doi.org/10.1016/j.atmosenv.2014.08.025

Kasdagli, M. I., Katsouyanni, K., Dimakopoulou, K., & Samoli, E. (2019). Air pollution and parkinson's disease: A systematic review and meta-analysis up to 2018. *International journal of hygiene and environmental health*, *222*(3), 402–409.

Kasthuriarachchi, N. Y., Rivellini, L. H., Adam, M. G., & Lee, A. K. Y. (2020). Light absorbing properties of primary and secondary brown carbon in a tropical urban environment. *Environmental Science & Technology*, *54*(17), 10808–10819.

Khare, P., Machesky, J., Soto, R., He, M., Presto, A. A., & Gentner, D. R. (2020). Asphalt-related emissions are a major missing nontraditional source of secondary organic aerosol precursors. *Science Advances*, *6*(36), eabb9785.

Laj, P., Bigi, A., Rose, C., Andrews, E., Lund-Myhre, C., Collaud-Coen, M., Lin, Y., Wiedensohler, A., Schulz, M., Ogren, J. A., et al. (2020). A global analysis of climate-relevant aerosol properties retrieved from the network of global atmosphere watch (gaw) near-surface observatories. *Atmospheric Measurement Techniques*, *13*(8), 4353–4392.

Lehner, B., Döll, P., Alcamo, J., Henrichs, T., & Kaspar, F. (2006). Estimating the impact of global change on flood and drought risks in europe: A continental, integrated analysis. *Climatic Change*, *75*(3), 273–299.

Li, G., Bei, N., Cao, J., Huang, R., Wu, J., Feng, T., Wang, Y., Liu, S., Zhang, Q., Tie, X., & Molina, L. T. (2017a). A possible pathway for rapid growth of sulfate during haze days in china. *Atmospheric Chemistry and Physics*, *17*(5), 3301–3316. https://doi.org/10.5194/acp-17-3301-2017

Li, J., Carlson, B. E., Yung, Y. L., Lv, D., Hansen, J., Penner, J. E., Liao, H., Ramaswamy, V., Kahn, R. A, Zhang, P., et al. (2022a). Scattering and absorbing aerosols in the climate system. *Nature Reviews Earth & Environment*, *3*(6), 363–379.

Li, J., Li, J., Wang, G., Ho, K. F., Han, J., Dai, W., Wu, C., Cao, C., & Liu, L. (2022b). In-vitro oxidative potential and inflammatory response of ambient pm2. 5 in a rural region of northwest china: Association with chemical compositions and source contribution. *Environmental Research*, *205*, 112466.

Li, W., Xu, L., Liu, X., Zhang, J., Lin, Y., Yao, X., Gao, H., Zhang, D., Chen, J., Wang, W., Harrison, R. M., Zhang, X., Shao, L., Fu, P., Nenes, A., & Shi, Z. (2017b). Air pollution–aerosol interactions produce more bioavailable iron for ocean ecosystems. *Science Advances*, *3*(3), e1601749. https://doi.org/10.1126/sciadv.1601749

Li, Z., Tang, Y., Song, X., Lazar, L., Li, Z., & Zhao, J. (2019). Impact of ambient pm2. 5 on adverse birth outcome and potential molecular mechanism. *Ecotoxicology and Environmental Safety*, *169*, 248–254.

Liu, P. S. K., Deng, R., Smith, K. A., Williams, L. R., Jayne, J. T., Canagaratna, M. R., Moore, K., Onasch, T. B., Worsnop, D. R., & Deshler, T. (2007). Transmission efficiency of an aerodynamic focusing lens system: Comparison of model

calculations and laboratory measurements for the aerodyne aerosol mass spectrometer. *Aerosol Science and Technology*, *41*(8), 721–733.

Liu, P., Ye, C., Xue, C., Zhang, C., Mu, Y., & Sun, X. (2020). Formation mechanisms of atmospheric nitrate and sulfate during the winter haze pollution periods in beijing: Gas-phase, heterogeneous and aqueous-phase chemistry. *Atmospheric Chemistry and Physics*, *20*(7), 4153–4165.

Liu, S., Aiken, A. C., Gorkowski, K., Dubey, M. K., Cappa, C. D., Williams, L. R., Herndon, S. C., Massoli, P., Fortner, E. C., Chhabra, P. S., et al. (2015). Enhanced light absorption by mixed source black and brown carbon particles in uk winter. *Nature communications*, *6*(1), 1–10.

Lucas, D. D., & Prinn, R. G. (2005). Parametric sensitivity and uncertainty analysis of dimethylsulfide oxidation in the clear-sky remote marine boundary layer. *Atmospheric Chemistry and Physics*, *5*(6), 1505–1525.

Mahowald, N. M., Scanza, R., Brahney, J., Goodale, C. L., Hess, P. G., Moore, J. K., & Neff, J. (2017). Aerosol deposition impacts on land and ocean carbon cycles. *Current Climate Change Reports*, *3*(1), 16–31.

Malm, W. C., Sisler, J. F., Huffman, D., Eldred, R. A, & Cahill, T. A. (1994). Spatial and seasonal trends in particle concentration and optical extinction in the united states. *Journal of Geophysical Research: Atmospheres*, *99*(D1), 1347–1370.

Martin-Vide, J., & Lopez-Bustins, J. A. (2006). The western mediterranean oscillation and rainfall in the iberian peninsula. *International Journal of Climatology: A Journal of the Royal Meteorological Society*, *26*(11), 1455–1475.

Massagué, J., Carnerero, C., Escudero, M., Baldasano, J. M., Alastuey, A., & Querol, X. (2019). 2005–2017 ozone trends and potential benefits of local measures as deduced from air quality measurements in the north of the barcelona metropolitan area. *Atmospheric Chemistry and Physics*, *19*(11), 7445–7465.

Matthew, B. M., Middlebrook, A. M., & Onasch, T. B. (2008). Collection efficiencies in an aerodyne aerosol mass spectrometer as a function of particle phase for laboratory generated aerosols. *Aerosol Science and Technology*, *42*(11), 884–898.

McCutcheon, J., Lutz, S., Williamson, C., Cook, J. M., Tedstone, A. J., Vanderstraeten, A., Wilson, S. A, Stockdale, A., Bonneville, S., Anesio, A. M., et al. (2021). Mineral phosphorus drives glacier algal blooms on the greenland ice sheet. *Nature communications*, *12*(1), 1–11.

McDonald, B. C., De Gouw, J. A., Gilman, J. B., Jathar, S. H., Akherati, A., Cappa, C. D., Jimenez, J. L., Lee-Taylor, J., Hayes, P. L., McKeen, S. A., et al. (2018). Volatile

chemical products emerging as largest petrochemical source of urban organic emissions. *Science*, *359*(6377), 760–764.

Meszaros, E. et al. (1999). *Fundamentals of atmospheric aerosol chemistry*. Akadémiai kiado.

Meteocat. (2023). *Anuari de dades de la xema*. Retrieved September 26, 2022, from https://www.meteo.cat/wpweb/climatologia/serveis-i-dades-climatiques/anuaris-de-dades-meteorologiques/xarxa-destacions-meteorologiques-automatiques/.xtml

Middlebrook, A. M., Bahreini, R., Jimenez, J. L., & Canagaratna, M. R. (2012). Evaluation of composition-dependent collection efficiencies for the aerodyne aerosol mass spectrometer using field data. *Aerosol Science and Technology*, *46*(3), 258–271.

Millán, M. M., Salvador, R., Mantilla, E., & Kallos, G. (1997). Photooxidant dynamics in the mediterranean basin in summer: Results from european research projects. *Journal of Geophysical Research: Atmospheres*, *102*(D7), 8811–8823.

Minguillón, M. C., Pérez, N., Marchand, N., Bertrand, A., Temime-Roussel, B., Agrios, K., Szidat, S., Van Drooge, B., Sylvestre, A., Alastuey, A., et al. (2016). Secondary organic aerosol origin in an urban environment: Influence of biogenic and fuel combustion precursors. *Faraday Discussions*, *189*, 337–359.

Minguillón, M. C., Perron, N., Querol, X., Szidat, S., Fahrni, S. M., Alastuey, A., Jimenez, J. L., Mohr, C., Ortega, A. M., Day, D. A., et al. (2011). Fossil versus contemporary sources of fine elemental and organic carbonaceous particulate matter during the daure campaign in northeast spain. *Atmospheric Chemistry and Physics*, *11*(23), 12067–12084.

Minguillón, M. C., Ripoll, A., Perez, N., Prévôt, A. S., Canonaco, F., Querol, X., & Alastuey, A. (2015). Chemical characterization of submicron regional background aerosols in the western mediterranean using an aerosol chemical speciation monitor. *Atmospheric Chemistry and Physics*, *15*(11), 6379–6391.

Minguillón, M., Querol, X., Alastuey, A., Monfort, E., Mantilla, E., Sanz, M., Sanz, F., Roig, A., Renau, A., Felis, C., Miró, J., & Artíñano, B. (2007). Pm10 speciation and determination of air quality target levels. a case study in a highly industrialized area of spain. *Science of The Total Environment*, *372*(2), 382–396. https://doi.org/https://doi.org/10.1016/j.scitotenv.2006.10.023

Mircea, M., Bessagnet, B., D'Isidoro, M., Pirovano, G., Aksoyoglu, S., Ciarelli, G., Tsyro, S., Manders, A., Bieser, J., Stern, R., García-Vivanco, M., Cuvelier, C., Aas, W., Prévôt, A. S. H., Aulinger, A., Briganti, G., Calori, G., Cappelletti, A.,

Colette, A., ... Carbone, S. (2019). Eurodelta iii exercise: An evaluation of air quality models' capacity to reproduce the carbonaceous aerosol. *Atmospheric Environment: X*, *2*, 100018. https://doi.org/https://doi.org/10.1016/j.aeaoa.2019.100018

Mohr, C., DeCarlo, P. F., Heringa, M. F., Chirico, R., Slowik, J. G., Richter, R., Reche, C., Alastuey, A., Querol, X., Seco, R., et al. (2012). Identification and quantification of organic aerosol from cooking and other sources in barcelona using aerosol mass spectrometer data. *Atmospheric Chemistry and Physics*, *12*(4), 1649–1665.

Morillas, H., França, F. M. F., Derluyn, H., Maguregui, M., Grégoire, D., & Madariaga, J. M. (2020). Decay processes in buildings close to the sea induced by marine aerosol: Salt depositions inside construction materials. *Science of The Total Environment*, *721*, 137687. https://doi.org/https://doi.org/10.1016/j.scitotenv.2020.137687

Morino, Y., Nagashima, T., Sugata, S., Sato, K., Tanabe, K., Noguchi, T., Takami, A., Tanimoto, H., Ohara, T., et al. (2015). Verification of chemical transport models for pm2. 5 chemical composition using simultaneous measurement data over japan. *Aerosol and Air Quality Research*, *15*(5), 2009–2023.

Myhre, G., Samset, B. H., Schulz, M., Balkanski, Y., Bauer, S., Berntsen, T. K., Bian, H., Bellouin, N., Chin, M., Diehl, T., et al. (2013). Radiative forcing of the direct aerosol effect from aerocom phase ii simulations. *Atmospheric Chemistry and Physics*, *13*(4), 1853–1877.

Na, K., Song, C., & Cocker, D. R. (2006). Formation of secondary organic aerosol from the reaction of styrene with ozone in the presence and absence of ammonia and water. *Atmospheric Environment*, *40*(10), 1889–1900.

Ng, N. L., Brown, S. S., Archibald, A. T., Atlas, E., Cohen, R. C., Crowley, J. N., Day, D. A., Donahue, N. M., Fry, J. L., Fuchs, H., et al. (2017). Nitrate radicals and biogenic volatile organic compounds: Oxidation, mechanisms, and organic aerosol. *Atmospheric chemistry and physics*, *17*(3), 2103–2162.

Ng, N. L., Herndon, S. C., Trimborn, A., Canagaratna, M. R., Croteau, P. L., Onasch, T. B., Sueper, D., Worsnop, D. R., Zhang, Q., Sun, Y. L., et al. (2011). An aerosol chemical speciation monitor (acsm) for routine monitoring of the composition and mass concentrations of ambient aerosol. *Aerosol Science and Technology*, *45*(7), 780–794.

Ng, N. L., Kwan, A. J., Surratt, J. D., Chan, A. W. H., Chhabra, P. S., Sorooshian, A., Pye, H. O. T., Crounse, J. D., Wennberg, P. O., Flagan, R. C., et al. (2008). Secondary

organic aerosol (soa) formation from reaction of isoprene with nitrate radicals (no 3). *Atmospheric Chemistry and Physics*, *8*(14), 4117–4140.

Nicolás, J., Chiari, M., Crespo, J., Orellana, I. G., Lucarelli, F., Nava, S., Pastor, C., & Yubero, E. (2008). Quantification of saharan and local dust impact in an arid mediterranean area by the positive matrix factorization (pmf) technique. *Atmospheric Environment*, *42*(39), 8872–8882.

Noziere, B., Kalberer, M., Claeys, M., Allan, J., D'Anna, B., Decesari, S., Finessi, E., Glasius, M., Grgic, I., Hamilton, J. F., et al. (2015). The molecular identification of organic compounds in the atmosphere: State of the art and challenges. *Chemical reviews*, *115*(10), 3919–3983.

Ostro, B., Tobias, A., Querol, X., Alastuey, A., Amato, F., Pey, J., Pérez, N., & Sunyer, J. (2011). The effects of particulate matter sources on daily mortality: A case-crossover study of barcelona, spain. *Environmental health perspectives*, *119*(12), 1781–1787.

Paatero, P. (1999). The multilinear engine—a table-driven, least squares program for solving multilinear problems, including the n-way parallel factor analysis model. *Journal of Computational and Graphical Statistics*, *8*(4), 854–888.

Paatero, P., & Hopke, P. K. (2003). Discarding or downweighting high-noise variables in factor analytic models. *Analytica Chimica Acta*, *490*(1-2), 277–289.

Paatero, P., Hopke, P. K., Song, X. H., & Ramadan, Z. (2002). Understanding and controlling rotations in factor analytic models. *Chemometrics and intelligent laboratory systems*, *60*(1-2), 253–264.

Paatero, P., & Tapper, U. (1994). Positive matrix factorization: A non-negative factor model with optimal utilization of error estimates of data values. *Environmetrics*, *5*(2), 111–126.

Paglione, M., Gilardoni, S., Rinaldi, M., Decesari, S., Zanca, N., Sandrini, S., Giulianelli, L., Bacco, D., Ferrari, S., Poluzzi, V., et al. (2020). The impact of biomass burning and aqueous-phase processing on air quality: A multi-year source apportionment study in the po valley, italy. *Atmospheric Chemistry and Physics*, *20*(3), 1233–1254.

Pandolfi, M., Alastuey, A., Pérez, N., Reche, C., Castro, I., Shatalov, V., & Querol, X. (2016). Trends analysis of pm source contributions and chemical tracers in ne spain during 2004–2014: A multi-exponential approach. *Atmospheric Chemistry and Physics*, *16*(18), 11787–11805.

Pandolfi, M., Mooibroek, D., Hopke, P., van Pinxteren, D., Querol, X., Herrmann, H., Alastuey, A., Favez, O., Hüglin, C., Perdrix, E., Riffault, V., Sauvage, S.,

van der Swaluw, E., Tarasova, O., & Colette, A. (2020). Long-range and local air pollution: What can we learn from chemical speciation of particulate matter at paired sites? *Atmospheric Chemistry and Physics*, *20*(1), 409–429. https://doi.org/10.5194/acp-20-409-2020

Pandolfi, M., Querol, X., Alastuey, A., Jimenez, J. L., Jorba, O., Day, D., Ortega, A., Cubison, M. J., Comerón, A., Sicard, M., et al. (2014). Effects of sources and meteorology on particulate matter in the western mediterranean basin: An overview of the daure campaign. *Journal of Geophysical Research: Atmospheres*, *119*(8), 4978–5010.

Parasin, N., Amnuaylojaroen, T., & Saokaew, S. (2021). Effect of air pollution on obesity in children: A systematic review and meta-analysis. *Children*, *8*(5), 327.

Parworth, C., Fast, J., Mei, F., Shippert, T., Sivaraman, C., Tilp, A., Watson, T., & Zhang, Q. (2015). Long-term measurements of submicrometer aerosol chemistry at the southern great plains (sgp) using an aerosol chemical speciation monitor (acsm). *Atmospheric Environment*, *106*, 43–55.

Pérez, N., Pey, J., Cusack, M., Reche, C., Querol, X., Alastuey, A., & Viana, M. (2010). Variability of particle number, black carbon, and pm10, pm2. 5, and pm1 levels and speciation: Influence of road traffic emissions on urban air quality. *Aerosol Science and Technology*, *44*(7), 487–499.

Petzold, A., Ogren, J. A., Fiebig, M., Laj, P., Li, S. M., Baltensperger, U., Holzer-Popp, T., Kinne, S., Pappalardo, G., Sugimoto, N., et al. (2013). Recommendations for reporting" black carbon" measurements. *Atmospheric Chemistry and Physics*, *13*(16), 8365–8379.

Petzold, A., & Schönlinner, M. (2004). Multi-angle absorption photometry—a new method for the measurement of aerosol light absorption and atmospheric black carbon. *Journal of Aerosol Science*, *35*(4), 421–441.

Pey, J., Pérez, N., Querol, X., Alastuey, A., Cusack, M., & Reche, C. (2010). Intense winter atmospheric pollution episodes affecting the western mediterranean. *Science of the total environment*, *408*(8), 1951–1959.

Pey, J., Querol, X., Alastuey, A., Forastiere, F., & Stafoggia, M. (2013). African dust outbreaks over the mediterranean basin during 2001ndash;2011: Pm_{10} concentrations, phenomenology and trends, and its relation with synoptic and mesoscale meteorology. *Atmospheric Chemistry and Physics*, *13*(3), 1395–1410. https://doi.org/10.5194/acp-13-1395-2013

Piscitello, A., Bianco, C., Casasso, A., & Sethi, R. (2021). Non-exhaust traffic emissions: Sources, characterization, and mitigation measures. *Science of the Total Environment*, *766*, 144440.

Porter, W. C., Jimenez, J. L., & Barsanti, K. C. (2021). Quantifying atmospheric parameter ranges for ambient secondary organic aerosol formation. *ACS Earth and Space Chemistry*, *5*(9), 2380–2397.

Pöschl, U. (2005). Atmospheric aerosols: Composition, transformation, climate and health effects. *Angewandte Chemie International Edition*, *44*(46), 7520–7540.

Poulain, L., Spindler, G., Grüner, A., Tuch, T., Stieger, B., van Pinxteren, D., Petit, J. E., Favez, O., Herrmann, H., & Wiedensohler, A. (2020). Multi-year acsm measurements at the central european research station melpitz (germany)–part 1: Instrument robustness, quality assurance, and impact of upper size cutoff diameter. *Atmospheric Measurement Techniques*, *13*(9), 4973–4994.

Putaud, J. P., Raes, F., Van Dingenen, R., Brüggemann, E., Facchini, M. C., Decesari, S., Fuzzi, S., Gehrig, R., Hüglin, C., Laj, P., et al. (2004). A european aerosol phenomenology—2: Chemical characteristics of particulate matter at kerbside, urban, rural and background sites in europe. *Atmospheric environment*, *38*(16), 2579–2595.

Qin, Y. M., Tan, H. B., Li, Y. J., Li, Z. J., Schurman, M. I., Liu, L., Wu, C., & Chan, C. K. (2018). Chemical characteristics of brown carbon in atmospheric particles at a suburban site near guangzhou, china. *Atmospheric Chemistry and Physics*, *18*(22), 16409–16418.

Querol, X., Alastuey, A., Rodriguez, S., Plana, F., Mantilla, E., & Ruiz, C. R. (2001). Monitoring of pm10 and pm2. 5 around primary particulate anthropogenic emission sources. *Atmospheric Environment*, *35*(5), 845–858.

Querol, X., Minguillón, M., Alastuey, A, Monfort, E, Mantilla, E, Sanz, M., Sanz, F, Roig, A, Renau, A, Felis, C, et al. (2007). Impact of the implementation of pm abatement technology on the ambient air levels of metals in a highly industrialised area. *Atmospheric Environment*, *41*(5), 1026–1040.

Quinn, P. K., Bates, T. S., Coffman, D., Onasch, T. B., Worsnop, D., Baynard, T., De Gouw, J. A., Goldan, P. D., Kuster, W. C., Williams, E., et al. (2006). Impacts of sources and aging on submicrometer aerosol properties in the marine boundary layer across the gulf of maine. *Journal of Geophysical Research: Atmospheres*, *111*(D23).

Ravishankara, A. R. (2003). Introduction: Atmospheric chemistry long-term issues. *Chemical Reviews*, *103*(12), 4505–4508.

Remer, L. A., Kleidman, R. G., Levy, R. C., Kaufman, Y. J., Tanré, D., Mattoo, S., Martins, J. V., Ichoku, C., Koren, I., Yu, H., et al. (2008). Global aerosol climatology from the modis satellite sensors. *Journal of Geophysical Research: Atmospheres*, *113*(D14).

Reyes-Villegas, E., Bannan, T., Le Breton, M., Mehra, A., Priestley, M., Percival, C., Coe, H., & Allan, J. D. (2018). Online chemical characterization of food-cooking organic aerosols: Implications for source apportionment. *Environmental science & technology*, *52*(9), 5308–5318.

Rich, D. Q., Zhang, W., Lin, S., Squizzato, S., Thurston, S. W., van Wijngaarden, E., Croft, D., Masiol, M., & Hopke, P. K. (2019). Triggering of cardiovascular hospital admissions by source specific fine particle concentrations in urban centers of new york state. *Environment international*, *126*, 387–394.

Ripoll, A., Minguillón, M. C., Pey, J., Jimenez, J. L., Day, D. A., Sosedova, Y., Canonaco, F., Prévôt, A. S. H., Querol, X., & Alastuey, A. (2015). Long-term real-time chemical characterization of submicron aerosols at montsec (southern pyrenees, 1570 m asl). *Atmospheric Chemistry and Physics*, *15*(6), 2935–2951.

Ripoll, A., Pey, J., Minguillón, M. C., Pérez, N., Pandolfi, M., Querol, X., & Alastuey, A. (2014). Three years of aerosol mass, black carbon and particle number concentrations at montsec (southern pyrenees, 1570 m a.s.l.) *Atmospheric Chemistry and Physics*, *14*(8), 4279–4295. https://doi.org/10.5194/acp-14-4279-2014

Ritchie, H., & Roser, M. (2017). Air pollution [https://ourworldindata.org/air-pollution]. *Our World in Data*.

Romakkaniemi, S., Arola, A., Kokkola, H., Birmili, W., Tuch, T., Kerminen, V. M., Räisänen, P., Smith, J. N., Korhonen, H., & Laaksonen, A. (2012). Effect of aerosol size distribution changes on aod, ccn and cloud droplet concentration: Case studies from erfurt and melpitz, germany. *Journal of Geophysical Research: Atmospheres*, *117*(D7).

Ropkins, K., Beebe, J., Li, H., Daham, B., Tate, J., Bell, M., & Andrews, G. (2009). Real-world vehicle exhaust emissions monitoring: Review and critical discussion. *Critical Reviews in Environmental Science and Technology*, *39*(2), 79–152.

Rudnick, R. L. (2018). Earth's continental crust. In W. M. White (Ed.), *Encyclopedia of geochemistry: A comprehensive reference source on the chemistry of the earth* (pp. 392–418). Springer International Publishing. https://doi.org/10.1007/978-3-319-39312-4_277

Saiz-Lopez, A., Borge, R., Notario, A., Adame, J. A., Paz, D., Querol, X., Artíñano, B., Gómez-Moreno, F. J., & Cuevas, C. A. (2017). Unexpected increase in the oxidation capacity of the urban atmosphere of madrid, spain. *Scientific reports*, *7*(1), 1–11.

Sakka, A., Gerasopoulos, E., Liakakou, E., Keramitsoglou, I., & Zacharias, N. (2020). Spatial variability of aerosols over greek archaeological sites using space-borne remote sensing. *Journal of Cultural Heritage*, *46*, 207–217.

Salameh, D., Detournay, A., Pey, J., Pérez, N., Liguori, F., Saraga, D., Bove, M. C., Brotto, P., Cassola, F., Massabò, D., et al. (2015). Pm2. 5 chemical composition in five european mediterranean cities: A 1-year study. *Atmospheric Research*, *155*, 102–117.

Salo, K., Hallquist, M., Jonsson, Å. M., Saathoff, H., Naumann, K.-H., Spindler, C., Tillmann, R., Fuchs, H., Bohn, B., Rubach, F., Mentel, T. F., Müller, L., Reinnig, M., Hoffmann, T., & Donahue, N. M. (2011). Volatility of secondary organic aerosol during oh radical induced ageing. *Atmospheric Chemistry and Physics*, *11*(21), 11055–11067. https://doi.org/10.5194/acp-11-11055-2011

Sandradewi, J., Prévôt, A. S. H., Szidat, S., Perron, N., Alfarra, M. R., Lanz, V. A, Weingartner, E., & Baltensperger, U. (2008). Using aerosol light absorption measurements for the quantitative determination of wood burning and traffic emission contributions to particulate matter. *Environmental science & technology*, *42*(9), 3316–3323.

Scerri, M. M., Genga, A., Iacobellis, S., Delmaire, G., Giove, A., Siciliano, M., Siciliano, T., & Weinbruch, S. (2019). Investigating the plausibility of a pmf source apportionment solution derived using a small dataset: A case study from a receptor in a rural site in apulia-south east italy. *Chemosphere*, *236*, 124376.

Schaap, M., van Loon, M., ten Brink, H. M., Dentener, F. J., & Builtjes, P. J. H. (2004). Secondary inorganic aerosol simulations for europe with special attention to nitrate. *Atmospheric Chemistry and Physics*, *4*(3), 857–874. https://doi.org/10.5194/acp-4-857-2004

Schembari, C., Bove, M. C., Cuccia, E., Cavalli, F., Hjorth, J., Massabò, D., Nava, S., Udisti, R., & Prati, P. (2014). Source apportionment of pm10 in the western mediterranean based on observations from a cruise ship. *Atmospheric Environment*, *98*, 510–518.

Seinfeld, J., & Pandis, S. (2008). Atmospheric chemistry and physics. 1997. *New York*.

Shah, R. U., Coggon, M. M., Gkatzelis, G. I, McDonald, B. C., Tasoglou, A., Huber, H., Gilman, J., Warneke, C., Robinson, A. L., & Presto, A. A. (2019).

Urban oxidation flow reactor measurements reveal significant secondary organic aerosol contributions from volatile emissions of emerging importance. *Environmental science & technology*, *54*(2), 714–725.

Shrivastava, M., Cappa, C. D., Fan, J., Goldstein, A. H., Guenther, A. B., Jimenez, J. L., Kuang, C., Laskin, A., Martin, S. T., Ng, N. L., et al. (2017). Recent advances in understanding secondary organic aerosol: Implications for global climate forcing. *Reviews of Geophysics*, *55*(2), 509–559.

Slowik, J. G., Stroud, C., Bottenheim, J. W., Brickell, P. C., Chang, R. Y. W., Liggio, J., Makar, P. A., Martin, R. V., Moran, M. D., Shantz, N. C., et al. (2010). Characterization of a large biogenic secondary organic aerosol event from eastern canadian forests. *Atmospheric Chemistry and Physics*, *10*(6), 2825–2845.

Soler, M. R., Arasa, R., Merino, M., Olid, M., & Ortega, S. (2011). Modelling local sea-breeze flow and associated dispersion patterns over a coastal area in north-east spain: A case study. *Boundary-layer meteorology*, *140*(1), 37–56.

Sonwani, S., Madaan, S., Arora, J., Suryanarayan, S., Rangra, D., Mongia, N., Vats, T., & Saxena, P. (2021). Inhalation exposure to atmospheric nanoparticles and its associated impacts on human health: A review. *Frontiers in Sustainable Cities*, *3*, 690444.

Stein, A. F., Draxler, R. R., Rolph, G. D., Stunder, B. J. B., Cohen, M. D., & Ngan, F. (2015). Noaa's hysplit atmospheric transport and dispersion modeling system. *Bulletin of the American Meteorological Society*, *96*(12), 2059–2077.

Sullivan, A. P., Hodas, N., Turpin, B. J., Skog, K., Keutsch, F. N., Gilardoni, S., Paglione, M., Rinaldi, M., Decesari, S., Facchini, M. C., et al. (2016). Evidence for ambient dark aqueous soa formation in the po valley, italy. *Atmospheric Chemistry and Physics*, *16*(13), 8095–8108.

Sun, X., Wang, H., Guo, Z., Lu, P., Song, F., Liu, L., Liu, J., Rose, N. L., & Wang, F. (2020). Positive matrix factorization on source apportionment for typical pollutants in different environmental media: A review. *Environmental Science: Processes & Impacts*, *22*(2), 239–255.

Sunyer, J., Esnaola, M., Alvarez-Pedrerol, M., Forns, J., Rivas, I., López-Vicente, M., Suades-González, E., Foraster, M., Garcia-Esteban, R., Basagaña, X., et al. (2015). Association between traffic-related air pollution in schools and cognitive development in primary school children: A prospective cohort study. *PLoS medicine*, *12*(3), e1001792.

Tang, M., Zhang, H., Gu, W., Gao, J., Jian, X., Shi, G., Zhu, B., Xie, L., Guo, L., Gao, X., et al. (2019). Hygroscopic properties of saline mineral dust from different

regions in china: Geographical variations, compositional dependence, and atmospheric implications. *Journal of Geophysical Research: Atmospheres*, *124*(20), 10844–10857.

Tang, W., Llort, J., Weis, J., Perron, M. M. G., Basart, S., Li, Z., Sathyendranath, S., Jackson, T., Sanz-Rodriguez, E., Proemse, B. C., et al. (2021). Widespread phytoplankton blooms triggered by 2019–2020 australian wildfires. *Nature*, *597*(7876), 370–375.

Thorpe, A., & Harrison, R. M. (2008). Sources and properties of non-exhaust particulate matter from road traffic: A review. *Science of the total environment*, *400*(1-3), 270–282.

Thurston, G. D., Ito, K., Hayes, C. G., Bates, D. V., & Lippmann, M. (1994). Respiratory hospital admissions and summertime haze air pollution in toronto, ontario: Consideration of the role of acid aerosols. *Environmental research*, *65*(2), 271–290.

Tobías, A., Carnerero, C., Reche, C., Massagué, J., Via, M., Minguillón, M. C., Alastuey, A., & Querol, X. (2020). Changes in air quality during the lockdown in barcelona (spain) one month into the sars-cov-2 epidemic. *Science of the total environment*, *726*, 138540.

Tong, Y., Qi, L., Stefenelli, G., Wang, D. S., Canonaco, F., Baltensperger, U., Prévôt, A. S. H., & Slowik, J. G. (2022). Quantification of primary and secondary organic aerosol sources by combined factor analysis of extractive electrospray ionisation and aerosol mass spectrometer measurements (eesi-tof and ams). *Atmospheric Measurement Techniques Discussions*, 1–50.

Tsigaridis, K., Daskalakis, N., Kanakidou, M., Adams, P. J., Artaxo, P., Bahadur, R., Balkanski, Y., Bauer, S. E., Bellouin, N., Benedetti, A., et al. (2014). The aerocom evaluation and intercomparison of organic aerosol in global models. *Atmospheric Chemistry and Physics*, *14*(19), 10845–10895.

Ulbrich, I. M., Canagaratna, M. R., Zhang, Q., Worsnop, D. R., & Jimenez, J. L. (2009). Interpretation of organic components from positive matrix factorization of aerosol mass spectrometric data. *Atmospheric Chemistry and Physics*, *9*(9), 2891–2918.

Van Dingenen, R., Raes, F., Putaud, J. P., Baltensperger, U., Charron, A., Facchini, M. C., Decesari, S., Fuzzi, S., Gehrig, R., Hansson, H. C., et al. (2004). A european aerosol phenomenology—1: Physical characteristics of particulate matter at kerbside, urban, rural and background sites in europe. *Atmospheric Environment*, *38*(16), 2561–2577.

Verma, V., Fang, T., Xu, L., Peltier, R. E., Russell, A. G., Ng, N. L., & Weber, R. J. (2015). Organic aerosols associated with the generation of reactive oxygen species (ros) by water-soluble pm2. 5. *Environmental science & technology*, *49*(7), 4646–4656.

WHO. (2016). *Ambient air pollution: A global assessment of exposure and burden of disease*. World Health Organisation.

WHO. (2021). Review of evidence on health aspects of air pollution: Revihaap project: Technical report.

Wang, Q., Sun, Y., Jiang, Q., Du, W., Sun, C., & Fu, Z., P.and Wang. (2015). Chemical composition of aerosol particles and light extinction apportionment before and during the heating season in beijing, china. *Journal of Geophysical Research: Atmospheres*, *120*(24), 12708–12722.

Wang, Y., Puthussery, J. V., Yu, H., Liu, Y., Salana, S., & Verma, V. (2022). Sources of cellular oxidative potential of water-soluble fine ambient particulate matter in the midwestern united states. *Journal of Hazardous Materials*, *425*, 127777.

Watson, J. G. (1979). *Chemical element balance receptor model methodology for assessing the sources of fine and total suspended particulate matter in portland, oregon*. Oregon Graduate Institute of Science; Technology.

Weber, S., Uzu, G., Favez, O., Borlaza, L. J. S., Calas, A., Salameh, D., Chevrier, F., Allard, J., Besombes, J. L., Albinet, A., et al. (2021). Source apportionment of atmospheric pm 10 oxidative potential: Synthesis of 15 year-round urban datasets in france. *Atmospheric Chemistry and Physics*, *21*(14), 11353–11378.

Xing, J., Shao, L., Zhang, W., Peng, J., Wang, W., Shuai, S., Hu, M., & Zhang, D. (2020). Morphology and size of the particles emitted from a gasoline-direct-injection-engine vehicle and their ageing in an environmental chamber. *Atmospheric Chemistry and Physics*, *20*(5), 2781–2794.

Xu, W., Han, T., Du, W., Wang, Q., Chen, C., Zhao, J., Zhang, Y., Li, J., Fu, P., Wang, Z., et al. (2017). Effects of aqueous-phase and photochemical processing on secondary organic aerosol formation and evolution in beijing, china. *Environmental Science & Technology*, *51*(2), 762–770.

Yang, M., Chu, C., Bloom, M. S., Li, S., Chen, G., Heinrich, J., Markevych, I., Knibbs, L. D., Bowatte, G., Dharmage, S. C., et al. (2018). Is smaller worse? new insights about associations of pm1 and respiratory health in children and adolescents. *Environment international*, *120*, 516–524.

Yu, Y., Guo, S., Wang, H., Shen, R., Zhu, W., Tan, R., Song, K., Zhang, Z., Li, S., Chen, Y., et al. (2022). Importance of semivolatile/intermediate-volatility organic compounds to secondary organic aerosol formation from chinese

domestic cooking emissions. *Environmental Science & Technology Letters*, *9*(6), 507–512.

Yubero, E., Carratalá, A., Crespo, J., Nicolás, J., Santacatalina, M., Nava, S., Lucarelli, F., & Chiari, M. (2011). Pm10 source apportionment in the surroundings of the san vicente del raspeig cement plant complex in southeastern spain. *Environmental Science and Pollution Research*, *18*(1), 64–74.

Yus-Díez, J., Bernardoni, V., Močnik, G., Alastuey, A., Ciniglia, D., Ivančič, M., Querol, X., Perez, N., Reche, C., Rigler, M., et al. (2021). Determination of the multiple-scattering correction factor and its cross-sensitivity to scattering and wavelength dependence for different ae33 aethalometer filter tapes: A multi-instrumental approach. *Atmospheric Measurement Techniques*, *14*(10), 6335–6355.

Yus-Díez, J., Via, M., Alastuey, A., Karanasiou, A., Minguillón, M. C., Perez, N., Querol, X., Reche, C., Ivančič, M., Rigler, M., et al. (2022). Absorption enhancement of black carbon particles in a mediterranean city and countryside: Effect of particulate matter chemistry, ageing and trend analysis. *Atmospheric Chemistry and Physics*.

Zhang, M., Wang, X., Yang, X., Dong, T., Hu, W., Guan, Q., Tun, H. M., Chen, Y., Chen, R., Sun, Z., et al. (2020). Increased risk of gestational diabetes mellitus in women with higher prepregnancy ambient pm2. 5 exposure. *Science of the Total Environment*, *730*, 138982.

Zhang, W., Lin, S., Hopke, P. K., Thurston, S. W., van Wijngaarden, E., Croft, D., Squizzato, S., Masiol, M., & Rich, D. Q. (2018a). Triggering of cardiovascular hospital admissions by fine particle concentrations in new york state: Before, during, and after implementation of multiple environmental policies and a recession. *Environmental Pollution*, *242*, 1404–1416. https://doi.org/https://doi.org/10.1016/j.envpol.2018.08.030

Zhang, X., Chen, X., & Zhang, X. (2018b). The impact of exposure to air pollution on cognitive performance. *Proceedings of the National Academy of Sciences*, *115*(37), 9193–9197.

Zhang, Y., Easter, R. C., Ghan, S. J., & Abdul-Razzak, H. (2002). Impact of aerosol size representation on modeling aerosol-cloud interactions. *Journal of Geophysical Research: Atmospheres*, *107*(D21), AAC–4.

Zhao, Y., Saleh, R., Saliba, G., Presto, A. A., Gordon, T. D, Drozd, G. T., Goldstein, A. H., Donahue, N. M., & Robinson, A. L. (2017). Reducing secondary organic aerosol

formation from gasoline vehicle exhaust. *Proceedings of the National Academy of Sciences*, *114*(27), 6984–6989.

Zheng, Y., Unger, N., Hodzic, A., Emmons, L., Knote, C., Tilmes, S., Lamarque, J.-F., & Yu, P. (2015a). Limited effect of anthropogenic nitrogen oxides on secondary organic aerosol formation. *Atmospheric Chemistry and Physics*, *15*(23), 13487–13506. https://doi.org/10.5194/acp-15-13487-2015

Zheng, Y., Unger, N., Hodzic, A., Emmons, L., Knote, C., Tilmes, S., Lamarque, J., & Yu, P. (2015b). Limited effect of anthropogenic nitrogen oxides on secondary organic aerosol formation. *Atmospheric Chemistry and Physics*, *15*(23), 13487–13506.

Zhou, H., Xu, Y., Yadong, L., Chenguang, T., Yimian, M., & Yang, C. (2021). Aerosol radiative and climatic effects on ecosystem productivity and evapotranspiration. *Current Opinion in Environmental Science Health*, *19*, 100218. https://doi.org/https://doi.org/10.1016/j.coesh.2020.10.006

Zhou, J., Elser, M., Huang, R., Krapf, M., Fröhlich, R., Bhattu, D., Stefenelli, G., Zotter, P., Bruns, E. A., Pieber, S. M., et al. (2019). Predominance of secondary organic aerosol to particle-bound reactive oxygen species activity in fine ambient aerosol. *Atmospheric chemistry and physics*, *19*(23), 14703–14720.

Zhou, L., Hopke, P. K, Paatero, P., Ondov, J. M., Pancras, J. P., Pekney, N. J., & Davidson, C. I. (2004). Advanced factor analysis for multiple time resolution aerosol composition data. *Atmospheric Environment*, *38*(29), 4909–4920.

Zografou, O., Gini, M., Manousakas, M. I., Chen, G., Kalogridis, A. C., Diapouli, E., Pappa, A., & Eleftheriadis, K. (2022). Combined organic and inorganic source apportionment on yearlong tof-acsm dataset at a suburban station in athens. *Atmospheric Measurement Techniques*, *15*(16), 4675–4692.

Part VIII

APPENDIX

A

APPENDIX

Supplement of Atmos. Chem. Phys., 21, 8323–8339, 2021
https://doi.org/10.5194/acp-21-8323-2021-supplement

Atmospheric Chemistry and Physics Open Access

Supplement of

Increase in secondary organic aerosol in an urban environment

Marta Via et al.

Correspondence to: Marta Via (marta.via@idaea.csic.es) and María Cruz Minguillón (mariacruz.minguillon@idaea.csic.es)

Supplementary material

Section 1. Supplementary tables and figures

Map data ©2021 Inst. Geogr. Nacional, Google, Institut Cartogràfic de Catalunya

Figure S 1. Location of Palau Reial and the Faculty of Physics in aerial view zoom to the site (Google Maps).

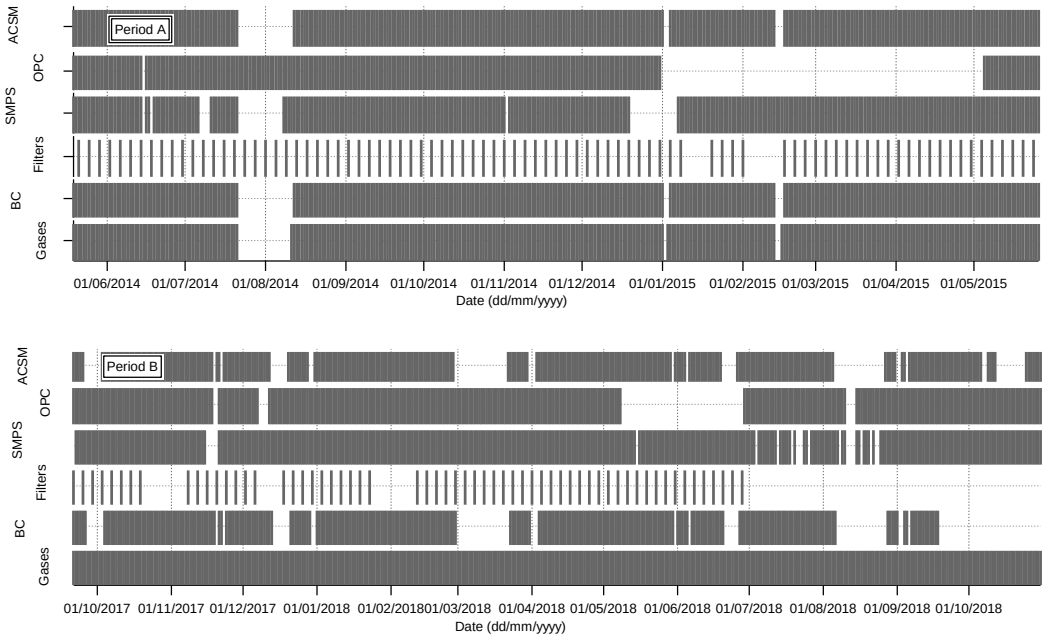

Figure S 2. Data availability for periods A and B.

Table S 1. Output correlations of runs of different number of factors (n) per each season in periods A and B. Bold rows correspond to those selected output runs.

A	n	Q/Qexp	a-value COA	a-value HOA	a-value BBOA	COA vs. m/z55	HOA vs. BC	BBOA vs. m/z60	LO-OOA vs. NO_3^-	MO-OOA vs. SO_4^{2-}	OA meas. vs OA model	
											R^2	Slope
May 2014	3	0.789 ± 0.009	0.3	0.3	-	0.56	0.63	-	0.44	0.04	0.94	1.023±0.011
	4	**0.706 ± 0.008**	**0.5**	**0.1**	**-**	**0.60**	**0.67**	**-**	0.37	**0.21**	0.96	0.996±0.008
	5	0.678 ± 0.011	0.2	0.5	0.1	0.61	0.65	0.28	0.47	0.10	0.98	1.029±0.008
Jun-Aug 2014	3	1.858±0.017	0.1	0.5	-	0.77	0.41	-	0.27	0.12	0.95	1.039±0.004
	4	**1.712±0.004**	**0.1**	**0.5**	**-**	**0.76**	**0.37**	**-**	**0.25**	**0.18**	**0.96**	**1.035±0.004**
	5	1.572±0.017	0.2	0.5	-	0.74	0.34	-	0.23	0.16	0.96	1.025±0.003
Sep-Oct 2014	3	3.188±0.017	0.1	0.5	-	0.66	0.68	-	0.35	0.07	0.95	0.9545±0.0041
	4	**2.929±0.008**	**0.1**	**0.3**	**-**	**0.35**	**0.68**	**-**	**0.35**	**0.08**	**0.96**	**0.968±0.003**
	5	2.76±0.03	0.1	0.5	0.5	0.64	0.68	0.4	0.32	0.09	0.97	0.991±0.004
Nov-Mar 2014-2015	3	9.44±0.05	0.3	05	-	0.68	0.68	-	0.65	0.30	0.97	1.019±0.002
	4	**9.21 ± 0.03**	**0.1**	**0.5**	**0.2**	**0.59**	**0.68**	**0.60**	**0.31**	**0.35**	**0.98**	**1.021±0.002**
	5	8.68 ± 0.07	0.3	0.5	0.1	0.73	0.67	0.60	0.20	0.37	0.98	1.020±0.002
Apr-May 2015	3	4.33±0.09	0.5	0.5	-	0.74	0.45	-	0.40	0.26	0.95	1.023±0.004
	4	**4.10±0.05**	**0.3**	**0.5**	**-**	**0.70**	**0.43**		**0.39**	**0.17**	**0.96**	**1.025±0.004**
	5	3.70±0.05	0.1	0.5	0.3	0.88	0.5	0.4	0.26	0.26	0.96	1.032±0.004
B	**n**	**Q/Qexp**	**a-value COA**	**a-value HOA**	**a-value BBOA**	**COA vs. m/z55**	**HOA vs. BC**	**BBOA vs. m/z60**	**LO-OOA vs. NO_3^-**	**MO-OOA vs. SO_4^{2-}**	**OA meas. Vs. OA app.**	
											R^2	**Slope**
Sep-Oct 2017	3	1.81±0.001	0.1	0.5	-	0.83	0.51	-	0.60	0.15	0.96	1.00 +0.14
	4	**1.053 ± 0.012**	**0.1**	**0.5**	**-**	**0.80**	**0.52**	**-**	**0.59**	**0.33**	**0.96**	**1.01x+0.09**
	5	0.977 ± 0.006	0.1	0.3	0.5	0.61	0.65	0.28	0.53	0.18	0.96	0.96x+0.09
Nov-Mar 2017-2018	4	0.873±0.003	0.3	0.5	0.2	0.68	0.78	0.87	0.80	0.46	0.97	1.013x+0.07
	5	**0.808±0.004**	**0.2**	**0.5**	**0.1**	**0.72**	**0.61**	**0.91**	**0.32**	**0.47**	**0.97**	**1.010x+0.032**
	6	0.765±0.002	0.3	0.5	0.3	0.70	0.78	0.91	0.41	0.47	0.97	1.01x+0.12
Apr-May 2018	3	1.076±0.000	0.1	0.5	-	0.78	0.65	-	0.51	0.18	0.97	1.0x+0.2
	4	**0.893±0.006**	**0.4**	**0.5**	**-**	**0.76**	**0.57**	**-**	**0.42**	**0.32**	**0.97**	**0.90x+0.13**
	5	0.778±0.006	0.3	0.2	0.3	0.69	0.56	0.57	0.42	0.31	0.97	1.00x+0.08
Jun-Aug 2018	3	0.957±0.013	0.5	0.5	-	0.69	0.31	-	0.04	0.05	0.97	1.00x+0.15
	4	**0.869 ± 0.008**	**0.5**	**0.5**	**-**	**0.76**	**0.44**	-	0.1	0.08	0.96	1.00x+0.14
	5	0.809 ± 0.001	0.5	0.4	-	0.76	0.47	-	0.14	0.07	0.96	1.12x+0.15
Sep-Oct 2018	3	1.493±0.008	0.5	0.5	-	0.73	0.74	-	0.25	0.27	0.95	1.02x+0.03
	4	**1.273±0.001**	**0.3**	**0.5**	**-**	**0.74**	**0.74**	**-**	**0.23**	**0.21**	0.97	1.02x-0.02
	5	0.923±0.003	0.3	0.2	0.1	0.73	0.73	0.55	0.17	0.16	0.97	1.03x-0.04

Table S2. Correlations of factors mass spectra with external anchor mass spectra (a), and factors time series with external markers (b).

(a)		Crippa et al., 2013, *Ng et al., 2010				Mohr et al., 2012				
		COA	HOA	BBOA*	OOA	COA	HOA	BBOA	SV-OOA	LV-OOA
A	COA	0.96	0.87	0.74	0.35	0.92	0.76	0.76	0.71	0.19
	HOA	0.77	0.96	0.62	0.34	0.71	0.93	0.62	0.61	0.14
	BBOA	0.25	0.13	0.67	0.36	0.38	0.08	0.35	0.34	0.27
	LO-OOA	0.13	0.06	0.31	0.95	0.27	0.03	0.28	0.66	0.97
	MO-OOA	0.10	0.05	0.25	0.93	0.22	0.02	0.24	‘.65	0.95
B	COA	0.98	0.71	0.66	0.27	0.86	0.58	0.66	0.65	0.16
	HOA	0.79	0.99	0.61	0.19	0.73	0.94	0.65	0.55	0.10
	BBOA	0.62	0.50	0.99	0.40	0.77	0.40	0.72	0.65	0.33
	LO-OOA	0.39	0.25	0.70	0.79	0.64	0.16	0.66	0.75	0.72
	MO-OOA	0.07	0.02	0.03	0.89	0.17	0.05	0.16	0.56	0.94

30

(b)	Period A	Apr-May 2015	Jun-Aug 2014	Sep - Oct 2014	Nov-Mar 2014-2015	Period B	Ap-May 2018	Jun-Aug 2018	Sep-Oct 2018	Nov-Mar 2017-2018
COA vs. m/z 55	0.58	0.69	0.76	0.35	0.63	0.71	0.76	0.76	0.74	0.72
COA vs. HOA	0.20	0.32	0.24	0.02	0.26	0.31	0.32	0.32	0.28	0.33
HOA vs. BC	0.62	0.42	0.40	0.70	0.63	0.68	0.57	0.57	0.74	0.68
HOA vs. NO	0.44	0.36	0.16	0.53	0.42	0.63	0.41	0.41	0.68	0.76
HOA vs. NO_2	0.49	0.33	0.39	0.51	0.49	0.55	0.51	0.51	0.70	0.75
HOA vs. NO_x	0.44	0.40	0.29	0.45	0.44	0.65	0.51	0.51	0.70	0.75
LO-OOA vs. m/z 43	0.51	0.48	0.25	0.60	-	0.41	0.86	0.86	0.84	0.66
LO-OOA vs. NO_3^-	0.29	0.39	0.74	0.34	-	0.60	0.40	0.68	0.75	0.58
MO-OOA vs. m/z 44	0.60	0.40	0.68	0.75	0.58	0.69	0.84	0.84	0.96	0.96
MO-OOA vs. SO_4^{2-}	0.02	0.09	0.13	0.03	0.03	0.10	0.32	0.32	0.31	0.47
BBOA vs. m/z 60	0.60	-	-	-	0.60	0.91	-	-	-	0.91
BBOA vs. m/z 73	0.55	-	-	-	0.55	0.61	-	-	-	0.61

(a)

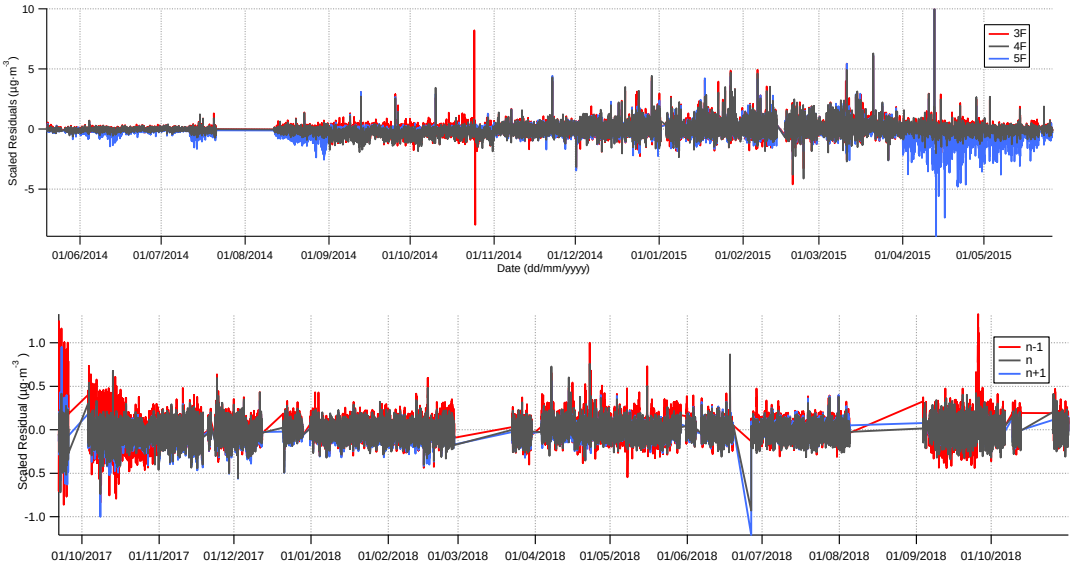
Scaled Residuals (µg·m-3)
3F
4F
5F
01/06/2014
01/07/2014
01/08/2014
01/09/2014
01/10/2014
01/11/2014
01/12/2014
01/01/2015
01/02/2015
01/03/2015
01/04/2015
01/05/2015
Date (dd/mm/yyyy)
Scaled Residual (µg·m-3)
n-1
n
n+1
01/10/2017
01/11/2017
01/12/2017
01/01/2018
01/02/2018
01/03/2018
01/04/2018
01/05/2018
01/06/2018
01/07/2018
01/08/2018
01/09/2018
01/10/2018

35

(b)

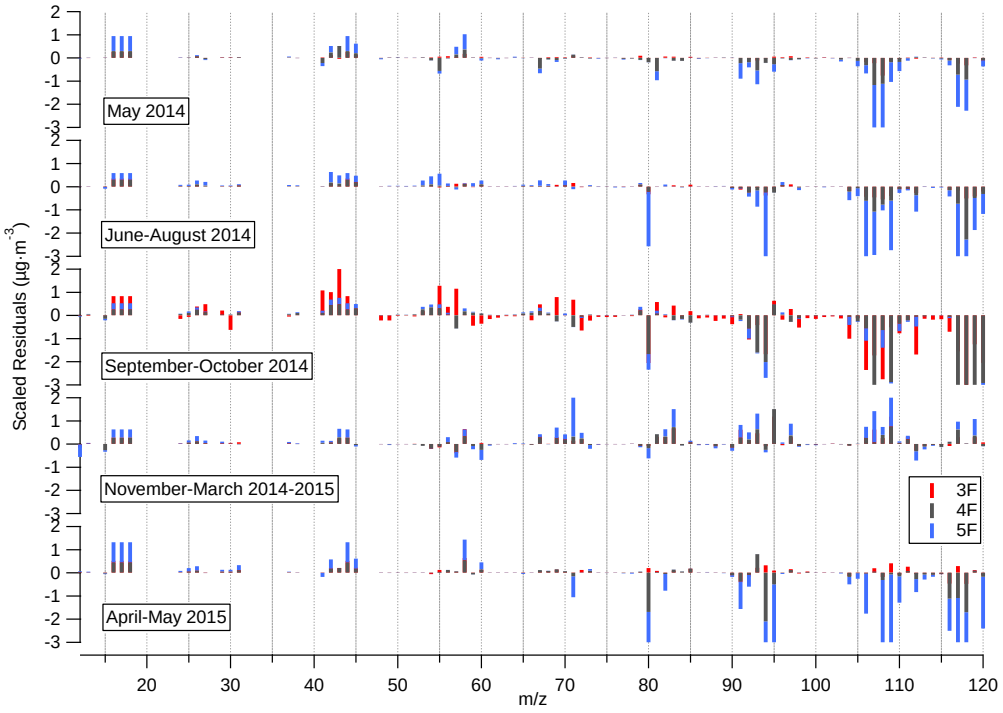
Scaled Residuals (µg·m-3)
May 2014
June-August 2014
September-October 2014
November-March 2014-2015
April-May 2015
3F
4F
5F
m/z

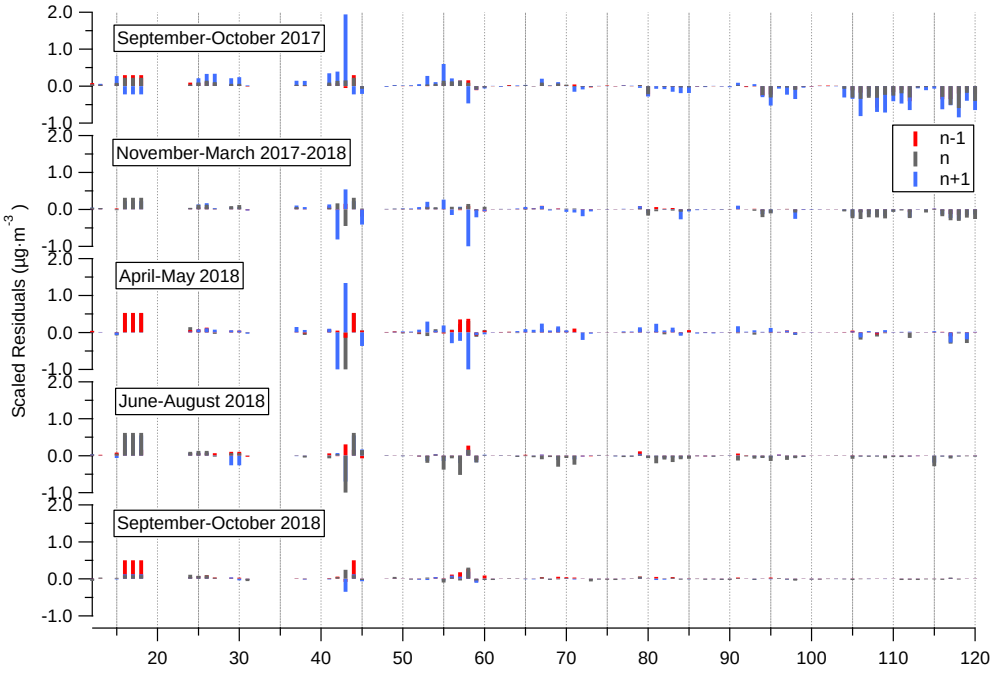

Figure S 3. Scaled residuals (a) time series (b) mass spectra for 3, 4, 5 factors in period A and for n-1, n and n+1 factors in Period B being n the number of factors of the chosen solution.

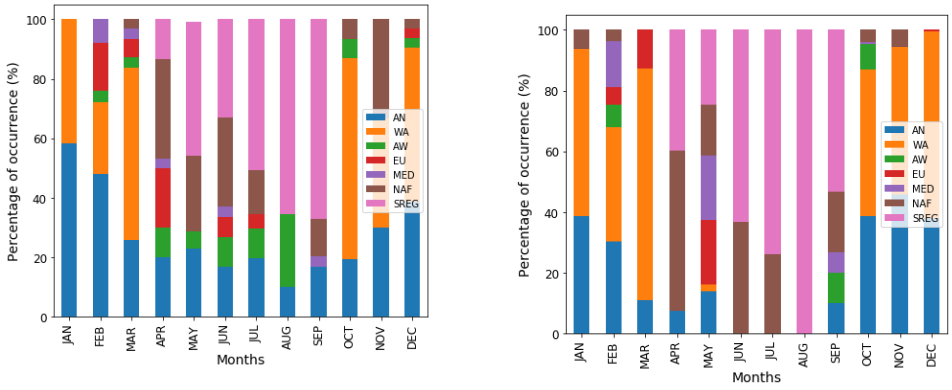

Figure S 4. Relative frequency of occurrence of episodes sorted by month for periods A (left) and B (right).

Table S 3. Comparison between i. total PM_1 from the sum of ACSM components (NR-PM_1) and BC concentrations and co-located measurements of PM_1 from SMPS and ii. ACSM species concentration vs. 24-h samples concentrations. Fit parameters correspond to least orthogonal distance regression method.

(i)		A			B		
y	x	R^2	Slope	Intercept	R^2	Slope	Intercept
NR-PM_1+BC	SMPS (Mass)	0.61	1.001 ± 0.006	0.37 ± 0.07	0.72	1.177 ± 0.006	-0.47± 0.05

(ii)		A			B		
y	x	R^2	Slope	Intercept	R^2	Slope	Intercept
SO_4^{2-} ACSM	SO_4^{2-} off-line	0.88	1.24±0.05	-0.31±0.10	0.93	1.05±0.04	0.01±0.08
NO_3^- ACSM	NO_3- off-line	0.84	1.9±0.1	-0.12±0.09	0.86	1.76±0.09	0.32±0.09
NH_4^+ ACSM	$NH4^+$ off-line	0.85	1.73±0.08	-0.27±0.07	0.71	1.68±0.13	0.05±0.09
OA ACSM	OC off-line	0.73	2.69±0.17	-0.9±0.4	0.86	2.94 ± 0.17	-1.4± 0.3

(a)

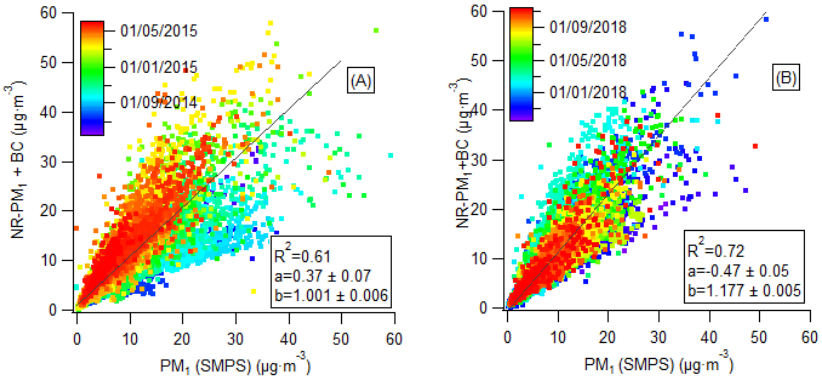

(b)

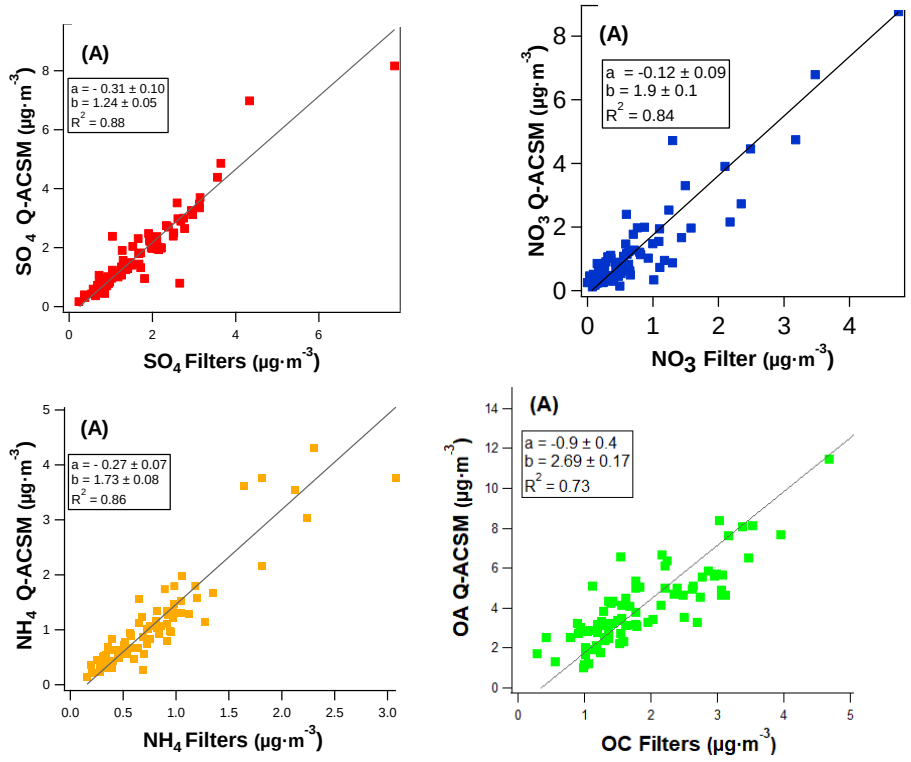

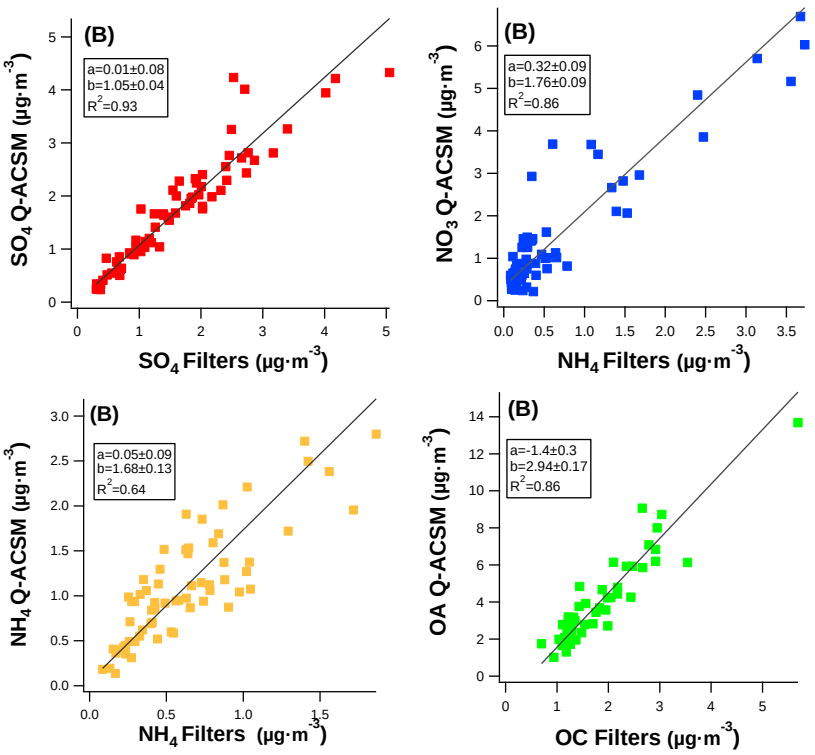

Figure S5. Intercomparison for periods A and B of (a) NR-PM_1 from Q-ACSM + BC from MAAP with PM_1 measurements from SMPS. (b) NR-PM1 species from Q-ACSM with SO_4^{2-}, NO_3^-, NH_4^+ and OC from filters, respectively.

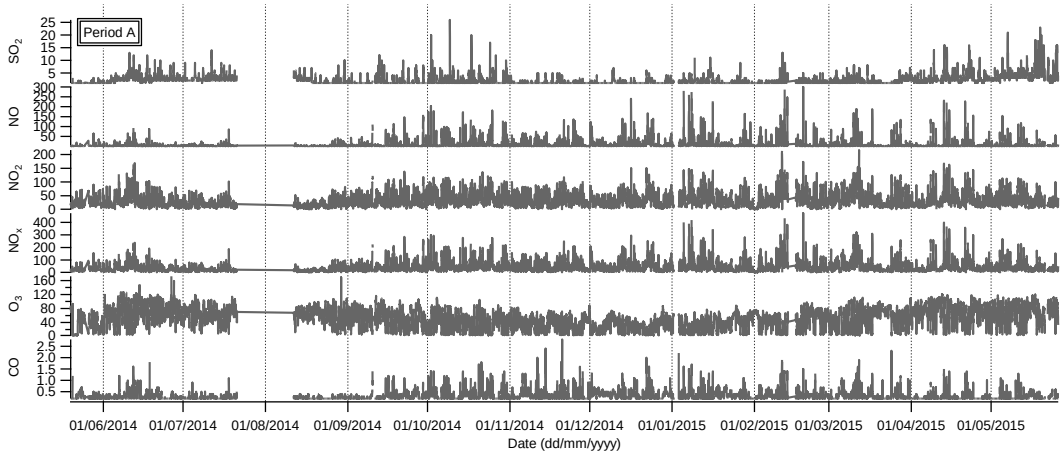

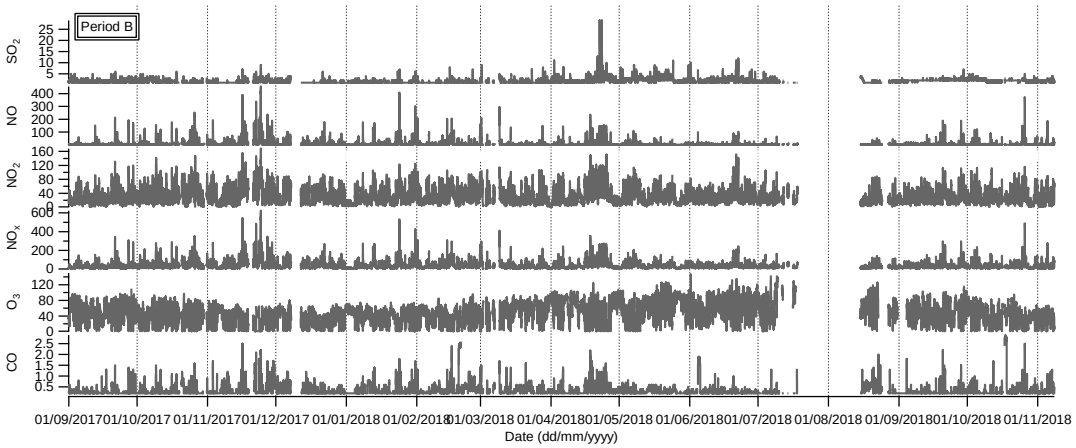

Figure S 6. Time series of co-located gases measurements for period A and B.

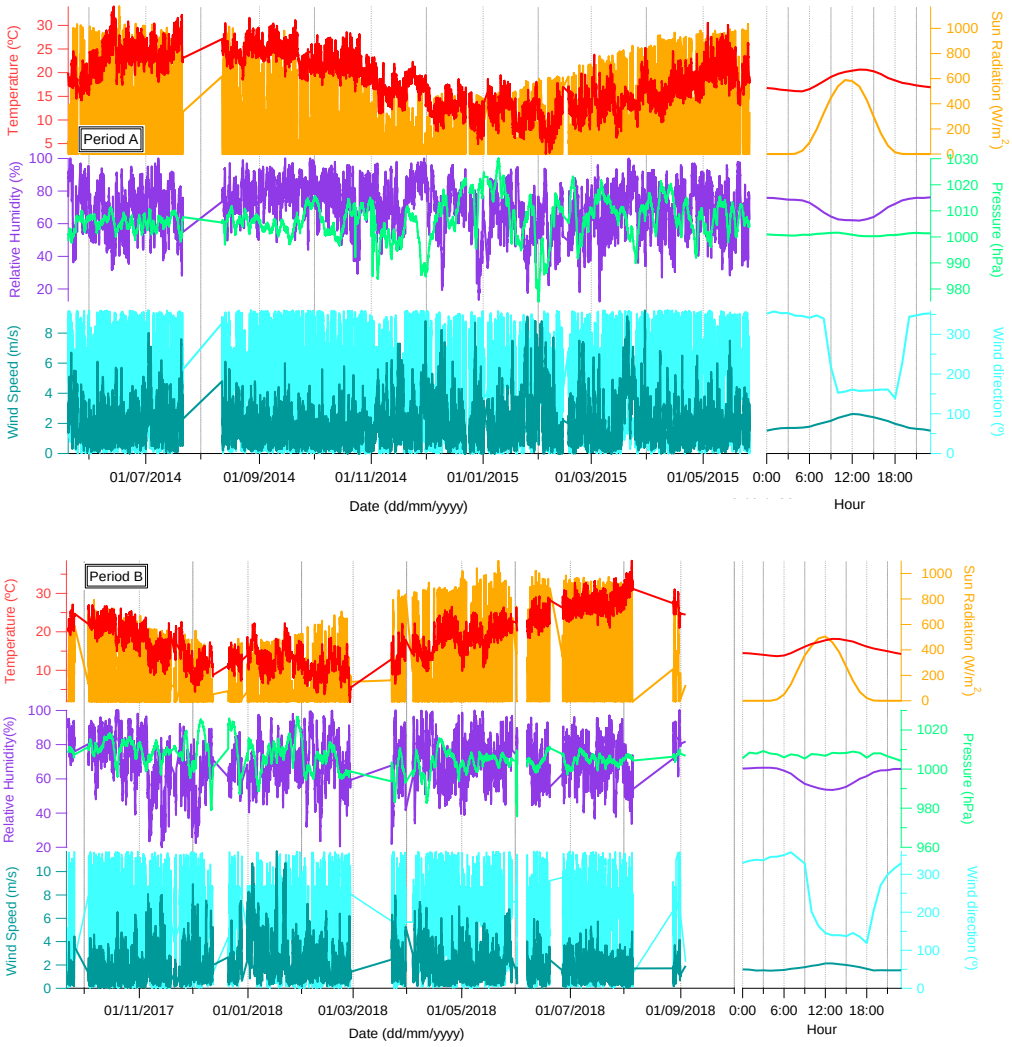

Figure S 7. Time series and diel patterns of meteorological variables for periods A (top) and B (bottom).

Table S4. Period-average mean, standard deviation and percentual change of variables under study for periods A and B.

			Period A		Period B		Change A to B
	Variables	Units	Average	Standard Deviation	Average	Standard Deviation	(%)
Meteorological parameters	Temperature	°C	18.2	5.7	18.4	6.8	+1%
	Relative Humidity	%	70.7	15.3	70.2	14.8	-0.7%
	Pressure	hPa	1006.5	7.3	1005.5	7.32	-0.1%
	Sun Radiation	$W \cdot m^{-2}$	180.0	266.0	178.9	268.5	-0.6%
	Wind Speed	$m \cdot s^{-1}$	2.0	1.4	2.0	1.5	0%
	Wind Direction	°	170.0	102.0	200.4	104.8	+30.4º
Gas-phase pollutants	O_3	$\mu g \cdot m^{-3}$	52.4	28.0	47.6	23.8	- 9%
	CO	$\mu g \cdot m^{-3}$	0.3	0.2	0.3	0.3	0%
	SO_2	$\mu g \cdot m^{-3}$	2.0	1.7	1.7	1.4	-15%
	NO	$\mu g \cdot m^{-3}$	8.3	19.2	8.5	1.2	+2%
	NO_2	$\mu g \cdot m^{-3}$	32.3	24.8	30.6	21.3	-5%
NR-PM_1 ACSM Species	OA	$\mu g \cdot m^{-3}$	4.2	2.8	4.0	2.8	-5%
	SO_4^{2-}	$\mu g \cdot m^{-3}$	1.9	1.5	1.5	1.2	-21%
	NO_3^-	$\mu g \cdot m^{-3}$	1.3	1.7	1.4	1.9	8%
	NH_4^+	$\mu g \cdot m^{-3}$	1.1	0.9	1.0	0.8	-9%
	Cl^-	$\mu g \cdot m^{-3}$	0.05	0.08	0.06	0.08	+20%
MAAP	BC	$\mu g \cdot m^{-3}$	1.7	1.6	1.4	1.4	-18%
ACSM + MAAP	PM_1	$\mu g \cdot m^{-3}$	10.1	6.7	9.6	6.6	-5%
OPC	PM_1	$\mu g \cdot m^{-3}$	8.3	5.4	9.1	5.0	+9%
SMPS	PM_1	$\mu g \cdot m^{-3}$	9.8	7.0	8.5	5.3	-13%
Filters	PM_1	$\mu g \cdot m^{-3}$	8.0	4.2	7.1	3.0	-11%
OA contribution	OA apportioned	$\mu g \cdot m^{-3}$	4.1	2.8	3.8	2.7	-7%
	COA	$\mu g \cdot m^{-3}$	0.7	0.7	0.6	0.5	-14%
	HOA	$\mu g \cdot m^{-3}$	0.8	1.1	0.5	0.8	-37%
	BBOA	$\mu g \cdot m^{-3}$	0.3	0.4	0.2	0.4	-33%
	LO-OOA	$\mu g \cdot m^{-3}$	1.5	1.0	1.1	1.2	-27%
	MO-OOA	$\mu g \cdot m^{-3}$	1.4	1.3	1.7	1.2	21%
	LO-OOA / MO-OOA *	(adim)	1.1	1.6	1.0	1.6	-9%

75 * Period-average of the ratio LO-OOA-to-MO-OOA.

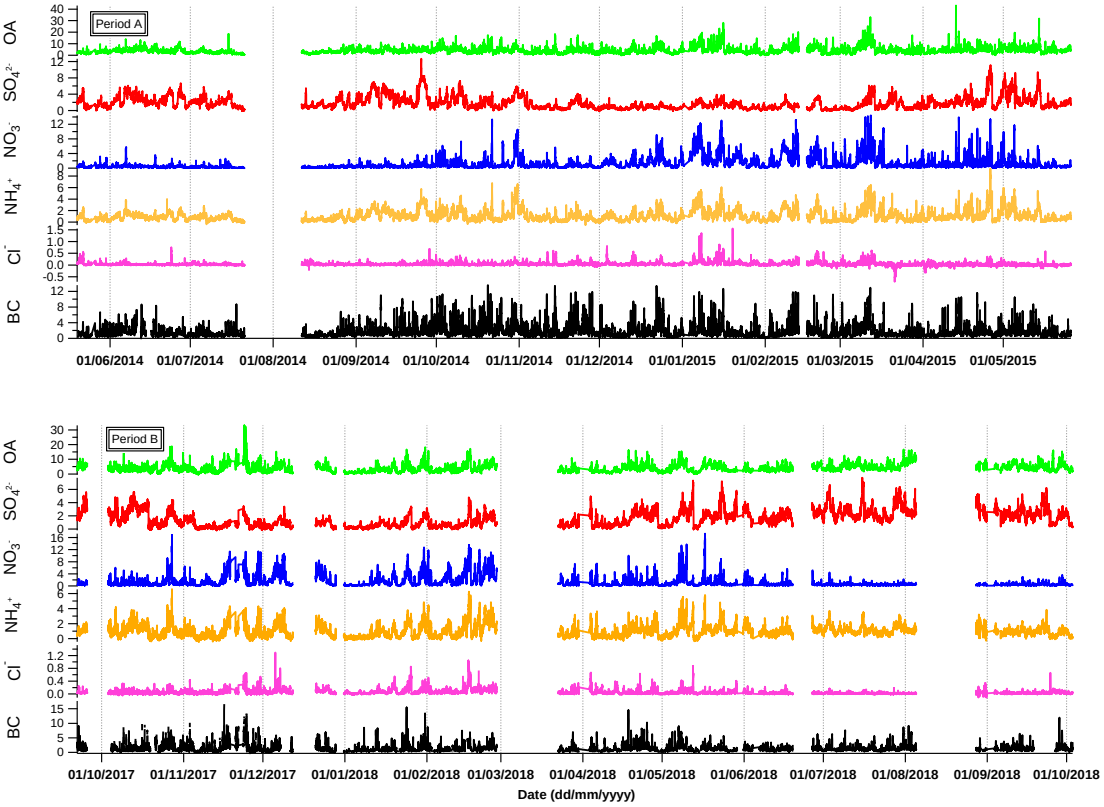

Figure S 8. Time series for NR-PM_1 species and BC concentrations in periods A (top) and B (bottom).

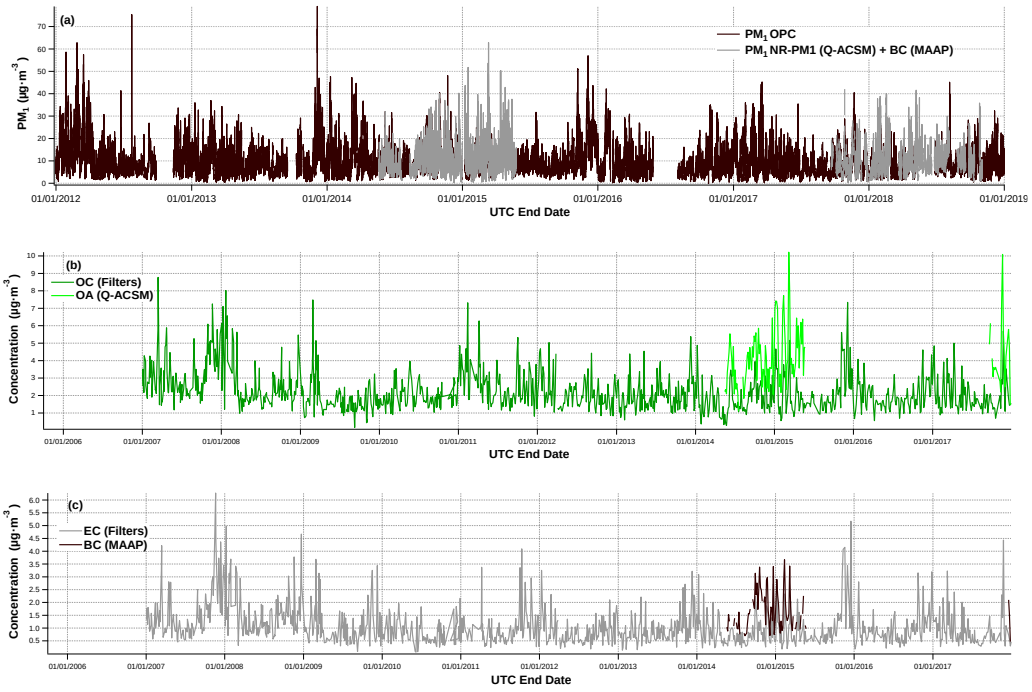

Figure S9. Figure R1. Long-term time series compared to this study two-period time series for respectively, (a) PM1 from OPC and Q-ACSM + MAAP. (b) OC from filters and OM from Q-ACSM. (c) EC from filters and BC from MAAP.

85

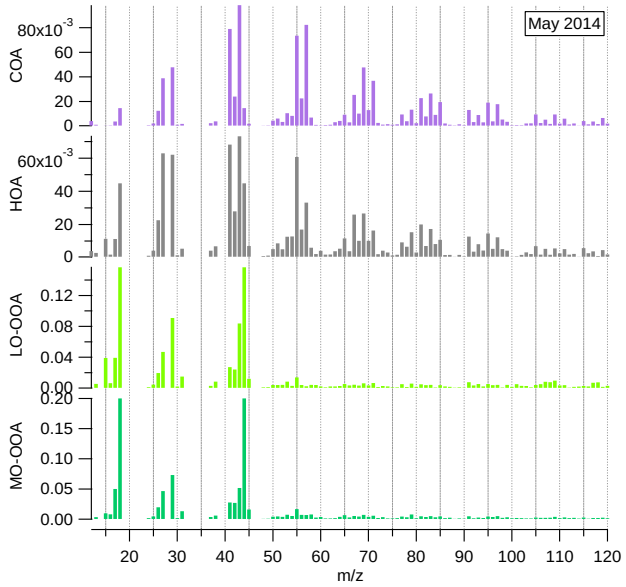
May 2014
COA
HOA
LO-OOA
MO-OOA
m/z

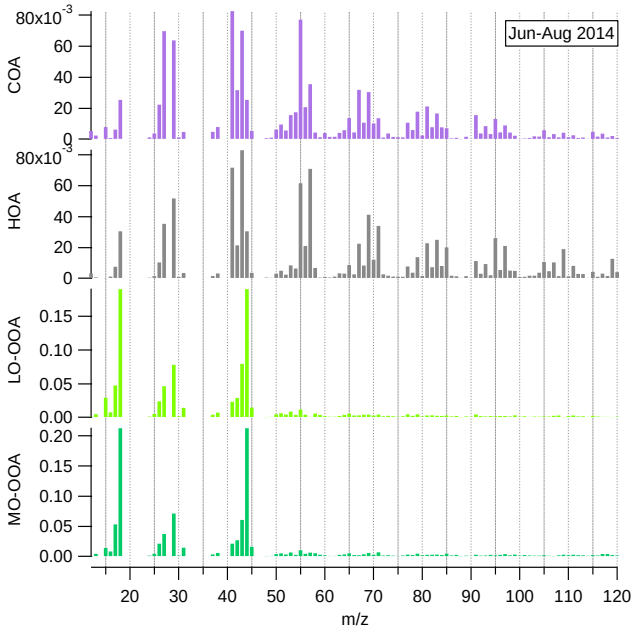
Jun-Aug 2014
COA
HOA
LO-OOA
MO-OOA
m/z

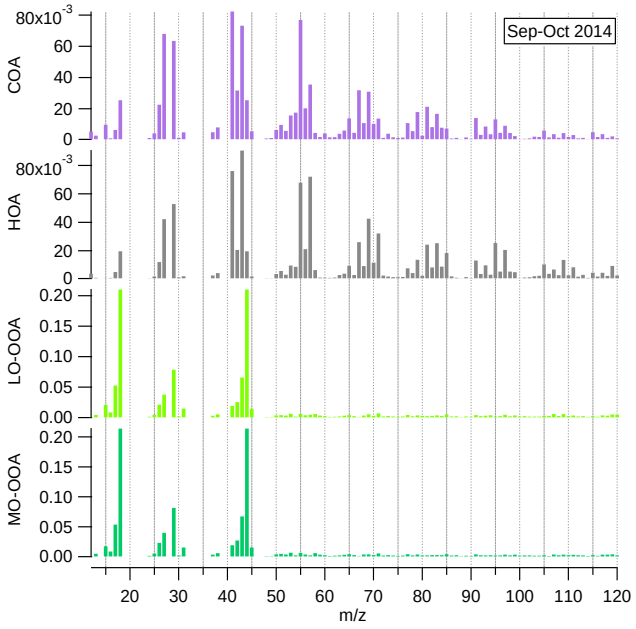
Sep-Oct 2014
COA
HOA
LO-OOA
MO-OOA
80x10-3
0.20
0.15
0.10
0.05
0.00
20 30 40 50 60 70 80 90 100 110 120
m/z

90

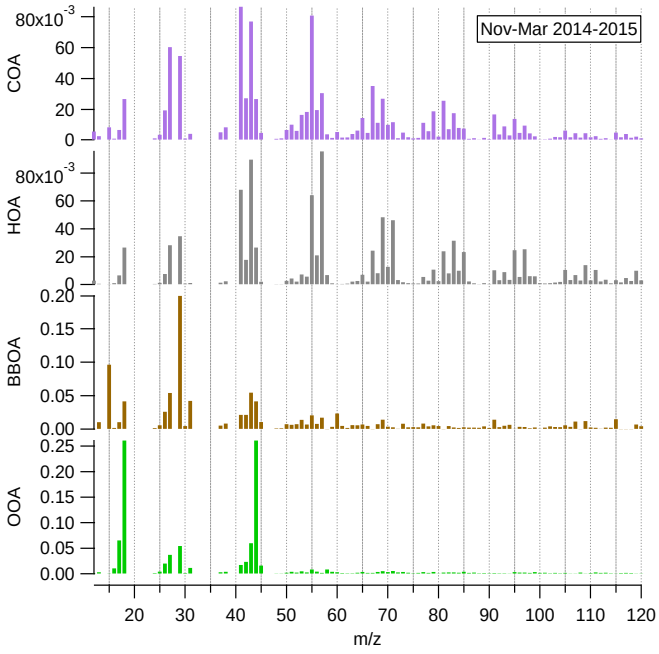
Nov-Mar 2014-2015
COA
HOA
BBOA
OOA
80x10-3
0.25
0.20
0.15
0.10
0.05
0.00
20 30 40 50 60 70 80 90 100 110 120
m/z

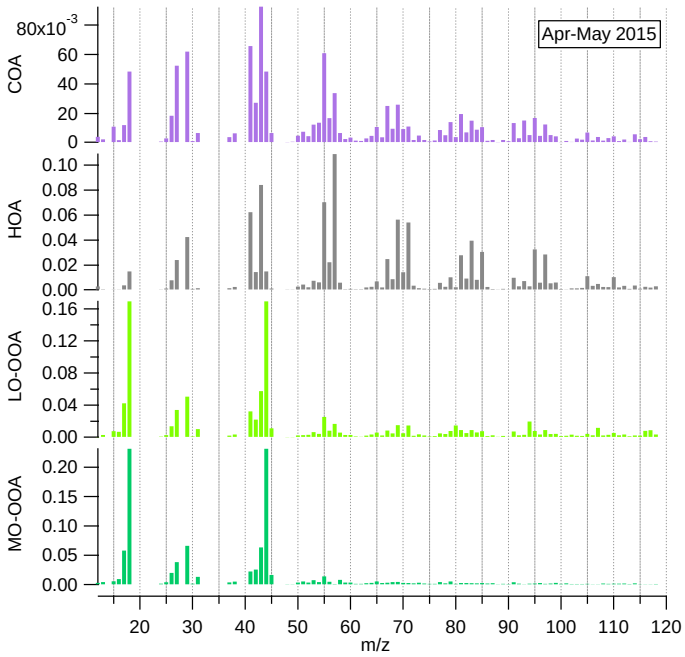
Apr-May 2015
COA
HOA
LO-OOA
MO-OOA
80x10-3
m/z

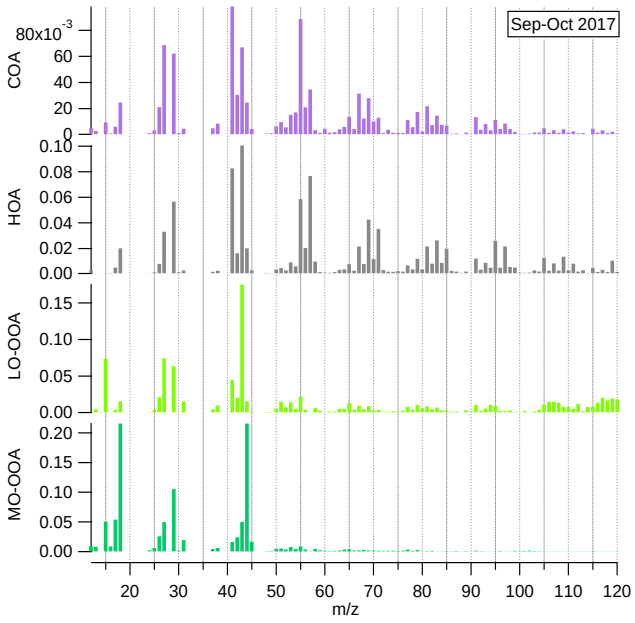
Sep-Oct 2017
COA
HOA
LO-OOA
MO-OOA
80x10-3
m/z

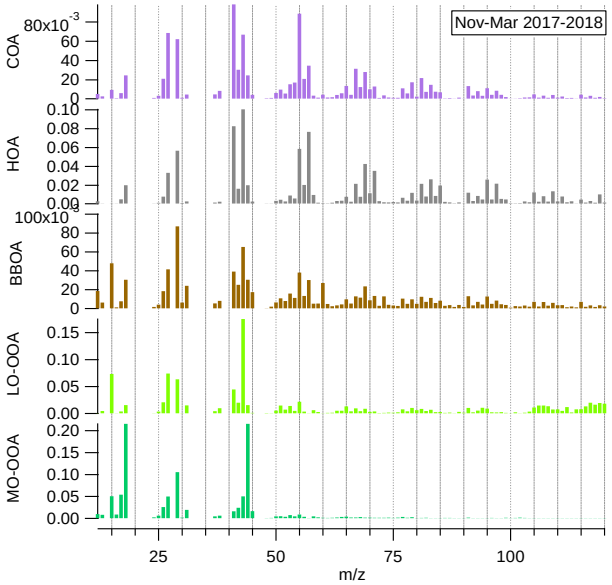
Nov-Mar 2017-2018
COA
HOA
BBOA
LO-OOA
MO-OOA
m/z

95

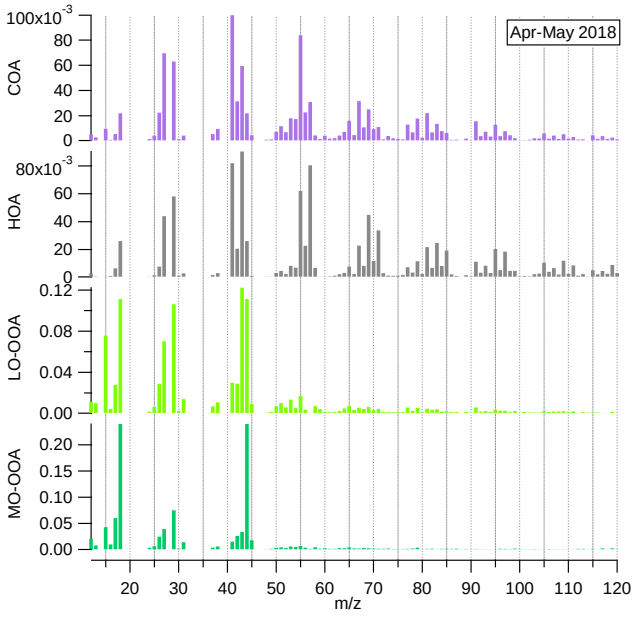
Apr-May 2018
COA
HOA
LO-OOA
MO-OOA
m/z

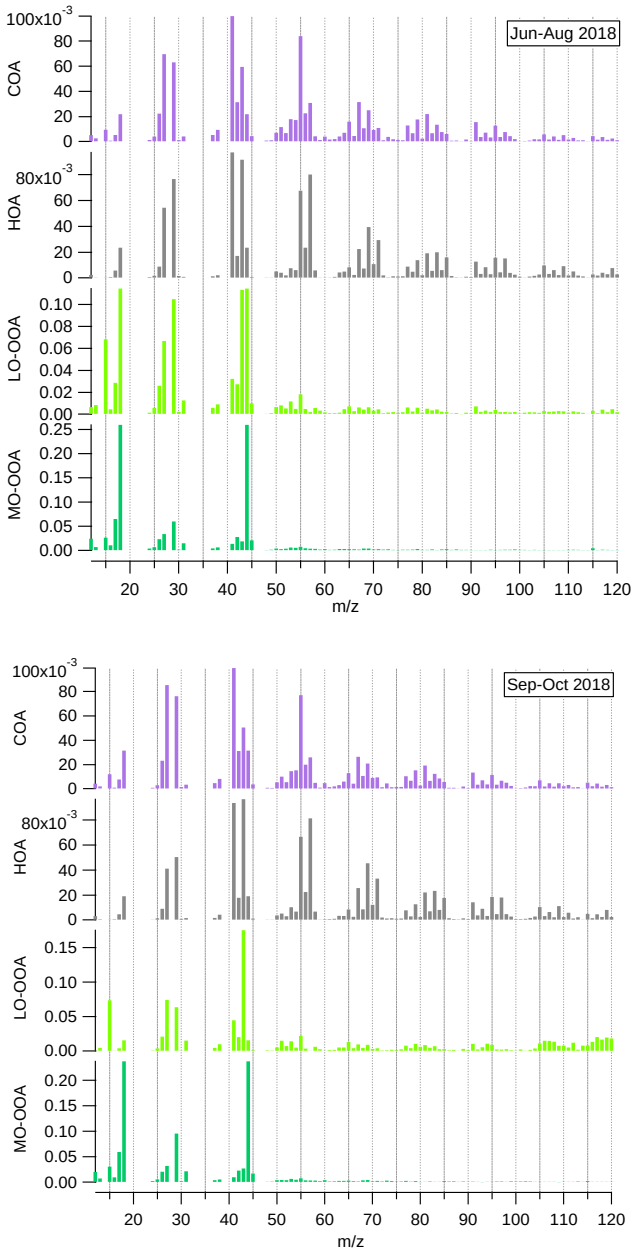

100 **Figure S 10. Seasonal profiles of subperiods of periods A and B by chronological order.**

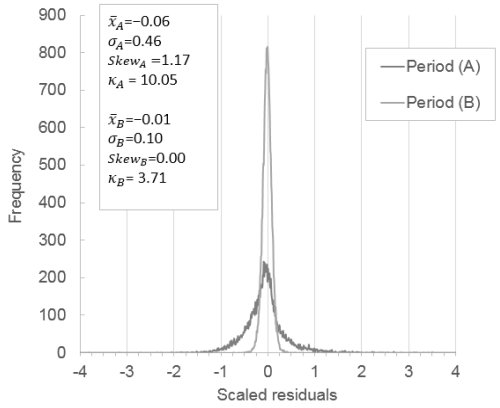

Figure S 11. Residual scaled distributions of PMF OA source distribution using ME-2 approach for periods A and B. Parameters of both distributions (mean, standard deviation and skewness and kurtosis coeffcients) are listed.

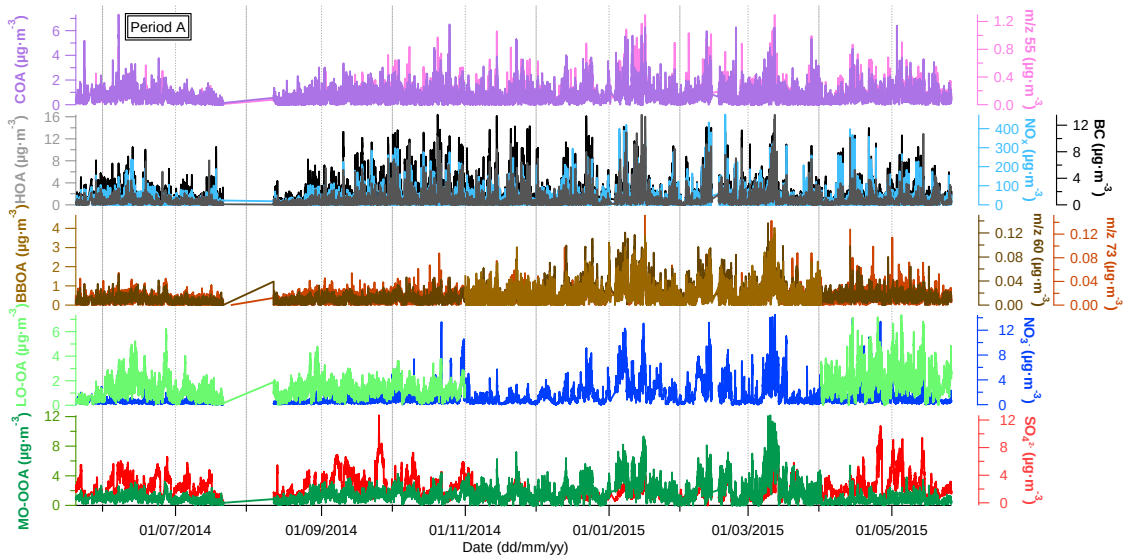

105

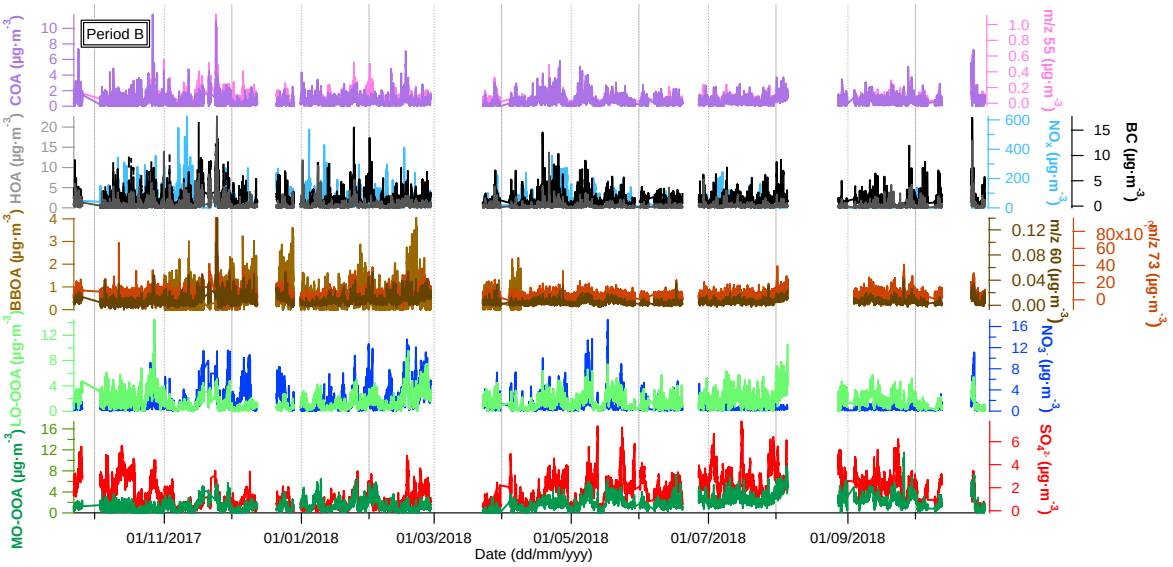

Figure S12. Time series of apportioned OA sources (left axis) and their markers (right axis) in period A and B.

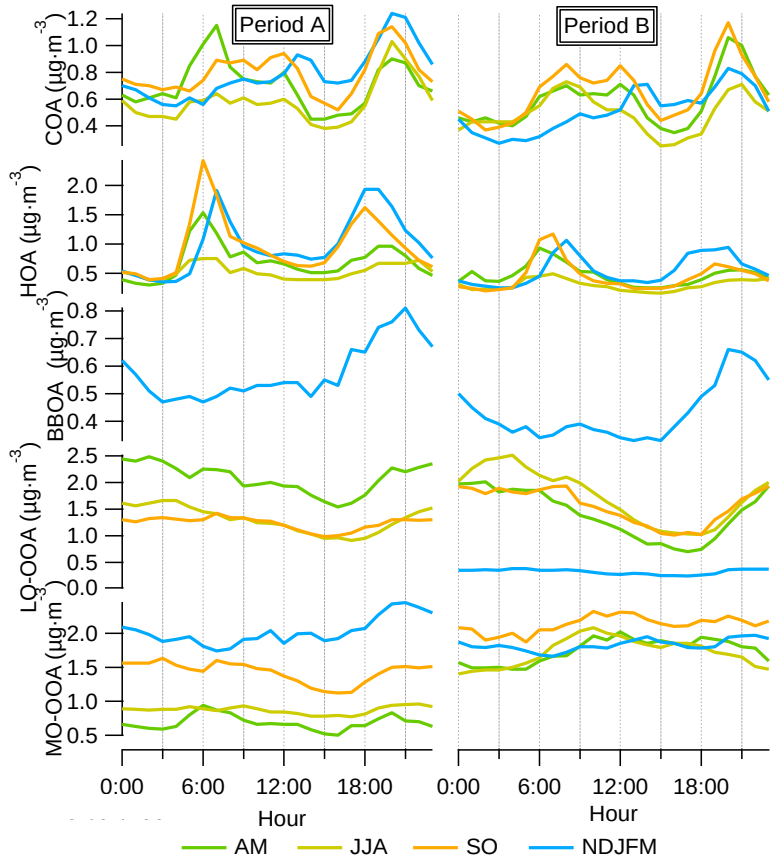

Figure S13. Diel cycle sorted by seasons for the five OA factors for period A and B. Note that the y-axis does not start at zero for the sake of clarity.

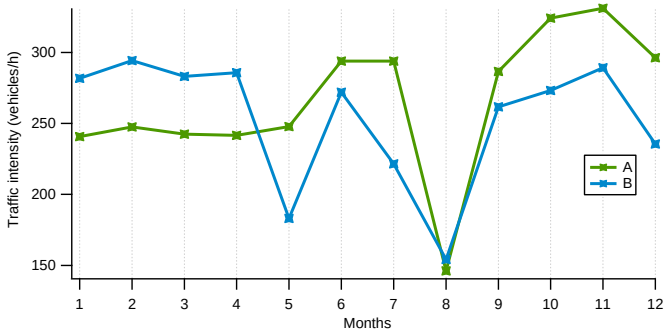

Figure S 14. Mean monthly pattern of traffic intensity at 400m away from site for period A and B.

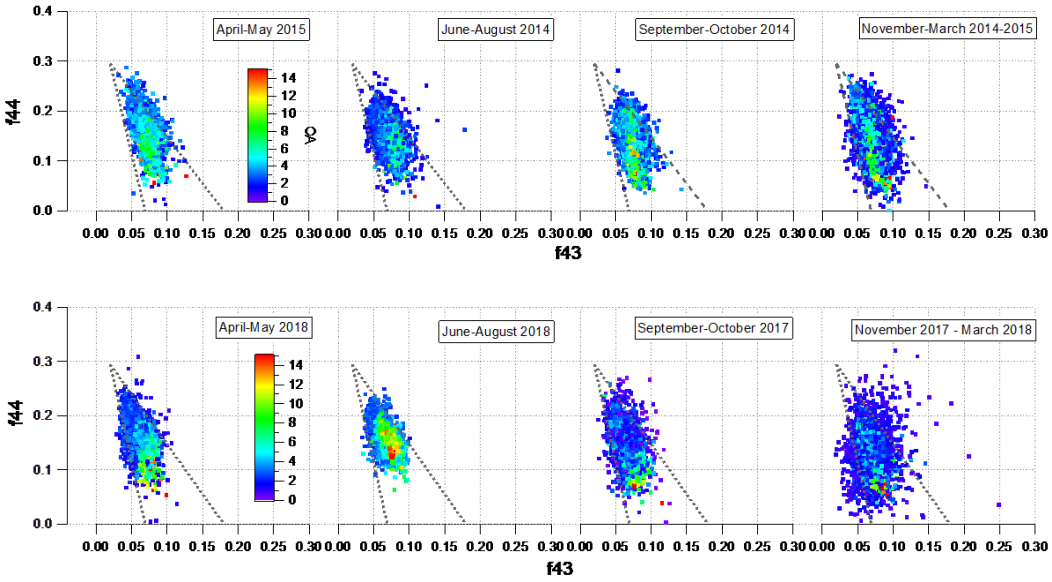

115

Figure S 15. Seasonal scatterplot of f44 and f43 arranged colored by OA concentrations. Top and bottom graphs correspond to period A and B respectively. Dashed lines correspond to the triangle plot (Ng et al., 2010).

(a)

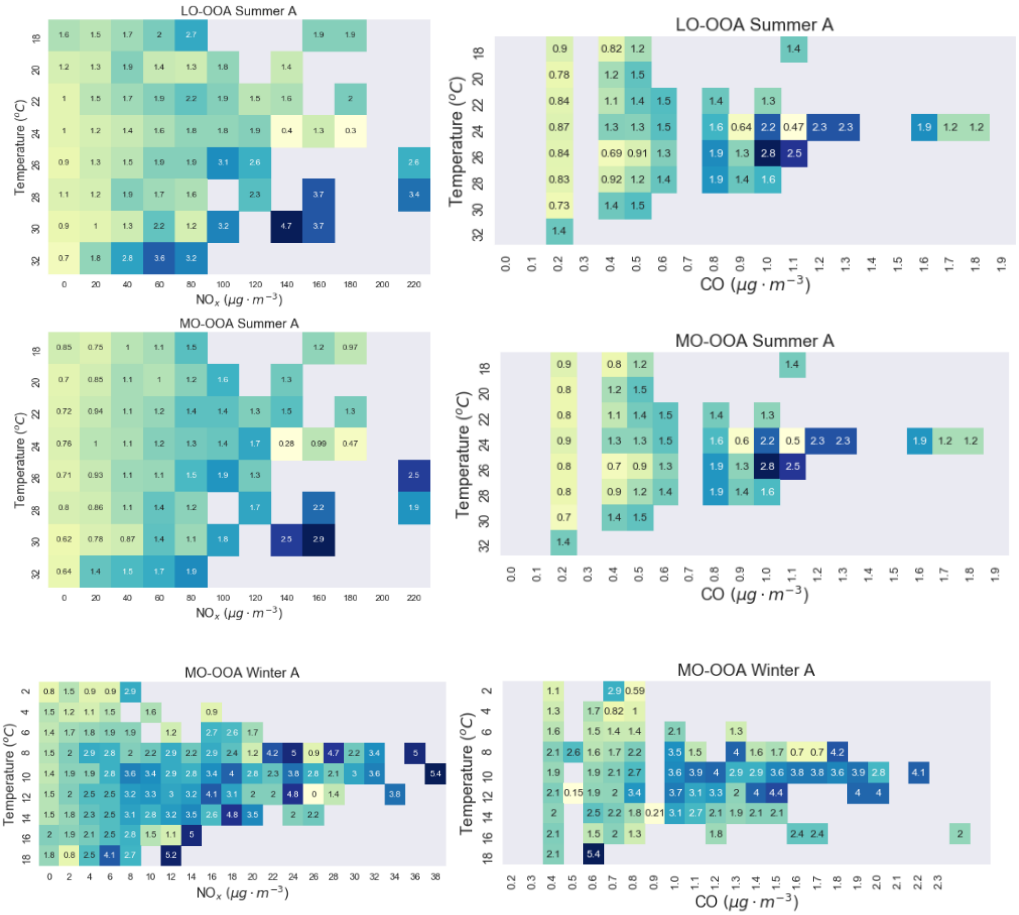
LO-OOA Summer A
Temperature (°C)
NO_x ($\mu g \cdot m^{-3}$)
LO-OOA Summer A
Temperature (°C)
CO ($\mu g \cdot m^{-3}$)
MO-OOA Summer A
Temperature (°C)
NO_x ($\mu g \cdot m^{-3}$)
MO-OOA Summer A
Temperature (°C)
CO ($\mu g \cdot m^{-3}$)

120

MO-OOA Winter A
Temperature (°C)
NO_x ($\mu g \cdot m^{-3}$)
MO-OOA Winter A
Temperature (°C)
CO ($\mu g \cdot m^{-3}$)

(b)

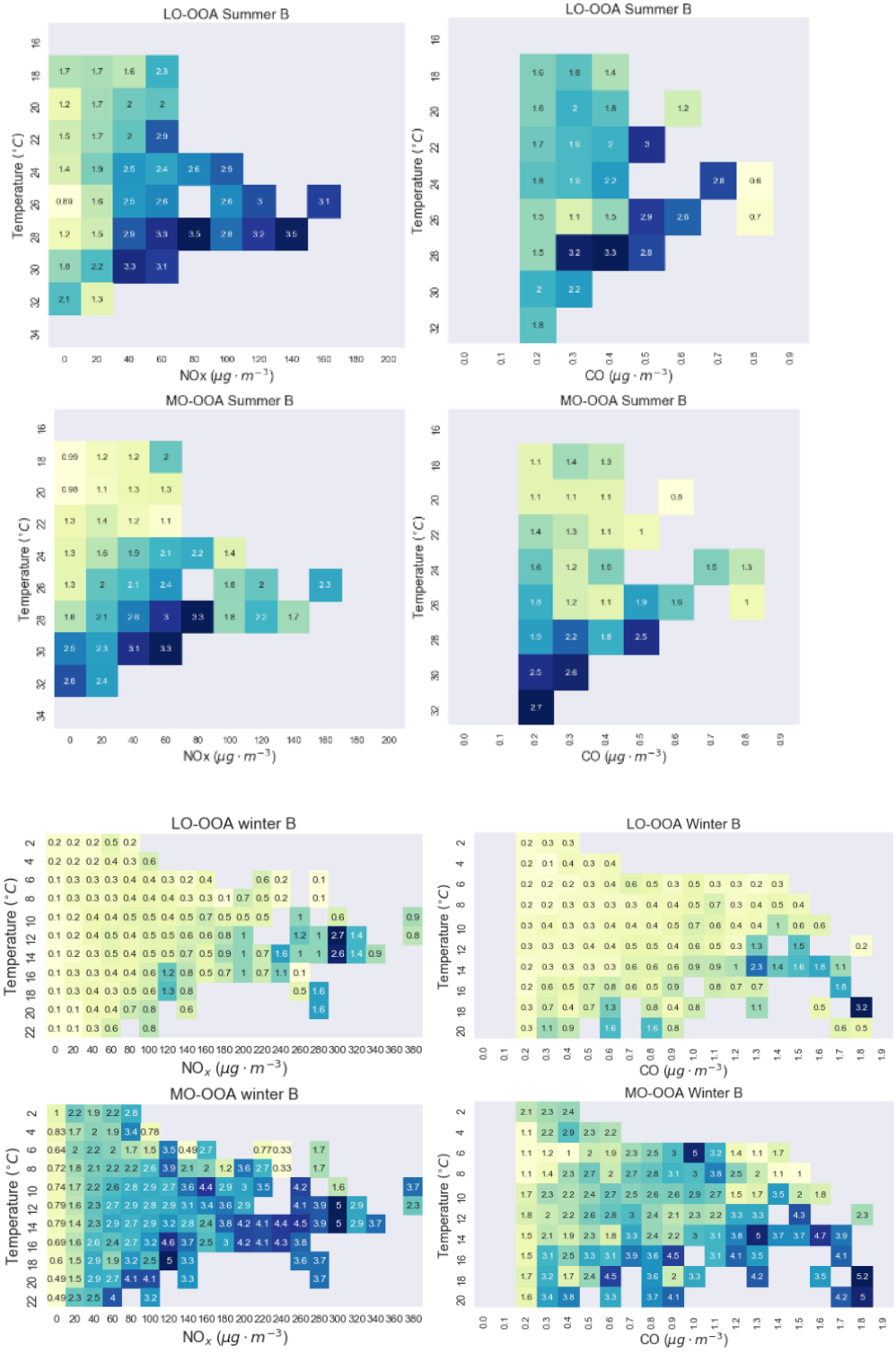

125 **Figure S 16. Heatmap of Temperature vs. NOx for summer (JJA) and winter (DJF) and LO-OOA and MO-OOA respectively for period A (a) and B (b). Figure S 1. Ozone (O_3) diel cycle for seasons in period A (top) and period B (bottom) at Palau Reial (PR) and Montseny (MSY).**

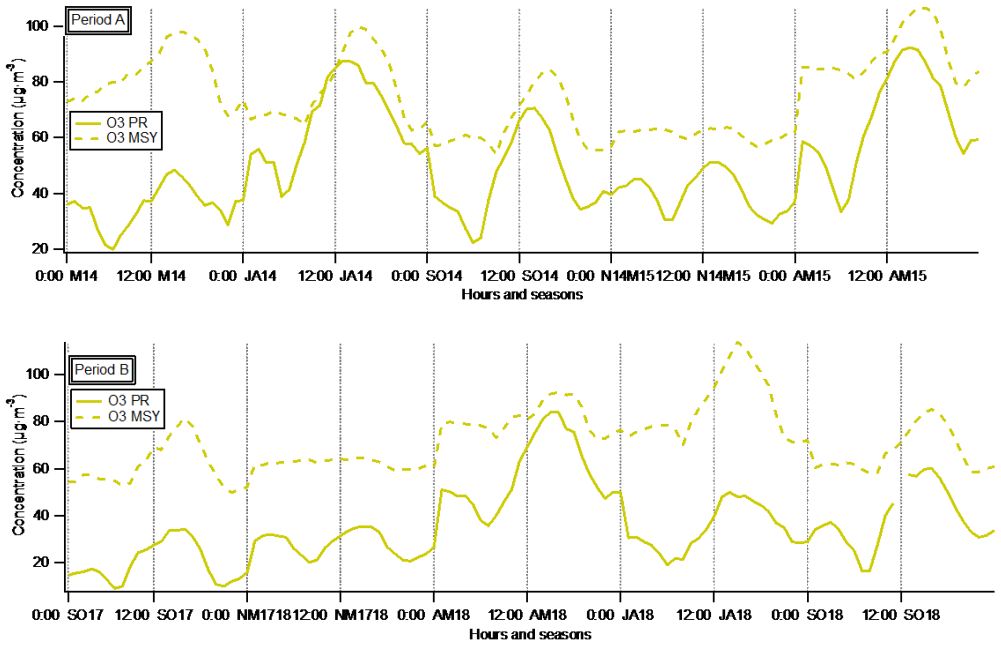

Figure S 17. Ozone diel cycle for seasons in period A and period B at Palau Reial (PR) and Montseny (MSY).

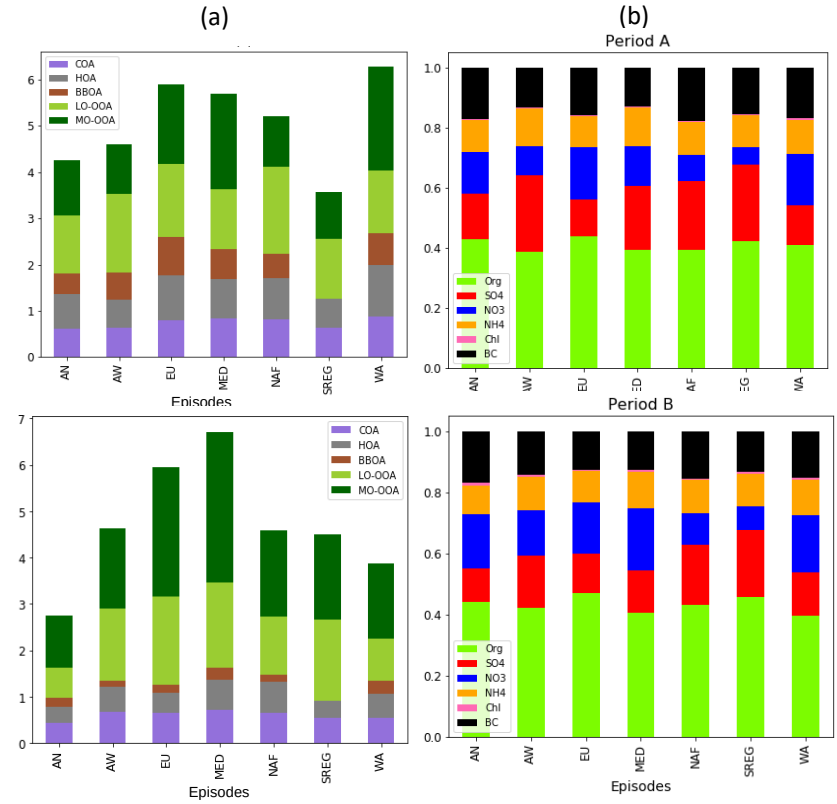

Figure S18. (a) Mean concentrations per each factor grouped by episodes. (c) Relative concentrations of NR-PM1 components grouped by episodes from left to right and for period A (top) and B (bottom).

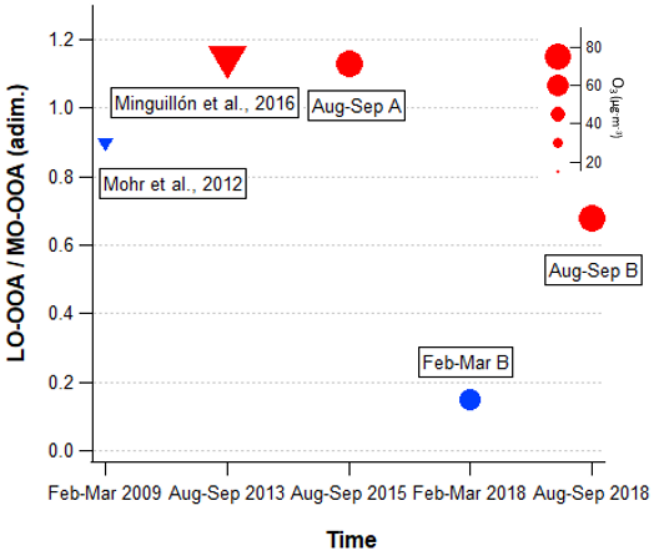

Figure S19. Scatterplot of the LO-OOA-to-MO-OOA ratio vs. time as a function of O3 concentrations (marker size) for the present and previous studies in February-March (blue markers) and August-September (red markers). Note that the Feb-Mar from period A was not included as only one OOA was retrieved.

Section 2. Off-line measurements methodology

PM_1 samples were collected on 150 mm-diameter quartz fiber filters using sequential automatic high-volume samplers Digitel (DHA 80, 30 $m^3 \cdot h^{-1}$). The sampling time was 24 hours midnight to midnight and concentrations were assigned to the start date. Sampling frequency was 1 every 3 days. PM1 levels were determined gravimetrically by conditioning and weighting the filters before and after sampling. Due to problems with the gravimetric determination, PM_1 mass concentration was reconstructed (PM_1 reconstructed) by the addition of all components and an estimation of 25% to account for water.

A complete chemical analysis of the collected PM_1 samples was carried out. A quarter of the filter was used for an acidic digestion (HNO_3:HF:$HClO_4$) following the methodology devised by Querol et al., 2001. The resulting solution was analysed by means of Inductively Coupled Plasma Atomic Emission Spectroscopy (ICP-AES, IRIS Advantage TJA solutions, THERMO) and Inductively Coupled Plasma Mass Spectrometry (ICP-MS, X Series II, THERMO) for the major and trace elements concentration determination, respectively. Few mg of the reference material NIST 1633b were added to a fraction of laboratory blank filters to check the accuracy of the analysis of the acidic digestions.

A quarter of the filter was water extracted and the concentrations of NO_3^- , SO_4^{2-}, and Cl^- were determined by Ion Chromatography (HPLC) using a WATERS ICpakTN anion column with a WATERS 432 conductivity detector. The concentration of NH_4^+ was determined with a Selective Electrode (MODEL 710 A+, THERMO Orion). SO_4^{2-} concentrations in the present study were those calculated from S concentrations determined by ICP-AES, in agreement with all previous works by the research group.

A rectangular portion (1.5 cm^{-2}) of the remaining filter was used for the analysis of organic carbon (OC) and elemental carbon (EC) by thermal-optical methods using a SUNSET OCEC analyser following the EUSAAR 2 protocol (Cavalli et al., 2010).

One blank filter was kept for each set of ten filters. Blank concentrations were subtracted from the total concentration measured for each sample, thus giving ambient concentrations.

Supplement of Atmos. Meas. Tech., 15, 5479–5495, 2022
https://doi.org/10.5194/amt-15-5479-2022-supplement

Atmospheric Measurement Techniques
Open Access
EGU

Supplement of

Rolling vs. *seasonal* PMF: real-world multi-site and synthetic dataset comparison

Marta Via et al.

Correspondence to: Marta Via (marta.via@idaea.csic.es)

Supplementary Information

Section 1: Synthetic dataset creation

The synthetic dataset mimics OA mass spectral analyses of a ToF-ACSM in Zurich. We used source-specific OA mass spectra retrieved from the AMS Spectral database (Ulbrich et al., 2009) and OA source concentration time series generated by the air quality model CAMx (Comprehensive Air Quality Model with Extensions) previously published by Jiang et al. (2019). The represented OA sources are HOA, BBOA, SOA from biogenic emissions (SOAbio), SOA from biomass burning (SOAbb) and SOA from traffic and other anthropogenic sources (SOAtr). Reference profiles selected were: HOA and BBOA from Crippa et al., (2013), SOAtr from Sage et al., (2008), SOAbio represented by a spectrum from Daellenbach et al. 2017 (summer-OOA), and SOAbb represented by a spectrum from Daellenbach et al. 2017 (winter-OOA). For every OA source the mass spectrum is multiplied with its concentration time series. In a first step, the concentrations of the species (m/zs) were calculated by multiplying the OA sources' mass spectra (normalised to 1) obtained from the AMS Spectral Database (Ulbrich et al., 2009) with its concentration time series of each from the CAMx Model and summing the five matrices up. The result is the mass spectral data matrix (I_{diff}). We assume that the ToF-ACSM detects 200 ions/s per µg/m^3 OA which allows for computing ion counts at a single organic m/z.

The error matrix was computed following the same steps as for real-world data. Since the OA measurements are computed as the difference between analyses of air+particle (Iopen) and air (Iclosed), these measurements are the basis of the uncertainty estimates. We assume that baseline spectrum (Ibaseline), and the intensity of closed spectrum (Iclosed) are constant over time, 1 hour long timestamps and airbeam correction constant and equal to 1.

The error related to Iclosed is described as:

$$e_{closed,ij} = \sqrt{(I_{closed\ ,ij} + I_{baseline,ij}) \cdot \frac{t_{closed}}{\sqrt{28}}} \quad (2)$$

The error related to Iopen is described as:

$$e_{open,ij} = \sqrt{(I_{open\ ,ij} + I_{baseline,ij}) \cdot \frac{t_{open}}{\sqrt{28}}} \quad (3)$$

With

$$t_{open} = t_{closed} = 90 \cdot 18\ (s) \quad (4)$$

and

$$I_{open} = I_{closed} + I_{diff} \quad (5)$$

Sorry

Thus the error related to Idiff is:

$$e_{ij} = max\left(1.2 \cdot \frac{1}{90 \cdot 18} \cdot \sqrt{\frac{28}{m/z}} \cdot \sqrt{{e_{open,ij}}^2 + {e_{closed,ij}}^2}\ , \frac{1}{1620}\right)\ (ions/s) \quad (6)$$

$$e_{ij}\ (\mu g/m3)) = \frac{1}{200\ (ions/s/\mu g/m3)} \cdot\ e_{ij}\ (ions/s) \quad (7)$$

Section 2: Figures and Tables.

Table S1. Multi-site assessment dataset characteristics.

Site	PMF m/z spectra	Publication	Rolling window	CE	Reference profiles	Pieber effect
BCN-PR	12-120 (92)	(Via et al., 2021)	14	fPhase	HOA, COA: Crippa et al., 2013 BBOA: Ng et al., 2010	No
CAO-AMX	13-100 (72)	-	14	0.5	HOA: Crippa MEGAPOLI BBOA: derived from this study.	No
DUB	16-100 (72)	Lin et al., (in prep)	14	1	HOA: Crippa et al., 2013 Peat, Wood, Coal: Lin et al., 2017	No
ATOLL	13-100 (72)	Chebaicheb et al., (in prep.)	14	fPhase	HOA, BBOA before seasonal bootstrap: Crippa et al. 2013 HOA, BBOA final solution: winter seasonal results	No

MGD	16-100 (70)	(Chen et al., 2021)	14	0.45	HOA before bootstrap: Crippa et al., 2013 HOA, BBOA final solution: seasonal winter solution	No
INO	13-120 (92)	Vasilescu et al., (in prep.)	14	0.5	HOA: Marmureanu et al., 2020; Vasilescu et al., (in prep.) BBOA: Ng et al., 2011	No
MRS-LCP	12-214 (185)	Chazeau et al., (in prep.)	14	fPhase	HOA: Ng et al, 2011 COA: Crippa et al., 2013 Sh-IndOA: SO2 TS from MRS-LCP site	Yes
SIR	13-100	(Zhang et al., 2019)	28	0.5	HOA: Crippa et al., 2013 BBOA: Frohlich et al., 2015	No
TAR	12-100 (73)	-	28	fPhase	HOA: Crippa et al., 2013 BBOA: seasonal winter solution	No

Table S2. Ancillary instrumentation at each site used for source apportionment.

Site	**Measurement**	**Instrumentation**
BCN-PR	NO_x	Thermo Scientific, Model 43i
CAO-AMX	NO_x	Ecotech 9841T

DUB	NO_x	https://aqicn.org/city/ireland/rathmines/
ATOLL	NO_x	Not available.
MGD	NO_x	https://aqicn.org/city/switzerland/magadino-cadenazzo/
INO	NO_x	Thermo Scientific model 42i
MRS-LCP	NO_x	NOx analyser model 200E (Teledyne)
	SO_2	SO2 analyser model 100E (Teledyne)
	UFP number	UFP monitor 3031 (TSI)
	Particle Size Distribution	MPSS (GRIMM)
SIR	NOx	T200UP Teledyne
TAR	NOx	Horiba APNA-360
	$PM_{2.5}$ and PM_{10}	MetOne BAM1020

Table S3. (a) Reference profiles and a-random ranges used in PMF running ofthe synthetic dataset. (b) Criteria and thresholds for run selection in the synthetic dataset.

(a)	Reference profile	Minimum a value	Maximum a-value	a-value step	
				Rolling	Seasonal
HOA	(Crippa et al., 2013)	0.1	0.2	0.05	0.05
BBOA	(Ng et al., 2011)	0.1	0.3	0.05	0.05

(b)	Criteria	Threshold	
		Seasonal	Rolling
HOA	Diel Squared-Pearson correlation with EC.	R^2>0.35 and p<0.05	R^2>0.50 and p<0.05
HOA	Diel Squared-Pearson correlation with NO_2.	R^2>0.2 and p<0.05	R^2>0.4 and p<0.05
BBOA	Explained variation of f60.	>0.20	>0.20
BBOA	Ratio of time series factor variable 60 and 44.	>0.30	>0.30
LO-OOA	Profile f43 (for differentiation).	All	>0.02
MO-OOA	Profile f44 (for differentiation).	All	>0.02

Table S4. Squared Pearson correlation coefficient and orthogonal distance fit slopes and intercepts for the OA vs. apportioned OA comparison. In columns, the period along which these calculations are performed and averaged and the two SA methods on trial, *rolling* (R) and *seasonal* (S).

Site	Resolution	Rolling		Seasonal	
		R^2	ODR fit	R^2	ODR fit
BCN-PR	Period	0.97	0.99x-0.04	0.97	1.00x-0.05
	Season	1.00	1.00-0.08	0.87	0.92x+0.035
	Fortnight	1.00	0.98+0.02	0.98	1.00x-0.01
	Day	1.00	0.99x-0.02	0.99	1.00x-0.05
CAO-AMX	Period	0.99	0.97x+0.14	0.99	0.96x+0.010
	Season	0.95	1.09x-0.24	1.00	0.97+0.05

	Fortnight	0.98	0.99x+0.08	0.97	1.02+0.07
	Day	0.99	0.97x+0.13	1.00	0.95x+0.08
DUB	Period	1.00	1.00x-0.01	1.00	0.99x+0.01
	Season	1.00	1.00x-0.02	1.00	1.01x-0.04
	Fortnight	1.00	1.00x-0.00	1.00	1.00x-0.00
	Day	1.00	0.99x-0.00	1.00	0.99+0.01
ATO LL	Period	0.99	1.00x+0.02	0.98	1.00x-0.02
	Season	1.00	1.00x-0.01	1.00	1.00x-0.00
	Fortnight	1.00	1.00x-0.02	1.00	1.00x-0.05
	Day	1.00	1.00x-0.02	1.00	1.00x-0.04
MGD	Period	0.99	1.00x+0.02	0.98	1.00-0.00
	Season	1.00	1.00x+0.02	0.99	1.01x-0.15
	Fortnight	1.00	1.00x-0.00	0.99	1.01x-0.12
	Day	1.00	1.00x-0.02	1.00	1.01x-0.06
INO	Period	0.88	1.07x-0.77	0.98	1.09x-1.14
	Season	1.00	0.99x+0.15	0.97	0.98x+0.15
	Fortnight	1.00	1.00x+0.58	0.97	1.07x-0.58
	Day	0.99	1.04x-0.50	0.98	1.06x+0.92
MRS-LCP	Period	1.00	1.00x-0.03	0.99	1.03x+0.16
	Season	1.00	1.00x-0.01	1.00	0.97x+0.10
	Fortnight	1.00	1.00x-0.04	1.00	1.01x-0.02
	Day	0.99	1.01x+0.03	0.99	1.02x-0.05

SIR	Period	1.00	0.95x+0.05	0.96	0.95x+0.02
	Season	1.00	0.93x+0.15	1.00	0.94x+0.15
	Fortnight	1.00	0.94x+0.08	1.00	0.95x+0.04
	Day	1.00	0.95x+0.05	0.99	0.96x+0.00
TAR	Period	1.00	0.92x+0.05	1.00	0.92x+0.05
	Season	1.00	0.92x+0.04	1.00	0.93x+0.01
	Fortnight	1.00	0.93x+0.02	1.00	0.93x+0.00
	Day	1.00	0.93x+0.03	1.00	0.93x+0.02
SYN	Period	1.00	1.14x-0.08	1.00	1.14x-0.07
	Season	1.00	1.15x-0.12	1.00	1.14x-0.12
	Fortnight	1.00	1.14x-0.08	1.00	1.14x-0.08
	Day	1.00	1.36x-0.07	1.00	1.36x-0.07

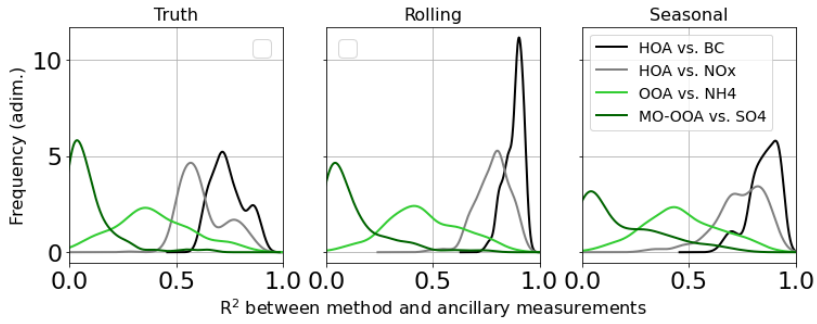

Figure S1. Histogram of the difference of *rolling* minus *seasonal* of the Pearson-squared correlation coefficient of the synthetic OA factors and their potential markers.

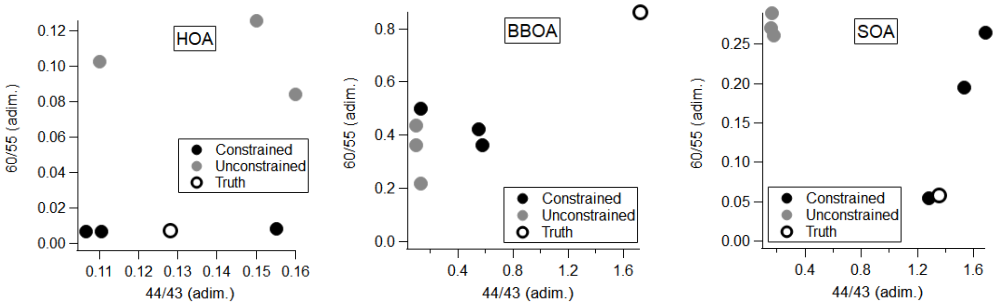

Figure S2. Scatterplots of m/z60-to-m/z55 ratio vs. m/z44-to-m/z43 ratio for the three basic factors in the synthetic dataset for each season.

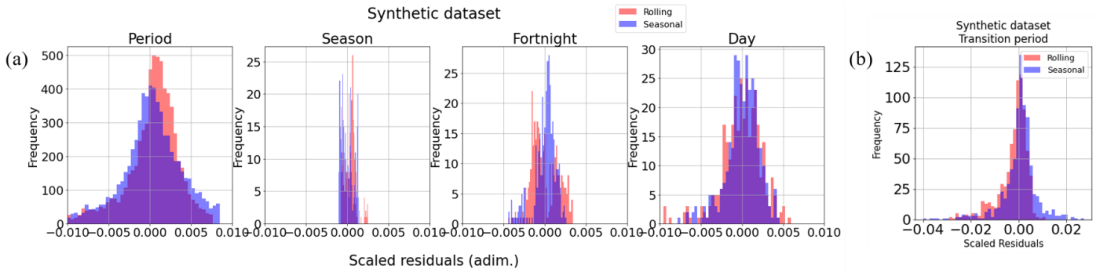

Figure S3. Scaled residuals distribution (a) for the whole period and 90-days, 14-days and 1-day resolutions. (b) transition periods. Number of bins is 50 in all cases.

Table S5. Welch's t-test rejections (marked with a bullet-dot) over the p<0.05 threshold value for all sites, factors and time spans (P: period; S: season; F: fortnight; D: day). Note that for 'other POA' the 'ALL' site does not show information, as they are shown at their respective sites. Hyphens and slashes flag those cells which have no representation in one site (this is, that site does not have this factor) and those which have more than one factor in a cell, respectively.

Welch's t-test	HOA				BBOA				Other POA				LO-OOA				MO-OOA				OOA				OA			
	P	S	F	D	P	S	F	D	P	S	F	D	P	S	F	D	P	S	F	D	P	S	F	D	P	S	F	D
BCN-PR	*	*	*			*			*	*	*	*	*				*				*							
CAO-AMX	*	*			*	*	*	*	-	-	-	-	*	*	*	*	*	*	*	*	*					*	*	*
DUB					-	-	-	-	//	//	//	//	*	*			*											
ATOLL	*	*	*	*	*	*	*	*	-	-	-	-	*		*		*	*	*	*	*	*	*	*	*	*	*	

MGD	*	*	*	*	*	*	*	*	*	*	*	*	*				*	*	*	*	*	*	*	*	*	*	*	*
INO	*	*	*		*				-	-	-	-	*	*	*	*	*	*	*									
MRS-LCP	*	*	*		*	*	*	*	/*	*/	*		/	*	*	*	*	*	*	*	*	*				*		
SIR	*	*	*	*	*	*			-	-	-	-	*	*	*	*	*	*	*	*	*	*	*		*			
TAR		*	*						-	-	-	-	*	*	*		*											
ALL	*	*	*	*	*				-	-	-	-	*				*	*	*	*	*	*	*	*	*	*	*	*

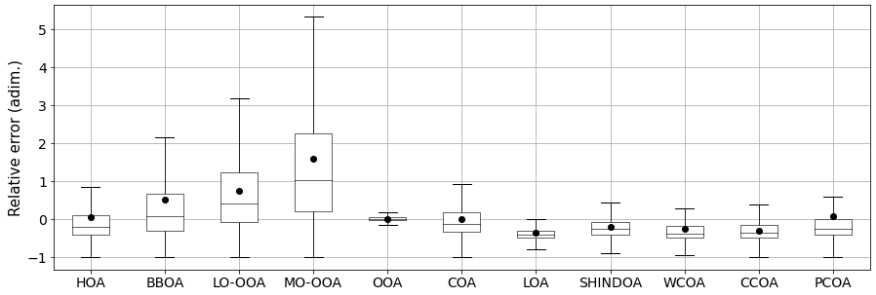

Figure S4. Boxplots of relative error *rolling* minus *seasonal*, i.e., the difference between methods divided by the mean of the concentrations between *seasonal* and *rolling*.

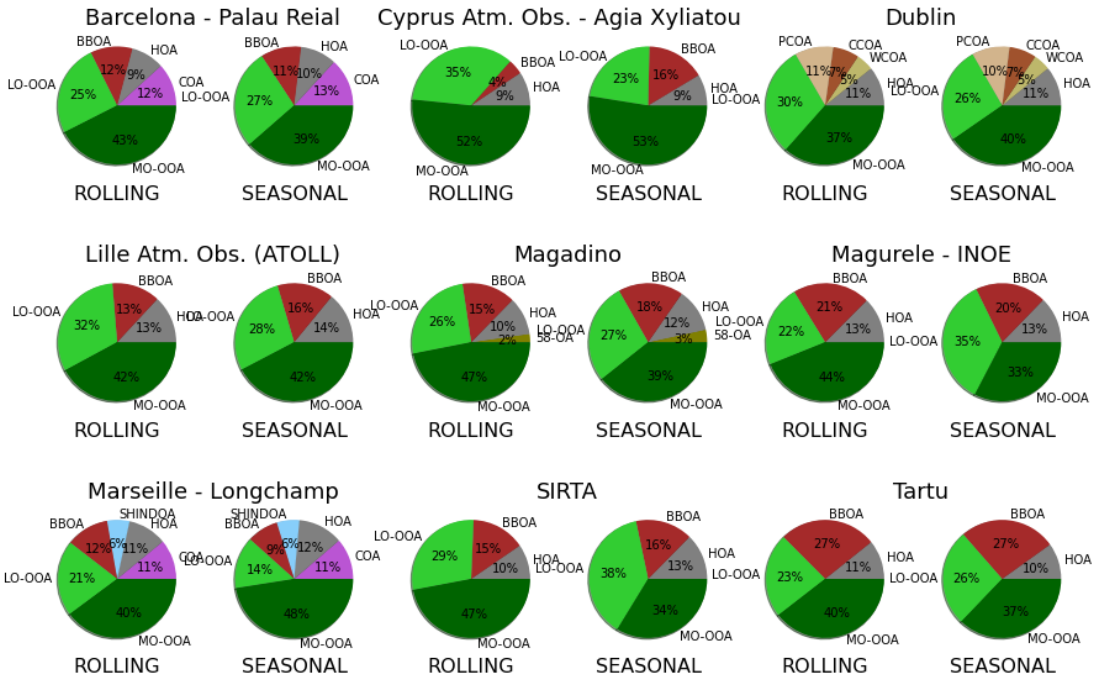

Figure S5. Pie plots for *rolling* and *seasonal* source apportionment solutions for each site. The factor acronyms correspond to: Hydrocarbon-like OA (HOA), Biomass Burning OA (BBOA), Less Oxidised Oxygenated OA (LO-OOA), More Oxidised Oxygenated OA (MO-OOA), Cooking-like OA (COA), Peat Combustion OA (PCOA), Coal Combustion OA (CCOA), Wood Combustion OA (WCOA), 58-related OA (58-OA) and Shipping + Industry OA (SHINDOA).

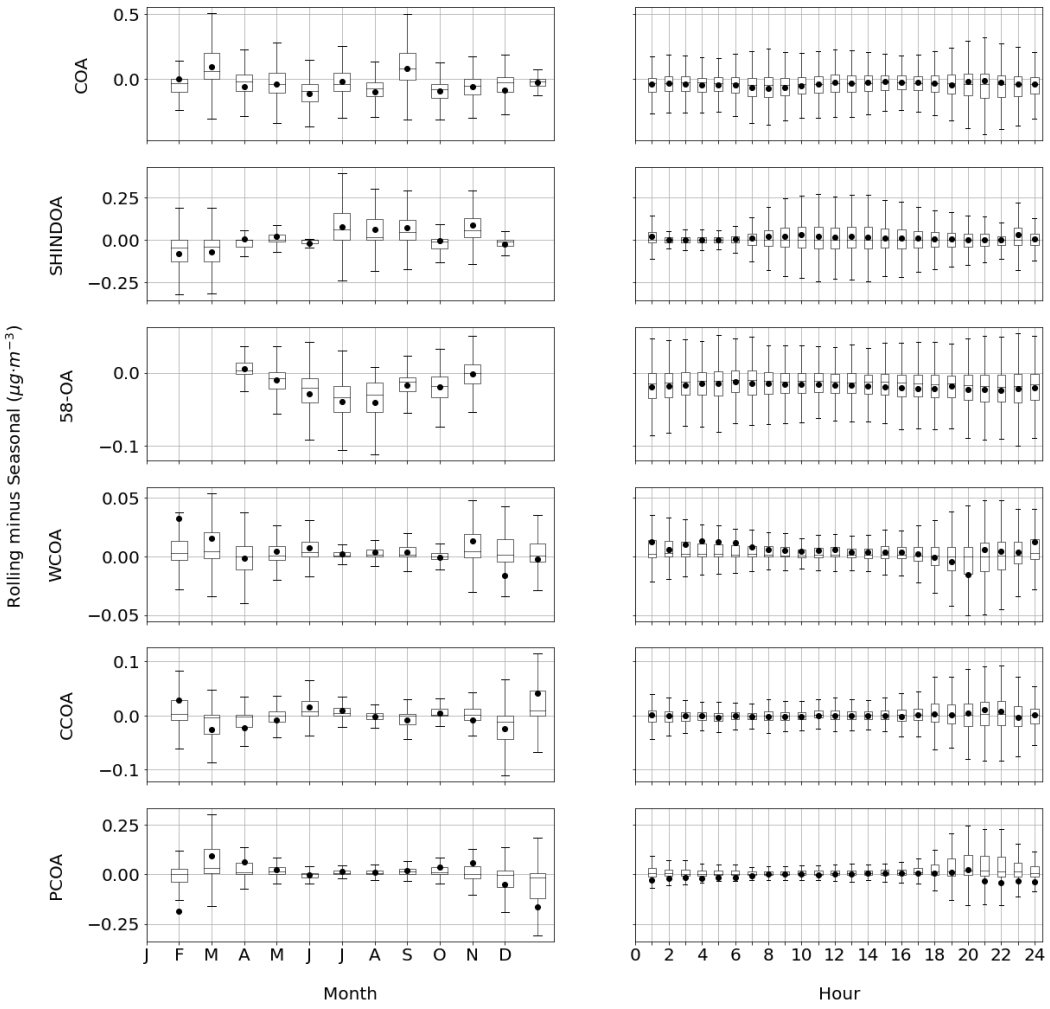

Figure S6. Boxplots of *rolling* minus *seasonal* factor concentrations per month and hour of the factors which are not present in all sites. Boxes show the Q1-to-Q3 range and the median, and whiskers extend up to the range of the data and round markers show the means.

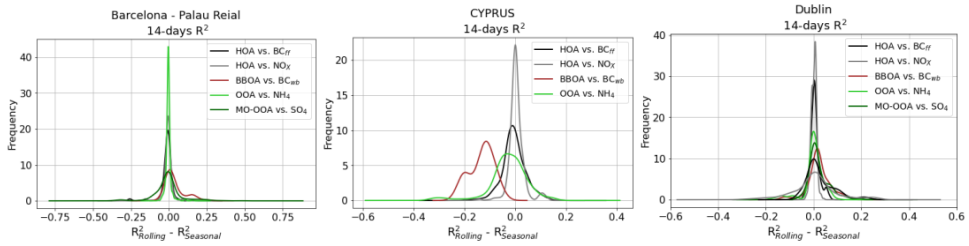

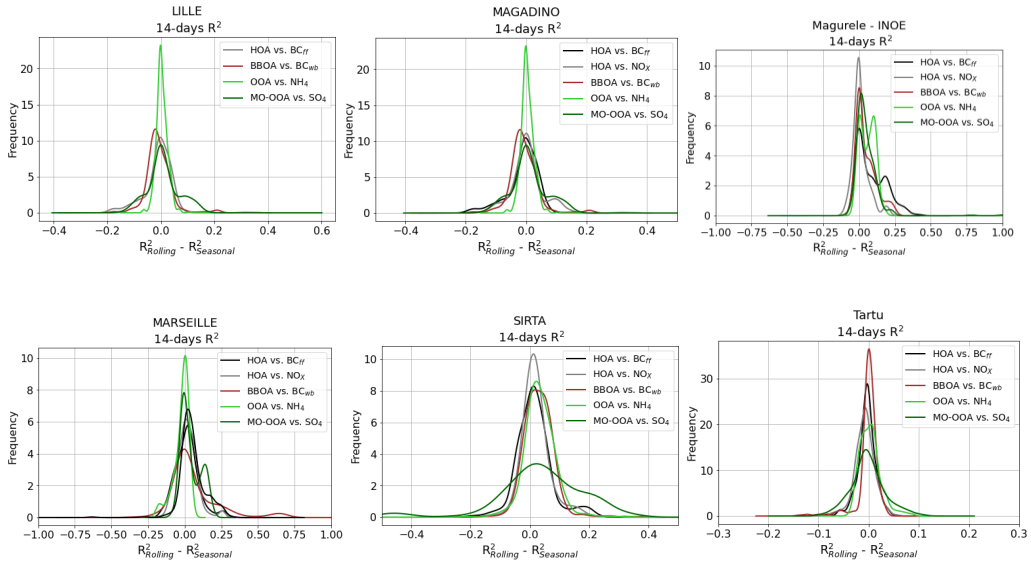

Figure S7. Kernel density estimation of difference between rolling and seasonal R^2 to correlated measurements.

Table S6. Pearson correlation coefficients between factors and co-located measurements for the *rolling* and *seasonal* during transition periods from one season to the following in each site and as a whole. Whole refers to the correlation between factors and markers of the concatenated time series of all sites.

R^2 in transition periods	HOA vs. BC_{ff}		HOA vs. NO_x		BBOA vs. BC_{wb}		MO-OOA vs. SO_4^{2-}		OOA vs. NH_4^+	
	R	S	R	S	R	S	R	S	R	S
BCN-PR	0.75	0.76	0.62	0.63	0.13	0.05	0.31	0.27	0.59	0.62
CAO-AMX	0.21	0.14	0.05	0.05	0.04	0.26	0.49	0.56	0.52	0.52
DUB	0.88	0.86	0.36	0.35	-	-	0.4	0.24	0.66	0.58
ATOLL	0.47	0.52	-	-	0.18	0.17	0.00	0.01	0.00	0.00
MAG	0.32	0.30	0.42	0.43	0.86	0.84	0.43	0.50	0.48	0.48
INO	0.12	0.08	0.24	0.12	0.65	0.57	0.21	0.17	0.61	0.40

MRS-LCP	0.54	0.54	0.56	0.54	0.88	0.54	0.3	0.12	0.57	0.61
SIRTA	0.44	0.43	0.48	0.43	0.68	0.74	0.48	0.25	0.56	0.50
TAR	0.27	0.25	0.31	0.31	0.73	0.74	0.12	0.27	0.21	0.15
Whole	0.49	0.47	0.25	0.15	0.49	0.51	0.26	0.27	0.44	0.39

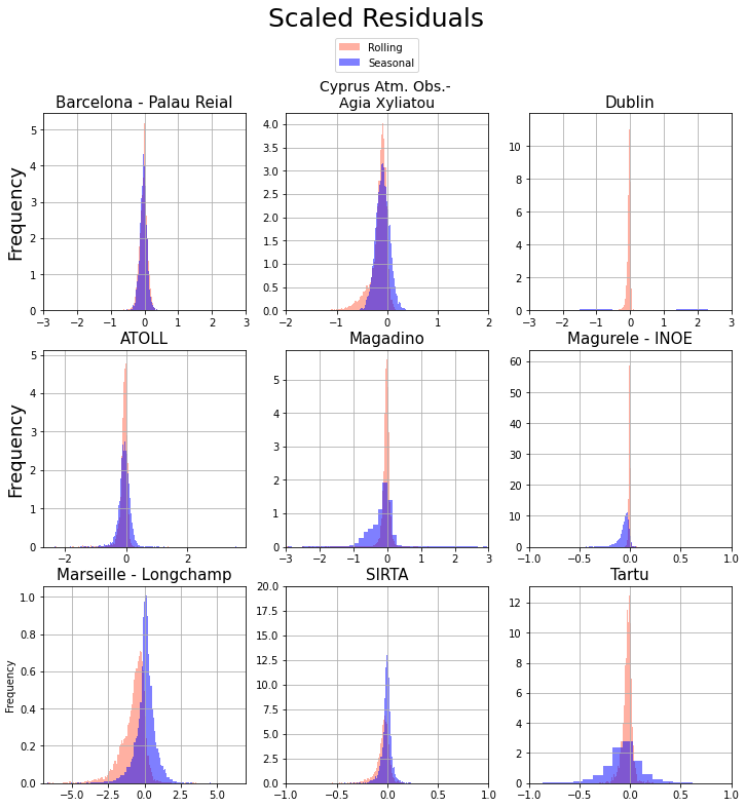

Figure S8. Scaled residuals histograms for all sites.

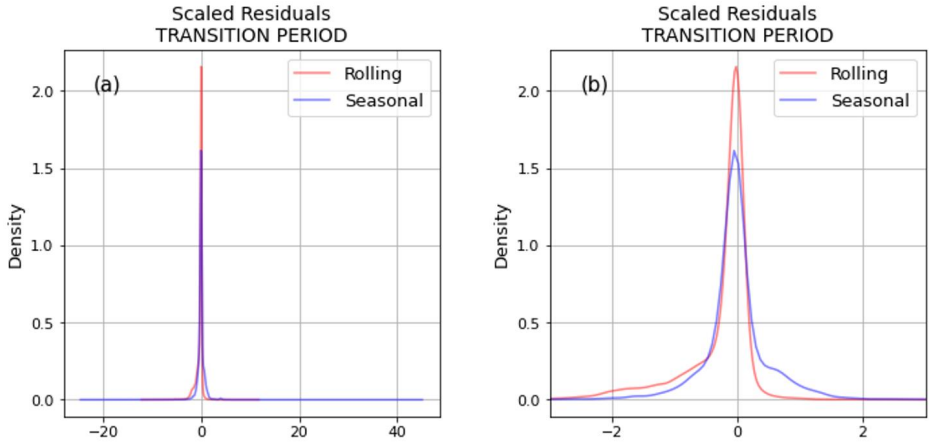

Figure S9. Kernel density estimation of scaled residuals of the *rolling* and *seasonal* solution in the transition periods between seasons where (b) represents a zoom of figure (a).

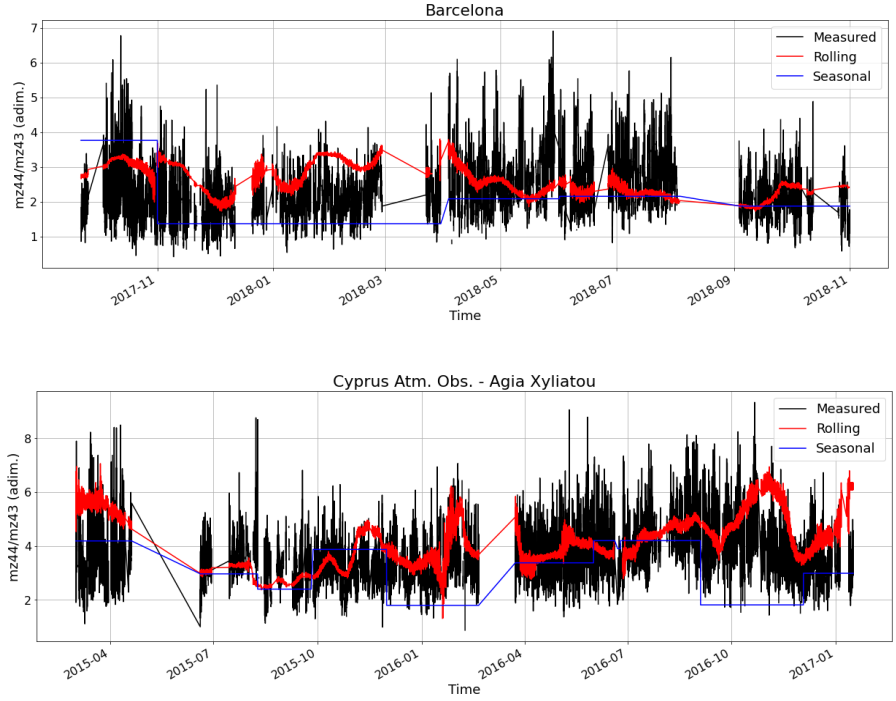

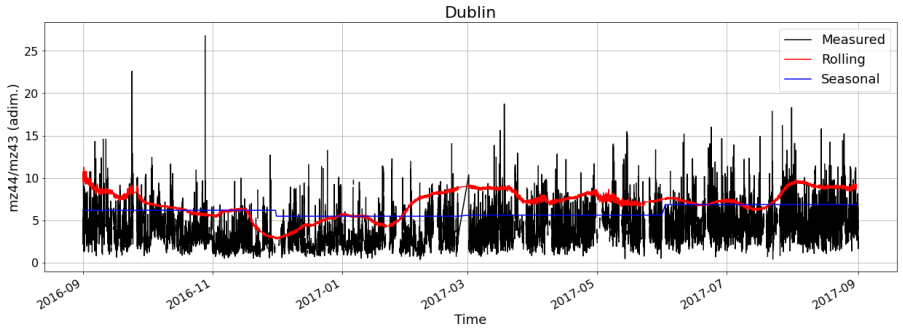
Dublin
Measured
Rolling
Seasonal
mz44/mz43 (adim.)
0
5
10
15
20
25
2016-09
2016-11
2017-01
2017-03
2017-05
2017-07
2017-09
Time

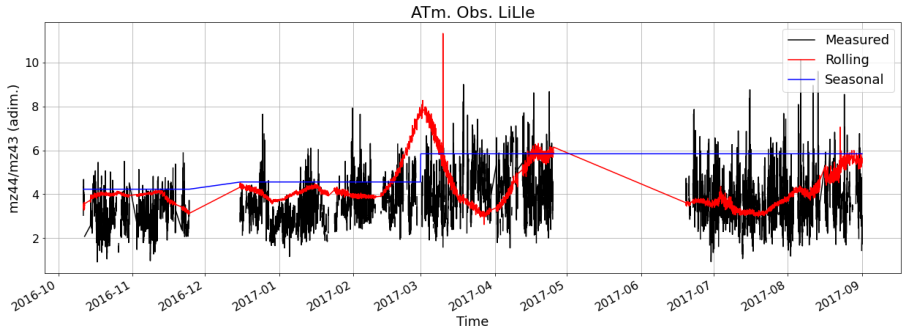
ATm. Obs. LiLle
Measured
Rolling
Seasonal
mz44/mz43 (adim.)
2
4
6
8
10
2016-10
2016-11
2016-12
2017-01
2017-02
2017-03
2017-04
2017-05
2017-06
2017-07
2017-08
2017-09
Time

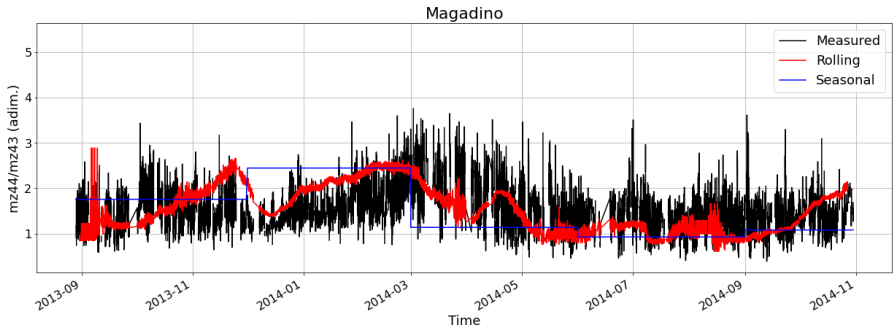
Magadino
Measured
Rolling
Seasonal
mz44/mz43 (adim.)
1
2
3
4
5
2013-09
2013-11
2014-01
2014-03
2014-05
2014-07
2014-09
2014-11
Time

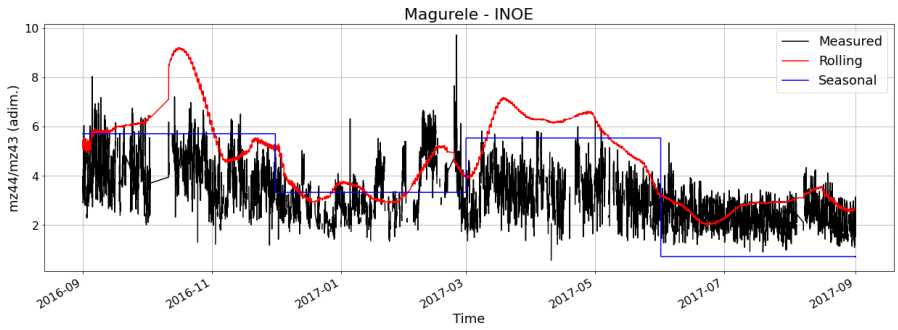
Magurele - INOE
Measured
Rolling
Seasonal
mz44/mz43 (adim.)
2
4
6
8
10
2016-09
2016-11
2017-01
2017-03
2017-05
2017-07
2017-09
Time

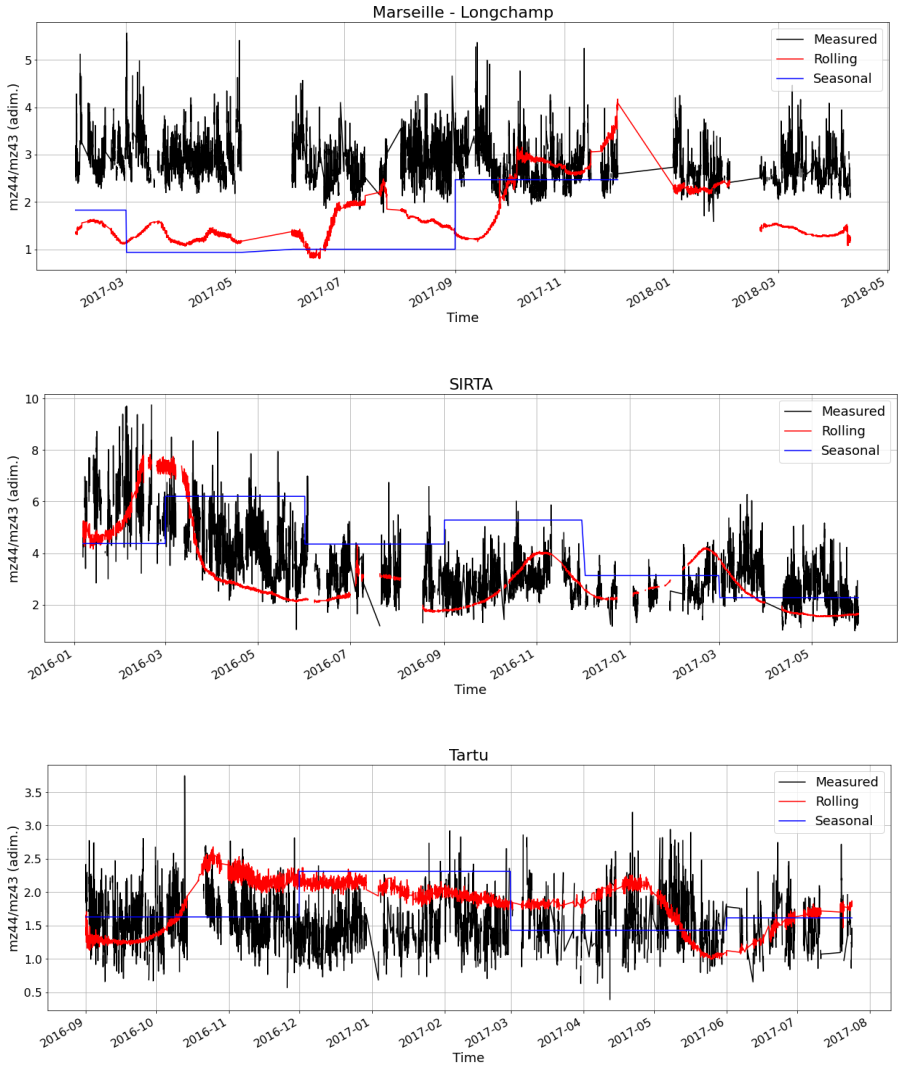

Figure S10. Time series of the *m/z44*-to-*m/z43* ratios for raw time series and SOA profiles for all the sites.

References

Chen, G., Sosedova, Y., Canonaco, F., Fröhlich, R., Tobler, A., Vlachou, A., Daellenbach, K., Bozzetti, C., Hueglin, C., Graf, P., Baltensperger, U., Slowik, J., El Haddad, I. and Prévôt, A.: Time dependent source apportionment of submicron organic aerosol for a rural site in an alpine valley using a rolling PMF window, Atmos. Chem. Phys. Discuss., 43, 1–52, doi:10.5194/acp-2020-1263, 2021.

Crippa, M., Decarlo, P. F., Slowik, J. G., Mohr, C., Heringa, M. F., Chirico, R., Poulain, L., Freutel, F., Sciare, J., Cozic, J., Di Marco, C. F., Elsasser, M., Nicolas, J. B., Marchand, N., Abidi, E., Wiedensohler, A., Drewnick, F.,

Schneider, J., Borrmann, S., Nemitz, E., Zimmermann, R., Jaffrezo, J. L., Prévôt, A. S. H. and Baltensperger, U.: Wintertime aerosol chemical composition and source apportionment of the organic fraction in the metropolitan area of Paris, Atmos. Chem. Phys., 13(2), 961–981, doi:10.5194/acp-13-961-2013, 2013.

Daellenbach, K. R., Uzu, G., Jiang, J., Cassagnes, L. E., Leni, Z., Vlachou, A., Stefenelli, G., Canonaco, F., Weber, S., Segers, A., Kuenen, J. J. P., Schaap, M., Favez, O., Albinet, A., Aksoyoglu, S., Dommen, J., Baltensperger, U., Geiser, M., El Haddad, I., Jaffrezo, J. L. and Prévôt, A. S. H.: Sources of particulate-matter air pollution and its oxidative potential in Europe, Nature, 587(7834), 414–419, doi:10.1038/s41586-020-2902-8, 2020.

Dee, D. P., Uppala, S. M., Simmons, A. J., Berrisford, P., Poli, P., Kobayashi, S., Andrae, U., Balmaseda, M. A., Balsamo, G., Bauer, P., Bechtold, P., Beljaars, A. C. M., van de Berg, L., Bidlot, J., Bormann, N., Delsol, C., Dragani, R., Fuentes, M., Geer, A. J., Haimberger, L., Healy, S. B., Hersbach, H., Hólm, E. V., Isaksen, L., Kållberg, P., Köhler, M., Matricardi, M., Mcnally, A. P., Monge-Sanz, B. M., Morcrette, J. J., Park, B. K., Peubey, C., de Rosnay, P., Tavolato, C., Thépaut, J. N. and Vitart, F.: The ERA-Interim reanalysis: Configuration and performance of the data assimilation system, Q. J. R. Meteorol. Soc., 137(656), 553–597, doi:10.1002/qj.828, 2011.

Jiang, J., Aksoyoglu, S., El-Haddad, I., Ciarelli, G., Denier Van Der Gon, H. A. C., Canonaco, F., Gilardoni, S., Paglione, M., Minguillón, M. C., Favez, O., Zhang, Y., Marchand, N., Hao, L., Virtanen, A., Florou, K., O'Dowd, C., Ovadnevaite, J., Baltensperger, U. and Prévôt, A. S. H.: Sources of organic aerosols in Europe: A modeling study using CAMx with modified volatility basis set scheme, Atmos. Chem. Phys., 19(24), 15247–15270, doi:10.5194/acp-19-15247-2019, 2019.

Ng, N. L., Canagaratna, M. R., Jimenez, J. L., Chhabra, P. S., Seinfeld, J. H. and Worsnop, D. R.: Changes in organic aerosol composition with aging inferred from aerosol mass spectra, Atmos. Chem. Phys., 11(13), 6465–6474, doi:10.5194/acp-11-6465-2011, 2011.

Skamarock, W. C. and Klemp, J. B.: A time-split nonhydrostatic atmospheric model for weather research and forecasting applications, J. Comput. Phys., 227(7), 3465–3485, doi:10.1016/j.jcp.2007.01.037, 2008.

Ulbrich, I. M., Canagaratna, M. R., Zhang, Q., Worsnop, D. R. and Jimenez, J. L.: Interpretation of organic components from Positive Matrix Factorization of aerosol mass spectrometric data, Atmos. Chem. Phys., 9(9), 2891–2918, doi:10.5194/acp-9-2891-2009, 2009.

Via, M., Minguillón, M. C., Reche, C., Querol, X. and Alastuey, A.: Increase in secondary organic aerosol in an urban environment, Atmos. Chem. Phys., 21(10), 8323–8339, doi:10.5194/acp-21-8323-2021, 2021.

Zhang, Y., Favez, O., Petit, J. E., Canonaco, F., Truong, F., Bonnaire, N., Crenn, V., Amodeo, T., Prévôt, A. S. H., Sciare, J., Gros, V. and Albinet, A.: Six-year source apportionment of submicron organic aerosols from near-continuous highly time-resolved measurements at SIRTA (Paris area, France), Atmos. Chem. Phys., 19(23), 14755–14776, doi:10.5194/acp-19-14755-2019, 2019.

Supplementary information

Section A. Figures and tables

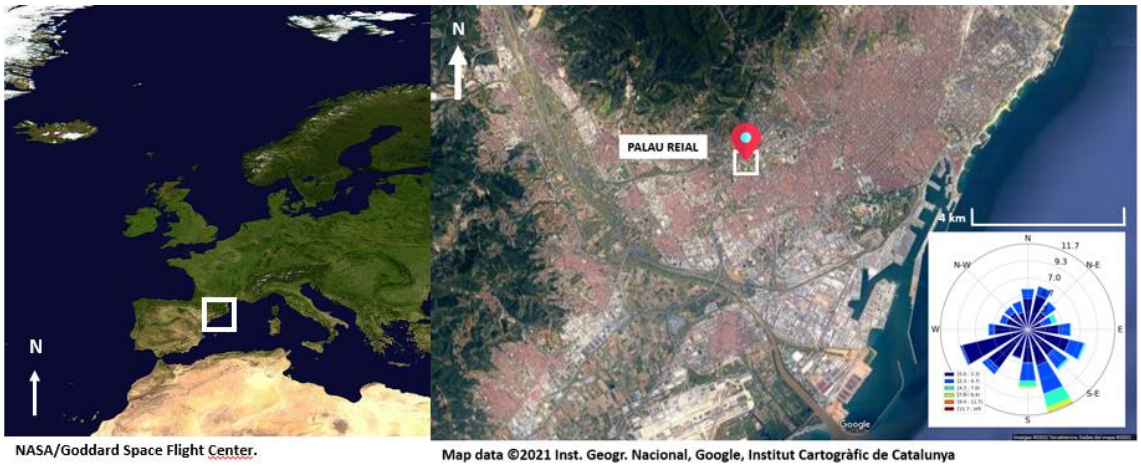

Figure S1. Site location map and windrose.

Table S1. Comparison of online and offline SIA compounds and bulk OA (adapted from (Via et al., 2021)**.**

y	x	R^2	Slope	Intercept
ACSM SO_4^{2-}	Offline SO_4^{2-}	0.89	1.32 ± 0.06	-0.19 ± 0.09
ACSM NO_3^-	Offline NO_3^-	0.84	1.72 ± 0.10	0.35 ± 0.12
ACSM NH_4^+	Offline NH_4^+	0.86	1.98 ± 0.13	-0.05 ± 0.09
ACSM Cl^-	Offline Cl^-	0.43	2.8 ± 0.4	0.023 ± 0.009
ACSM OA	Offline OC	0.73	2.96 ± 0.19	-1.5 ± 0.4

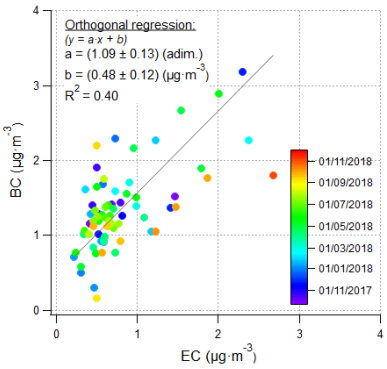

Figure S2. Scatterplot of black carbon (BC) measurements from aethalometer averaged to a resolution of 24 hours every 4 days vs. elemental carbon (EC) concentrations obtained from offline filters. The orthogonal fit of the linear regression is presented in the graph.

Table S2. Signal-to-noise values of all the species in the input matrix for the multi-time resolution PMF. The species marked with a * represent weak variables (signal-to-noise below 2).

HR	2.89	OA	4.00		
		NR-PM1	3.45	SO4	3.27
				NO3	3.15
				NH4	3.29
				Chl	4.09
		BC	3.86	BC_{lf}	4.34
				BC_{sf}	3.37
LR	4.15	Al	0.46*		
		Ca	1.28*		
		K	5.16		
		Mg	1.91*		
		Na	0.54*		
		Ti	1.86*		
		V	8.99		
		Cr	0.71*		
		Mn	4.88		
		Co	4.19		
		Ni	0.94*		
		Cu	6.60		
		Zn	6.26		
		As	6.83		
		Rb	5.07		
		Cd	1.35*		
		Sn	7.93		
		Sb	5.63		
		Pb	8.17		

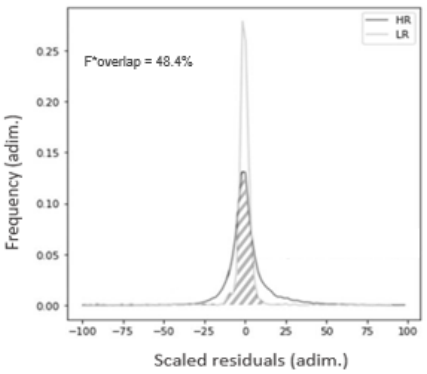

Figure S3. HR and LR histograms. The shaded area corresponds to the intersection of histograms, also expressed in percentage in the figure.

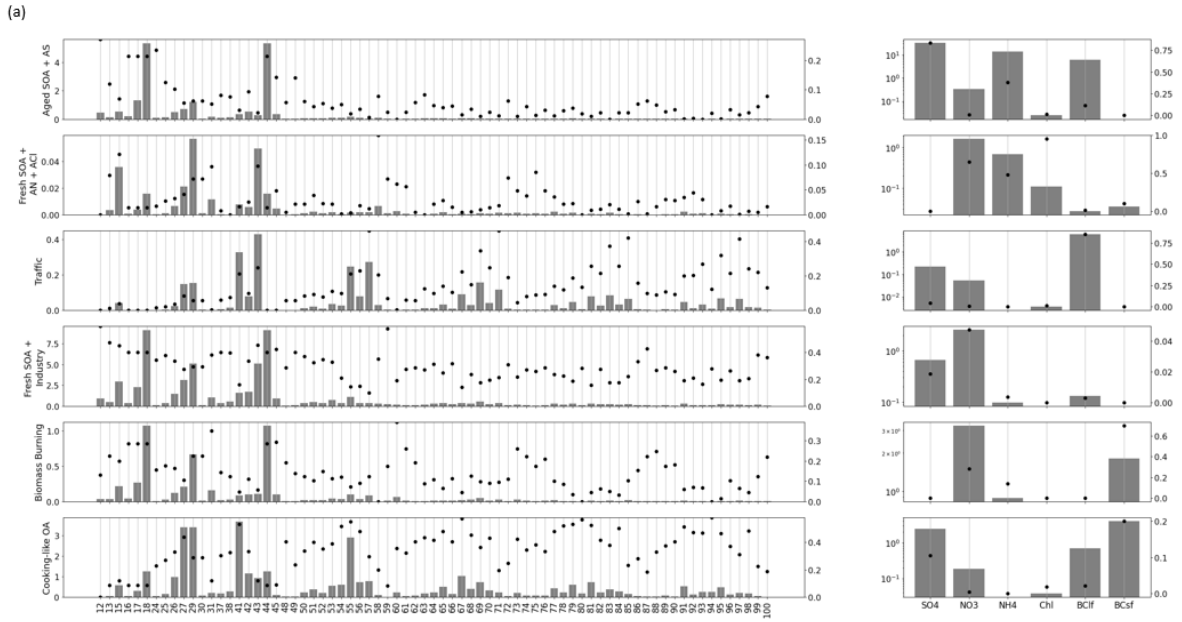
(a)
Aged SOA + AS
Fresh SOA + AN + ACl
Traffic
Fresh SOA + Industry
Biomass Burning
Cooking-like OA
SO4
NO3
NH4
Chl
BCIf
BCsf

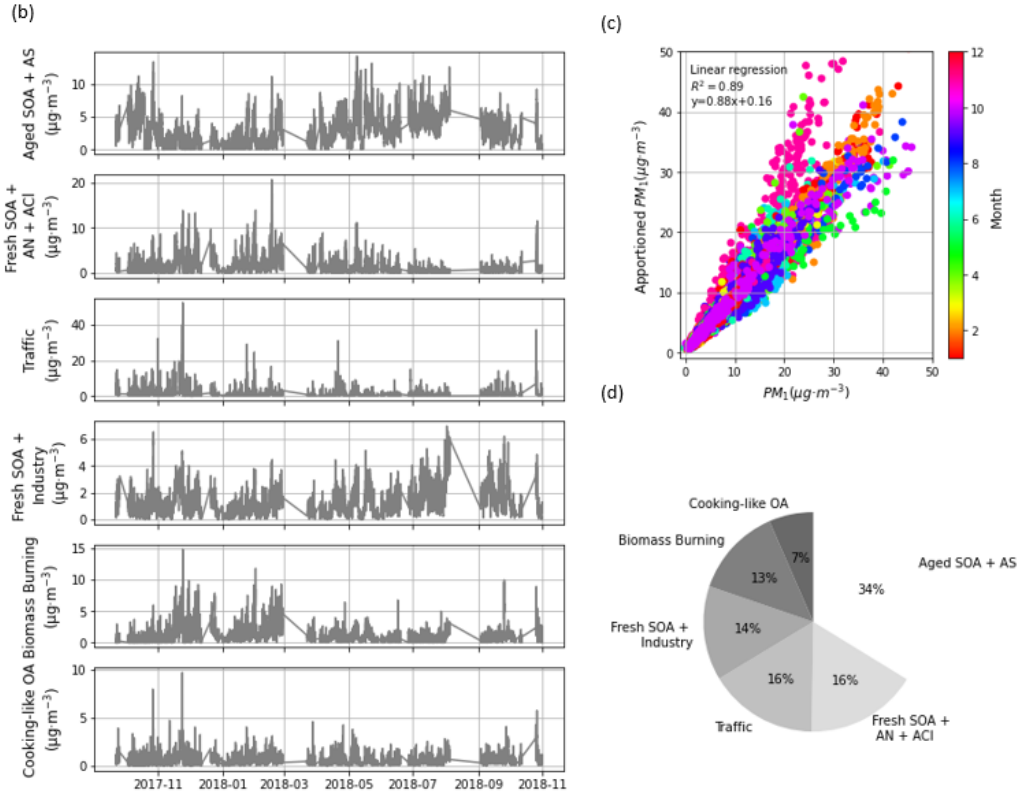
(b)
Aged SOA + AS (μg m⁻³)
Fresh SOA + AN + ACl (μg m⁻³)
Traffic (μg m⁻³)
Fresh SOA + Industry (μg m⁻³)
Biomass Burning (μg m⁻³)
Cooking-like OA (μg m⁻³)
2017-11
2018-01
2018-03
2018-05
2018-07
2018-09
2018-11
(c)
Linear regression
R² = 0.89
y=0.88x+0.16
Apportioned PM1 (μg m⁻³)
PM1 (μg·m⁻³)
Month
(d)
Cooking-like OA
Biomass Burning
Aged SOA + AS
Fresh SOA + Industry
Traffic
Fresh SOA + AN + ACl
7%
13%
34%
14%
16%
16%

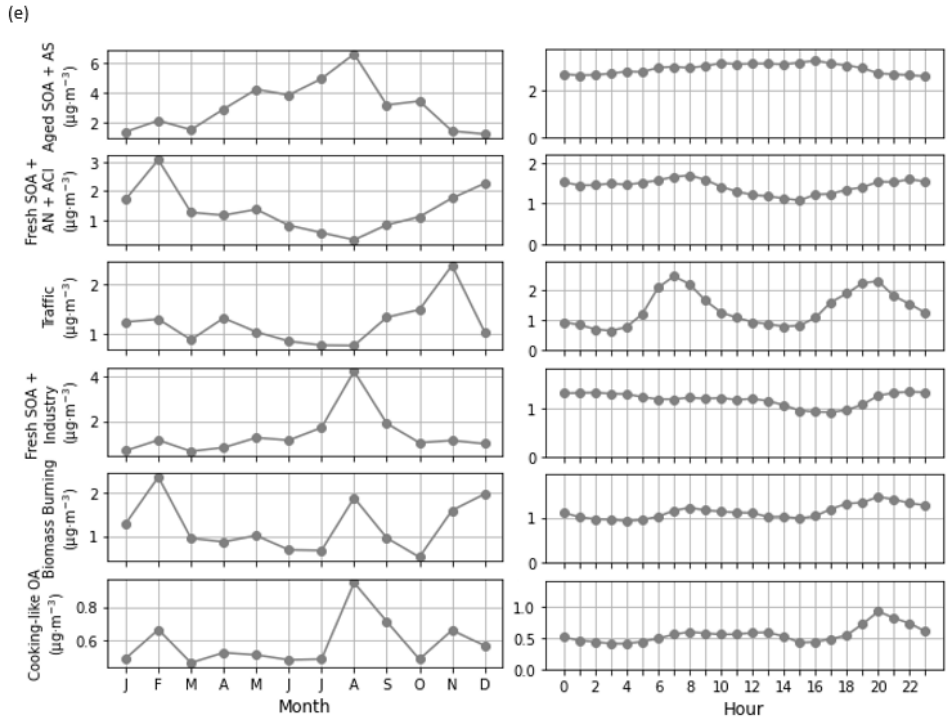

Figure S4. Source apportionment of the HR subdataset (a) Source profiles (b) Time series (c) Mass closure (d) Pie of apportionment (e) Monthly and diel cycles. Note that zero does not start at zero in the latter plots. For the profiles plot, bars (left axis) show the normalised concentrations of each species in each factor, circles (right axis) show the percentage of each species attributed to each factor, and percentages show the proportion of OA to the total mass of that factor. Also, the left panel is dedicated to the unit-mass-resolution OA species and the right one (in log scale) to the SIA, BC species.

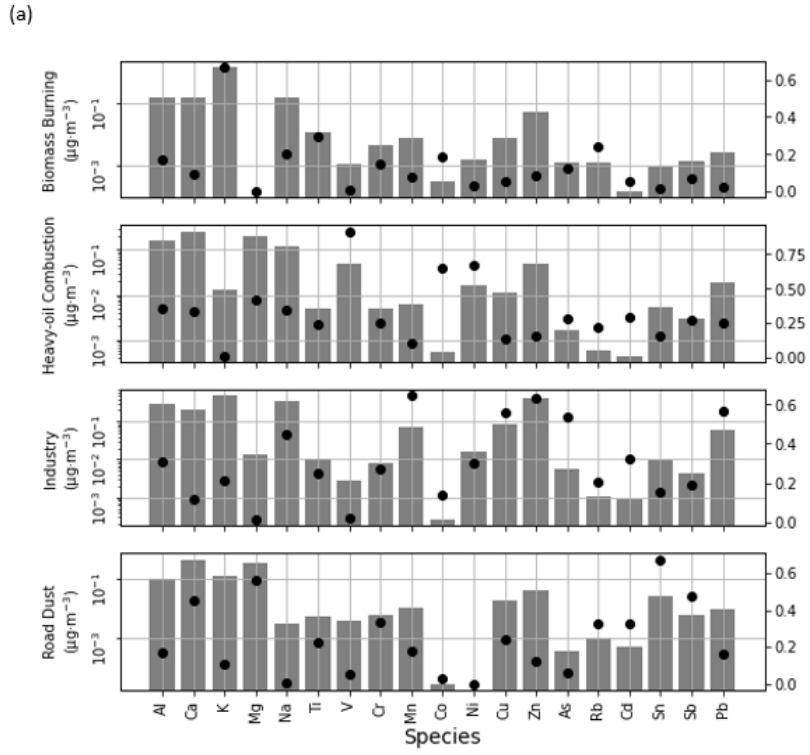

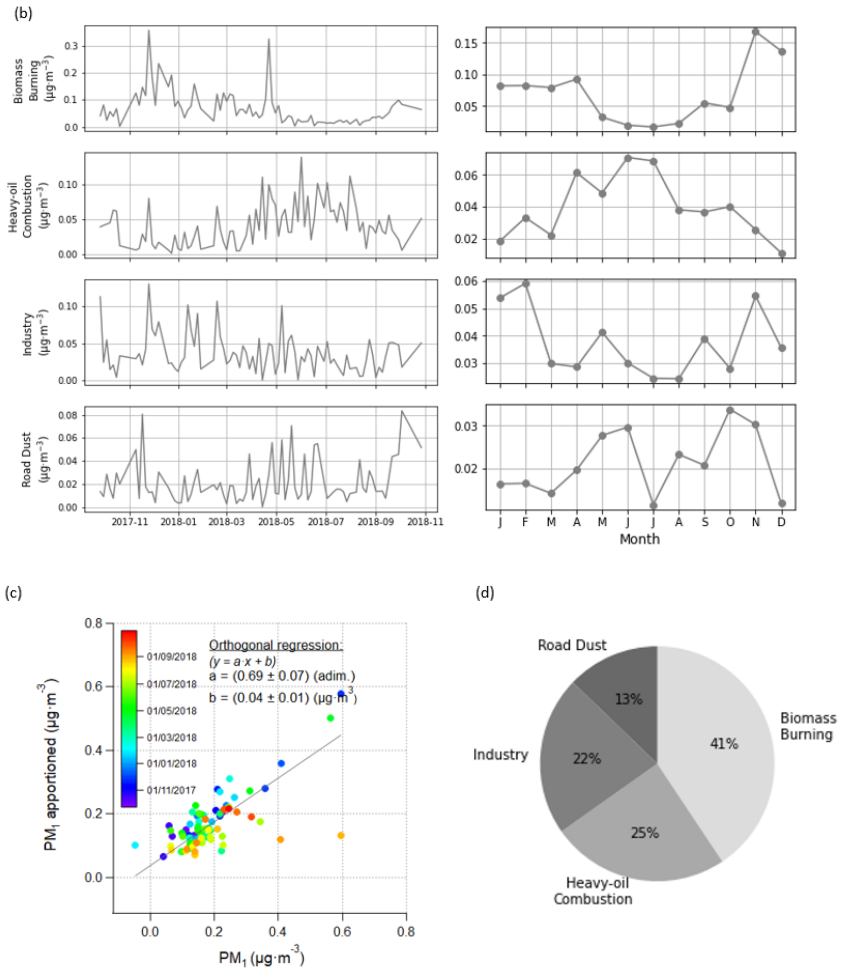

Figure S5. Source apportionment of the low-resolution dataset. (a) Profiles. (b) Time series and monthly cycles. (c) Mass closure. (d) Pie of apportionment. For the profiles plot, bars (left axis) show the normalised concentrations of each species in each factor, circles (right axis) show the percentage of each species attributed to each factor.

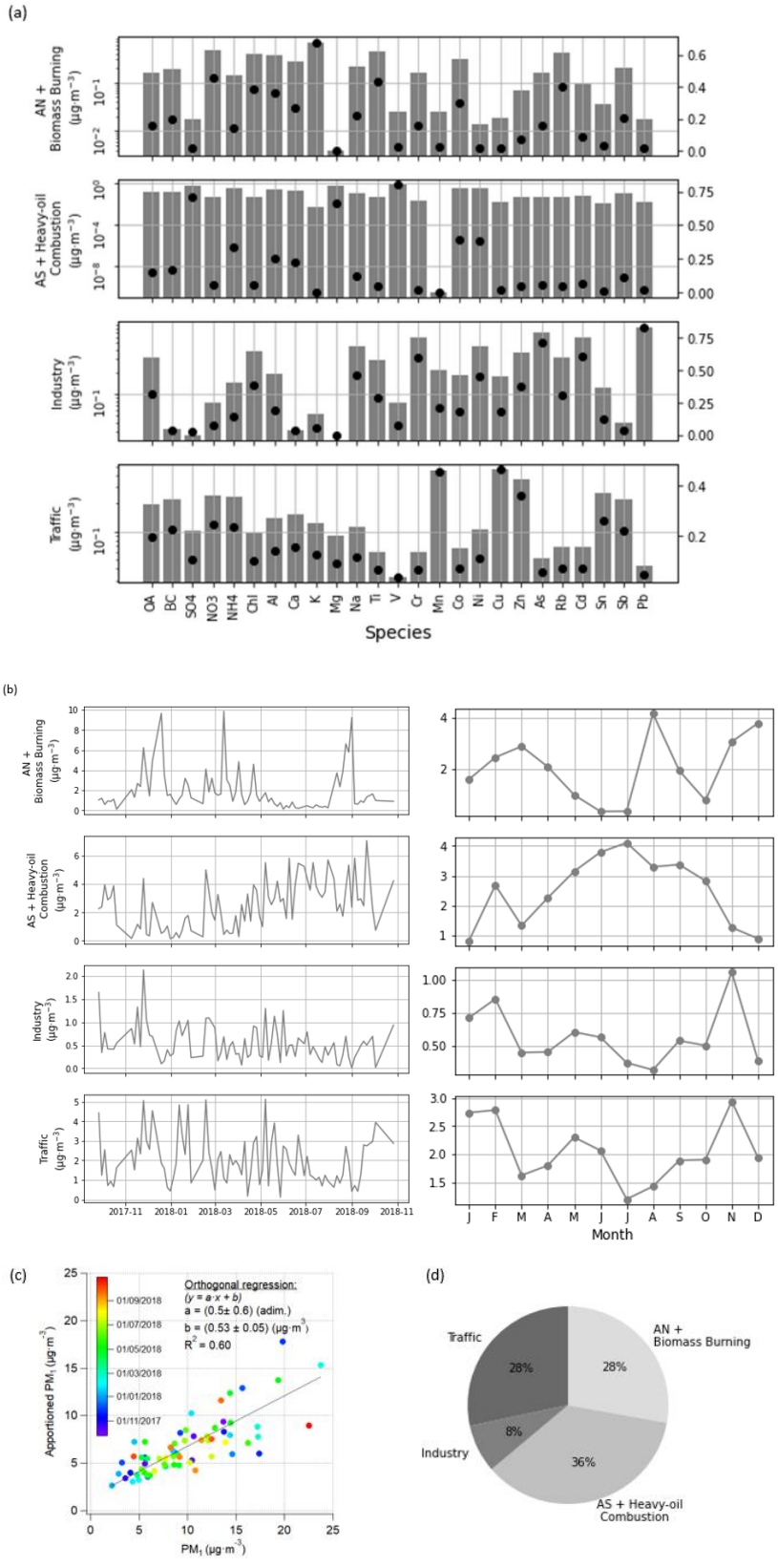

Figure S6. Source apportionment of the pseudo-conventional dataset. (a) Profiles. (b) Time series and monthly cycles. (c) Mass closure. (d) Pie of apportionment. For the profiles plot, bars (left axis) show the normalised concentrations of each species in each factor, circles (right axis) show the percentage of each species attributed to each factor.

(a)

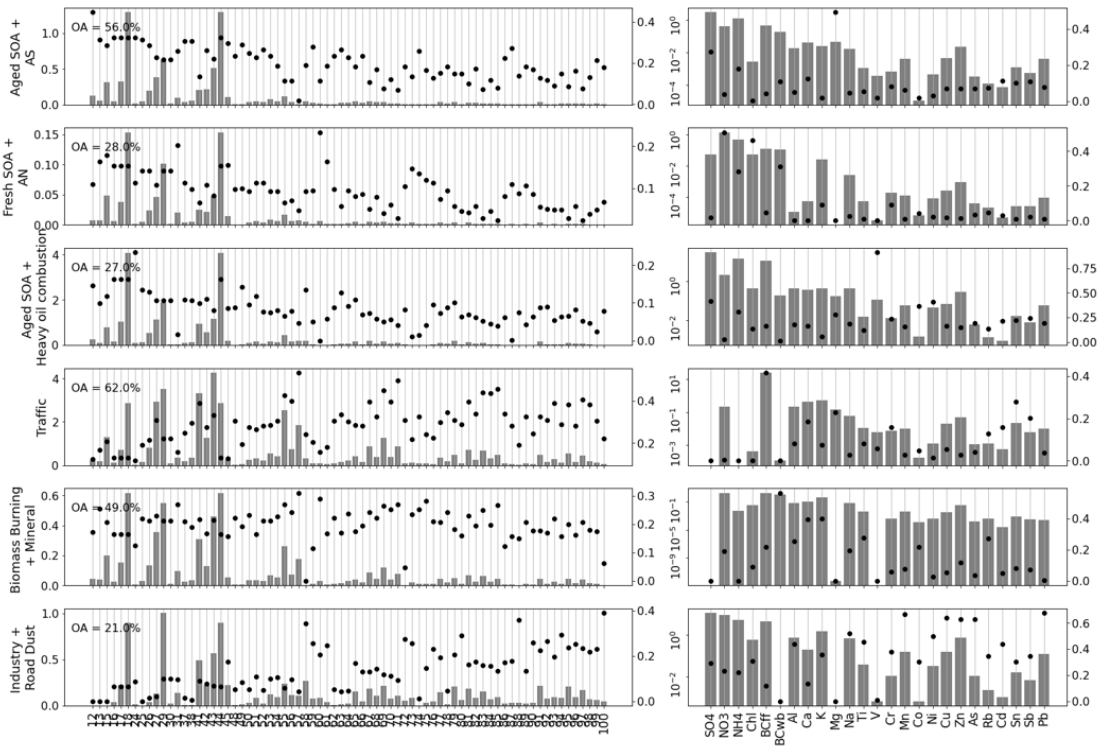
Aged SOA + AS
OA = 56.0%
Fresh SOA + AN
OA = 28.0%
Aged SOA + Heavy oil combustion
OA = 27.0%
Traffic
OA = 62.0%
Biomass Burning + Mineral
OA = 49.0%
Industry + Road Dust
OA = 21.0%
SO4 NO3 NH4 Chl BCff BCwb Al Ca K Mg Na Ti V Cr Mn Co Ni Cu Zn As Rb Cd Sn Sb Pb

49

(b)

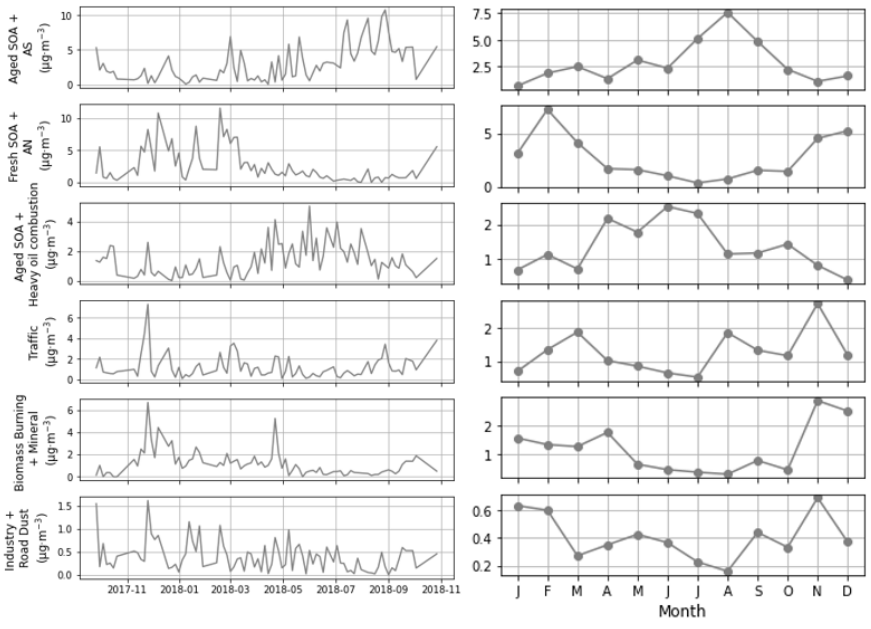
Aged SOA + AS (μg·m⁻³)
Fresh SOA + AN (μg·m⁻³)
Aged SOA + Heavy oil combustion (μg·m⁻³)
Traffic (μg·m⁻³)
Biomass Burning + Mineral (μg·m⁻³)
Industry + Road Dust (μg·m⁻³)
2017-11 2018-01 2018-03 2018-05 2018-07 2018-09 2018-11
J F M A M J J A S O N D
Month

50

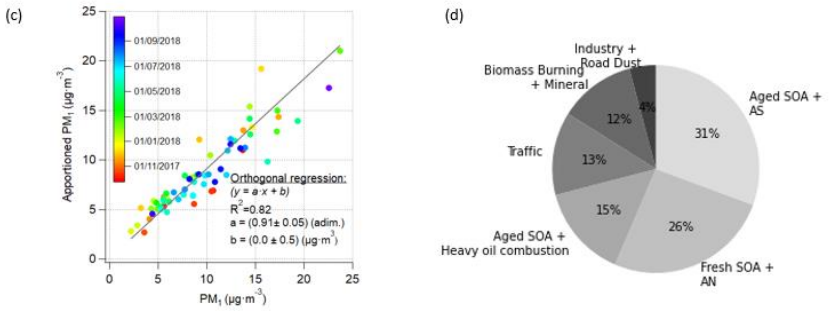

51

52 **Figure S7. Source apportionment of the base case dataset. (a) Profiles. (b) Time series and**
53 **monthly cycles. (c) Mass closure. (d) Pie of apportionment. For the profiles plot, bars (left**
54 **axis) show the normalised concentrations of each species in each factor, circles (right axis)**
55 **show the percentage of each species attributed to each factor, and percentages show the**
56 **proportion of OA to the total mass of that factor. Also, the left panel is dedicated to the**
57 **unit-mass-resolution OA species and the right one (in log scale) to the rest of the species.**

58

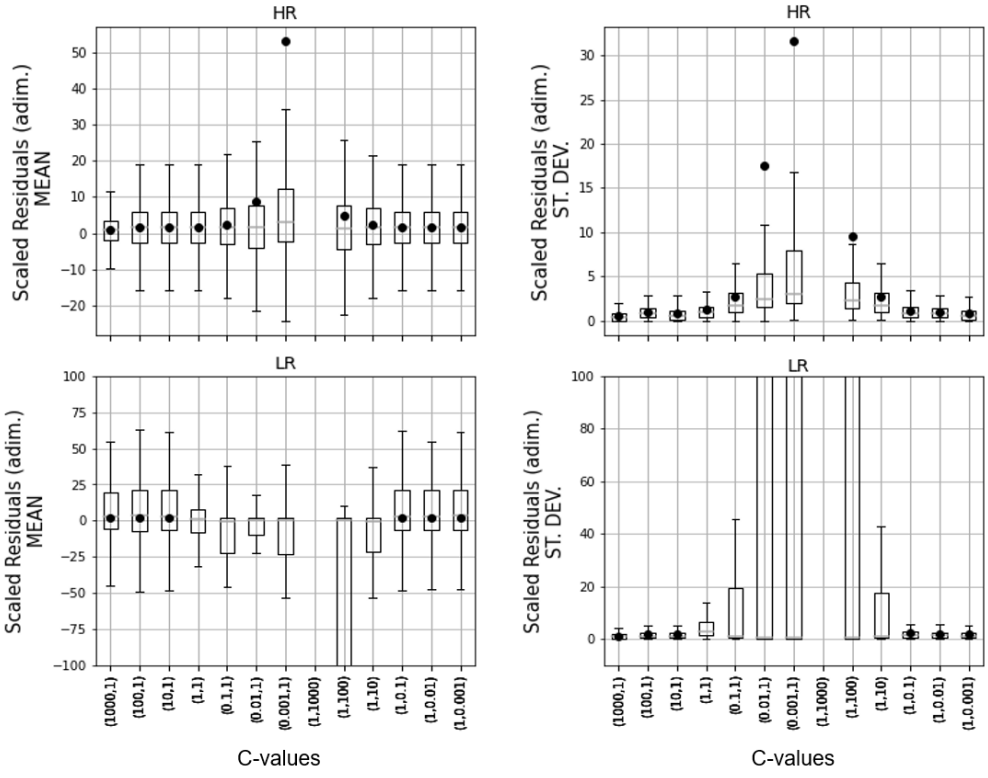

59

60

61 **Figure S8. HR (top) and LR (bottom) scaled residuals mean (left) and standard deviation**
62 **(right) for all C values. Boxes show the Q1–Q3 range with the median (horizontal line) and**
63 **the mean (circles), and whiskers extend up to the 1.5*IQR range (IQR=Q3-Q1).**

64

65

66

67

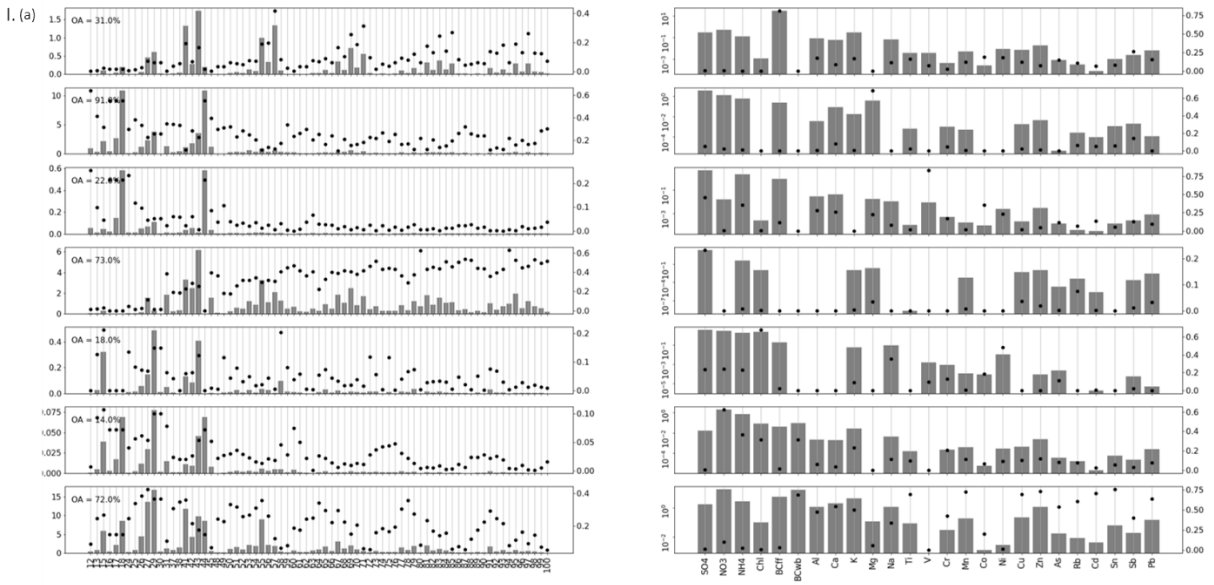
I. (a)
OA = 31.0%
OA = 91.0%
OA = 22.0%
OA = 73.0%
OA = 18.0%
OA = 14.0%
OA = 72.0%
SO4
NO3
NH4
Chl
BCff
BCwb
Al
Ca
K
Mg
Na
Ti
V
Cr
Mn
Co
Ni
Cu
Zn
As
Rb
Cd
Sn
Sb
Pb

68

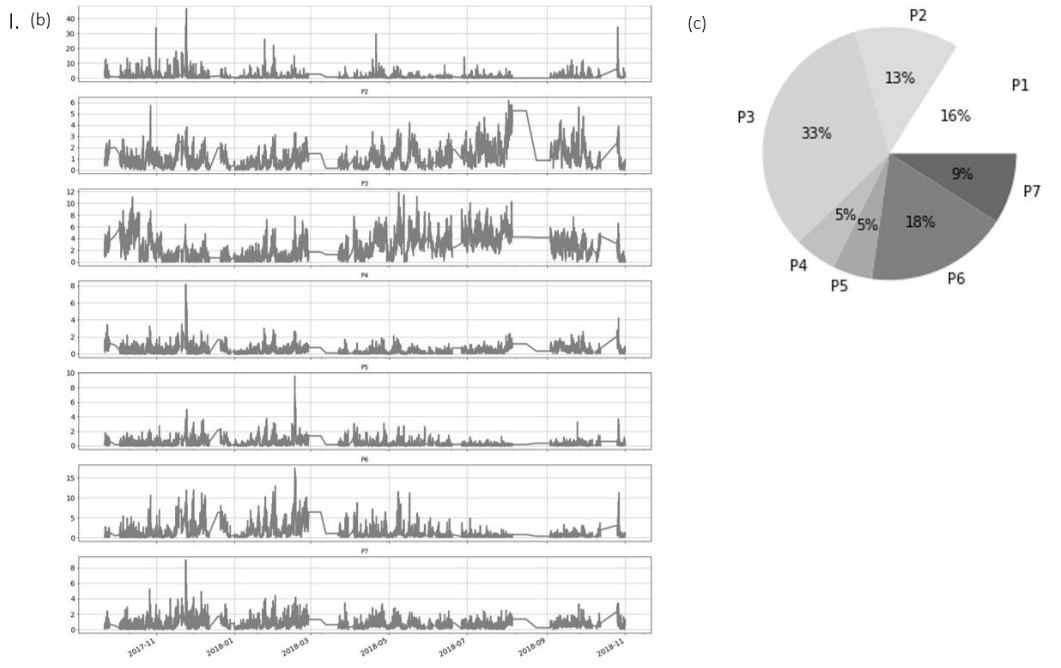
I. (b)
P2
P3
P4
P5
P6
P7
2017-11
2018-01
2018-03
2018-05
2018-07
2018-09
2018-11
(c)
P1
P2
P3
P4
P5
P6
P7
13%
16%
33%
9%
5%
5%
18%

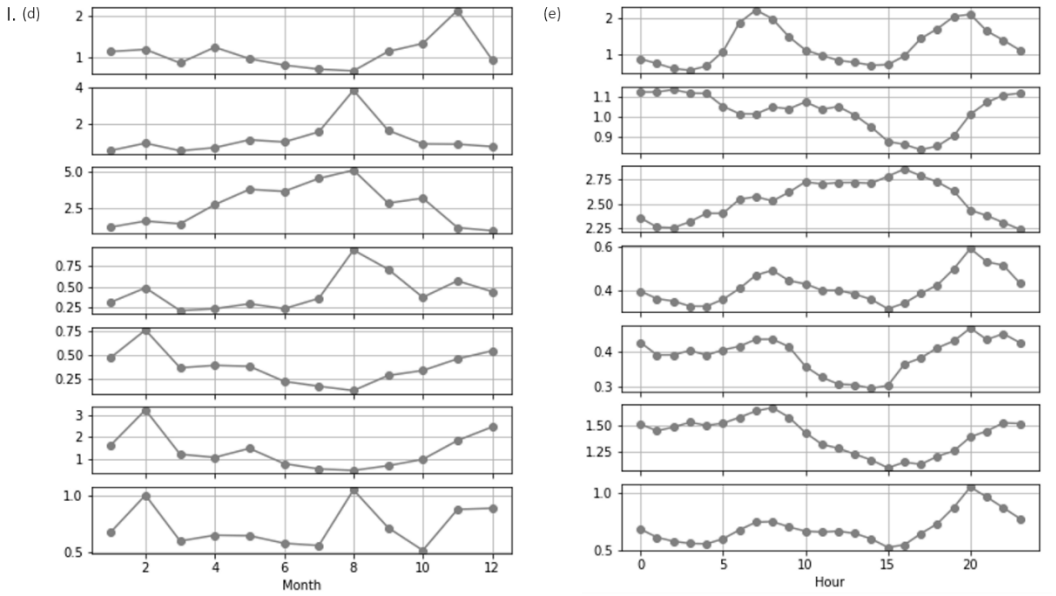
I. (d)
(e)
Month
Hour

69

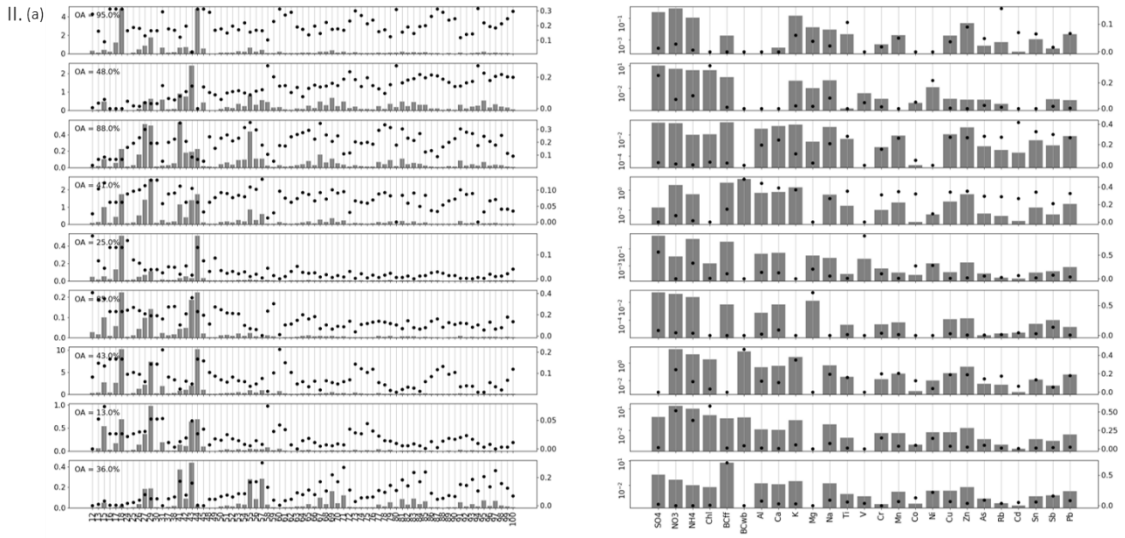
II. (a)
SO4
NO3
NH4
Chl
BCff
BCwb
Al
Ca
K
Mg
Na
Ti
V
Cr
Mn
Co
Ni
Cu
Zn
As
Rb
Cd
Sn
Sb
Pb

70

71

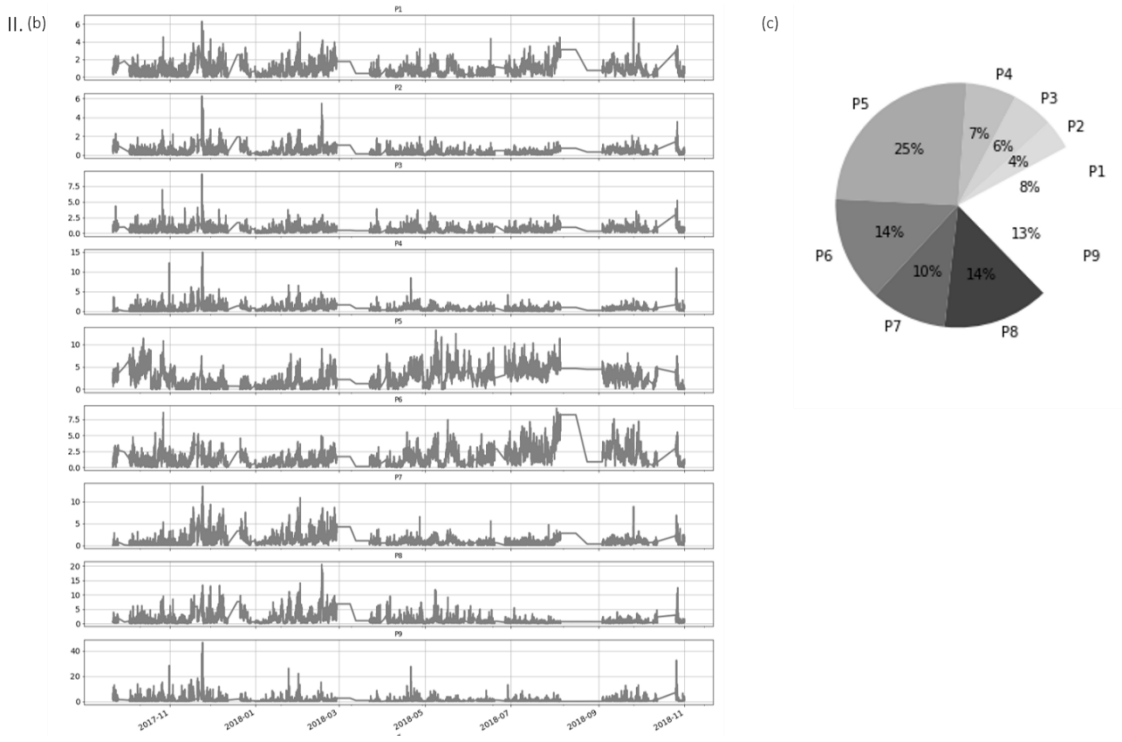

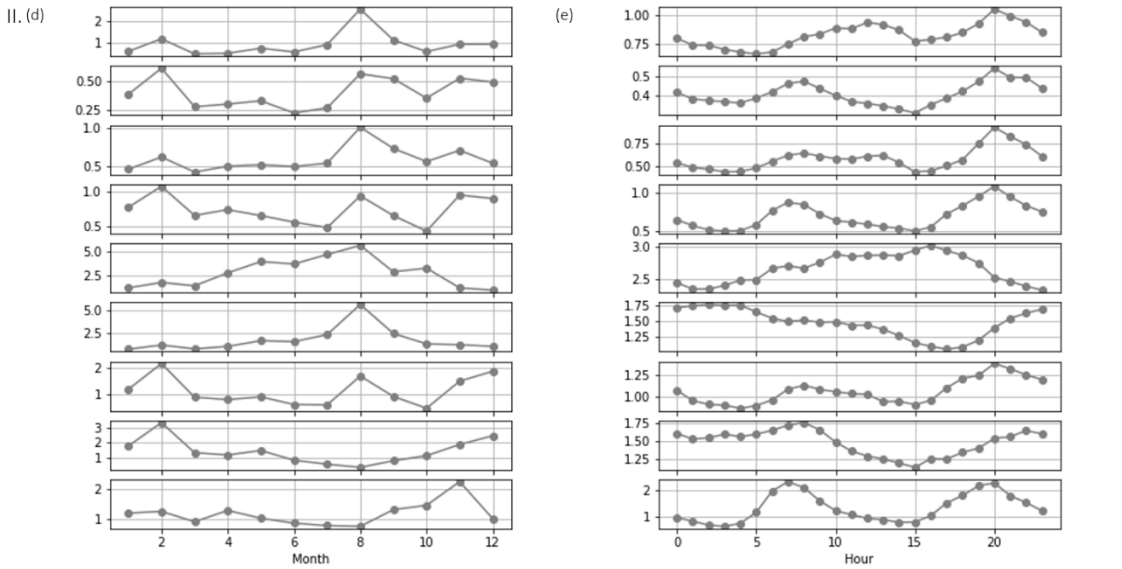

Figure S9. Source apportionment results for the multi-time resolution dataset with I. one less factor II. one more factor respect to the chosen solution. (a) Profiles. (b) Time series. (c) Pie of apportionment. (d) Monthly plot. (e) Diel plot. For the profiles plot, bars (left axis) show the normalised concentrations of each species in each factor, circles (right axis) show the percentage of each species attributed to each factor, and percentages show the proportion of OA to the total mass of that factor. Also, the left panel is dedicated to the unit-mass-resolution OA species and the right one (in log scale) to the rest of the species.

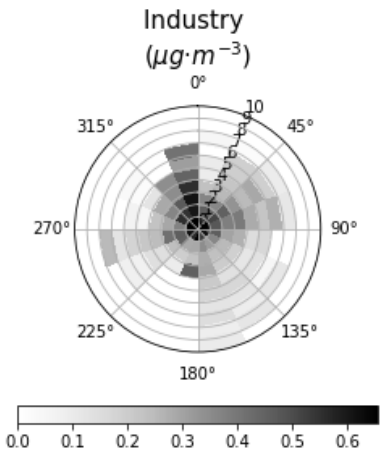

Figure S10. Pollution rose of the industry factor. Concentrations of the industrial factor are depicted in µg·m-3 sorted by wind direction (angular axis) and speed (in m/s, radial axis).

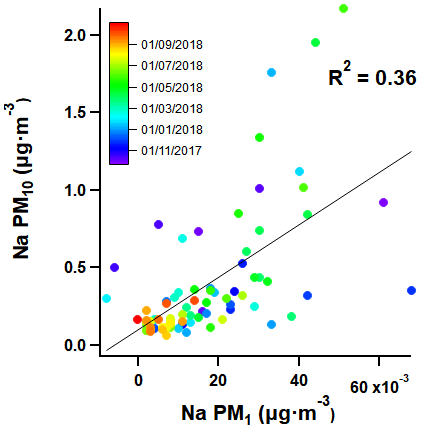

Figure S11. Scatter plots of PM_{10} vs. PM_1 concentrations for Na.

Section B. Profile k-means clustering.

Clustering, according to Rani and Rohil (2013), can be defined as grouping of data into classes or clusters, so that objects within a cluster have high similarity in comparison to one another but are very dissimilar to objects in other clusters. Clustering methods can be classified into partitioning and hierarchical, depending on if the whole data is split into the several clusters or if the individual objects are agglomerated until solid clusters are created, respectively. This study uses the so-called *k-means* clustering approach (Hartigan and Wong, 1979), an un-supervised partitioning approach based in the partitioning of *n* observations into *k* clusters. This algorithm launches *k* random cluster centres (hereinafter centroids) and assigns each observation to the nearest centroid based on the squared Euclidean distance. The centroids coordinates are then redefined as the average of all the belonging observations coordinates and the process is repeated to assign to the observations the closest cluster centroid. This operation is iteratively repeated until convergence is reached, this is, until the centroids and clustering observations assignation are stable over iterations.

k-means clustering is applied to the profiles of all runs of the final MTR-PMF solution. The number of clusters is set to match the number of factors of the run. This method can group similar profiles into different clusters, allowing for great similarity of profiles within a cluster but also distinction to other factor profiles. The mean and standard deviation of the profiles of the same

cluster is retrieved. The time series, relative contributions and explained variations are obtained averaging all the data of the factors belonging to the same profile cluster. The slope of the standard deviation vs. the mean of the time series in percentage are, respectively, a 42%, 47%, 49%, 13%, 49%, 48%, 37%, 36% for the AS+ Heavy oil combustion, AN + ACl, Aged SOA, traffic, biomass burning, fresh SOA, COA, and industry factors.

Figure S12 contains the profiles outcoming clustering and their standard deviations:

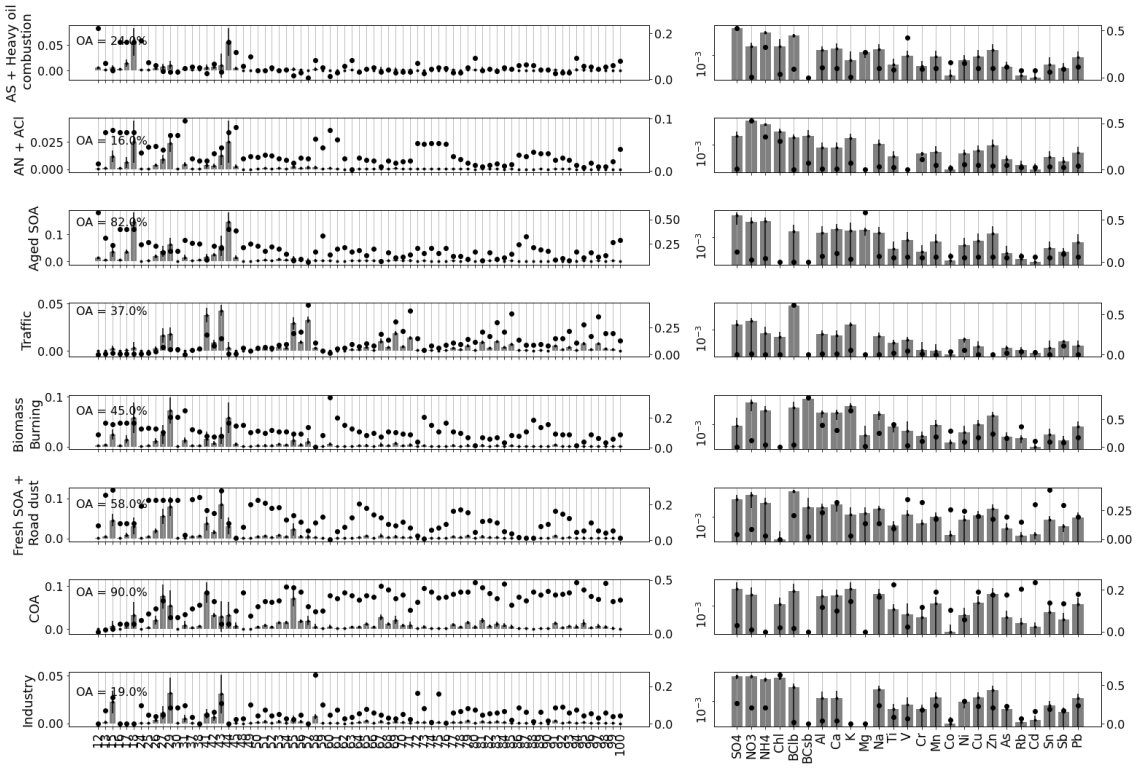

Figure S12. MTR-PMF solution profiles with clustering error estimation for the mass concentrations in error bars. Analogously to the other figures, the points refer to the relative contribution of each species in each factor, and the left panel shows the OA species and the right panel the SIA, BC, metals species in log scale.

These errors are in most cases dragging all metals to zero concentrations, indicating the high variability in attribution amongst profiles considered similar. An exception is the stability of K attributed by the biomass burning source. However, regarding OA *m/z*s, SIA and BC, the key markers of each factor are stable, e.g. SO_4^{2+} and NH_4^+ for AS + heavy oil combustion, NO_3^- and NH_4^+ for the AN + ACl, *m/z44* for the aged SOA etc.

Section C. LR dataset source apportionment

The PMF outcomes resulted in four sources, shown in Figure S6: Biomass burning (44%), Heavy-oil combustion (25%), Industry (22%) and Road dust (13%) (Fig. S5d). The biomass burning factor apportions almost all of the K mass (Fig. S5a) as was expected since a 97% of this ion in PM_1 is attributed to biomass burning in Reche et al., (2012). This factor is sufficiently described by this ion, as in (Dall'Osto et al., 2013). It contains some Ti, Rb mass as well, probably due to certain mineral dust apportionment (Fig. S5a). The time series and monthly patterns underline this source seasonality, with a marked increase in cold months (Fig S5b). The shipping profile (Fig. S5a) presents significantly high levels of Ni and V metals related to heavy oil combustion

in shipping in other studies (Moldanová et al., 2009; Pandolfi et al., 2011) with a ratio of 3.15, comparable to that report mentioned. There is also a remarkably high concentration of Co in this factor, driven as well from the oil composition (Corbin et al., 2018; Duyck et al., 2007). This source increases during the warm period, related to the advection of maritime plumes enhanced by the summer breeze development (Fig. S5b). The industry factor was characterized by industrial markers such as Mn, Zn, Cu, As, Pb as the western industrial sources in Brines et al. (2019) (Fig. S5a). The time series of this factor does not show a significant seasonality (S5b). The road dust factor was identified by the significative content of non-exhaust traffic markers (Sn, Sb) and mineral ions (Mg, Ca, Al, Ti, Rb, Fig. S5a), resuspended by traffic, especially during the summer dry months, as the time series in Figure S5b confirms.

Section D. Solution error

The solution error assessment must account for three kinds of errors: rotational ambiguity error and clustering error. The latter is conceived as the standard deviation of the clustering standard deviation, accounting for the inter-profile variability amongst a cluster.

The statistical error is estimated in SA in SoFi by means of the bootstrap technique (Efron, 1979). This technique consists on the variation quantification within the identified factors when resampling modifications on the input are done. These variations over the factors allow to estimate the statistical uncertainty. However, in the current study, in which the bootstrap technique is not stable for the MTR-PMF in SoFi for the current data subset and will not be evaluated.

The rotational ambiguity accounts for the amount of error committed due to the multiple solutions **G**, **F** with the same Q value (Henry, 1987). For this error assessment, Mooibroek et al. (2022) and Paatero et al. (2014) conceived the DISP technique, in which with a controlled dQ, profiles were slightly displaced. The variability in the outcoming factors accounted for this rotational ambiguity. This method has been adapted to SoFi as follows. The solution profiles are constrained with a random a-value from 0.05 to 0.95 for all species. Then only the outcoming sources with a $d(Q/Q_{exp})$ of 0.14 are selected, analogously to the DISP method. The variability of the selected solutions should be an assessment of the error committed due to the rotational ambiguity.

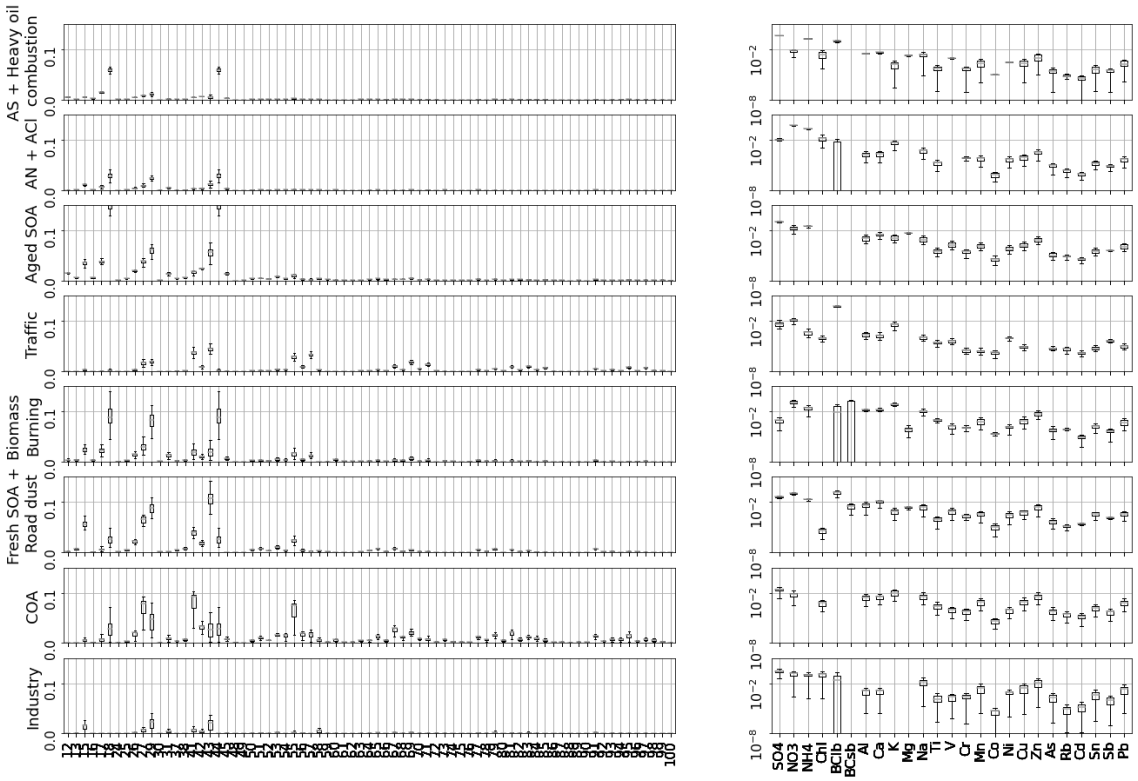

Figure S13. MTR solution profiles containing their variability due to rotational ambiguity. The boxes account for the Q1, Q2 range, the horizontal lines for the median values and the whiskers for the 1.5*IQR (IQR = Q3-Q1). Analogously to the other figures, the points refer to the relative contribution of each species in each factor, and the left panel shows the OA species and the right panel the SIA, BC, metals species in log scale.

Figure S13 represents the rotational ambiguity of each factor its profiles. In this graph, the narrower the boxes are, the more rotational error for that species.

- AS + heavy oil combustion: the rotational stability of this compound is high, especially for the key species such as the SO_4^{2+}, NH_4^+, V, Co, and Ni.
- AN + ACl: The rotational error is low for the key ions NO_3^-, NH_4^+, and Cl^-, but he BC_{lb} is rather unstable. However, this specie is not relevant in this source.
- Aged SOA: stability of this factor is high.
- Traffic: The main key species for this ion such as *m/z57* and BC_{lb} are very stable.
- Biomass burning: The m/z44 of this factor is rather unstable, indicating an unstable degree of ageing of the biomass burning factor. The biomass burning factors m/z60, m/z73 and K are rather stable, however, the BC_{sb} (another biomass burning marker) attribution is less robust.
- Fresh SOA + Road dust: Even if the variability of m/z43 is higher than in other factors, its range of variability would not imply a sufficient change of the *m/z43*-to-*m/z44* ratio to acknowledge it as an aged SOA factor. The BC_{lb}, Sn, and Sb, boxes are rather narrow, reinforcing the influence of traffic in this factor.
- COA: The rotational ambiguity of this factor key ions (m/z55, m/z29, m/z41) is not negligible but even if these species went to the lowest concentration of the range in the boxplots, the factor would still be ascertained as a COA.
- Industry: The profile is rather stable except for the BClb, which is not relevant to this factor.

Hereinunder, the clustering (e_c) and rotational (e_r) errors are shown in errorbars, as well as their error propagation, calculated as:

$$e = \sqrt{e_c^2 + e_r^2} \quad (1)$$

The Figure S14 contains the total errors as errorbars.

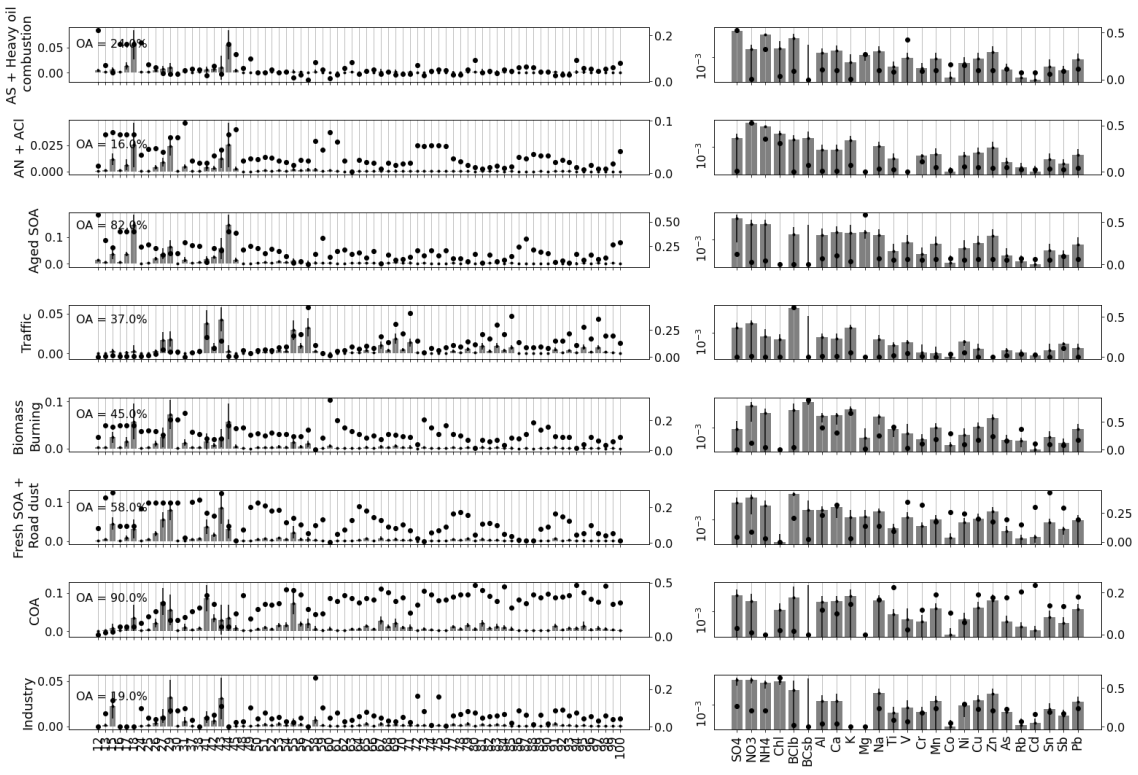

Figure S14. MTR solution profiles containing the total error assessment, depicted as error bars, of the solution profiles, accounting the variability due to rotational ambiguity and clustering. Analogously to the other figures, the points refer to the relative contribution of each species in each factor, and the left panel shows the OA species and the right panel the SIA, BC, metals species in log scale.

Section E. Better environmental feasibility of the (1,5) weightings SA respect to that of (1,2)

From a mathematical point of view, the solution whose weightings were optimal due to the maximum match of $F_{overlap}$ with $F^*_{overlap}$ (43.4%) was that of (C_{HR}, C_{LR}) = (1,2). For this case, the $F_{overlap}$ was 43%. Nevertheless, the environmental feasibility of SA results was also checked for those combinations of $F_{overlap}$ >35%, which were (1,0.1), (1,0.2), (1,0.5), and (1,5), and only the latter provided sources of environmental accuracy. Indeed, the SA results of this weighting combination were more advantageous respect to those of the mathematically optimal solution of weightings of (C_{HR}, C_{LR}) = (1,2). Here, this disregarded solution is presented in terms of profiles, time series, mass closure, pie of apportionment and monthly and seasonal diel cycles.

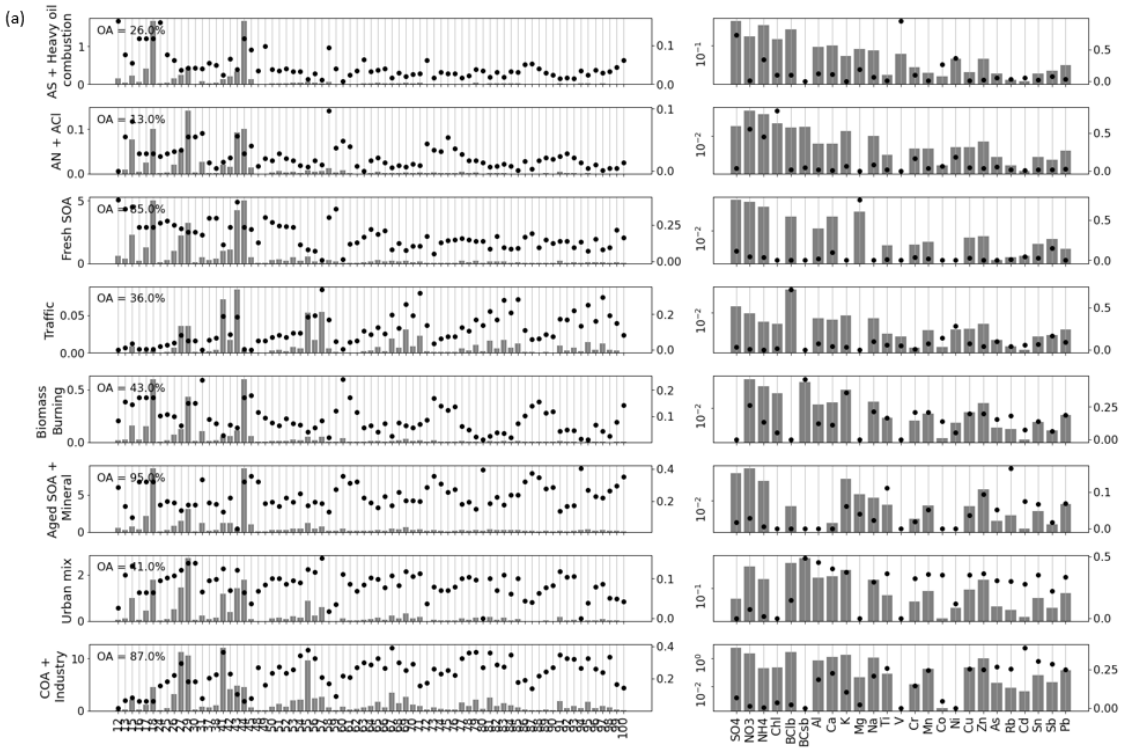
(a)
AS + Heavy oil combustion
OA = 26.0%
AN + ACI
OA = 13.0%
Fresh SOA
OA = 85.0%
Traffic
OA = 36.0%
Biomass Burning
OA = 43.0%
Aged SOA + Mineral
OA = 95.0%
Urban mix
OA = 41.0%
COA + Industry
OA = 87.0%
SO4 NO3 NH4 Chl BCib BCsb Al Ca K Mg Na Ti V Cr Mn Co Ni Cu Zn As Rb Cd Sn Sb Pb

208

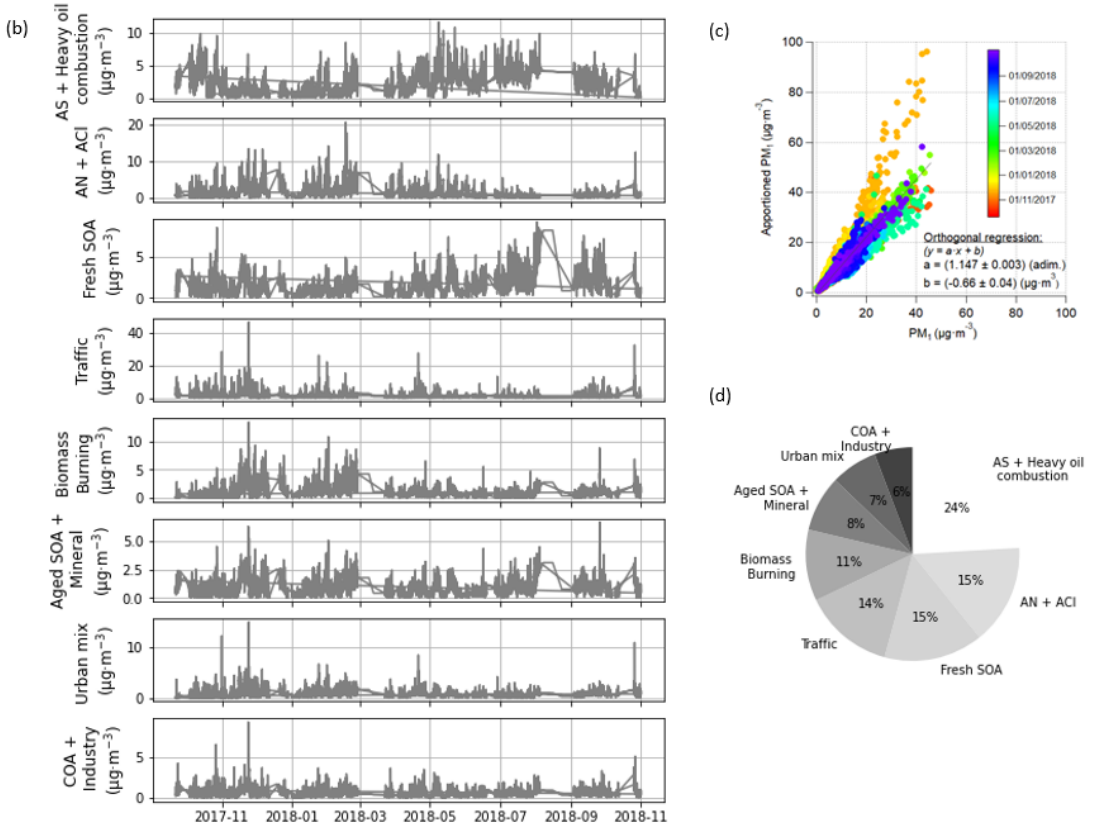
(b)
AS + Heavy oil combustion (µg·m⁻³)
AN + ACI (µg·m⁻³)
Fresh SOA (µg·m⁻³)
Traffic (µg·m⁻³)
Biomass Burning (µg·m⁻³)
Aged SOA + Mineral (µg·m⁻³)
Urban mix (µg·m⁻³)
COA + Industry (µg·m⁻³)
2017-11 2018-01 2018-03 2018-05 2018-07 2018-09 2018-11
(c)
Apportioned PM$_1$ (µg·m^{-3})
PM$_1$ (µg·m^{-3})
01/09/2018
01/07/2018
01/05/2018
01/03/2018
01/01/2018
01/11/2017
Orthogonal regression:
(y = a·x + b)
a = (1.147 ± 0.003) (adim.)
b = (-0.66 ± 0.04) (µg·m^{-3})
(d)
COA + Industry
Urban mix
AS + Heavy oil combustion
Aged SOA + Mineral
Biomass Burning
AN + ACI
Traffic
Fresh SOA
6%
7%
24%
8%
11%
15%
14%
15%

209

210

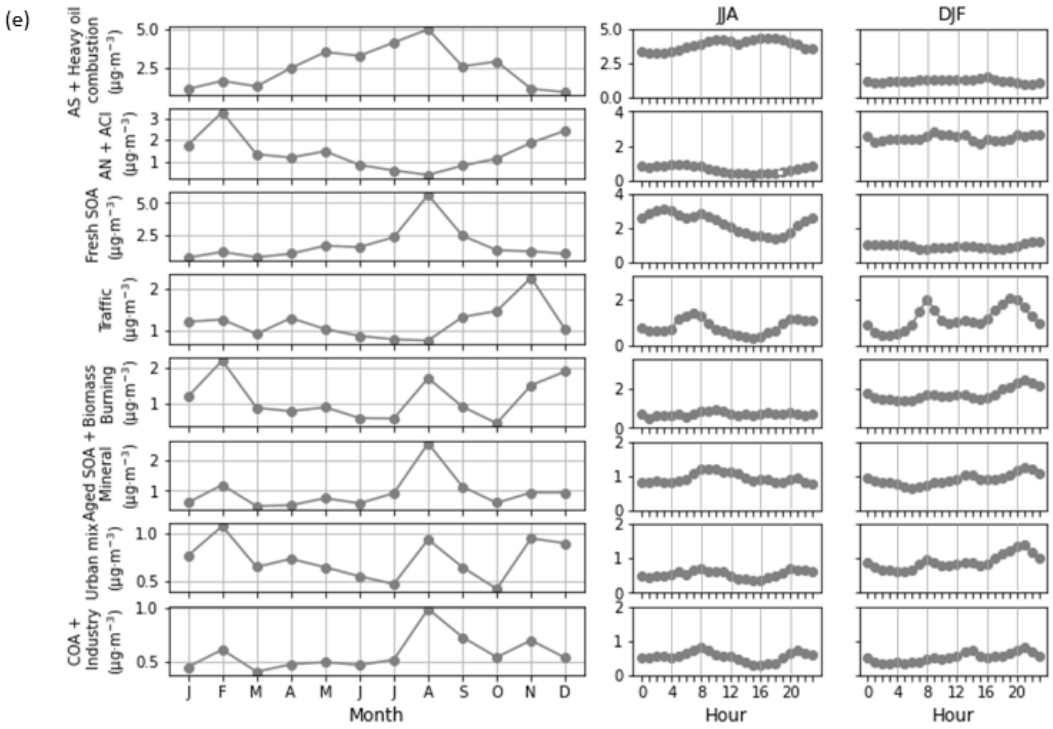

Figure S15. MTR solution of the C_{HR}, C_{LR} = (1, 5) combination. (a) Profiles. (b) Time series. (c) Mass closure. (d) Pie of apportionment. (e) Monthly and summer diel and winter diel cycles plots, from left to right. For the profiles plot, bars (left axis) show the normalised concentrations of each species in each factor, circles (right axis) show the percentage of each species attributed to each factor, and percentages show the proportion of OA to the total mass of that factor. Also, the left panel is dedicated to the unit-mass-resolution OA species and the right one (in log scale) to the rest of the species.

The main advantages of the (1,5) solution (Fig. 7) respect to that from Figure S15 are:

- The COA and the industrial sources are disentangled meaningfully.

- This differentiation of COA and industrial factor caused the urban mix factor to disappear in the chosen solution. This factor was not revealing any emission source but combining all those PMF species which were not attributed to any other source.

- The SOA fresh/aged factors are reversed in terms of mass apportionment. The chosen solution shows greater aged SOA proportion, which is more sensible as this was reported like that in (Via et al., 2021).

- The fresh SOA in the chosen solution presents some traffic markers as well. This association reveals that SOA formation could be triggered by traffic emissions.

For all these reasons, the (C_{HR}, C_{LR}) = (1,5) solution was selected instead of the mathematically optimal solution.

Bibliography

Brines, M., Dall'Osto, M., Amato, F., Minguillón, M. C., Karanasiou, A., Grimalt, J. O., Alastuey, A., Querol, X. and van Drooge, B. L.: Source apportionment of urban PM1 in

Barcelona during SAPUSS using organic and inorganic components, Environ. Sci. Pollut. Res., 26(31), 32114–32127, doi:10.1007/s11356-019-06199-3, 2019.

Corbin, J. C., Mensah, A. A., Pieber, S. M., Orasche, J., Michalke, B., Zanatta, M., Czech, H., Massabò, D., Buatier De Mongeot, F., Mennucci, C., El Haddad, I., Kumar, N. K., Stengel, B., Huang, Y., Zimmermann, R., Prévôt, A. S. H. and Gysel, M.: Trace Metals in Soot and PM2.5 from Heavy-Fuel-Oil Combustion in a Marine Engine, Environ. Sci. Technol., 52(11), 6714–6722, doi:10.1021/acs.est.8b01764, 2018.

Dall'Osto, M., Querol, X., Amato, F., Karanasiou, A., Lucarelli, F., Nava, S., Calzolai, G. and Chiari, M.: Hourly elemental concentrations in PM2.5 aerosols sampled simultaneously at urban background and road site during SAPUSS -diurnal variations and PMF receptor modelling, Atmos. Chem. Phys., 13(8), 4375–4392, doi:10.5194/acp-13-4375-2013, 2013.

Duyck, C., Miekeley, N., Porto da Silveira, C. L., Aucélio, R. Q., Campos, R. C., Grinberg, P. and Brandão, G. P.: The determination of trace elements in crude oil and its heavy fractions by atomic spectrometry, Spectrochim. Acta - Part B At. Spectrosc., 62(9), 939–951, doi:10.1016/j.sab.2007.04.013, 2007.

Efron, B.: Bootstrap Methods: Another Look at the Jackknife, Ann. Stat., 7(1), doi:10.1214/aos/1176344552, 1979.

Hartigan, J. A. . and Wong, M. . A. .: Algorithm AS 136 : A K-Means Clustering Algorithm Author (s): J Published by : Wiley for the Royal Statistical Society Stable URL : http://www.jstor.org/stable/2346830, J. R. Stat. Soc. Ser. C (Applied Stat., 28(1), 100–108, 1979.

Henry, R. C.: Current factor analysis receptor models are ill-posed, Atmos. Environ., 21(8), 1815–1820, doi:10.1016/0004-6981(87)90122-3, 1987.

Moldanová, J., Fridell, E., Popovicheva, O., Demirdjian, B., Tishkova, V., Faccinetto, A. and Focsa, C.: Characterisation of particulate matter and gaseous emissions from a large ship diesel engine, Atmos. Environ., 43(16), 2632–2641, doi:10.1016/j.atmosenv.2009.02.008, 2009.

Mooibroek, D., Sofowote, U. M. and Hopke, P. K.: Source apportionment of ambient PM10 collected at three sites in an urban-industrial area with multi-time resolution factor analyses, Sci. Total Environ., 850(April), 157981, doi:10.1016/j.scitotenv.2022.157981, 2022.

Paatero, P., Eberly, S., Brown, S. G. and Norris, G. A.: Methods for estimating uncertainty in factor analytic solutions, Atmos. Meas. Tech., 7(3), 781–797, doi:10.5194/amt-7-781-2014, 2014.

Pandolfi, M., Gonzalez-Castanedo, Y., Alastuey, A., de la Rosa, J. D., Mantilla, E., de la Campa, A. S., Querol, X., Pey, J., Amato, F. and Moreno, T.: Source apportionment of PM10 and PM2.5 at multiple sites in the strait of Gibraltar by PMF: Impact of shipping emissions, Environ. Sci. Pollut. Res., 18(2), 260–269, doi:10.1007/s11356-010-0373-4, 2011.

Rani, Y. and Rohil, H.: A study of hierarchical clustering algorithms, 2015 Int. Conf. Comput. Sustain. Glob. Dev. INDIACom 2015, 3(10), 537–541, 2013.

Reche, C., Viana, M., Amato, F., Alastuey, A., Moreno, T., Hillamo, R., Teinilä, K., Saarnio, K., Seco, R., Peñuelas, J., Mohr, C., Prévôt, A. S. H. and Querol, X.: Biomass burning contributions to urban aerosols in a coastal Mediterranean City, Sci. Total Environ., 427–428, 175–190, doi:10.1016/j.scitotenv.2012.04.012, 2012.

Via, M., Minguillón, M. C., Reche, C., Querol, X. and Alastuey, A.: Increase in secondary organic aerosol in an urban environment, Atmos. Chem. Phys., 21(10), 8323–8339, doi:10.5194/acp-21-8323-2021, 2021.

DECLARATION

The authors declare that they have no conflict of interest.

Barcelona, May 2023

Marta Via González


idaea
INSTITUTO DE DIAGNÓSTICO AMBIENTAL Y ESTUDIOS DEL AGUA


EXCELENCIA
SEVERO
OCHOA


CSIC
CONSEJO SUPERIOR DE INVESTIGACIONES CIENTÍFICAS